



## **Terms and Conditions of Use of Digitised Theses from Trinity College Library Dublin**

### **Copyright statement**

All material supplied by Trinity College Library is protected by copyright (under the Copyright and Related Rights Act, 2000 as amended) and other relevant Intellectual Property Rights. By accessing and using a Digitised Thesis from Trinity College Library you acknowledge that all Intellectual Property Rights in any Works supplied are the sole and exclusive property of the copyright and/or other IPR holder. Specific copyright holders may not be explicitly identified. Use of materials from other sources within a thesis should not be construed as a claim over them.

A non-exclusive, non-transferable licence is hereby granted to those using or reproducing, in whole or in part, the material for valid purposes, providing the copyright owners are acknowledged using the normal conventions. Where specific permission to use material is required, this is identified and such permission must be sought from the copyright holder or agency cited.

### **Liability statement**

By using a Digitised Thesis, I accept that Trinity College Dublin bears no legal responsibility for the accuracy, legality or comprehensiveness of materials contained within the thesis, and that Trinity College Dublin accepts no liability for indirect, consequential, or incidental, damages or losses arising from use of the thesis for whatever reason. Information located in a thesis may be subject to specific use constraints, details of which may not be explicitly described. It is the responsibility of potential and actual users to be aware of such constraints and to abide by them. By making use of material from a digitised thesis, you accept these copyright and disclaimer provisions. Where it is brought to the attention of Trinity College Library that there may be a breach of copyright or other restraint, it is the policy to withdraw or take down access to a thesis while the issue is being resolved.

### **Access Agreement**

By using a Digitised Thesis from Trinity College Library you are bound by the following Terms & Conditions. Please read them carefully.

I have read and I understand the following statement: All material supplied via a Digitised Thesis from Trinity College Library is protected by copyright and other intellectual property rights, and duplication or sale of all or part of any of a thesis is not permitted, except that material may be duplicated by you for your research use or for educational purposes in electronic or print form providing the copyright owners are acknowledged using the normal conventions. You must obtain permission for any other use. Electronic or print copies may not be offered, whether for sale or otherwise to anyone. This copy has been supplied on the understanding that it is copyright material and that no quotation from the thesis may be published without proper acknowledgement.

**Efficient methods for the computation of high  
frequency electromagnetic wave scattering from  
piecewise smooth surfaces using the integral  
equation formulation**

Luca Rossi

Department of Electronic and Electrical Engineering

University of Dublin

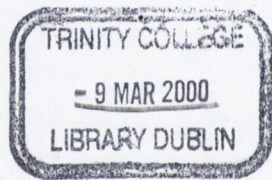
Trinity College

Submitted for the Degree of

Doctor of Philosophy

---

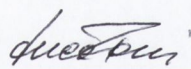
7th October 1999



*Thesis*  
5418

I, the undersigned, declare that this thesis is entirely my own work, except where otherwise accredited, and that it has not been submitted for a degree in any other university or institution. This thesis may be borrowed or copied upon request with the permission of the Librarian, University of Dublin, Trinity College.

Signed on the 7th of October 1999.



Luca Rossi

## ABSTRACT

---

The motivation for this work is the need for rigorous, efficient, accurate and robust computational methods for implementing deterministic radio wave propagation models to enable planners and operators make good use of UHF (Ultra High Frequency) wireless communication resources. The approach to propagation modelling is to abstract the real-world physical problem by a simpler physical problem containing those salient features judged to influence more strongly the behaviour of radio wave propagation. It is then argued that a physically exact surface integral equation formulation is a particularly appropriate starting point for making further progress towards the construction of a model. The philosophy being that it is better to strip down extraneous detail from an exact solution than to try to shore up inadequacies in an approximate starting position.

This thesis is concerned with efficient computational methods for the surface integral equations thus arising. The subject, then, of this thesis is time-harmonic electromagnetic wave scattering by very large (with respect to the wavelength of the incident field), piecewise-smooth perfect electrical conductors embedded in a homogeneous medium such as free space.

The early chapters establish the standard methods for handling such problems, including the Method of Moments (MoM). This is a technique used to discretise integral equations. For some illustrative problems numerical results are also presented.

Much of the thesis is concerned with methods speeding up iterative solutions of integral equations. One such method is the Fast Multipole Method (FMM). The FMM, being the basis of many of the novel efficient algorithms proposed, is outlined and its main principles are illustrated along with examples. It is compared

with standard numerical techniques used to solve discretised integral equations. In addition to the FMM, recently developed methods which have been applied to radio propagation modelling by the Trinity College group are reviewed. These include the Fast Far-Field Approximation (FAFFA) and the Tabulated Interaction Method (TIM).

The Tabulated Interaction Method is presented in more detail since one contribution of this thesis is to extend this method somewhat. The TIM is an efficient scheme for the computation of electromagnetic (EM) wave scattering from massive smooth conductors. Specifically, interactions between pairs of large subdomains are transmitted by plane waves travelling along the line connecting the subdomain centre-points, and the surface current density on linear subdomains of the surface is represented by a superposition of reference currents.

A novel extension of the TIM, referred to in this thesis as the Analytical Interaction Method (ANIM), renders it flexible by replacing the table with an approximate formula. This significantly reduces the storage requirement associated with TIM particularly if multiple frequencies or multiple facet sizes are in use. Numerical results are presented to demonstrate the accuracy of the proposed scheme and the computational complexity of ANIM is also discussed.

The Tabulated Interaction Method is then developed in matrix form. It is demonstrated that the matrix produced is sparse and a significant reduction in storage requirements may be achieved. The Tabulated Interaction Method is also applied to the problem of electromagnetic scattering by periodic structures. Numerical results are provided to demonstrate the possibility of tackling this class of problems with substantial storage and CPU time savings.

The remainder of the thesis is concerned with three-dimensional problems. The evaluation of the impedance matrix terms for the Electric Field Integral Equation when discretised using the Rao-Wilton-Glisson approach is considered in detail it being a key task in the work that follows. Specifically, the problem of the integration of the linear-shape functions times the three-dimensional Green's function on a

plane triangle is investigated. A simple fully numerical technique is introduced as an alternative to the typical approach recommended in the literature. Numerical results are provided to illustrate the accuracy of the new method proposed.

A novel development of a three-dimensional Multi-Level Fast Far-Field (MLFAFFA) approximation method for electromagnetic scattering by electrically large conductors is next presented. Its implementation is described in detail. Both the storage requirements and computational complexity of the new technique are carefully analysed. Numerical results comparing the scattered field and surface current density computed using the 3D MLFAFFA with reference solutions computed using traditional approaches are also presented. The agreement achieved is highly satisfactory.

The open question of how to carry the very substantial savings of TIM and ANIM over to fully three-dimensional problems is the final topic to be addressed in the thesis. While more work is required before this question can be considered answered some useful insights have been gained and clear directions for further research have been identified.

## ACKNOWLEDGEMENTS

---

First of all, I would like to thank Dr. Peter Cullen for providing me with supervision over the past three years and for all his help. I would also like to thank deeply my parents and Sabine, my companion, who have always, patiently, encouraged me.

Special acknowledgements go to my *desk neighbours*, who have supported me until the end of my unforgettable experience at the Comms Lab. I would mention Alex, Conor, Eamonn K., Eamonn O., Eugene, Liam, Max, Peter, Ronan, Sylvia, Joe from next door, Mohammed from downstairs and Marco for our coffee breaks and chats at Brewbaker's.

Thanks are also due to Teltec Ireland for funding the three years of study and to the reviewers of this thesis for their suggestions.



---

## CONTENTS

---

<b>Declaration</b>	<b>i</b>
<b>Dedication</b>	<b>ii</b>
<b>Abstract</b>	<b>ii</b>
<b>Acknowledgements</b>	<b>v</b>
<b>1 Introduction</b>	<b>1</b>
1.1 Organisation . . . . .	4
<b>2 Integral Equation Methods</b>	<b>8</b>
2.1 Surface integral equations . . . . .	9
2.2 The Method of Moments . . . . .	12
2.2.1 Point matching . . . . .	14
2.2.2 Subsectional (subdomain) bases . . . . .	14
2.3 Example: using the EFIE to estimate TM-wave scattering by PEC cylinders in two dimensions . . . . .	15
2.3.1 Application of the Method of Moments (MoM) . . . . .	16
2.4 MFIE for TM-wave scattered from PEC cylinders . . . . .	19
2.5 CFIE for TM-wave scattered from PEC cylinders . . . . .	21
2.6 MoM solution of the EFIE in three-dimensions . . . . .	25

---

2.6.1	Development of basis functions . . . . .	26
2.6.2	Testing the EFIE . . . . .	29
2.6.3	Derivation of the matrix equation . . . . .	30
2.7	The Conjugate Gradient (CG) method . . . . .	31
2.8	The Conjugate Gradient-Fast Fourier Transform (CG-FFT) method	33
2.8.1	One-Iteration FFT algorithm . . . . .	35
2.9	Numerical results . . . . .	37
2.9.1	Example of application of the CG-FFT method . . . . .	37
2.9.2	Three-dimensional case: EFIE results for simple geometries .	39
2.10	Summary . . . . .	41
<b>3</b>	<b>The Fast Multipole Method</b>	<b>46</b>
3.1	Rationale of the Fast Multipole Method (FMM) . . . . .	46
3.2	Formulation of the FMM . . . . .	48
3.3	Some numerical results . . . . .	51
3.4	Recent developments of the FMM . . . . .	54
3.4.1	Computational issues related to the FMM . . . . .	54
3.4.2	FMM in the three-dimensional case . . . . .	56
3.5	Summary . . . . .	60
<b>4</b>	<b>The Tabulated Interaction Method</b>	<b>62</b>
4.1	The Fast Far-Field Approximation (FAFFA) . . . . .	62
4.2	The Tabulated Interaction Method (TIM) . . . . .	66

---

4.3	Electromagnetic scattering from large terrain profiles: an example of application of FAFFA and TIM . . . . .	73
4.4	Summary . . . . .	76
<b>5</b>	<b>Novel enhancements to TIM</b>	<b>78</b>
5.1	Motivation of the Analytical Interaction Method (ANIM) . . . . .	78
5.2	Formulation of ANIM . . . . .	80
5.3	Numerical results . . . . .	87
5.3.1	Numerical results for Jerslev profile . . . . .	87
5.3.2	Numerical results for Hjørringvei profile . . . . .	88
5.3.3	Comparison with measured data and reference results . . . . .	89
5.4	Matrix formulation of TIM/ANIM . . . . .	90
5.5	Application of TIM/ANIM matrix formulation to electromagnetic scattering from periodic surfaces . . . . .	95
5.6	Summary . . . . .	98
<b>6</b>	<b>Evaluation of EFIE matrix terms in the RWG approach</b>	<b>111</b>
6.1	Calculation of the impedance matrix elements: the typical approach	111
6.1.1	Numerical evaluation of integrals involving different triangles	112
6.1.2	Numerical evaluation of integrals involving the same triangle	114
6.2	Alternative approach to the numerical evaluation of integrals involving the same triangle . . . . .	122
6.3	Numerical results . . . . .	127
6.4	Summary . . . . .	129

---

<b>7</b>	<b>The Multi-Level Fast Far-Field Algorithm</b>	<b>131</b>
7.1	Formulation of the MLFAFFA . . . . .	132
7.1.1	The far-field approximation applied to the RWG basis set . . .	132
7.1.2	Choosing the far-field/near-field regions . . . . .	135
7.1.3	Multi-level scheme . . . . .	137
7.2	Implementation of the MLFAFFA . . . . .	138
7.2.1	Memory requirements . . . . .	138
7.2.2	The algorithm . . . . .	139
7.2.3	Computational cost . . . . .	144
7.3	Numerical results . . . . .	145
7.4	Summary . . . . .	147
<b>8</b>	<b>Conclusions</b>	<b>155</b>
<b>A</b>	<b>Review of basic electromagnetics</b>	<b>159</b>
A.1	Maxwell's equations . . . . .	159
A.2	Equivalence theorem and Induction theorem . . . . .	162
A.2.1	Equivalence theorem . . . . .	163
A.2.2	Induction theorem . . . . .	164
A.3	Surface integral equations . . . . .	165
<b>B</b>	<b>High Frequency Techniques</b>	<b>170</b>
B.1	Geometric Optics . . . . .	170
B.2	Physical Optics . . . . .	172
B.3	Geometrical Theory of Diffraction . . . . .	173

---

B.4	Uniform Theory of Diffraction . . . . .	174
B.5	Method of Equivalent Currents . . . . .	175
B.6	Physical Theory of Diffraction . . . . .	175
B.7	The Incremental Length Diffraction Theory . . . . .	176
<b>C</b>	<b>Differential Equations Solvers</b>	<b>178</b>
C.1	Finite Difference Time Domain . . . . .	178
C.2	Finite Element Method . . . . .	180
<b>D</b>	<b>Mathematical formulae for ANIM in three dimensions</b>	<b>183</b>
D.1	Extension of ANIM to the three-dimensional case . . . . .	183
D.2	Far-field scattered by a triangular patch illuminated by a plane wave using the PO approximation . . . . .	185
D.3	Plane wave expansion of the near-field . . . . .	191
D.4	Conclusion . . . . .	193
	<b>Bibliography</b>	<b>198</b>

---

## LIST OF FIGURES

---

2.1	Illustration of the electromagnetic scattering problem formulated using surface integral equations. . . . .	10
2.2	Scattering from a PEC cylinder of radius $a$ . The $TM_z$ electric plane wave illuminates the cylinder from $x = -\infty$ . The cylinder extends from $z = -\infty$ to $\infty$ . . . . .	15
2.3	EFIE results for the problem of Fig. 2.2: amplitude of current density on the surface of the cylinder versus degrees. The number of unknowns is 81 and the radius of the cylinder is $a = 3\lambda$ . . . . .	20
2.4	EFIE results for the problem of Fig. 2.2 when the number of unknowns is 300 and 900. . . . .	21
2.5	Cylinder cross section and parameters used in the MFIE (2.55): $\hat{\mathbf{k}}$ is the unit vector associated with the plane wave illuminating the scatterer, $\theta$ is the angle of incidence, $R_m$ is the distance between the integration point $(x', y')$ and the observation point $(x_m, y_m)$ , $\hat{\mathbf{n}}$ is the normal unit vector and $\Omega_m$ is the polar angle associated with $\hat{\mathbf{n}}$ . . .	22
2.6	MFIE results for the problem of Fig. 2.2: amplitude of current density on the surface of the cylinder versus degrees. The number of unknowns is 81 and the radius of the cylinder is $a = 3\lambda$ . . . . .	23
2.7	MFIE results for the problem of Fig. 2.2: amplitude of current density on the surface of the cylinder versus radians. The number of unknowns is 900 and the radius of the cylinder is $a = 3\lambda$ . . . . .	24

- 
- 2.8 EFIE/MFIE results for the problem of Fig. 2.2 when  $ka = 2.405$ . The MFIE solution is not affected by non-uniqueness problem. The EFIE solution instead shows instability due to numerical errors caused by non-uniqueness. . . . . 25
- 2.9 CFIE results for the problem of Fig. 2.2 when  $ka = 2.405$ : The CFIE given in (2.60) has been implemented with  $b = 0.7$  and the number of unknowns is 81. . . . . 26
- 2.10 A triangle pair over which the RWG basis function  $\mathbf{f}_n(\mathbf{r})$  is defined. 27
- 2.11 Plot of the amplitude of the truncated Hankel function. The interval of interest, where the electric current is located, is  $x \in [0, L]$ , with  $L = 1m = 32\lambda$ . . . . . 37
- 2.12 Amplitude of the Fourier transform of the function illustrated in Fig. 2.11. This is the result of an FFT performed over the samples of the Hankel function (frequency of sampling: 8 samples per wavelength). 38
- 2.13 Amplitudes of the electric current density evaluated using an *one step* FFT algorithm and the usual MoM, discretising the integral equation and solving the resulting matrix equation. The two functions perfectly match over the interval of interest  $x \in [0, L]$ , with  $L = 1m$ . . . . . 39
- 2.14 Amplitudes of the electric fields obtained using two different calculations. The dashed line represents the amplitude of the electric field returned by the convolution of the electric current and the Hankel function respectively illustrated in Fig. 2.14 and Fig. 2.11. The result is the known term of the equation in the  $k$ -space, i.e. the incident field in the interval  $[0, L]$ , with  $L = 1m$  and 0 elsewhere. The field due to the current, i.e. the scattered field, evaluated by numerical integration is the solid line: it equals the incident field over the interval  $[0, L]$  and decays outside the interval, but it is not zero. . . 40

- 
- 2.15 Surface patch grid employed to model the electric current density over a square flat plate. . . . . 41
- 2.16 Amplitude of the horizontal component of the electric current density over the square flat plate at a cut over the vertical direction in the middle of the square. The number of unknowns, i.e. the number of non-boundary edges, is 176. The incident electric field is assumed to be directed along the horizontal direction and propagates normally to the plate. The side of the plate is  $\lambda$ . . . . . 42
- 2.17 Surface patch grid employed to model the electric current density over a circular disk. . . . . 43
- 2.18 Amplitude of the electric current density over the radial direction on the disk. The circular disk is of radius  $a = 2\lambda$  and a vertical electric dipole illuminates it from a point centred on the disk at a height of  $0.1a$ . The number of edges is 792. . . . . 44
- 2.19 Amplitude of the horizontal component of the electric current density over the square flat plate at a cut over the vertical direction in the middle of the square. The number of unknowns, i.e. the number of non-boundary edges is, 736. The incident electric field is assumed to be directed along the horizontal direction and propagates normally to the plate. The side of the plate is  $2\lambda$  long. . . . . 45
- 2.20 Amplitude of the horizontal component of the electric current density over the square flat plate at a cut over the horizontal direction in the middle of the square. The number of unknowns, i.e. the number of non-boundary edges, is 225. The incident electric field is assumed to be directed along the horizontal direction and propagates normally to the plate. The side of the plate is  $2\lambda$ . . . . . 45



- 
- 3.1 FMM main concepts: in (a) the field of two current elements of  $G_l$ , such as  $n_a$  and  $n_b$  is evaluated at two current elements of  $G_{l'}$ ,  $m_a$  and  $m_b$ . The actions of the two elements  $n_a$  and  $n_b$  are first aggregated at the centre of the group  $G_l$ , then translated over the group  $G_{l'}$  and disaggregated at the points  $m_a$  and  $m_b$ . The term derived from the aggregation step may be *reused* for other interactions of  $G_l$  with different groups. The FMM main concepts may be illustrated using a network representation as in (b). . . . . 48
- 3.2 The groups indexed by  $l$  scatters over the group indexed by  $l'$ . Each element of  $G_l$ , say  $n$ , is a line source of current amplitude  $I_n = 1$ . The sum  $\sum_{n=1}^N Z_{mn} I_n$  is evaluated for the set of *receiving points* around the centre  $l'$ . The number of points is  $M = N = 72$ . The aggregation of elements of  $G_l$  at the centre  $l$  requires  $\mathcal{O}(N)$  operations, so does the disaggregation of the field *received* at the point  $l'$ . The translation is performed using (3.8). . . . . 52
- 3.3 Amplitude of the sum (3.15) employing the FMM approximation and equation (3.8) with  $P = 10$  for the geometry illustrated in Fig. 3.2. The dashed line represents the values of the sum (3.15) at  $M = 72$  points located at a radius  $\lambda$  around the centre of the group  $G_{l'}$ . The result is affected by an evident instability due to the truncation of the series (3.8) at a too-small  $P$  with respect to the theoretical limit  $\infty$ . . . . . 53
- 3.4 Amplitude of the sum (3.15) employing the FMM approximation and equation (3.8) with  $P = 20$  for the geometry illustrated in Fig. 3.2. The dashed line represents matches exactly the solid line. In this case the FMM approximation returns the exact result obtained by evaluating numerically the sum (3.15). . . . . 54

3.5	FMM results for the scattering by a PEC cylinder: the amplitude of the current density matches perfectly the solution returned by the EFIE inverted using a CG algorithm. Both the solutions are affected by the instability typical of the EFIE. . . . .	55
3.6	Behaviour of the translation function $\tilde{\alpha}_{\nu l}(\alpha)$ associated with the geometry of Fig. 3.2. The function has maximum value at $\phi_{\nu l} = \pi/4$ , i.e. over the direction $l \rightarrow l'$ and gradually decays outside a narrow interval centred at $\alpha = \phi_{\nu l}$ . . . . .	56
3.7	Geometry of the FMM in the three-dimensional case: the group $G_l$ scatters over the group $G_{\nu}$ . The electric current associated with the domains $T_n^+$ and $T_n^-$ , i.e. $I_n$ , radiates the electric field at $T_m^+$ , which is the triangle included in $G_{\nu}$ . The evaluation of the field scattered by $G_l$ over $G_{\nu}$ requires the calculation of only a fraction of the impedance term $Z_{mn}$ (2.79), because domain $T_m^-$ does not belong to the group $G_{\nu}$ . . . . .	58
4.1	Far-field approximation in the two-dimensional case: the electric field due to the group $G_l$ at $G_{\nu}$ is evaluated using (4.8). . . . .	65
4.2	Geometry for the evaluation of the far-field scattered by a strip of length $L$ illuminated by a plane wave. . . . .	71
4.3	Two collinear groups and geometric quantities used in FAFFA. . . . .	72
4.4	Line source illuminates an undulating terrain modelled by a two-dimensional surface. $m$ and $n$ are discretisation points where the current $J_z$ is assumed to take the values $J_m$ and $J_n$ . . . . .	74
4.5	Example of application of FAFFA and TIM to the numerical evaluation of the field strength over a terrain profile which extends for several thousands of wavelengths. . . . .	76

---

5.1	A half plane is illuminated by a $TM_z$ plane wave at a low grazing angle $\theta_i$ . The electric current residing on the half plane located at ( $s > 0, \theta_s = 0, z = 0$ ) is determined: point $\tilde{x}$ , closed contour $\Gamma$ in the neighbourhood of $\tilde{x}$ , surface $S$ , rectangular and cylindrical reference coordinate systems. . . . .	81
5.2	Amplitude of the scattered far-field due to a PEC strip of length $L = 256\lambda$ . The strip is impinged by a plane wave at an angle $\theta_i = 175/180\pi$ and the field is evaluated at a far distance $R_0 = 100L$ . The results displayed are obtained applying the analytical expression given in (5.33) and the numerical results returned by a classical forward moment method (MoM). . . . .	85
5.3	Field strength over Jerslev profile. The terrain extension over the $x$ direction is of the order of tens of thousands the incident wavelength: terrain profile, line source location and simulation results (field strength at 2.4m above the terrain). . . . .	100
5.4	Field strength over Jerslev profile. The terrain extension over the $x$ direction is of the order of tens of thousands the incident wavelength: simulation results (field strength at 2.4m above the terrain). . . . .	101
5.5	Field strength over Hjorringvei profile. The terrain extension over the $x$ direction is of the order of tens of thousands the incident wavelength: terrain profile, line source location and simulation results (field strength at 2.4m above the terrain). . . . .	102
5.6	Field strength over Hjorringvei terrain profile. . . . .	103
5.7	Field strength over Jerslev terrain profile. . . . .	104
5.8	Simple scatterer geometry for the application of matrix formulation of TIM/ANIM. . . . .	104
5.9	Sparse matrix obtained using TIM for the example of Fig. 5.8. . . . .	105

5.10	$TM_z$ plane wave incident on a periodic surface with period $a$ . . . .	105
5.11	Physical meaning of the periodic Green's function: the function describes the interaction between the observation point $m$ and all the periodic shifted versions of $n_0$ , which are defined as $n_p$ , with $p = -\infty \cdots -1, 1, \infty$ . . . . .	106
5.12	Plane waves due to periodic shifted versions of $G_V$ illuminating the group $G_I$ . In the example here illustrated, four different angles of incidence are counted which, in turn, excite eight different basis functions. These are the fields radiated by groups $G_{V_p}$ , with $p = -2, -1, 1, 2$ . . . . .	107
5.13	Unit cell of a periodic scatterer illuminated by a plane wave. . . . .	108
5.14	Comparison of the far-field patterns for the problem illustrated in Fig. 5.13: the TIM differs from the exact solution for its non-smoothness. . . . .	108
5.15	Comparison of the far-field patterns for the problem illustrated in Fig. 5.13: exact calculation of the near-field interaction renders the TIM solution smoother with respect to the result shown in Fig. 5.14.	109
5.16	Introduction of the buffer zone to allow the use of FAFFA between two near neighbours. . . . .	109
5.17	Far-field patterns obtained using a buffer-zone approach. . . . .	110
6.1	Geometry of the impedance term calculation when $m \neq n$ : the current associated with the edge $l_n$ radiates over the domain $T_m^+$ . In the figure, only the interaction between the domains $T_n^+$ and $T_m^+$ is displayed. Each triangle is characterised by a local planar coordinate system, such as $(x_n, y_n)$ and $(x_m, y_m)$ . . . . .	112

6.2	Geometry of the self term calculation for the triangle $T$ . The local coordinate systems $(x, y)$ and $(\rho, \phi)$ are displayed. Given the observation point $(x_0, y_0)$ , three triangles are considered: $T_1, T_2$ and $T_3$ obtained by a connection of the observation point with the three vertices of $T$ . The integral given in (6.17) may be considered as the sum of three integrals, each one computed over the triangular domain $T_i$ , $i = 1, 2, 3$ . More precisely, the integral over the whole domain $T$ is split into the sum of two integrals: one over a disk of radius $\epsilon \rightarrow 0$ centred at $(x_0, y_0)$ , which evaluates to zero, and the other over the three triangles $T_i$ , $i = 1, 2, 3$ . Each integral over $T_i$ may now be carried out referring to the polar coordinate system $(\rho, \phi)$ , obtaining the final result (6.81). . . . .	127
6.3	Behaviour of the function $r(\phi)$ as given in (6.72) and the resulting functions (6.75) and (6.76) employed in the evaluation of the integral using the alternative approach. . . . .	130
7.1	The geometry of the far-field approximation: reference point $O \in S$ and far points $P$ and $Q$ . . . . .	133
7.2	Approximated and exact far-field patterns due to a given current distribution over a square flat plate of sides $l\lambda$ , $l = 0.5, 1.0, 2.0$ and $4.0$ . . . . .	136
7.3	Storage requirements (in MB) for the implementation of the MLFAFFA and the classical CG methods. . . . .	139
7.4	Tree-structured grid of groups at all levels in the MLFAFFA. At each level, a square contains triangular patches where current elements are defined. . . . .	149
7.5	Far-field interactions at different levels in the MLFAFFA. . . . .	150

7.6	MLFAFFA downward sweep at the final level $N_l$ : the near field interaction between $n$ and $m$ is labelled as $nf$ . . . . .	151
7.7	Geometry of the scattering problem and triangular mesh associated with the scatterer. . . . .	152
7.8	Amplitude of the scattered far-field due to the MLFAFFA and the CG currents induced on the plate when $\theta_i = \pi/4$ . . . . .	153
7.9	Amplitude of the MLFAFFA, the CG-FFT and the CG $J_x/ \mathbf{H}^i $ solutions along the cut at $x = L/2$ . . . . .	153
7.10	Amplitude of the scattered far-field due to the MLFAFFA and the CG currents induced on the plate when $\theta_i = \pi/2$ . . . . .	154
A.1	Geometry for boundary conditions of electric and magnetic field: the interface between two different media (solid line) and its normal unit vector $\hat{\mathbf{n}}$ . Medium 1 has properties $\epsilon_1, \mu_1$ , medium 2 has properties $\epsilon_2, \mu_2$ . . . . .	160
A.2	Equivalence theorem geometry and transformation: (a) is the original problem, where $S$ is a surface which encloses the sources, its exterior is free space; (b) is the equivalent geometry to determine the fields $(\mathbf{E}_{ext}, \mathbf{H}_{ext})$ outside $S$ due to the equivalent sources $\mathbf{J}_S$ and $\mathbf{M}_S$ . . . . .	162
A.3	Induction theorem geometry and transformation: (a) is the original problem; (b) is the resulting problem to be solved to determine the scattered fields $(\mathbf{E}_s, \mathbf{H}_s)$ outside the scatterer. . . . .	164
A.4	Illustration to explain the surface equivalence principle: two media of different properties are separated by $S$ , $\Gamma_1$ and $\Gamma_2$ are the volumes enclosed by $S$ and $S_\infty - S$ . $S_\infty$ extends to infinity. The presence of a perfect electric conductor in $\Gamma_2$ is also assumed. . . . .	166

---

B.1	Geometrical optics reflection from a doubly curved surface. . . . .	171
B.2	Edge diffraction geometry. . . . .	174
C.1	FDTD method . . . . .	179
C.2	FEM problem . . . . .	181
D.1	Geometry of the discretisation (D.5) for the three-dimensional case.	186
D.2	Physical Optics approximation for the current on $T$ . The vector $\hat{n}$ points outwards the plane containing $T$ . . . . .	187
D.3	Geometry of the far-field evaluation for a planar triangular patch illuminated by a plane wave incident at angles $\theta_i$ and $\phi_i$ . In (a) the triangle $T$ and the observation point $(r, \theta, \phi)$ are illustrated, with the spherical coordinate system centred at the centroid of $T$ and the rectangular coordinate system $(x_c, y_c, z_c)$ . In (b) the plane of the triangle is illustrated with the two different coordinate system $(x_c, y_c)$ and $(x', y')$ . For each point $\mathbf{r}'$ , its coordinate $\tilde{x}$ with respect to the centroid $C$ of $T$ is such that $x_c + \tilde{x} = x'$ . Similar relation holds for $y_c$ . The closed form integral $I_T$ given in (D.40) is evaluated referring to the coordinate system $(x', y')$ . . . . .	196
D.4	Geometry for the calculation of the near-field scattered by $T$ . . . . .	197

## LIST OF TABLES

---

6.1	Numerical and reference results for five different observation points.	126
-----	--	-----

---

---



---

**LIST OF SYMBOLS**

---

EFIE	Electric Field Integral Equation
MFIE	Magnetic Field Integral Equation
MoM	method of Moments
PEC	Perfect Electric Conductor
CFIE	Combined Field Integral Equation
RWG	Rao-Wilton-Glisson
CG	Conjugate Gradient
CG-FFT	Conjugate Gradient-Fast Fourier Transform
FFT	Fast Fourier Transform
FAFFA	Fast Far-Field Approximation
TIM	Tabulated Interaction Method
UHF	Ultra High Frequency
ANIM	Analytical Interaction Method
NBS	Natural Basis Set
MLFAFFA	Multi-Level Fast Far-Field Algorithm
MLFMA	Multi-Level Fast Multipole Algorithm

---

## INTRODUCTION

---

The subject of this thesis is electromagnetic scattering by large, piecewise smooth, perfect electric conductors (PEC), embedded in a homogeneous medium such as free space. The motivation for this work is the need for rigorous, efficient, accurate and robust numerical methods for Ultra High Frequency radio wave propagation for use in the wireless communication industry.

The problem of electromagnetic scattering will be formulated as an integral equation. The approach to propagation modeling adopted in this thesis is to begin with a physically rigorous formulation and introduce approximations in a considered, careful and controlled manner. In this way a decreased generality of applicability is traded for computational efficiency in obtaining numerical solutions for a restricted class of problems. This is in contrast to the more popular approach of beginning with an approximate model and refining it to increase accuracy at the expense of adding complexity. It will become evident that the surface integral equation formulation of electromagnetic scattering problems lends itself well to this approach.

Mobile radio propagation presents us with a number of generic problems. The most familiar generic problem arising in land mobile propagation is the corrugated one-dimensional perfect electrical conducting (PEC) surface. Often this is associated with terrain propagation. It is a valid model if the terrain height variation in the directions perpendicular to vertical plane containing the transmitter and receiver is everywhere small in comparison to the width of the Fresnel ellipsoid [4] so that the terrain may be considered invariant in that direction. It also requires that the terrain height variations are such as to discount the possibilities of echoes from terrain features not cut by this vertical plane. In this case, if the propagation is either transverse magnetic  $TM_z$  or transverse electric  $TE_z$  the electromagnetic

---

problem is a scalar one. Moreover, if the surface is smooth and the angle of incidence low, forward propagation will predominate [56]. Considering the surface to be a homogeneous dielectric may enhance this generic model, further enhancements can be achieved by considering a piecewise homogeneous dielectric. For grazing incidence neither approach is likely to be worth the extra computational effort. This kind of generic model has very wide application for the prediction attenuation of low-angle wave propagation over irregular terrain. The height profile (array of heights) associated with this generic problem is usually derived from a digital terrain model (DTM) stored in geographical database and accessed using a geographical information system (GIS). Unconnected one-dimensional surfaces arise when two-dimensional propagation in the horizontal plane is considered. When calculating fields around buildings in circumstances where the antenna heights are well below rooftop height and the terrain is reasonably level (simple micro-cell case) it can be sufficient to use multiple paraxial PEC cylinders (by cylinder it is meant a closed two-dimensional entity) to represent the buildings. The cross-section of the cylinders is taken to be the building plan outline or footprint. This abstraction is made by most of the popular two-dimensional deterministic micro-cell propagation models such as ray-tracing. Further enhancements include the use of homogeneous or piece-wise homogeneous (to allow the representation of internal and external structure) dielectric cylinders. An increasingly important generic problem is the two dimensional smooth surface. This surface, like its one-dimensional counterpart, may be assumed to be a homogeneous PEC, a dielectric or a piece-wise homogeneous dielectric. The most complex two-dimensional surfaces arise when propagation in and around buildings located on irregular terrain must be considered. The main differences between this case and the previous one is the abrupt changes in surface height which occur at the location of building walls and in the possibility of inhomogeneity (rooms, windows etc. in buildings). Typically, two-dimensional surface problems are solved in a piecewise manner using geometrical optics or GTD. The development of numerical methods for the computation of electromagnetic wave scattering from *large, smooth and piecewise linear-planar* perfect electrically

---

conductors using surface integral equations is the main subject of this thesis. By large surfaces it is meant that typical length scales are  $\mathcal{O}(10) - \mathcal{O}(10^5)$  wavelengths. By smooth, it is meant that the effects of random roughness are not taken into account.

Traditional approaches to the solution of surface integral equations using general purpose methods can run into trouble for even quite modestly sized problems, even on the best available computer resources. Over recent years, however, exceptionally fast, accurate and robust schemes have emerged for tackling the problem of solving surface integral equations in two dimensions, achieving massive computational savings over traditional approaches for the case of large, smooth and slowly varying surfaces without compromising accuracy. Results have been obtained by Trinity College Electromagnetic Scattering group ([57]-[58], [61]-[64], [66]-[67]) and by others ([47]-[49], [52]-[55]). Investigation of this class of problems and of the possibility of their extension from two to three dimensions has been carried out by the author with the following results.

- The Analytical Interaction Method has been developed. This fast numerical scheme may be applied to the problem of Ultra High Frequency wave propagation over irregular terrain. Numerical results are provided to demonstrate the excellent agreement of the new technique with typical and alternative fast methods.
- The matrix formulation of the Tabulated Interaction Method/Analytical Interaction Method has been introduced and its application to the problem of electromagnetic scattering from periodic structures has been investigated.
- A fully numerical technique for the integration of linear shape functions times the three-dimensional Green's function has been developed. The method applies to the discretisation of the Electric Field Integral Equation using the Rao-Wilton-Glisson approach. Numerical results demonstrate the accuracy of the approach proposed by comparing it with typical non-fully numerical

techniques.

- The Fast Far-Field Approximation has been extended to the three-dimensional case, for an arbitrarily shaped scatterer using the Rao-Wilton-Glisson approach. A multi-level numerical technique is built upon the far-field approximation with reduced memory requirements and substantial computational savings with respect to the classical Method of Moments-Conjugate Gradient scheme. Numerical results show the accuracy of the technique proposed.
- The possibility of extending the Analytical Interaction Method to three dimensions using the Physical Optics approximation has been considered. The author hopes that future research will build upon his initial investigation.

## 1.1 Organisation

The body of this thesis may be divided into three main parts. The first part including chapters 2 and 3 is devoted to the introduction of the Integral Equation formulation and fast numerical methods. Chapters 4 and 5 deal with electromagnetic wave scattering in two dimensions. Finally, chapters 6 and 7 deal with electromagnetic wave scattering in three dimensions. This thesis consists hence of the following chapters:

**Chapter 2** introduces the integral equation formulation for electromagnetic scattering problems. The Electric Field Integral Equation (EFIE) and the Magnetic Field integral Equation (MFIE) are stated. The Method of Moments (MoM) is described for the discretisation of the EFIE/MFIE. A sample application of the method is presented for the two-dimensional case. The EFIE and MFIE are compared for the classical problem of electromagnetic scattering from perfect electric conductors (PEC). It is noted that both solutions of the integral equations are non-unique for closed scatterers. The Combined Field Integral Equation (CFIE) overcomes this problem.

The EFIE formulation in three dimensions is also presented. This equation is discretised using the Rao-Wilton-Glisson (RWG) approach. The RWG basis functions are introduced and the MoM matrix is obtained.

The Conjugate-Gradient (CG) method is reviewed. This method permits the solution of any matrix equation. The storage requirements of this algorithm are of  $\mathcal{O}(N^2)$ . The computational complexity of the CG method is also of  $\mathcal{O}(N^2)$ . For the case of electromagnetic scattering from electrically large objects, the storage and computational complexity can rapidly become too large to allow the numerical solution of the discretised integral equation.

For planar scatterers, the Conjugate Gradient-Fast Fourier Transform (CG-FFT) method is presented. This scheme reduces the computational complexity of the solution of the MoM-CG matrix equation to  $\mathcal{O}(N \log N)$ .

**Chapter 3** describes the Fast Multipole Method (FMM). The basic concepts of this technique are introduced. The method is presented for the two-dimensional case and some numerical experiments are presented to demonstrate the accuracy of the FMM approximation. The computational complexity of the FMM implementation is reduced with respect to that of CG to  $\mathcal{O}(N^{1.33})$ . The FMM is also introduced for the three-dimensional case, using RWG basis functions.

**Chapter 4** presents the Fast Far-Field Approximation and the Tabulated Interaction Method (TIM), a relative of the Fast Far-Field Approximation (FAFFA). The latter is reviewed in two-dimensions. Then the formulation of TIM is derived. It is shown that TIM offers great computational savings, providing accurate UHF path loss predictions over many tens of thousands of wavelengths. The computational time for the TIM is of the order of seconds for the solution of problems which require a time of the order of days when solved using a classical MoM-CG scheme.

**Chapter 5** describes the Analytical Interaction Method (ANIM), a novel method

conceived to render the TIM more flexible with respect to the frequency. TIM requires tabulation of certain quantities. ANIM does away with the need for tabulation by proposing using carefully derived analytical results. ANIM offers the same computational performance as TIM and is built upon a classical problem of electromagnetic scattering, namely plane wave scattering by a half plane. The analytical result for this problem may be integrated with success into the TIM framework. The final result is a numerical technique which preserves both the accuracy and the computational acceleration of TIM. Numerical results are provided to demonstrate the behaviour of ANIM with respect to reference solutions and measurements. Comparative data on the computational savings achieved by ANIM is also provided.

A novel matrix formulation of the TIM/ANIM is also introduced in this chapter and is applied to the problem of electromagnetic scattering by periodic structures. Numerical results are provided and commented. The chapter may be seen as the end of the presentation of the work carried out by the author for two-dimensional electromagnetic scattering problems. The next two chapters are devoted to the development of a fast and accurate numerical technique for the three-dimensional case.

**Chapter 6** introduces the reader to a key numerical problem arising in the MoM discretisation of the EFIE in the three-dimensional case when applying RWG basis functions. The problem is the numerical integration of the linear-shape function times the three-dimensional Green's function. This operation must always be performed. The standard approach is reviewed, and simplified expressions are derived for some typical integrals employed in this approach. A novel alternative fully numerical integration scheme is proposed by the author. This technique allows the rapid and reliable numerical integration of the quantity of interest. It is simpler than the standard method. Numerical results are provided which compare the accuracy of the new method with the standard approach and with a set of reference results.

**Chapter 7** introduces the Multi-level Fast Far-Field Algorithm (MLFAFFA) for the three-dimensional case. The novel implementation has been developed by the author and may be applied successfully to the general problem of electromagnetic scattering by arbitrarily shaped objects. MLFAFFA is an improvement of FAFFA. It has a multi-level structure and is formulated in three dimensions. The criterion for the selection of the far-field area is developed and carefully described and the storage requirements are discussed. The technique requires less storage than the typical MoM-CG scheme. This is essentially because not all the impedance matrix need be computed and stored. Moreover, the computational complexity of the method is shown to be of  $\mathcal{O}(\beta(N)N)$  where  $\beta(N) \ll N$  when  $N \gg N_0$ . The author observed that  $N_0 \approx 10^4$ . Numerical results are provided to demonstrate the accuracy of MLFAFFA compared with reference solutions.

The surface integral equation formulation is one of the available ways of solving the problem of electromagnetic scattering. For sake of completeness, two chapters of the Appendix outline the principles of high frequency techniques and differential equation solvers.

The extension of ANIM to three dimensions is an interesting prospect. Some issues that arise in this extension are outlined in the last chapter of the Appendix. Specifically, some mathematical tools for an extension of the Analytical Interaction Method to three dimensions are provided using the Physical Optics approximation. While more work is required to accomplish this task, directions for further research are provided.



---

## INTEGRAL EQUATIONS IN ELECTROMAGNETIC SCATTERING

---

In this chapter, the problem of electromagnetic scattering is presented using the integral equation formulation. In section 2.1, the surface integral equations used throughout this thesis are stated following [21]. Specifically, the Electric Field Integral Equation and the Magnetic Field Integral Equation (EFIE and MFIE) are stated for the case of electromagnetic scattering by homogeneous bodies embedded in free space.

In section 2.2, the Method of Moments (MoM) is introduced. A sample application of MoM is presented in section 2.3 for the discretisation of the EFIE and in section 2.4 for the MFIE. The problem of the non-uniqueness of the solutions of both EFIE and MFIE is discussed in section 2.5 and the Combined Field Integral Equation is introduced to overcome this feature.

Section 2.6 outlines the application of the MoM to electromagnetic scattering in three dimensions. The popular Rao-Wilton-Glisson (RWG) [33] basis set is described. The Conjugate Gradient (CG) method is presented in section 2.7: this iterative algorithm provides a robust procedure for the solution of a system of linear equations and has been used by the author in carrying out all his numerical experiments.

For planar scatterers an elegant alternative to the usual MoM-CG is represented by the Conjugate Gradient-Fast Fourier Method (CG-FFT); this is described in section 2.8. Finally, some numerical results are presented in section 2.9 to help illustrate the salient features of the integral equation methods.

## 2.1 Surface integral equations

In this section, the Electric Field Integral Equation (EFIE) and the Magnetic Field Integral Equation (MFIE) are stated following [21]. In Fig. 2.1 a homogeneous, penetrable body is illuminated by an incident electromagnetic field ( $\mathbf{E}_i, \mathbf{H}_i$ ) radiated by a source located in region 1. Region 1 is free space and region 2 is characterised by constant magnetic permeability  $\mu_r$  and constant dielectric permittivity  $\epsilon_r$ . The impedance of region 1 is

$$\zeta_1 = \sqrt{\frac{\mu_r \mu_0}{\epsilon_r \epsilon_0}} \quad (2.1)$$

of region 2 (free space) is

$$\zeta_2 = \sqrt{\frac{\mu_0}{\epsilon_0}} \quad (2.2)$$

Given the geometry of Fig. 2.1, the following coupled EFIEs may be obtained [21]

$$\hat{\mathbf{n}} \times \mathbf{E}_i(\mathbf{r}) = -\mathbf{M}_1(\mathbf{r}) - \hat{\mathbf{n}} \times \left( \frac{\zeta_1}{jk_1} (\nabla \nabla \cdot \mathbf{A}_1 + k_1^2 \mathbf{A}_1) - \nabla \times \mathbf{F}_1 \right) \quad \mathbf{r} \in S^+ \quad (2.3)$$

$$0 = \mathbf{M}_1(\mathbf{r}) - \hat{\mathbf{n}} \times \left( \frac{\zeta_2}{jk_2} (\nabla \nabla \cdot \mathbf{A}_2 + k_2^2 \mathbf{A}_2) - \nabla \times \mathbf{F}_2 \right) \quad \mathbf{r} \in S^- \quad (2.4)$$

where the symbol  $S^+$  ( $S^-$ ) denotes that the surface integral equations are enforced at infinitesimal distance outside (inside) the scatterer surface  $S$ . In addition,  $\hat{\mathbf{n}}$  is the unit normal vector illustrated in Fig. 2.1 that points outwards  $S$ . As an alternative, coupled MFIEs are obtained [21]

$$\hat{\mathbf{n}} \times \mathbf{H}_i(\mathbf{r}) = \mathbf{J}_1(\mathbf{r}) - \hat{\mathbf{n}} \times \left( \nabla \times \mathbf{A}_1 + \frac{\nabla \nabla \cdot \mathbf{F}_1 + k_1^2 \mathbf{F}_1}{jk_1 \zeta_1} \right) \quad \mathbf{r} \in S^+ \quad (2.5)$$

$$0 = -\mathbf{J}_1(\mathbf{r}) - \hat{\mathbf{n}} \times \left( \nabla \times \mathbf{A}_2 + \frac{\nabla \nabla \cdot \mathbf{F}_2 + k_2^2 \mathbf{F}_2}{jk_2 \zeta_2} \right) \quad \mathbf{r} \in S^- \quad (2.6)$$

The equivalent electric and magnetic sources  $\mathbf{J}_1$  and  $\mathbf{M}_1$  are defined (following [21]) so that

$$\mathbf{J}_1(\mathbf{r}) = \hat{\mathbf{n}} \times \mathbf{H}_1 \quad \mathbf{r} \in S \quad (2.7)$$

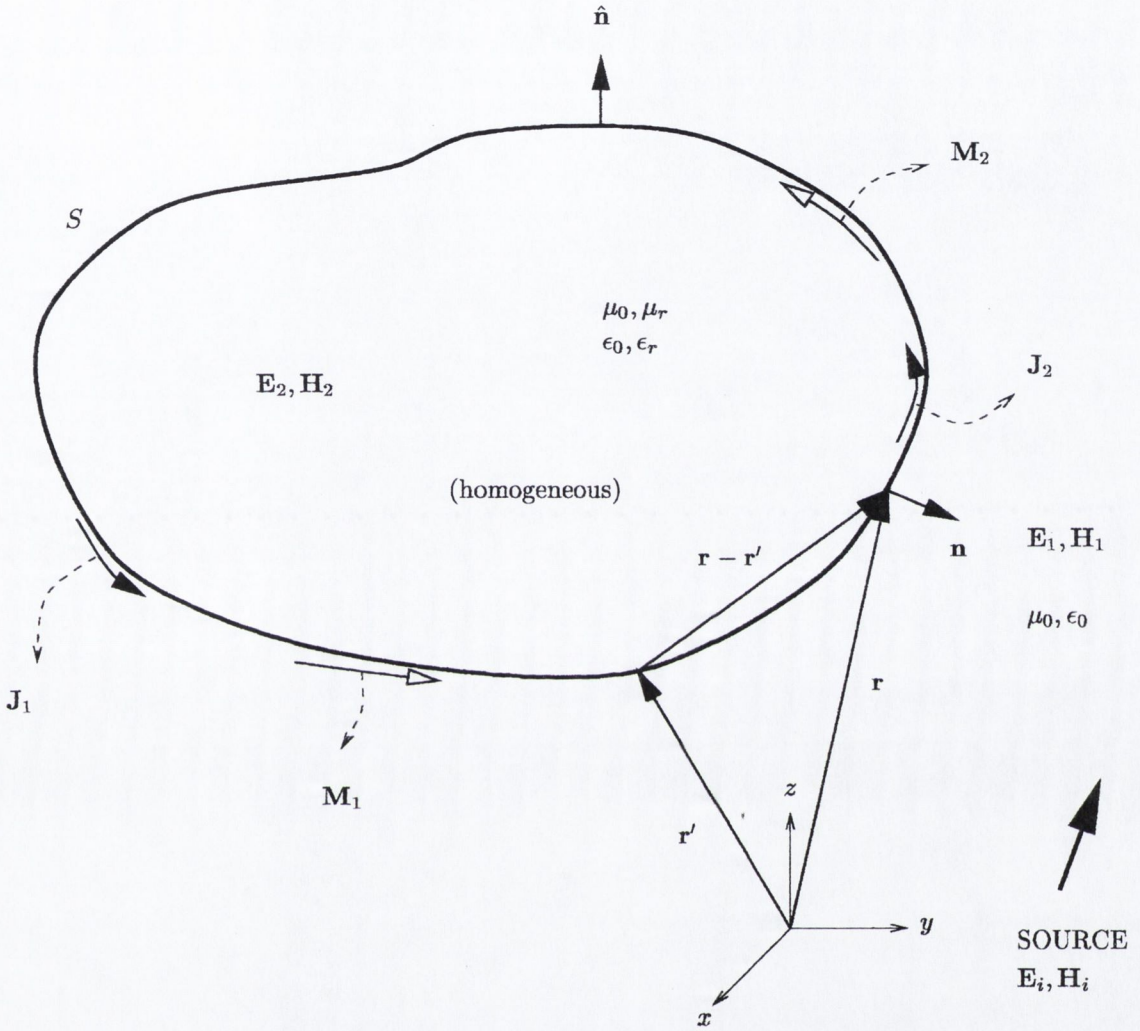


Figure 2.1: Illustration of the electromagnetic scattering problem formulated using surface integral equations.

$$\mathbf{M}_1(\mathbf{r}) = -\hat{\mathbf{n}} \times \mathbf{E}_1 \quad \mathbf{r} \in S \quad (2.8)$$

and  $\mathbf{A}_1, \mathbf{F}_1, \mathbf{A}_2$  and  $\mathbf{F}_2$  are the magnetic ( $\mathbf{A}_i$ ) and electric ( $\mathbf{F}_i$ ) vector potentials given by [21]

$$\mathbf{A}_1(\mathbf{r}) = \int_S \mathbf{J}_1(\mathbf{r}') \frac{e^{-jk_1|\mathbf{r}-\mathbf{r}'|}}{4\pi|\mathbf{r}-\mathbf{r}'|} dS' \quad (2.9)$$

$$\mathbf{F}_1(\mathbf{r}) = \int_S \mathbf{M}_1(\mathbf{r}') \frac{e^{-jk_1|\mathbf{r}-\mathbf{r}'|}}{4\pi|\mathbf{r}-\mathbf{r}'|} dS' \quad (2.10)$$

$$\mathbf{A}_2(\mathbf{r}) = \int_S \mathbf{J}_1(\mathbf{r}') \frac{e^{-jk_2|\mathbf{r}-\mathbf{r}'|}}{4\pi|\mathbf{r}-\mathbf{r}'|} dS' = - \int_S \mathbf{J}_2(\mathbf{r}') \frac{e^{-jk_2|\mathbf{r}-\mathbf{r}'|}}{4\pi|\mathbf{r}-\mathbf{r}'|} dS' \quad (2.11)$$

$$\mathbf{F}_2(\mathbf{r}) = \int_S \mathbf{M}_1(\mathbf{r}') \frac{e^{-jk_2|\mathbf{r}-\mathbf{r}'|}}{4\pi|\mathbf{r}-\mathbf{r}'|} dS' = - \int_S \mathbf{M}_2(\mathbf{r}') \frac{e^{-jk_2|\mathbf{r}-\mathbf{r}'|}}{4\pi|\mathbf{r}-\mathbf{r}'|} dS'. \quad (2.12)$$

The functions

$$\frac{e^{-jk_1|\mathbf{r}-\mathbf{r}'|}}{4\pi|\mathbf{r}-\mathbf{r}'|} \quad (2.13)$$

and

$$\frac{e^{-jk_2|\mathbf{r}-\mathbf{r}'|}}{4\pi|\mathbf{r}-\mathbf{r}'|} \quad (2.14)$$

are the Green's functions  $G_1$  and  $G_2$  (see also (A.27)) for medium 1 and 2, respectively. The operator  $\nabla$  is defined as<sup>1</sup>

$$\nabla = \frac{\partial}{\partial x} \hat{\mathbf{x}} + \frac{\partial}{\partial y} \hat{\mathbf{y}} + \frac{\partial}{\partial z} \hat{\mathbf{z}} \quad (2.15)$$

and  $\nabla\nabla$  may be represented as the matrix<sup>2</sup>

$$\nabla\nabla = \begin{pmatrix} \frac{\partial^2}{\partial x^2} & \frac{\partial^2}{\partial x\partial x} & \frac{\partial^2}{\partial x\partial z} \\ \frac{\partial^2}{\partial y\partial x} & \frac{\partial^2}{\partial y^2} & \frac{\partial^2}{\partial y\partial z} \\ \frac{\partial^2}{\partial z\partial x} & \frac{\partial^2}{\partial z\partial y} & \frac{\partial^2}{\partial z^2} \end{pmatrix}. \quad (2.16)$$

The coupled EFIEs (2.3-2.4) must be solved to obtain the unknowns  $\mathbf{J}_1$  and  $\mathbf{M}_1$ . The same holds true for the coupled MFIEs (2.5-2.6). The fields  $\mathbf{E}_1$  and  $\mathbf{H}_1$  at the exterior of  $S$  may be expressed as [21]

$$\mathbf{E}_1(\mathbf{r}) = \left( \frac{\zeta_1}{jk_1} (\nabla\nabla \cdot \mathbf{A}_1 + k_1^2 \mathbf{A}_1) - \nabla \times \mathbf{F}_1 \right) \quad (2.17)$$

$$\mathbf{H}_1(\mathbf{r}) = \left( \nabla \times \mathbf{A}_1 + \frac{\nabla\nabla \cdot \mathbf{F}_1 + k_1^2 \mathbf{F}_1}{jk_1 \zeta_1} \right). \quad (2.18)$$

<sup>1</sup>In rectangular coordinates. For the expression of the operator  $\nabla$  in cylindrical or spherical coordinates, see [13], appendix II.

<sup>2</sup>In rectangular coordinates.

The fields  $\mathbf{E}_2$  and  $\mathbf{H}_2$  at the interior of  $S$  may be expressed as [21]

$$\mathbf{E}_2(\mathbf{r}) = \left( \frac{\zeta_2}{jk_2} (\nabla\nabla \cdot \mathbf{A}_2 + k_2^2 \mathbf{A}_2) - \nabla \times \mathbf{F}_2 \right) \quad (2.19)$$

$$\mathbf{H}_2(\mathbf{r}) = \left( \nabla \times \mathbf{A}_2 + \frac{\nabla\nabla \cdot \mathbf{F}_2 + k_2^2 \mathbf{F}_2}{jk_2 \zeta_2} \right). \quad (2.20)$$

In the case where the homogeneous region 2 is a perfect electric conductor (PEC), the EFIE becomes [21]

$$\hat{\mathbf{n}} \times \mathbf{E}_i(\mathbf{r}) = -\hat{\mathbf{n}} \times \left( \frac{\zeta_1}{jk_1} (\nabla\nabla \cdot \mathbf{A} + k_1^2 \mathbf{A}) \right) \quad \mathbf{r} \in S^+ \quad (2.21)$$

and the MFIE is

$$\hat{\mathbf{n}} \times \mathbf{H}_i(\mathbf{r}) = \mathbf{J}_S(\mathbf{r}) - \hat{\mathbf{n}} \times (\nabla \times \mathbf{A}) \quad \mathbf{r} \in S^+ \quad (2.22)$$

where

$$\mathbf{J}_S(\mathbf{r}) = \hat{\mathbf{n}} \times \mathbf{H}_1 \quad \mathbf{r} \in S \quad (2.23)$$

and

$$\mathbf{A}(\mathbf{r}) = \int_S \mathbf{J}_S(\mathbf{r}') \frac{e^{-jk_1|\mathbf{r}-\mathbf{r}'|}}{4\pi|\mathbf{r}-\mathbf{r}'|} dS'. \quad (2.24)$$

## 2.2 The Method of Moments

In this section the method of Moments (MoM) is introduced. For an extended review of this method, the reader is referred to [7]. Any integral equation arising in electromagnetic wave scattering may be expressed as

$$L(f) = g \quad (2.25)$$

where  $L$  is an operator,  $g$  is the source or excitation (known function) and  $f$  is the field or response (unknown function to be determined). A problem of analysis involves the determination of  $f$  when  $L$  and  $g$  are given.

To introduce the Method of Moments, a definition of the inner product  $\langle \cdot, \cdot \rangle$  of two functions is needed. The inner product is a scalar chosen to satisfy

$$\langle f, g \rangle = \langle g, f \rangle \quad (2.26)$$

$$\langle f, f^* \rangle \geq 0 \quad (2.27)$$

$$\langle \alpha f + \beta g, h \rangle = \alpha \langle f, h \rangle + \beta \langle g, h \rangle \quad (2.28)$$

where  $\alpha$  and  $\beta$  are scalars and  $*$  denotes a complex conjugate. The Method of Moments is a general procedure for solving equations  $L(f) = g$ . Let  $f$  be expanded in a series of functions  $\{f_1, f_2, \dots\}$  in the domain of  $L$ , as

$$f = \sum_n \alpha_n f_n \quad (2.29)$$

where the  $\alpha_n$  are constants. The  $f_n$  are called *basis functions*. Hence the equation to be solved becomes

$$\sum_n \alpha_n L(f_n) = g \quad (2.30)$$

It is assumed that a suitable inner product  $\langle f, g \rangle$  has been defined for the specific problem. A set of *testing functions*<sup>3</sup>  $\{w_1, w_2, \dots\}$  is now defined and the following operation is performed

$$\sum_n \alpha_n \langle w_m, Lf_n \rangle = \langle w_m, g \rangle \quad (2.31)$$

with  $m = 1, 2, \dots$ . This set of equations may be written in matrix form as<sup>4</sup>

$$\sum_n L_{mn} \alpha_n = g_m \quad (2.32)$$

<sup>3</sup>The particular choice  $w_n = f_n$  is known as Galerkin's method.

<sup>4</sup>Observe that the matrix may be either of infinite or finite order, depending on the definition of basis and testing functions.

or

$$L\alpha = g \quad (2.33)$$

where<sup>5</sup>

$$L = [L_{mn}] = \langle w_m, Lf_n \rangle \quad (2.34)$$

$$g = [g_m] = \langle w_m, g \rangle \quad (2.35)$$

The solution is then given by

$$\alpha = L^{-1}g \quad (2.36)$$

provided that the matrix  $L$  is non-singular. The solution

$$f = \sum_n \alpha_n f_n \quad (2.37)$$

may be exact or approximate depending upon the choice of the basis and testing functions.

### 2.2.1 Point matching

The integration involved in evaluating  $\langle w_m, Lf_n \rangle$  of (2.34) is often difficult to perform in problems of practical interest. A way to obtain an approximate solution of (2.30) is to force the equation to be satisfied at discrete points in the region of interest. This procedure is called *point-matching* method. It is equivalent to use Dirac delta functions (defined in section A.3) as testing functions.

### 2.2.2 Subsectional (subdomain) bases

An approximation useful for practical problems involves the use of basis functions  $f_n$  each of which exists only over subsections of the domain of  $f$ . As a consequence,

<sup>5</sup>To express a vector  $v$ , the following notation is employed:  $v = [v_n] = [v_1, v_2, \dots]$ .

each  $\alpha_n$  of the expansion (2.29) affects the approximation of the domain of  $f$  only over a subsection of the region of interest. This technique usually simplifies the evaluation of the matrix terms. Sometimes it is convenient to use the point-matching method in conjunction with subsectional bases.

2.3 Example: using the EFIE to estimate TM-wave scattering by PEC cylinders in two dimensions

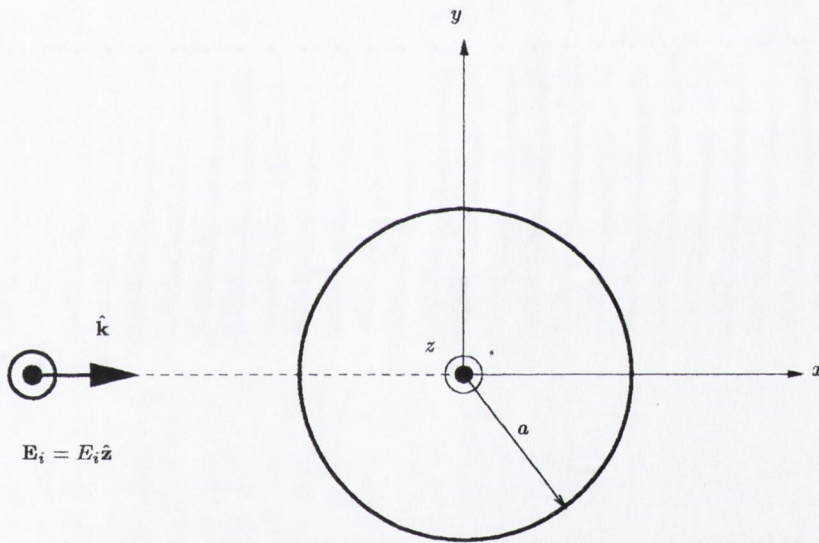


Figure 2.2: Scattering from a PEC cylinder of radius  $a$ . The  $TM_z$  electric plane wave illuminates the cylinder from  $x = -\infty$ . The cylinder extends from  $z = -\infty$  to  $\infty$ .

Consider the case (illustrated in Fig. 2.2) where a  $TM_z$  plane wave is incident on a PEC cylinder with its axis along the  $z$  axis from  $-\infty$  to  $\infty$ . In this case, the current density on the surface of the cylinder does not depend on  $z$ . For the geometry of Fig. 2.2, the surface integro-differential equation is scalar and the vector notation may be abandoned, considering instead the  $z$  components of the electric field and current density,  $E_i$  and  $J_z$ , respectively. Hence, (2.21) becomes

$$E_i = \frac{jk^2}{\omega\epsilon_0} A \tag{2.38}$$

where it is assumed that the homogeneous space exterior to the PEC cylinder is



free space ( $k^2 = \omega^2 \epsilon_0 \mu_0$ ). Moreover it follows from (2.24) that

$$A = \int_{z' \in (-\infty, \infty)} \int_C J_z(x', y') G(|\mathbf{r} - \mathbf{r}'|) dx' dy' dz' \quad (2.39)$$

where  $C$  is the cross-section of the cylinder at any value  $z'$  and

$$G(|\mathbf{r} - \mathbf{r}'|) = \frac{e^{-jk|\mathbf{r} - \mathbf{r}'|}}{4\pi|\mathbf{r} - \mathbf{r}'|} \quad (2.40)$$

where  $\mathbf{r}$  and  $\mathbf{r}' \in C$ . The integral can be further simplified to

$$A = \int_C J_z(x', y') dx' dy' \int_{z' \in (-\infty, \infty)} G(|\mathbf{r} - \mathbf{r}'|) dz' \quad (2.41)$$

giving [18]

$$A = \int_C J_z(x', y') \frac{1}{4j} H_0^{(2)}(k\sqrt{[(x-x')^2 + (y-y')^2]}) dx' dy' \quad (2.42)$$

where  $H_0^{(2)}$  is the zeroth order Hankel function of second kind. Thus, the following integral equation must be solved for  $J_z$

$$E_i(x, y) = \frac{k^2}{4\omega\epsilon_0} \int_C J_z(x', y') H_0^{(2)}(k\sqrt{[(x-x')^2 + (y-y')^2]}) dx' dy' \quad (2.43)$$

where  $(x, y) \in C$  and  $(x', y') \in C$ . (2.43) may now be discretised using the Method of Moments (MoM), introduced in section 2.2.

### 2.3.1 Application of the Method of Moments (MoM)

The first step in the discretisation of (2.43) consists of replacing the actual contour  $C$  with a piecewise linear approximation.  $C$  is modeled using a set of connected flat strips, labelled as  $D_i$ ,  $i = 1 \dots N$ . Obviously, this approximation becomes more accurate as the size of the domains  $D_i$  reduces. The error introduced can be defined as the *modeling error*.

The discretisation of  $J_z$  may be achieved using pulse basis set, i.e.

$$J_z(x, y) \approx \sum_{n=1}^N J_n p_n(x, y) \quad (2.44)$$

where the set of functions  $p_n(x, y)$ ,  $n = 1 \dots N$ , are defined

$$p_n(x, y) = \begin{cases} 1 & \text{if } (x, y) \in D_n \\ 0 & \text{otherwise} \end{cases} \quad (2.45)$$

The functions  $p_n(x, y)$ ,  $n = 1 \dots N$ , are called pulse basis functions. The error introduced in this step can be defined as the *discretisation error*. At some positions, depending on the geometry of the scatterer, a given pulse basis function set may not be able to efficiently represent the true current. This is the case of a strip, for example, where an approximation produced using a set of pulses results in a poor agreement<sup>6</sup> with the expected behaviour of the current (which is singular, as described in [30]) at the edges of the strip. In such cases, [31] a hybrid basis set can be employed to provide a better accuracy. Near the edges of the scatterer triangular pulses or functions that possess a singular behaviour may be employed to approximate the current. Upon substitution of (2.44), (2.43) becomes

$$E_i(x, y) \approx \frac{k^2}{4\omega\epsilon_0} \sum_{n=1}^N J_n \int_{D_n} H_0^{(2)}(k\sqrt{[(x-x')^2 + (y-y')^2]}) p_n(x', y') dx' dy' \quad (2.46)$$

Choosing the set of testing function (see section 2.2)

$$w_m = \delta(x - x_m) \quad x_m \in D_m \quad (2.47)$$

where  $m = 1 \dots N$  and  $\delta(\cdot)$  is the Dirac function, the following matrix equation is obtained

$$E_i(x_m, y_m) = \frac{k^2}{4\omega\epsilon_0} \sum_{n=1}^N J_n \int_{D_n} H_0^{(2)}(k\sqrt{[(x_m - x')^2 + (y_m - y')^2]}) dx' dy' \quad (2.48)$$

<sup>6</sup>Unless, obviously, very short pulse functions are used.

or

$$E_i(x_m, y_m) = \sum_{n=1}^N Z_{mn} J_n \quad (2.49)$$

where  $Z_{mn}$  is the *impedance matrix* defined as

$$Z_{mn} = \frac{k^2}{4\omega\epsilon_0} \int_{D_n} H_0^{(2)}(k\sqrt{[(x_m - x')^2 + (y_m - y')^2]}) dx' dy' \quad (2.50)$$

Typically (2.50) must be evaluated numerically. Observe that there are two distinct cases: the first is when  $m \neq n$ , then the function

$$H_0^{(2)}(k\sqrt{[(x_m - x')^2 + (y_m - y')^2]}) \quad (2.51)$$

can be integrated numerically without any difficulty, being continuous over the domain  $D_n$ ; the second and more difficult case is when  $m = n$ , then the integrand is singular and care must be taken in carrying out the numerical integration. It is important to point out here that the integral *exists and is bounded*, although the function (2.51) is singular when  $(x', y') \in D_n$ . The application of an ordinary quadrature method is not sufficient for an accurate evaluation of the self-terms  $Z_{mm}$  of the matrix. The self-terms of an impedance matrix are relatively large (they take into account for electromagnetic self-interaction of the current residing on a surface domain) and their accurate evaluation is critical. This is also true in the three-dimensional case. This issue will be considered in chapter 6. For the time being, it is sufficient to say that when  $m = n$  the impedance matrix self-term can be approximated by [13]

$$Z_{mm} \approx \frac{k^2}{4\omega\epsilon_0} \left( 1 - j \frac{2}{\pi} \left( \log \left( \frac{\gamma k w_m}{4e} \right) - 1 \right) \right) w_m \quad (2.52)$$

where  $w_m$  is the length of the flat strip  $D_m$  and  $\gamma = 1.78107$ . Another type of error has been introduced, which can be defined as *approximation error* associated with the evaluation of the integrals by quadrature techniques.

Hence, the discretised integral equation

$$E_i(x_m, y_m) = \sum_{n=1}^N Z_{mn} J_n \quad (2.53)$$

must be solved, where the incident field  $E_i(x, y)$  is a  $TM_z$  plane wave (see Fig. 2.2).

$$E_i(x, y) = e^{-jk\hat{\mathbf{k}}\cdot\mathbf{r}} \quad (2.54)$$

and  $\mathbf{r} = x\hat{\mathbf{x}} + y\hat{\mathbf{y}}$ ,  $\hat{\mathbf{k}} = \hat{\mathbf{x}}$  (the incident wave impinges the cylinder from  $-\infty$ ).

(2.53) was set up for the problem illustrated in Fig. 2.2 with  $a = 3\lambda$ , where  $\lambda$  is the wavelength of the incident radiation:  $\lambda = 2\pi/k$ . The number of unknowns was chosen to be  $N = 81$  for this example. This number corresponds to a density of about 4 cells (intervals where the current is assumed to be constant) per wavelength. In [21], pp. 43-44, it is reported that an overall accuracy of 1% in the current density may be obtained for this case increasing the cell density up to 32 cells per wavelength. The matrix equation was solved using the CG iterative scheme introduced in section 2.7. The number of iterations necessary to solve the matrix equation was 31. Fig. 2.3 illustrates the current density obtained using the MoM-CG procedure. The horizontal axis relates to the polar angle  $\phi$  of any point  $(x, y)$  on the cylinder surface:  $(x, y) = a(\cos \phi, \sin \phi)$ , where  $a$  is the radius of the cylinder. The current density is illustrated as a function of  $\phi$ .

The current behaviour is non-smooth, in contrast to the exact solution reported in [21], the reason being that the number  $N$  of samples employed in this case is small. Fig. 2.4 illustrates the current density behaviour (for  $0 < \phi < \pi$ ) when  $N = 300$  and  $N = 900$ . Smoothness is gradually achieved as the number of unknowns is increased.

## 2.4 MFIE for TM-wave scattered from PEC cylinders

It is obvious that also (2.22) may be discretised and solved numerically. The discretisation procedure is derived in [21], pp. 240-243, here the final form of the

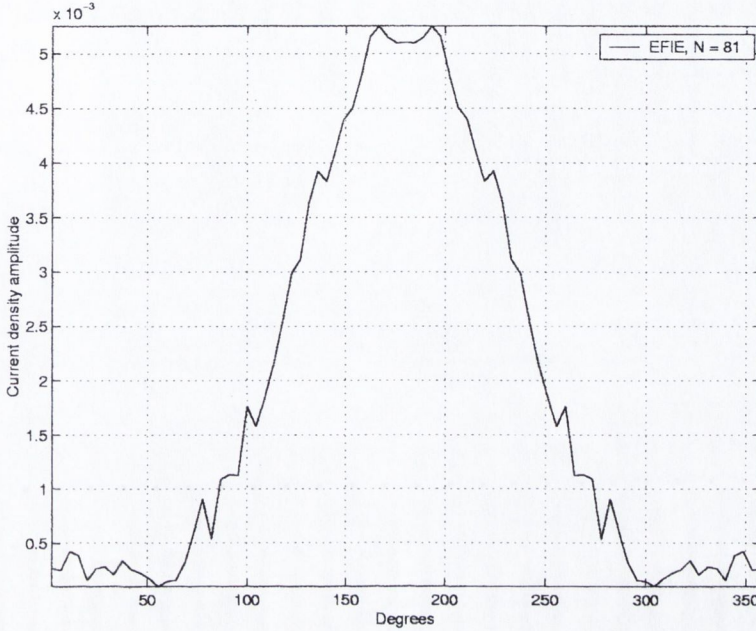


Figure 2.3: EFIE results for the problem of Fig. 2.2: amplitude of current density on the surface of the cylinder versus degrees. The number of unknowns is 81 and the radius of the cylinder is  $a = 3\lambda$ .

resulting matrix equation is reported and the results of its solution are shown for the same example geometry discussed in the EFIE case. The MFIE matrix equation for the  $TM_z$  case is

$$H_i(x_m, y_m) = \sum_{n=1}^N Z_{mn} J_n \quad (2.55)$$

where

$$H_i(x_m, y_m) = -\cos(\theta - \Omega_m) e^{-jk(x_m \cos(\theta) + y_m \sin(\theta))} \quad (2.56)$$

$$Z_{mn} = \begin{cases} \frac{\zeta_0}{2} & \text{if } m = n \\ \frac{jk\zeta_0}{4} \int_{D_n} \Psi_m H_0^{(1)}(kR_m) dx' dy' & \text{otherwise} \end{cases} \quad (2.57)$$

and

$$R_m = \sqrt{[(x_m - x')^2 + (y_m - y')^2]} \quad (2.58)$$

$$\Psi_m = \sin(\Omega_m) \left( \frac{y_m - y'}{R_m} \right) + \cos(\Omega_m) \left( \frac{x_m - x'}{R_m} \right) \quad (2.59)$$

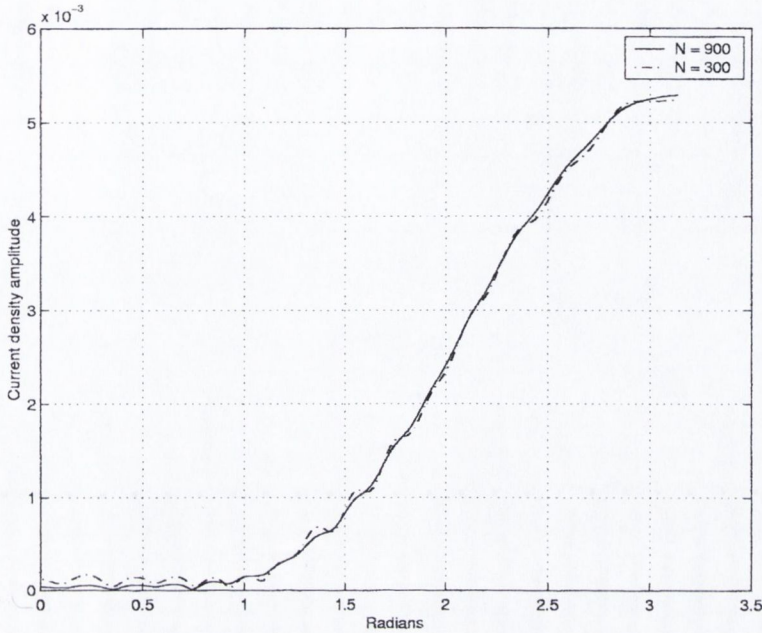


Figure 2.4: EFIE results for the problem of Fig. 2.2 when the number of unknowns is 300 and 900.

Referring to Fig. 2.5,  $\Omega_m$  is the polar angle related to the unit vector normal to the surface of the scatterer at the point  $(x_m, y_m)$ :  $\hat{\mathbf{n}} = \cos(\Omega_m)\hat{\mathbf{x}} + \sin(\Omega_m)\hat{\mathbf{y}}$ ,  $\zeta_0$  is the free space impedance:  $\zeta_0 = \sqrt{\mu_0/\epsilon_0}$ .

The results obtained by solving (2.22) numerically are illustrated in Fig. 2.6. They are in good agreement with the results returned by the EFIE discussed in the previous section. The non-symmetry of the result of Fig. 2.6 is due to the small number  $N$  employed for the discretisation of (2.22). Indeed, a better solution is illustrated in Fig. 2.7 for the case where  $N = 900$ .

## 2.5 CFIE for TM-wave scattered from PEC cylinders

At this stage, it has been shown that the current density residing on the surface of a PEC closed scatterer satisfies both the EFIE and MFIE. However [17], both the EFIE and MFIE are affected by non-uniqueness. The uniqueness of EFIE fails at those values of  $k$  for which there are interior modes of resonance<sup>7</sup> for a closed

<sup>7</sup>As defined in [3], in the loss-free case, electromagnetic fields can exist within a source-free region enclosed by a perfect conductor. These fields can exist only at specific frequencies, called

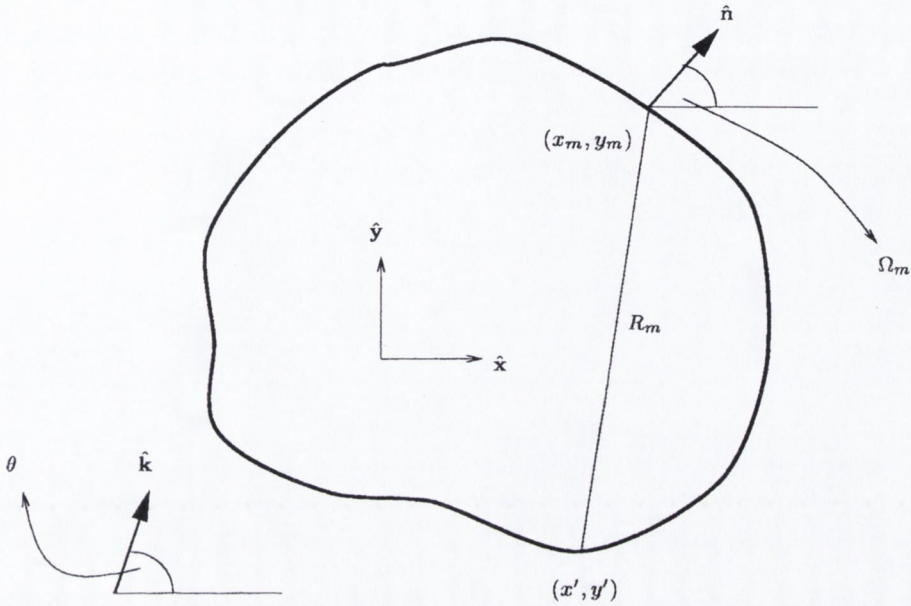


Figure 2.5: Cylinder cross section and parameters used in the MFIE (2.55):  $\hat{\mathbf{k}}$  is the unit vector associated with the plane wave illuminating the scatterer,  $\theta$  is the angle of incidence,  $R_m$  is the distance between the integration point  $(x', y')$  and the observation point  $(x_m, y_m)$ ,  $\hat{\mathbf{n}}$  is the normal unit vector and  $\Omega_m$  is the polar angle associated with  $\hat{\mathbf{n}}$ .

scatterer. Similarly, the uniqueness of MFIE fails at those values of  $k$  for which there are interior modes of resonance. To illustrate the effects of non-uniqueness, refer to Fig. 2.8 where the current density amplitudes obtained either using the EFIE and the MFIE are illustrated, assuming the radius of the cylinder such that  $ka = 2.405$ . Here, the results returned by MFIE and EFIE differ substantially because while the EFIE renders a solution only the MFIE returns the correct one.

The question arises: what occurs numerically when the EFIE is solved at a resonant value of  $k$ ? At these frequencies the integral operator of the EFIE has a non-null set of eigenvectors (functions) for the eigenvalue 0. Thus, to each solution of the integral equation due to an external excitation (the incident wave) may be added the eigenfunction corresponding to the null eigenvalue and the resulting function is still a solution of the original problem. Numerically speaking, in the implementation of the EFIE, the matrix of the algebraic system is nearly singular and the solution becomes highly unstable as it is illustrated in Fig. 2.8. The same behaviour is exhibited by the MFIE at magnetic resonant frequencies. Nevertheless,

---

*resonant frequencies.*

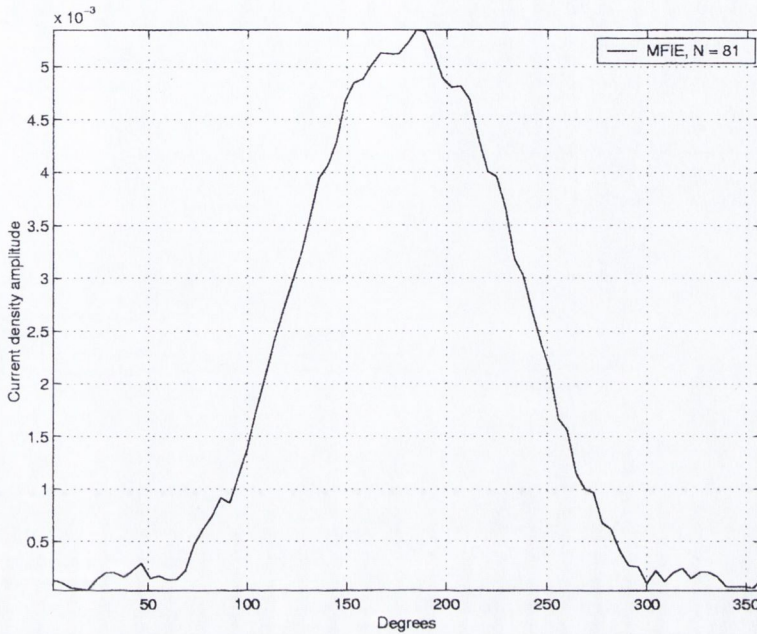


Figure 2.6: MFIE results for the problem of Fig. 2.2: amplitude of current density on the surface of the cylinder versus degrees. The number of unknowns is 81 and the radius of the cylinder is  $a = 3\lambda$ .

as Jones points out [17], if a choice has to be made between EFIE and MFIE, *the better gambit is the MFIE*. In fact, the MFIE is classified as an integral equation of the second kind (i.e. the unknown function appears either inside and outside the integral operator), for which the theory has broader foundations. Moreover, in order to achieve a better accuracy, the size of the algebraic system usually is increased subdividing the scatterer in smaller flat strips. While this operation affects the whole matrix of the EFIE by decreasing all its elements, which are integrals evaluated over the smaller domains, it does increase the diagonal dominance of the MFIE matrix which does not become ill-conditioned (see [17]), as may be verified referring to (2.57).

An alternative formulation that provides unique and stable solutions for all closed scatterers at all frequencies is the Combined Field Integral Equation (CFIE), which is a linear combination of the EFIE and MFIE:

$$CFIE = (b)EFIE + (1 - b)MFIE \quad (2.60)$$

where  $b$  is a real number between 0 and 1. The penalty is that (2.60) becomes more



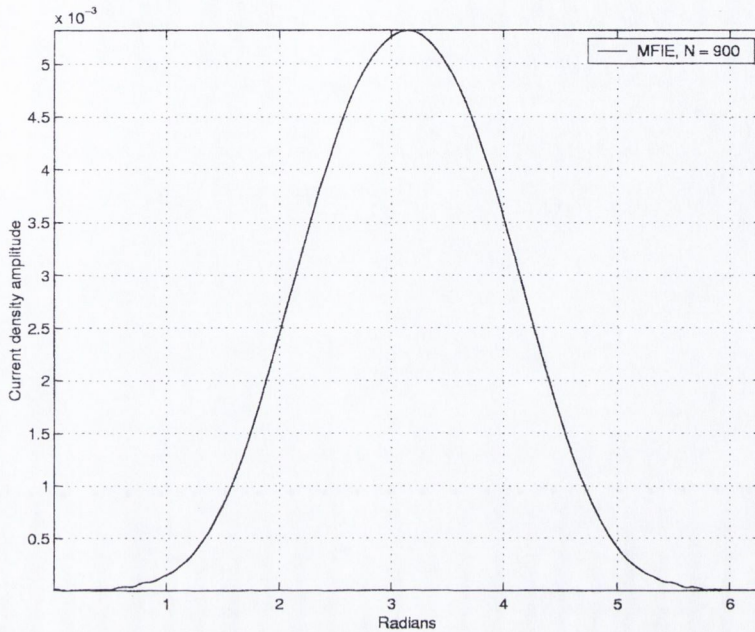


Figure 2.7: MFIE results for the problem of Fig. 2.2: amplitude of current density on the surface of the cylinder versus radians. The number of unknowns is 900 and the radius of the cylinder is  $a = 3\lambda$ .

complicated and requires a greater computational effort to calculate the impedance matrix entries. The proof of CFIE uniqueness is given in [21], pp. 241-242, and it is based on the fact that when the incident field is null, the flow of power into the scatterer interior must vanish and this implies, if  $b \neq 0$  and  $b \neq 1$ , that the surface tangential fields evaluate to zero: the CFIE has no interior resonance solutions unless  $b = 0$  (MFIE) or  $b = 1$  (EFIE). Fig. 2.9 shows the results returned by the CFIE for a circular cylinder of radius  $a$  such that  $ka = 2.405$ . CFIE result obviously matches MFIE result; as expected, for  $b = 0.7$  (the value 0.7 was chosen following the suggestions given by Jones [17]). It must be emphasised that the CFIE approach is not the only way to combat the defect of non-uniqueness of either the EFIE or MFIE. Another approach eliminates the resonant solutions by modifying the resultant matrix equations, for example using additional equations obtained by extending the boundary conditions into some interior points, as described in [32].

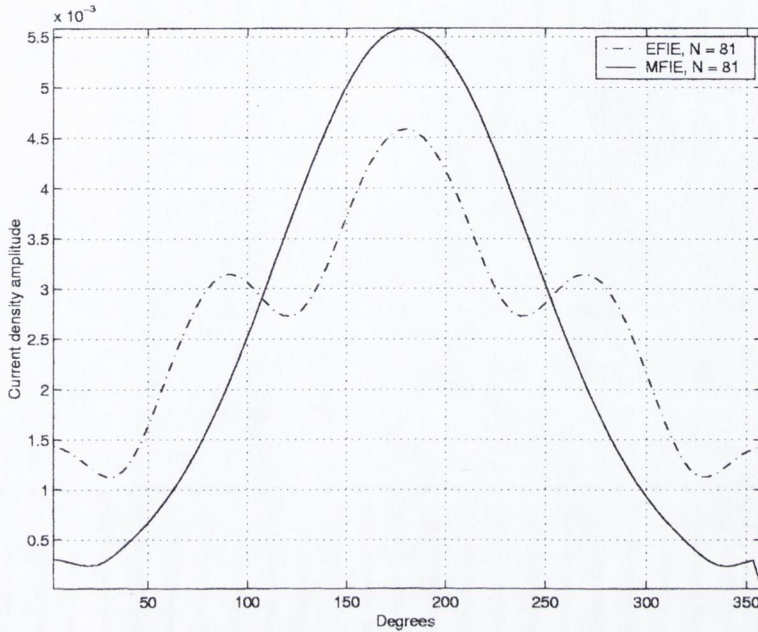


Figure 2.8: EFIE/MFIE results for the problem of Fig. 2.2 when  $ka = 2.405$ . The MFIE solution is not affected by non-uniqueness problem. The EFIE solution instead shows instability due to numerical errors caused by non-uniqueness.

## 2.6 MoM solution of the EFIE in three-dimensions

Recalling the integral equation (2.21) and the definition of scattered electric field  $\mathbf{E}_s$  given in section A.2, it is readily found that the scattered field may be obtained in terms of the vector potential  $\mathbf{A}$  and the scalar potential  $\Phi$  [33]

$$\mathbf{E}_s = -j\omega\mathbf{A} - \nabla\Phi \quad (2.61)$$

where

$$\mathbf{A}(\mathbf{r}) = \frac{\mu_0}{4\pi} \int_S \mathbf{J}_S \frac{e^{-jkR}}{R} dS' \quad (2.62)$$

and

$$\Phi(\mathbf{r}) = \frac{1}{4\pi\epsilon_0} \int_S \sigma \frac{e^{-jkR}}{R} dS' \quad (2.63)$$

It is assumed that the medium surrounding the scatterer is free space,  $R = |\mathbf{r} - \mathbf{r}'|$  is the distance between an arbitrarily located observation point  $\mathbf{r}$  and a source

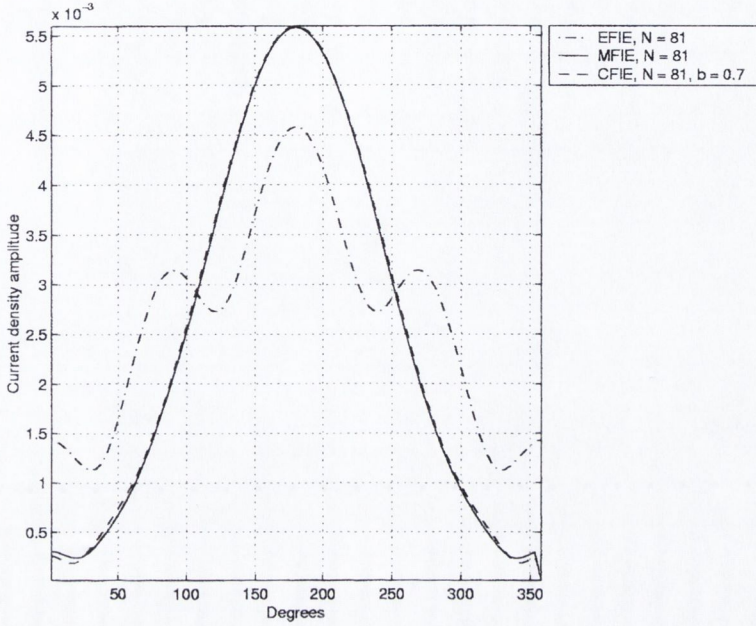


Figure 2.9: CFIE results for the problem of Fig. 2.2 when  $ka = 2.405$ : The CFIE given in (2.60) has been implemented with  $b = 0.7$  and the number of unknowns is 81.

point  $\mathbf{r}'$  on  $S$ . The function  $\sigma$  is the surface charge density, related to  $\mathbf{J}_S$  using the *continuity equation*

$$\nabla' \cdot \mathbf{J}_S = -j\omega\sigma \quad (2.64)$$

The EFIE becomes then

$$\hat{\mathbf{n}} \times \mathbf{E}_i(\mathbf{r}) = \hat{\mathbf{n}} \times (j\omega\mathbf{A} + \nabla\Phi) \quad \mathbf{r} \in S \quad (2.65)$$

### 2.6.1 Development of basis functions

To facilitate the discretisation of the integral equation (2.65), first the surface  $S$  may be represented as an aggregation of simple domains. This operation is often called *surface patch modeling*. Planar triangular patch models are particularly appropriate. They are able to approximate any surface or boundary and their density can be varied accordingly to the local resolution required. It is hence assumed that the surface  $S$  is modeled in terms of an appropriate collection of

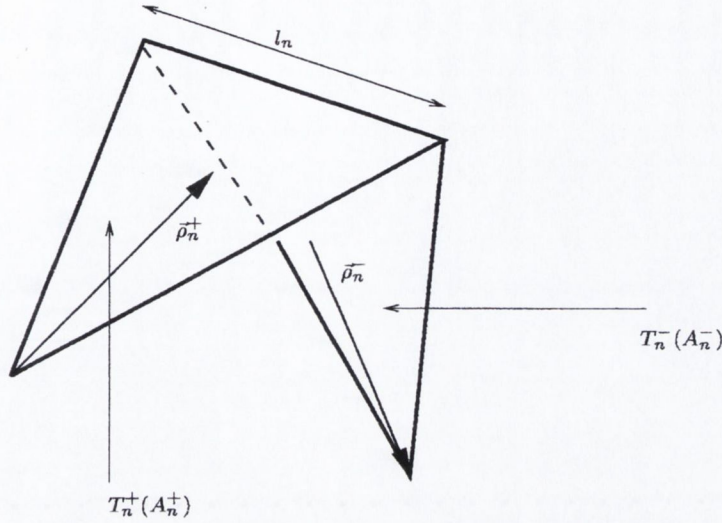


Figure 2.10: A triangle pair over which the RWG basis function  $\mathbf{f}_n(\mathbf{r})$  is defined.

triangular facets, with edges, vertices and *boundary edges*<sup>8</sup>. Using this surface model, it is possible to introduce the Rao-Wilton-Glisson (RWG) basis set for the current. Each RWG basis function is associated with an interior edge and vanishes everywhere else on  $S$  except on the pair of triangles attached to the edge. Referring to Fig. 2.10, let the edge associated with the  $n$ -th basis function be  $l_n$ ; the two triangles where the basis function  $\mathbf{f}_n$  does not vanish are referred to as  $T_n^+$  and  $T_n^-$ . The plus or minus superscripts are determined by the choice of the positive current reference direction for the  $n$ -th edge: the current is assumed to flow across  $l_n$  from  $T_n^+$  to  $T_n^-$ . The basis function associated with the edge  $n$  is defined as follows

$$\mathbf{f}_n(\mathbf{r}) = \begin{cases} \frac{l_n}{2A_n^+} \vec{\rho}_n^+ & \text{if } \mathbf{r} \in T_n^+ \\ \frac{l_n}{2A_n^-} \vec{\rho}_n^- & \text{if } \mathbf{r} \in T_n^- \\ 0 & \text{otherwise} \end{cases} \quad (2.66)$$

where the position vector  $\vec{\rho}_n^+$  is defined with reference to the vertex of  $T_n^+$  opposite  $l_n$  and lies within  $T_n^+$ , as illustrated in Fig. 2.10. Similarly is defined  $\vec{\rho}_n^-$ .  $A_n^+$  is the

<sup>8</sup>Given a triangular patch, three edges are associated with it. Each edge can be an *interior edge* or a *boundary edge* whether if the surface electric current located on  $S$  has a component normal to the edge itself or not. For example, the edges on the perimeter of a triangular mesh associated with an open surface are boundary edges.

area of the triangle  $T_n^+$  and  $A_n^-$  is the area of the triangle  $T_n^-$ . Finally, as already pointed out,  $l_n$  is the length of the edge  $n$ . The basis function  $\mathbf{f}_n$ , used to represent the surface current  $\mathbf{J}_s$ , has several important properties which are listed below.

- The current has no component normal to the boundary of the domain where it does not vanish<sup>9</sup>.
- The component of current normal to the edge associated with it is constant and continuous across the edge<sup>10</sup>.
- The surface divergence of the basis function is constant over each triangle:

$$\nabla' \cdot \mathbf{f}_n(\mathbf{r}') = \begin{cases} \frac{l_n}{A_n^+} & \text{if } \mathbf{r}' \in T_n^+ \\ \frac{-l_n}{A_n^-} & \text{if } \mathbf{r}' \in T_n^- \\ 0 & \text{otherwise} \end{cases} \quad (2.67)$$

- The moment of the basis function is given by  $(A_n^+ + A_n^-)\mathbf{f}_n^{avg}$ , with

$$(A_n^+ + A_n^-)\mathbf{f}_n^{avg} = \int_{T_n^+ + T_n^-} \mathbf{f}_n dS = \frac{l_n}{2} (\bar{\rho}_n^{c+} + \bar{\rho}_n^{c-}) \quad (2.68)$$

where  $\bar{\rho}_n^{c+}$  is the value of  $\rho_n^+$  at the centroid of  $T_n^+$  and a similar definition holds for  $\bar{\rho}_n^{c-}$ .

After having identified a suitable set of basis function for approximating the surface current  $\mathbf{J}_s$ , i.e.  $\mathbf{J}_s \approx \sum_{n=1}^N I_n \mathbf{f}_n$ , it is useful to consider the physical significance of the coefficients  $I_n$ . Each coefficient  $I_n$  may be interpreted as the normal component of current density flowing across the  $n$ -th edge. This is due to the fact that the three different basis functions will be defined over the  $n$ -th edge, but only that one associated with it, i.e.  $\mathbf{f}_n$ , has a normal component across it, which is constant (see properties listed above).

<sup>9</sup>This property guarantees the non-existence of surface charge at the perimeter of an open surface, as physically expected.

<sup>10</sup>Given the unit vector  $\hat{\mathbf{l}}_n$  aligned along  $l_n$  it is  $\hat{\mathbf{l}}_n \times \mathbf{f}_n = 1$ .

### 2.6.2 Testing the EFIE

To carry out the MoM solution of (2.65), the next step is to select a testing procedure, i.e. (2.65) is enforced at some points of  $S$ . A basis function set has been defined, now a testing function set must be chosen. The optimal approach is called *Galerkin's method* and defines the testing functions to be identical to the basis functions  $\mathbf{f}_n$ . Then the integral equation (2.65) can be tested as

$$\langle \hat{\mathbf{n}} \times \mathbf{E}_i, \mathbf{f}_m \rangle = \langle \hat{\mathbf{n}} \times (j\omega \mathbf{A} + \nabla \Phi), \mathbf{f}_m \rangle \quad (2.69)$$

where the inner product is defined as follows

$$\langle \mathbf{f}, \mathbf{g} \rangle = \int_S \mathbf{f} \cdot \mathbf{g} dS \quad (2.70)$$

Thus, it is possible to write

$$\langle \mathbf{E}_i, \mathbf{f}_m \rangle = \langle j\omega \mathbf{A}, \mathbf{f}_m \rangle + \langle \nabla \Phi, \mathbf{f}_m \rangle \quad (2.71)$$

Making use of vector algebra identity and the properties of  $\mathbf{f}_m$  at the edges of  $S$  [33], the equation is reduced to

$$\langle \mathbf{E}_i, \mathbf{f}_m \rangle = \langle j\omega \mathbf{A}, \mathbf{f}_m \rangle - \int_S \Phi \nabla_S \cdot \mathbf{f}_m dS \quad (2.72)$$

where  $\nabla_S$  is the surface divergence operator<sup>11</sup>. Now, note that the inner products  $\langle j\omega \mathbf{A}, \mathbf{f}_m \rangle$  and  $\langle \nabla \Phi, \mathbf{f}_m \rangle$  may be evaluated with a single-point numerical quadrature formula using the value of  $\mathbf{A}$  and  $\Phi$  at the centroid of the domain. Specifically, for the integral involving  $\Phi$  it may be written

$$\int_S \Phi \nabla_S \cdot \mathbf{f}_m dS = l_m \left( \frac{1}{A_m^+} \int_{T_m^+} \Phi dS - \frac{1}{A_m^-} \int_{T_m^-} \Phi dS \right) \approx l_m \left( \Phi(\mathbf{r}_m^{c+}) - \Phi(\mathbf{r}_m^{c-}) \right) \quad (2.73)$$

where  $\mathbf{r}_m^{c+}$  is the position vector associated with the centroid of  $T_m^+$  and  $\mathbf{r}_m^{c-}$  is the position vector associated with the centroid of  $T_m^-$  (this means that the function  $\Phi$

<sup>11</sup>For example if a rectangular coordinate system is defined in the plane of the triangular patch, i.e.  $dS = dx dy$ , then the  $\nabla_S$  operator may be expressed as  $\frac{\partial}{\partial x} \hat{\mathbf{x}} + \frac{\partial}{\partial y} \hat{\mathbf{y}}$ .

is evaluated at these points and it is assumed that does not vary substantially in the surface domain considered so that it may be considered constant)<sup>12</sup>. Similarly for  $\mathbf{A}$  it can be written that

$$\langle \mathbf{A}, \mathbf{f}_m \rangle = l_m \left( \frac{1}{2A_m^+} \int_{T_m^+} \mathbf{A} \cdot \vec{\rho}_m^+ dS + \frac{1}{2A_m^-} \int_{T_m^-} \mathbf{A} \cdot \vec{\rho}_m^- dS \right) \approx \frac{l_m}{2} \left( \mathbf{A}(\mathbf{r}_m^{c+}) \cdot \vec{\rho}_m^{c+} + \mathbf{A}(\mathbf{r}_m^{c-}) \cdot \vec{\rho}_m^{c-} \right) \quad (2.74)$$

At this stage all the mathematical tools necessary to discretise the integral equation (2.72) are provided. In the next section, the matrix equation is derived.

### 2.6.3 Derivation of the matrix equation

Recalling that the current is approximated by the sum

$$\mathbf{J}_s(\mathbf{r}) \approx \sum_{n=1}^N I_n \mathbf{f}_n(\mathbf{r}), \quad (2.75)$$

and given the fact that the two potential fields  $\mathbf{A}$  and  $\Phi$  depend on  $\mathbf{J}_s$  and  $\sigma$ :

$$\mathbf{A}(\mathbf{r}) = \frac{\mu_0}{4\pi} \int_S \mathbf{J}_s \frac{e^{-jkR}}{R} dS' \quad (2.76)$$

$$\Phi(\mathbf{r}) = \frac{1}{4\pi\epsilon_0} \int_S \sigma \frac{e^{-jkR}}{R} dS' \quad (2.77)$$

(2.72) is discretised as

$$V_m = \sum_{n=1}^N Z_{mn} I_n \quad (2.78)$$

where

$$Z_{mn} = l_m \left( j\omega \left( A_{mn}^+ \cdot \frac{\vec{\rho}_m^{c+}}{2} + A_{mn}^- \cdot \frac{\vec{\rho}_m^{c-}}{2} \right) + \Phi_{mn}^- - \Phi_{mn}^+ \right) \quad (2.79)$$

<sup>12</sup>Obviously this one-point quadrature rule may be improved applying the usual numerical integration techniques, such as Romberg or Gauss rules, described in [21], pp. 525-530.

and

$$V_m = l_m \left( \mathbf{E}_m^+ \cdot \frac{\bar{\rho}_m^+}{2} + \mathbf{E}_m^- \cdot \frac{\bar{\rho}_m^-}{2} \right) \quad (2.80)$$

with

$$A_{mn}^+ = \frac{\mu_0}{4\pi} \int_S \mathbf{f}_n(\mathbf{r}') \frac{e^{-jkR_m^+}}{R_m^+} \quad (2.81)$$

$$\Phi_{mn}^+ = -\frac{1}{4\pi j\omega\epsilon_0} \int_S \nabla'_S \cdot \mathbf{f}_n(\mathbf{r}') \frac{e^{-jkR_m^+}}{R_m^+} \quad (2.82)$$

$$R_m^+ = |\mathbf{r}_m^{c+} - \mathbf{r}'| \quad (2.83)$$

and

$$\mathbf{E}_m^+ = \mathbf{E}_i(\mathbf{r}_m^{c+}) \quad (2.84)$$

Similar definitions hold for  $A_{mn}^-$ ,  $\Phi_{mn}^-$ ,  $R_m^-$  and  $\mathbf{E}_m^-$  with the obvious difference of sign. Once all the necessary elements are evaluated, one may solve the resulting system of linear equations (2.78) for the unknown vector of coefficients  $I_n$ ,  $n = 1 \dots N$ .

## 2.7 The Conjugate Gradient (CG) method

In this section, the matrix equation (2.78) is denoted as  $ZI = V$  and it is of interest to evaluate the vector of coefficients  $I = [I_1 \dots I_N]$ . The procedure here outlined is iterative and the number of the iteration will be indicated by a superscript. Hence, the estimate of the vector  $I$  at the  $m$ -th iteration will be  $I^m$ . Also, Galerkin's method is considered. As described in [33], this yields a symmetric impedance matrix  $Z$ .

To determine the surface current density distribution in terms of basis functions, the system of linear equations (2.78) must be solved. Among various techniques



available, the most suitable appears to be the Conjugate Gradient (CG) method, developed independently by Stiefel and Hestenes and given in [34]. The CG method is an iterative method which terminates in at most  $N$  steps (if  $N$  is the size of the unknown vector) if no round-off errors are encountered. Starting with an initial estimate of the solution, say  $I^1$ , one determines successively new estimates  $I^2 \dots I^k$  of the solution  $I$ . Referring to (2.78), at each step the residual  $r^k = V - ZI^k$  is computed and if no round-off error is encountered one will reach an estimate  $I^m$  ( $m \leq N$ ) at which  $r^m = 0$ . This estimate is the desired solution  $I$ . Obviously, since round-off errors always occur, the estimate at step  $N$ ,  $I^N$ , will not be the *exact* solution  $I$  but will be a good approximation of it. One could restart with the estimate  $I^N$  as the initial estimate  $I^1$ , so as to diminish the effects of the round-off errors. In the CG method, the error vector  $I - I^k$  is diminished in length at each step  $k$ . However, the *squared residual*  $|V - ZI^k|^2 = |r^k|^2$  normally oscillates and may even increase at each step (except for the last). The CG algorithm has a very simple structure and its implementation is straightforward. Referring to (2.78), starting with an initial guess  $I^1$ , the two following quantities must be computed:

$$r^1 = V - ZI^1 \quad (2.85)$$

$$p^1 = Z^*r^1 \quad (2.86)$$

where  $Z^*$  is the transpose-conjugate of the matrix  $Z$  (in the case of Galerkin's method,  $Z$  is symmetric). Then the iteration starts and for each  $i > 1$ , the following quantities must be evaluated sequentially:

$$a^i = \frac{|Z^*r^i|^2}{|Zp^i|^2} \quad (2.87)$$

$$I^{(i+1)} = I^i + a^i p^i \quad (2.88)$$

$$r^{(i+1)} = r^i - a^i Zp^i \quad (2.89)$$

$$b^i = \frac{|Z^*r^{(i+1)}|^2}{|Z^*r^i|^2} \quad (2.90)$$

$$p^{(i+1)} = Z^* r^{(i+1)} + b^i p^i \quad (2.91)$$

The iteration is stopped when the residual error  $r^k = V - ZI^k$  is less than a certain constant fixed *a priori*. A detailed analysis of the CG theoretical foundations is beyond the scope of this section. At this stage, it is sufficient to briefly refer to [35] where an exhaustive survey of the most popular methods for the solution of large matrix equations is given. The most important features of the CG method are

- The core storage required is  $N^2 + 6N + 2$ .
- The number of arithmetic operations required is  $2N^2 + 6N$  *per iteration*.

By comparison with other popular methods, it is found that the application of the CG algorithm to the analysis of large bodies scattering by the moment method yields to *stable, reliable, consistent and accurate* results faster than any other methods currently used. Convergence of the algorithm has been analysed and characterised in [36] and [37]. As an observation, it has been reported in [10] that roughly  $Pc(Z)$  iterations are required to produce accuracy to  $P$  decimal places, where  $c(Z)$  is the condition number<sup>13</sup> of  $Z$ .

## 2.8 The Conjugate Gradient-Fast Fourier Transform (CG-FFT) method

The MoM-CG is not the only technique available to solve the EFIE in the three-dimensional case. For planar scatterers, there exists an alternative approach to the solution of the EFIE, which is elegant, simple to implement and faster than the MoM-CG. This technique is based on the fact that the integro-differential operator which relates the electric current density to the electric scattered field is a convolution for the case of planar scatterers. Using this fact, it is possible to use

<sup>13</sup>The condition number is a non-negative number used to estimate the amount by which small errors in the right hand side of the equation  $ZI = V$ , i.e.  $V$ , or changes in  $Z$  itself, can change the solution  $I$ . The condition number is defined in terms of a particular matrix norm.

the Fourier Transforms of the fields to efficiently compute the integrals at each iteration of the CG algorithm. Making use of the Fast Fourier Transform (FFT) [38] algorithm, this step is accomplished by  $N \log N$  operations instead of  $N^2$  operations which characterises a matrix-vector multiplication CG-algorithm using the MoM-CG approach.

To elucidate the Conjugate Gradient-Fast Fourier Transform (CG-FFT) method, recall the integral equation (2.65); in the case of a planar<sup>14</sup> scatterer  $S$ , located in the  $(x, y)$  plane, this becomes

$$\begin{aligned}
 -j\omega\epsilon_0 \begin{pmatrix} E_i^x(x, y) \\ E_i^y(x, y) \end{pmatrix} &= \omega^2\epsilon_0\mu_0 \int_S \begin{pmatrix} J_S^x(x', y') \\ J_S^y(x', y') \end{pmatrix} G(R) dx' dy' + \\
 &\begin{pmatrix} \frac{\partial}{\partial x} \\ \frac{\partial}{\partial y} \end{pmatrix} \int_S \left( \frac{\partial}{\partial x'} J_S^x(x', y') + \frac{\partial}{\partial y'} J_S^y(x', y') \right) G(R) dx' dy' \quad (2.92)
 \end{aligned}$$

where

$$G(R) = \frac{e^{-jkR}}{4\pi R} \quad (2.93)$$

and

$$R = \sqrt{(x - x')^2 + (y - y')^2} \quad (2.94)$$

Now, each of the two surface integrals in (2.92) is a convolution; the first is a convolution of the the current density  $\mathbf{J}_S$  and the Green's function  $G$  and the second is a convolution of the derivative of the current density components and the Green's function. The right-hand side of (2.92), if discretised by using a RWG basis set, returns the impedance matrix-vector multiplication of the MoM. Let  $\mathcal{Z}$  be the integro-differential operator which relates the electric current to the incident electric field. Then, because of the convolutional property of  $\mathcal{Z}$ , it may be written

<sup>14</sup>The  $x$  and  $y$  components of the electric field and current are indicated by the suitable superscripts.

that

$$\mathbf{Z}\mathbf{J}_S = FFT^{-1} \left( \tilde{G}(k_x, k_y) \begin{pmatrix} (\omega^2 \epsilon_0 \mu_0 - k_x^2) & -k_x k_y \\ -k_x k_y & (\omega^2 \epsilon_0 \mu_0 - k_y^2) \end{pmatrix} \begin{pmatrix} \tilde{J}_S^x(k_x, k_y) \\ \tilde{J}_S^y(k_x, k_y) \end{pmatrix} \right) \quad (2.95)$$

where  $\omega = k^2/\epsilon_0\mu_0$  and where  $\tilde{G}(k_x, k_y)$  is the Fourier transform of  $G(x, y)$

$$\tilde{G}(k_x, k_y) = \int_{-\infty}^{\infty} \int_{-\infty}^{\infty} G(x, y) e^{-j2\pi k_x x} e^{-j2\pi k_y y} dx dy \quad (2.96)$$

Similar definitions hold for the two components of the electric current density and the symbol FFT relates to the operation of evaluating the Fourier Transform of any function, using the fast algorithm [38]. The samples of the surface current density components may be thus determined by a CG scheme. At each iteration  $i$  of the CG algorithm the new Fourier Transform of  $\mathbf{J}_S^{(i)}$  is evaluated and each sample of the array  $FFT(\mathbf{J}_S^{(i)})$  at a pair of coordinates  $(k_x, k_y)$  in the transformed domain (using a popular terminology, the  $k$ -space) is multiplied by the term  $FFT(\mathbf{Z})$  which is a function of the pair  $(k_x, k_y)$  and of the Fourier transform of the function  $G$ . The iterative process is halted when the residual error between the incident field and the field scattered by the estimate of the electric current is less than a threshold value. The author has experienced that the number of iterations needed to solve the EFIE by the CG-FFT is in general greater than that one needed by the MoM-CG procedure. However, a single iteration of the CG-FFT is much faster than in the MoM-CG case. The CG-FFT method is illustrated in detail in [21], pp. 170-175. Further insight can be derived referring to [39]-[42].

### 2.8.1 One-Iteration FFT algorithm

This section is dedicated to an important point which arises in the discussion of the CG-FFT method. Recalling (2.92), it may be written that

$$\tilde{G}(k_x, k_y) \begin{pmatrix} (\omega^2 \epsilon_0 \mu_0 - k_x^2) & -k_x k_y \\ -k_x k_y & (\omega^2 \epsilon_0 \mu_0 - k_y^2) \end{pmatrix} \begin{pmatrix} \tilde{E}_i^x(k_x, k_y) \\ \tilde{E}_i^y(k_x, k_y) \end{pmatrix} = -j\omega 4\pi \epsilon_0 \begin{pmatrix} \tilde{E}_i^x(k_x, k_y) \\ \tilde{E}_i^y(k_x, k_y) \end{pmatrix} \quad (2.97)$$

Now, it may appear possible first to solve the equation in the  $k$ -space, which is a linear matrix equation for each pair  $(k_x, k_y)$  and successively calculate the unknown functions using an inverse FFT. Thus only one step of the iterative scheme would be necessary. However, this reasoning is misleading because when the convolution of the Green's function and the current or its derivatives is performed, the resulting function is defined over a domain of the plane  $(x, y)$  which is larger than the domain  $S$ . The value of the scattered field is known only on  $S$ : it is equal to the incident field by boundary conditions. Thus, not all the necessary information is supplied for the solution of the integral equation in the  $k$ -space. In other words, to carry out the calculation of the unknown current using a one-step scheme is possible *only if the scattered field due to the current is known over a domain larger than the planar surface of the scatterer  $S$* . It is interesting to explore whether an approximation to the scattered field outside the domain  $S$  can be suggested in order to evaluate the current in one step with sufficient accuracy.

Suppose to have a PEC strip of length  $L$  located over the  $x$  axis and of infinite size over the  $z$  direction, i.e. the domain  $S$  is the set  $x \in [0, L], z \in (-\infty, \infty)$  and a  $TM_z$  plane wave is normally incident upon it. Thus, the integral equation becomes

$$1 = \frac{k\zeta_0}{4} \int_0^L J_z(x') H_0^{(2)}(k|x-x'|) dx' \quad (2.98)$$

for

$$x \in [0, L] \quad (2.99)$$

Hence, the approach to follow is first, truncate the Hankel function  $H_0^{(2)}(k|x|)$ , say between  $-L$  and  $L$  and evaluate the FFT of the function obtained; next, assuming that the scattered field given by the integral in (2.98) vanishes for  $x$  outside the interval  $[0, L]$ , perform an FFT of the resulting field, i.e. the pulse function which is 1 for  $x \in [0, L]$ . Finally the electric current density can be evaluated by an inverse FFT of the quotient between the two FFTs of the resulting field and the Hankel function respectively. Numerical result for this example are given in the next section.

## 2.9 Numerical results

In this section, four sets of results are provided. The first set relates to the section 2.8.1. The other three sets of results demonstrate the application of the EFIE to calculate the three-dimensional electromagnetic scattering by a square flat plate and a circular disk.

### 2.9.1 Example of application of the CG-FFT method

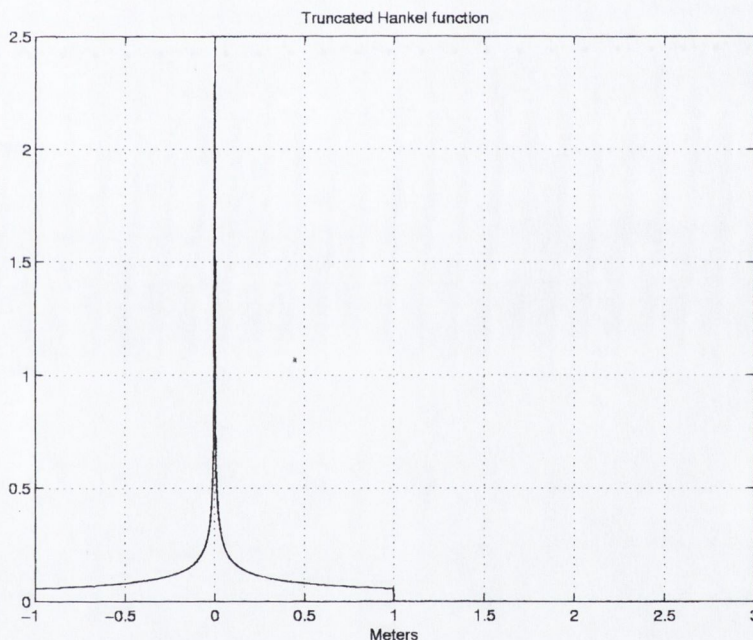


Figure 2.11: Plot of the amplitude of the truncated Hankel function. The interval of interest, where the electric current is located, is  $x \in [0, L]$ , with  $L = 1m = 32\lambda$ .

Fig. 2.11 is the amplitude of a truncated Hankel function as used for the inversion of (2.98). A strip of length  $L = 32\lambda = 1m$  is illuminated normally by a plane wave with wave-vector of amplitude  $k = 2\pi/\lambda$ . The frequency of sampling employed in the FFT is 8 samples per wavelength. The truncated Hankel function is defined over the interval  $x \in [-1, 1]$  and zero elsewhere. The result of the computation of the FFT of the truncated Hankel function is illustrated in Fig. 2.12. Assume that the field scattered by the unknown current is equal to the incident field over the strip (this is exact by boundary conditions) and zero elsewhere. The FFT of this field is then divided by the FFT of the Hankel function. The result is an approximation

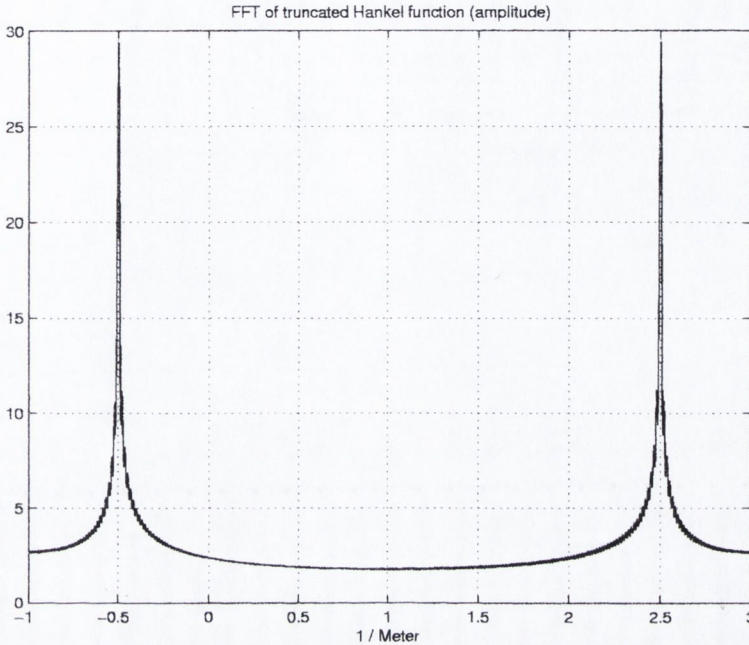


Figure 2.12: Amplitude of the Fourier transform of the function illustrated in Fig. 2.11. This is the result of an FFT performed over the samples of the Hankel function (frequency of sampling: 8 samples per wavelength).

of the FFT of the unknown electric current. By inverting this quotient, using an FFT operation, the electric current density over the strip is found. The result is illustrated in Fig. 2.13, where also the exact MoM solution, obtained using a discretisation of the integral equation (2.98), is given. It is evident that the result of the integral equation in  $k$ -space is completely reliable and is produced using a procedure having complexity of  $\mathcal{O}(N \log N)$ , if  $N$  is the number of current samples. The CG algorithm requires instead  $N^2$  operations per iteration. It is now interesting to compare the field due to the current distribution evaluated by a CG algorithm and the approximated field that has been employed to calculate the current using an FFT algorithm. The result is given in Fig. 2.14, where it can be seen clearly how the scattered field due to the CG current equalises the incident field over the strip location and, as for the amplitude, decays rapidly to less than 10% of the incident field outside the interval  $[0, L]$ . The field of the FFT method is also illustrated: it has been assumed that it is zero outside the strip location. Obviously, the latter approximation permits to achieve the excellent agreement of Fig. 2.13 due to the fact that the actual field rapidly tends to zero outside  $[0, L]$ .

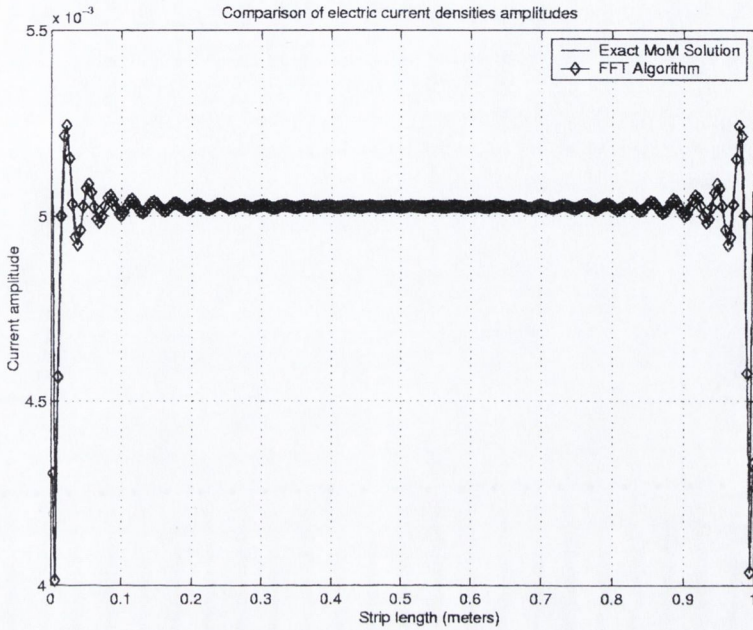


Figure 2.13: Amplitudes of the electric current density evaluated using an *one step* FFT algorithm and the usual MoM, discretising the integral equation and solving the resulting matrix equation. The two functions perfectly match over the interval of interest  $x \in [0, L]$ , with  $L = 1m$ .

### 2.9.2 Three-dimensional case: EFIE results for simple geometries

Fig. 2.15 illustrates the surface patch model for a square flat plate of side equal to  $1m = \lambda$ . This scatterer is described in terms of triangular patches, and an integral equation analysis has been carried out to evaluate the electric current density on the surface of the plate when a plane wave is incident normally upon it. Referring to Fig. 2.15, the horizontal direction is the  $x$  direction while the vertical direction is the  $y$  direction hence the propagation vector is parallel to the  $z$  direction.

The amplitude of the  $x$  component of the current density is presented in Fig. 2.16 along the line  $x = L/2$ , where  $L$  is the length of the side of the plate and  $(x, y) \in [0, L]$ . The number of unknowns in this case is 176.

Fig. 2.17 shows the surface patch model for a circular disk of radius  $a = 1m = 2\lambda$ . Again the scatterer is described in terms of triangular patches more refined at the centre of the disk. The incident electric field is due to a dipole located normally over the centre of the disk at a height  $0.1a$ . In this case, 792 edges (unknowns) are sufficiently necessary to represent the surface current density over the scatterer,



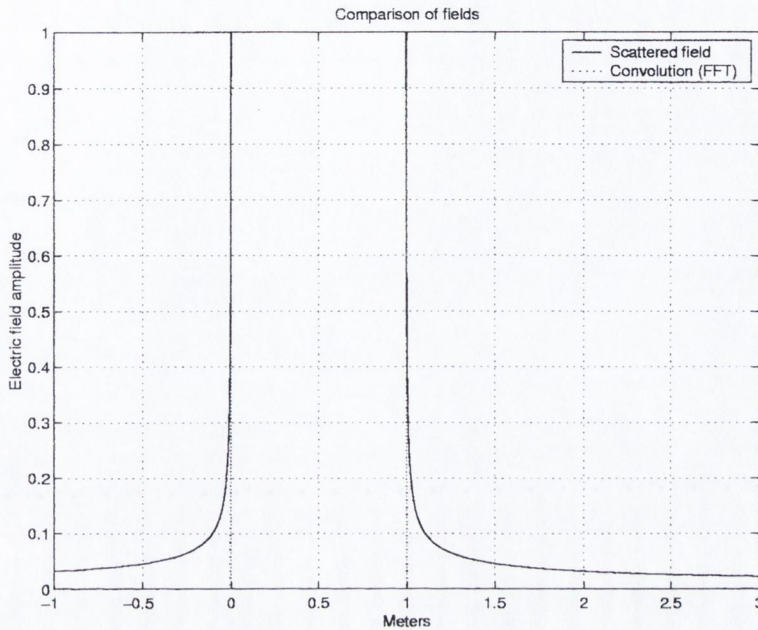


Figure 2.14: Amplitudes of the electric fields obtained using two different calculations. The dashed line represents the amplitude of the electric field returned by the convolution of the electric current and the Hankel function respectively illustrated in Fig. 2.14 and Fig. 2.11. The result is the known term of the equation in the  $k$ -space, i.e. the incident field in the interval  $[0, L]$ , with  $L = 1m$  and 0 elsewhere. The field due to the current, i.e. the scattered field, evaluated by numerical integration is the solid line: it equals the incident field over the interval  $[0, L]$  and decays outside the interval, but it is not zero.

which is illustrated (its amplitude) in Fig. 2.18 against the radial length.

Finally, in Fig. 2.19 and Fig. 2.20 the current distributions along the cut over the vertical ( $y$ ) direction and horizontal ( $x$ ) direction are given for a square flat plate of side of length  $1m = 2\lambda$  illuminated normally by a plane wave. The result in Fig. 2.19 is the  $x$  component of such current along the  $y$  direction in the middle of the square when the number of unknowns is 736. In Fig. 2.20, the upper graph is the  $x$  component of the current along the  $x$  direction in the middle of the plate when the number of unknowns is 225. The lower graph is the result of Fig. 2.19. Obviously the values of the functions are the same around the centre of the plate.

All the results of the last set have been evaluated using a CG algorithm for the solution of the MoM matrix equation. The self-terms of such matrix have been evaluated exploiting the fully numerical technique proposed in [76] and presented in section 6.2 of this thesis. The results for the square flat plate of side of length  $\lambda$  (see Fig. 2.16) can be compared with [33], Fig. 6. The results given for the circular

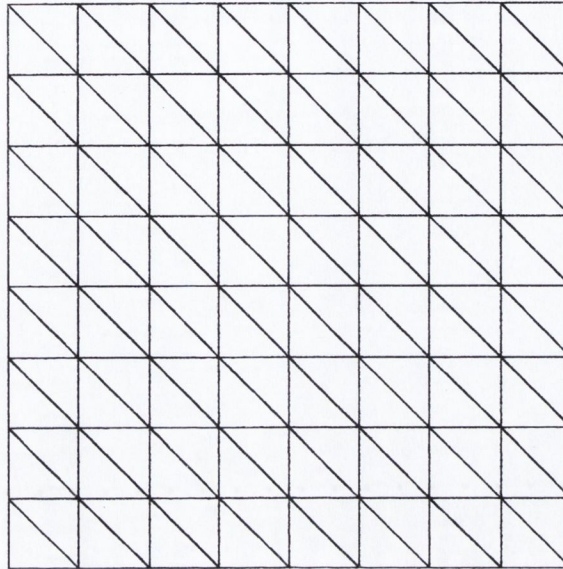


Figure 2.15: Surface patch grid employed to model the electric current density over a square flat plate.

disk (see Fig. 2.18) can be instead verified against those reported in [43], Fig. 3. Finally the result presented for the case of the square plate of side of length  $2\lambda$  can be compared with Fig. 10, [44].

## 2.10 Summary

In this chapter, the integral equation formulation of electromagnetic scattering problems was presented. In the first section the mathematical derivation of the equivalence principle stated in section A.2 was first described by introducing the Green's function. Specifically, at the end of section A.3, the expression of the EFIE and MFIE was derived in the case of electromagnetic scattering by perfectly conducting bodies. Application of the EFIE to the case of a  $TM_z$  plane wave scattered by a two-dimensional (infinite) circular cylinder was then shown. The method of moments, a discretisation procedure of the continuous field integral equations was briefly illustrated. The application of this method produces a matrix equation which may be solved using standard matrix solution algorithms. For the EFIE arising in the case of electromagnetic scattering by a two-dimensional cylinder, the method of moments basis functions were chosen to be pulse functions and the inte-

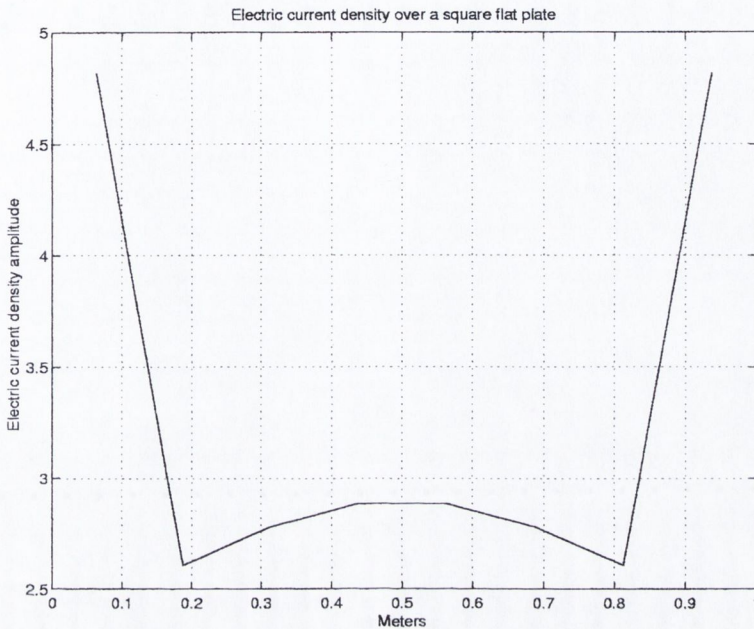


Figure 2.16: Amplitude of the horizontal component of the electric current density over the square flat plate at a cut over the vertical direction in the middle of the square. The number of unknowns, i.e. the number of non-boundary edges, is 176. The incident electric field is assumed to be directed along the horizontal direction and propagates normally to the plate. The side of the plate is  $\lambda$ .

gral equation was forced at the centres of the domains of the pulse basis functions. This operation was defined as *testing*. As discussed in [7], practical issues must be addressed during the selection of basis functions:

- the desired accuracy of the approximate solution;
- the complexity of the matrix entries;
- computational requirements that place an upper limit to the size of the matrix.

After having solved the EFIE, the MFIE has been formulated for the same problem, i.e. scattering by an infinite cylinder. Numerical results were presented to demonstrate the accuracy of the solution of both integral equations. For closed PEC scatterers, both the EFIE and the MFIE are affected by non-uniqueness. It was shown that when the radius of the cylinder satisfies a particular condition, the EFIE solution is highly unstable and inaccurate. To overcome this difficulty, the

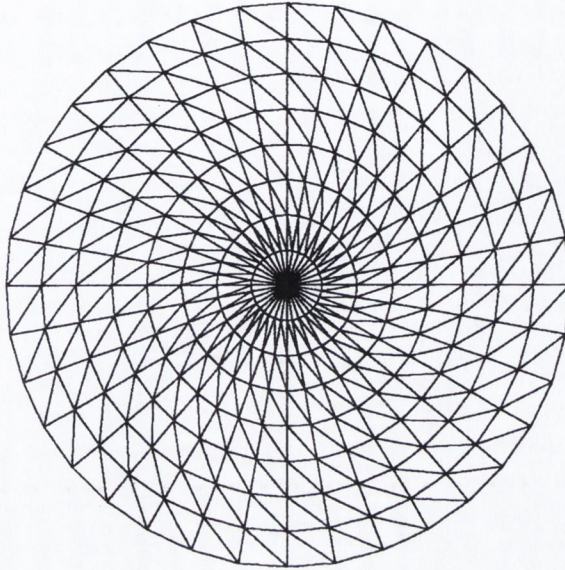


Figure 2.17: Surface patch grid employed to model the electric current density over a circular disk.

CFIE was introduced.

The EFIE for three-dimensional scatterer was presented. The RWG vector basis functions were introduced and the EFIE was discretised using the MoM approach. The resulting matrix was derived. The linear system of equations must be solved to determine the unknown coefficients of the basis functions. The CG algorithm is a well-known technique to solve matrix equations. It is an iterative method which require  $\mathcal{O}(PQ)$  operations, where  $P$  is the number of iterations and  $Q$  is the operation count per iteration. The direct methods to solve matrix equations, such as the Gaussian inversion, given for example in [12], possess a complexity<sup>15</sup> of  $\mathcal{O}(N^3)$ , where  $N$  is the number of unknowns. It was shown that a CG-FFT implementation, restricted to planar scatterer<sup>16</sup> has a complexity of  $\mathcal{O}(PN \log N)$  which is attractive when  $N$  is large.

In the final section of this chapter, some numerical results were presented to illustrate the CG-FFT in the two-dimensional case and demonstrate the validity of

<sup>15</sup>A function  $f(n)$  is  $\mathcal{O}(g(n))$  if there exists a constant  $C$  where  $f(n) \leq Cg(n)$ .  $\mathcal{O}(g(n))$  is the asymptotic complexity, or complexity, of  $f(n)$ .

<sup>16</sup>Or, in general, to integral equations with convolutional kernels.

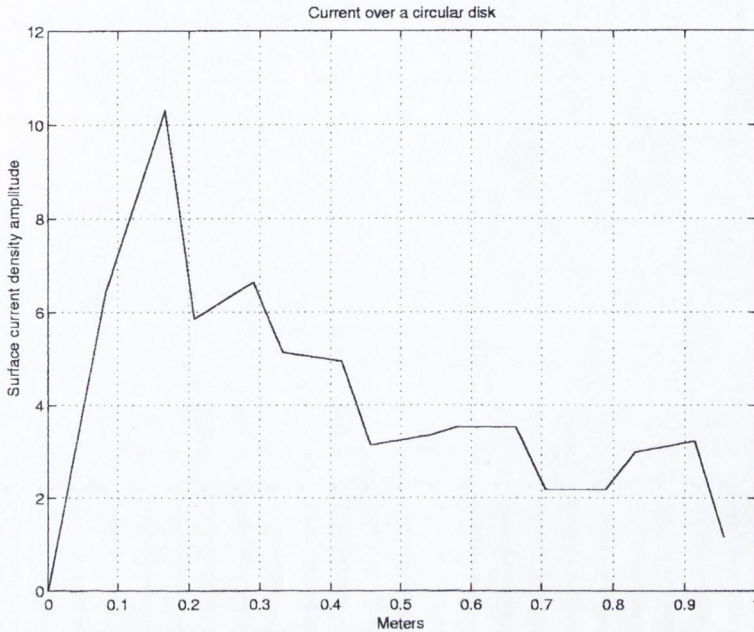


Figure 2.18: Amplitude of the electric current density over the radial direction on the disk. The circular disk is of radius  $a = 2\lambda$  and a vertical electric dipole illuminates it from a point centred on the disk at a height of  $0.1a$ . The number of edges is 792.

the RWG vector basis functions approach for three-dimensional scatterer. Numerical results also showed the accuracy of a novel numerical integration technique proposed in section 6.2 of this thesis for the evaluation of the self-terms of the impedance matrix. It was illustrated that for simple geometries, such as a square flat plate and a circular flat disk of transverse dimensions of order of  $\lambda$ , an accurate implementation of the MoM requires as much as  $10^3$  unknowns. It is evident that for electrically large scatterers (of transverse dimensions of order of thousands of  $\lambda$ ), the CG solution becomes prohibitive: storage constraints preclude the possibility to store the entire impedance matrix and the number of operations become enormous if the convergence rate of the algorithm is not fast. For electrically large bodies, iterative methods must be suitably enhanced. This is the subject of chapters 3 and 7.

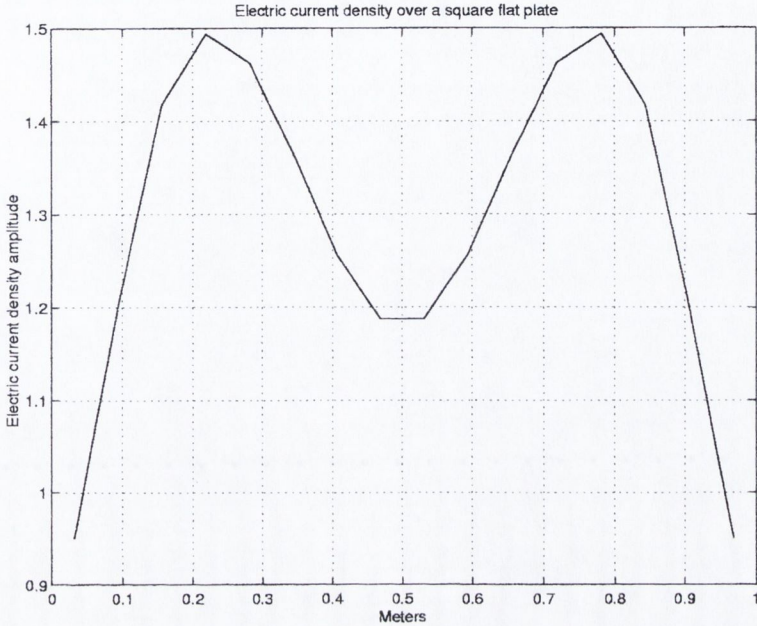


Figure 2.19: Amplitude of the horizontal component of the electric current density over the square flat plate at a cut over the vertical direction in the middle of the square. The number of unknowns, i.e. the number of non-boundary edges is, 736. The incident electric field is assumed to be directed along the horizontal direction and propagates normally to the plate. The side of the plate is  $2\lambda$  long.

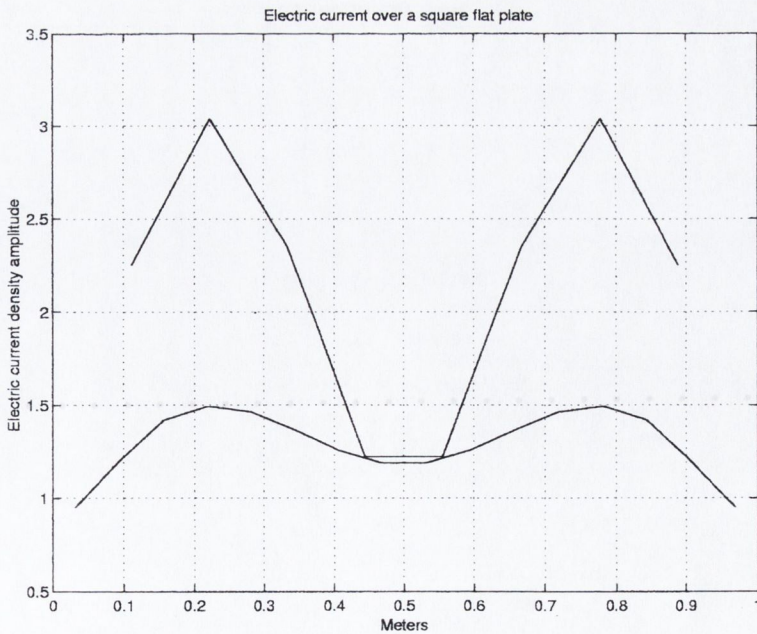


Figure 2.20: Amplitude of the horizontal component of the electric current density over the square flat plate at a cut over the horizontal direction in the middle of the square. The number of unknowns, i.e. the number of non-boundary edges, is 225. The incident electric field is assumed to be directed along the horizontal direction and propagates normally to the plate. The side of the plate is  $2\lambda$ .

---

## THE FAST MULTIPOLE METHOD

---

Chapter 2 presented the integral equation formulation of electromagnetic scattering by arbitrarily shaped bodies. Once discretised by the method of moments, the resulting matrix equation may be then inverted using the CG method which requires about  $\mathcal{O}(N^2)$  operations for the matrix-vector multiplications necessary to carry out the iterative method. Rokhlin [47] developed a Fast Multipole Method (FMM) for acoustic wave scattering problems. The FMM has been applied to electromagnetic scattering computation by Lu and Chew [48]. By taking into account the interactions between current elements more efficiently, the number of floating point operations needed to compute a matrix-vector multiplication is reduced to  $\mathcal{O}(N^{1.33})$  in two dimensions. The storage requirements associated with the method in two dimensions are also  $\mathcal{O}(N^{1.33})$ . This allows the solution of electromagnetic scattering by electrically large bodies.

This chapter deals with the description of the FMM method. First a short section is presented to get acquainted with the FMM terminology. The formulation developed by Lu and Chew is then described where upon some relevant numerical experiments are provided to demonstrate the validity of the FMM approximation and its application to the solution of the EFIE in the case of a simple problem. The final section of this chapter is dedicated to the formulation of the FMM in the three-dimensional case and recent enhancements are also described and referenced.

### 3.1 Rationale of the Fast Multipole Method (FMM)

In this section, the basic concept of the Fast Multipole Method (FMM) is described. Referring to Fig. 3.1(a), suppose to deal with a two-dimensional scatterer for which an EFIE has been set up and discretised using the MoM described section 2.2.

Consider two groups of discretisation points. Each point is defined as a *current element* and geometrically is the centre of the interval  $D_n$  where the pulse basis functions (2.45) are defined. The evaluation of the field due to the group  $G_l$  over  $G_{l'}$  of Fig. 3.1(a) is required. According to the typical approach, this field is given by

$$\sum_{n_l \in G_l} Z_{(m_l, n_l)} I_{n_l} \quad m_l \in G_{l'} \quad (3.1)$$

where  $n_l, l = 1 \cdots L$ , are the  $L$  points of  $G_l$ ,  $m_l, l = 1 \cdots L$ , are the  $L$  points of  $G_{l'}$  and  $Z_{(m_l, n_l)}$  is the impedance matrix element given in (2.50). It is assumed, without loss of generality, that the two groups contain the same number of points. Hence, to evaluate the  $L$  fields at the points of  $G_{l'}$  it is necessary to perform  $L^2$  operations.

Assume now that it is possible to express the field due to  $G_l$  as a sum of plane waves and that this expression is valid outside a circle of radius  $a_l$  enclosing all the current elements of  $G_l$ , as illustrated in Fig. 3.1(a). Then, the field over  $G_{l'}$  may be evaluated simply shifting these plane waves from the centre of  $G_{l'}$  to all points  $m_l$ . The plane waves illuminating the group  $G_{l'}$  are emanated by each group of current elements outside the circle of radius  $a_{l'}$  illustrated in Fig. 3.1(a). This is the main computational advantage of FMM: to *group* current elements, with reference to the centre of the group, to *reuse* this field for all the group to group interactions, such as the one illustrated in Fig. 3.1(a) and for each *receiving group*, such as  $G_{l'}$  in Fig. 3.1(a), to *disaggregate* the plane waves incoming from all the groups outside the circle of radius  $a_{l'}$ .

To establish further the basic foundations of the FMM, refer to Fig. 3.1(b). The FMM consists of aggregating the effect of  $L$  current elements of a group, to translate it to another group and to disaggregate it to the  $L$  current elements of the receiving group. It is like in a telecommunication network, where  $L$  neighbour points are efficiently connected to other  $L$  points through two nodes and a link between the nodes, using  $2L + 1$  branches instead of the  $L^2$  branches necessary to provide all



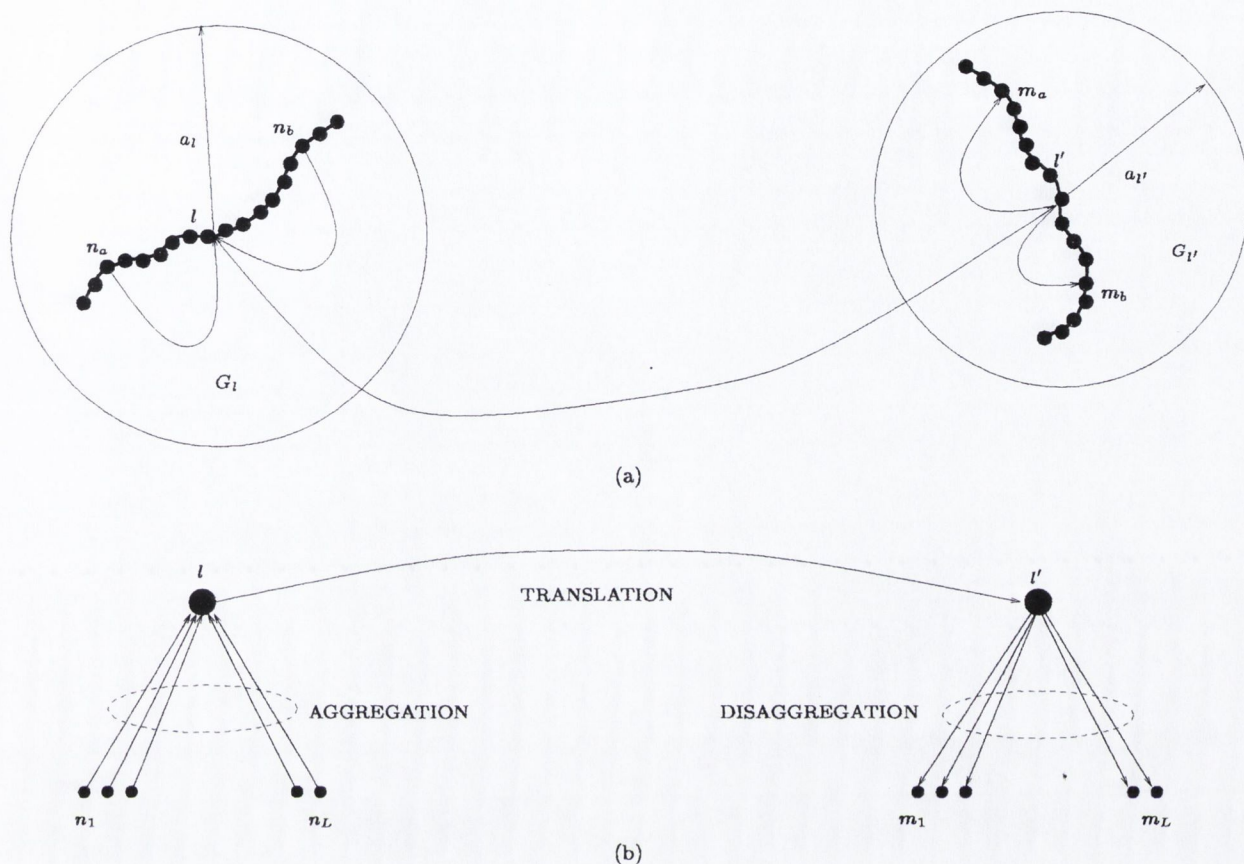


Figure 3.1: FMM main concepts: in (a) the field of two current elements of  $G_l$ , such as  $n_a$  and  $n_b$  is evaluated at two current elements of  $G_{l'}$ ,  $m_a$  and  $m_b$ . The actions of the two elements  $n_a$  and  $n_b$  are first aggregated at the centre of the group  $G_l$ , then translated over the group  $G_{l'}$  and disaggregated at the points  $m_a$  and  $m_b$ . The term derived from the aggregation step may be reused for other interactions of  $G_l$  with different groups. The FMM main concepts may be illustrated using a network representation as in (b).

possible point-to-point connections.

### 3.2 Formulation of the FMM

Consider the surface integral equation which governs the scattering of a  $TM_z$  plane wave by a metallic scatterer  $S$ :

$$\frac{\omega\mu_0}{4} \int_S J_z(\mathbf{r}') H_0^{(2)}(k|\mathbf{r} - \mathbf{r}'|) dS' = E_z^{inc}(\mathbf{r}), \tag{3.2}$$

where  $\mathbf{r} \in S$ ,  $J_z$  is the induced current on the scatterer and  $E_z^{inc}$  is the incident electric field. (3.2) may be discretised to give:

$$\sum_{n=1}^N Z_{mn} I_n = V_m \quad (3.3)$$

with

$$V_m = E_z^{inc}(\mathbf{r}_m) \quad (3.4)$$

$$I_n = J_z(\mathbf{r}_n) \quad (3.5)$$

$$Z_{mn} = \begin{cases} \frac{\omega\mu_0}{4} \left( 1 - \frac{2j}{\pi} \log \left( \frac{1.781k\Delta_n}{4e} \right) \right) \Delta_n & \text{if } m = n \\ \frac{\omega\mu_0}{4} H_0^{(2)}(kr_{mn}) \Delta_n & \text{if } m \neq n \end{cases} \quad (3.6)$$

where  $r_{mn} = |\mathbf{r}_m - \mathbf{r}_n|$  is the distance between the points which interact. The matrix-vector multiplication  $\sum_{n=1}^N Z_{mn} I_n$  is the main computational task in the execution of the CG algorithm. The FMM speeds up this multiplication and decreases the storage requirements associated with the implementation of a CG algorithm.

The main idea of the FMM has been explained in section 3.1 and employs the concepts of aggregation, translation and disaggregation illustrated in Fig. 3.1. In the two-dimensional case, the FMM is based on the following identity [48]

$$H_0^{(2)}(kr_{mn}) = \frac{1}{2\pi} \int_0^{2\pi} \tilde{\beta}_{m'l'}(\alpha) \tilde{\alpha}_{l'l}(\alpha) \tilde{\beta}_{ln}(\alpha) d\alpha \quad (3.7)$$

where

$$\tilde{\alpha}_{l'l}(\alpha) = \lim_{P \rightarrow \infty} \sum_{p=-P}^P H_p^{(2)}(kr_{l'l}) e^{-jp(\phi_{l'l} - \alpha - \pi/2)} \quad (3.8)$$

and

$$\tilde{\beta}_{m'l'}(\alpha) = e^{jk r_{m'l'} \cos(\alpha - \phi_{m'l'})} \quad \tilde{\beta}_{l'n}(\alpha) = e^{jk r_{l'n} \cos(\alpha - \phi_{l'n})} \quad (3.9)$$

where in general  $\phi_{ij}$  is the angle that the line  $r_{ij}$  makes with the  $x$ -axis, i.e. the polar angle associated with  $\mathbf{r}_{ij} = \mathbf{r}_i - \mathbf{r}_j$ . The series (3.8) is truncated by retaining  $2P + 1$  ( $p = -P \cdots P$ ) terms, where  $P$  is a finite integer. This operation is possible because the series is convergent, as described in [48].

Assume that the whole scatterer is partitioned into  $L$  groups of current elements and each group contains  $N/L$  current elements where  $N$  is the total number of current coefficients to be determined. Then, the field scattered by all non-near groups  $G_l$  at a point  $m$  of group  $G_{l'}$  may be written as

$$\frac{\omega\mu}{8\pi} \int_0^{2\pi} d\alpha \tilde{\beta}_{ml'}(\alpha) \sum_{l \in FF_{l'}} \tilde{\alpha}_{l'l}(\alpha) \sum_{n \in G_l} \tilde{\beta}_{ln}(\alpha) I_n = V'_m \quad (3.10)$$

where  $V'_m$  indicates that the contribution from the near groups must be added to get  $V_m$  and the symbol  $FF_{l'}$  refers to the set of groups which are located not near the group  $G_{l'}$ . The integral can now be replaced with a  $Q$ -point summation yielding the final expression

$$\frac{\omega\mu}{4Q} \sum_{q=1}^Q \tilde{\beta}_{ml'}(\alpha_q) \sum_{l \in FF_{l'}} \tilde{\alpha}_{l'l}(\alpha_q) \sum_{n \in G_l} \tilde{\beta}_{ln}(\alpha_q) I_n = V'_m \quad (3.11)$$

Equation (3.11) is the essence of the FMM code: to evaluate the contribution due to the current elements of the group  $G_l$  over the group  $G_{l'}$ , first the aggregation is accomplished evaluating the sum

$$\sum_{n \in G_l} \tilde{\beta}_{ln}(\alpha) I_n = \mathcal{C}_l(\alpha) \quad (3.12)$$

then the interaction is translated from the centre of  $G_l$  to the centre of  $G_{l'}$  using the operation

$$\tilde{\alpha}_{l'l}(\alpha) \mathcal{C}_l(\alpha) = \mathcal{A}_{l'l}(\alpha). \quad (3.13)$$

Finally the incident contribution is disaggregated from the centre of  $G_{l'}$  to the point  $m$

$$\tilde{\beta}_{ml'}(\alpha) \mathcal{A}_{l'l}(\alpha) \quad (3.14)$$

Now, it is readily observed that the final step of the FMM operation is a phase shift operation to evaluate the field of a plane wave at the point  $m \in G_\nu$  once the value of this wave is known at the centre of  $G_\nu$ . This operation must be carried out for all possible values of the variable  $\alpha$  which is related to the angle of incidence of the plane wave on the group  $G_\nu$ . Hence, the FMM permits to transform the non-near interactions between groups of current elements into a sum of plane waves. The non-near interactions are strictly occurring via cylindrical waves, but they can be replaced with a suitable sum of plane waves. Then the implementation of aggregation and dissemination is simply done via a phase shift *which depends only on the location of the current element relative to the centre of the group to which it belongs*. In [48] it is suggested that the number  $Q$  of samples necessary to numerically integrate (3.7) is proportional to  $L$ , the number of groups, from sampling theorem. Moreover, it is argued that  $L = \sqrt{N}$  is an optimum value to minimise the computational complexity of the matrix-vector multiplication, which drops down to  $\mathcal{O}(N^{1.33})$  in the case of a further nested version of the algorithm. The memory requirements are similar to the operation count, but no formal expression is reported for them.

### 3.3 Some numerical results

In this section, some numerical results are presented to validate the FMM approximation using the algorithm proposed in [48]. The first result refers to the geometry illustrated in Fig. 3.2. A set of line current elements is distributed on a circle of radius  $\lambda$  at equally spaced angles. For this example,  $N = 72$ . The quantity

$$\sum_{n=1}^N Z_{mn} I_n \quad (3.15)$$

is evaluated, with  $I_n = 1, n = 1 \cdots N$  and  $Z_{mn}$  is the impedance matrix term given by

$$Z_{mn} = \frac{\omega \mu_0}{4} H_0^{(2)}(kr_{mn}) \quad (3.16)$$

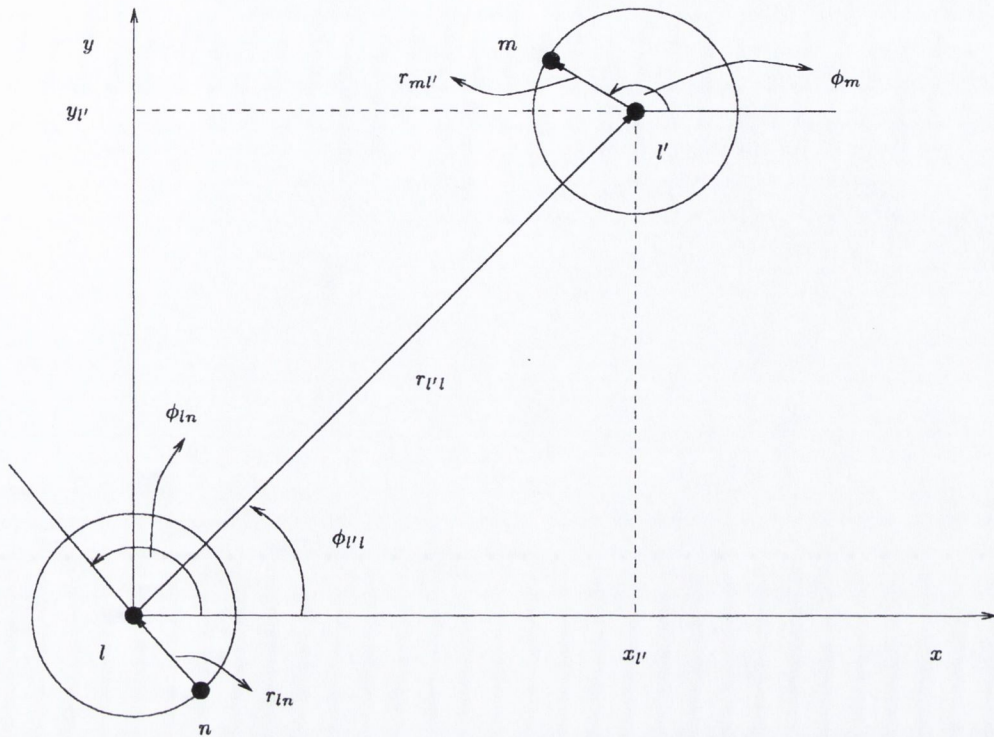


Figure 3.2: The groups indexed by  $l$  scatters over the group indexed by  $l'$ . Each element of  $G_l$ , say  $n$ , is a line source of current amplitude  $I_n = 1$ . The sum  $\sum_{n=1}^N Z_{mn} I_n$  is evaluated for the set of receiving points around the centre  $l'$ . The number of points is  $M = N = 72$ . The aggregation of elements of  $G_l$  at the centre  $l$  requires  $\mathcal{O}(N)$  operations, so does the disaggregation of the field received at the point  $l'$ . The translation is performed using (3.8).

where  $r_{mn}$  is the distance between the point  $m$  and  $n$ . The set of  $M = N$  observation points labelled by  $m$  lying on a circle centred on  $\mathbf{r}_l' = (x_l', y_l') = (5\lambda, 5\lambda)$  is considered. The Hankel function term in (3.16) is then replaced by the integral given in (3.7) and the accuracy of the approximation due to the truncation of the series (3.8) is tested. The integral (3.7) is evaluated numerically as in (3.11). The number  $Q$  is selected to be equal to  $M$  and two experiments are carried out to verify the sensitivity of (3.11) with respect to the value of  $P$  in the series (3.8). Fig. 3.3 illustrates the amplitude of the sum (3.15) when  $P = 10$ , as a function of the angular position of the observation points around the receiving centre. As is evident, the accuracy of the FMM approximation is not satisfactory, because for  $P = 10$  the series (3.8) does not converge to the actual result. However, it suffices only to increase the value of  $P$  up to 20 to get the excellent agreement illustrated in Fig. 3.4, where the two functions perfectly match.

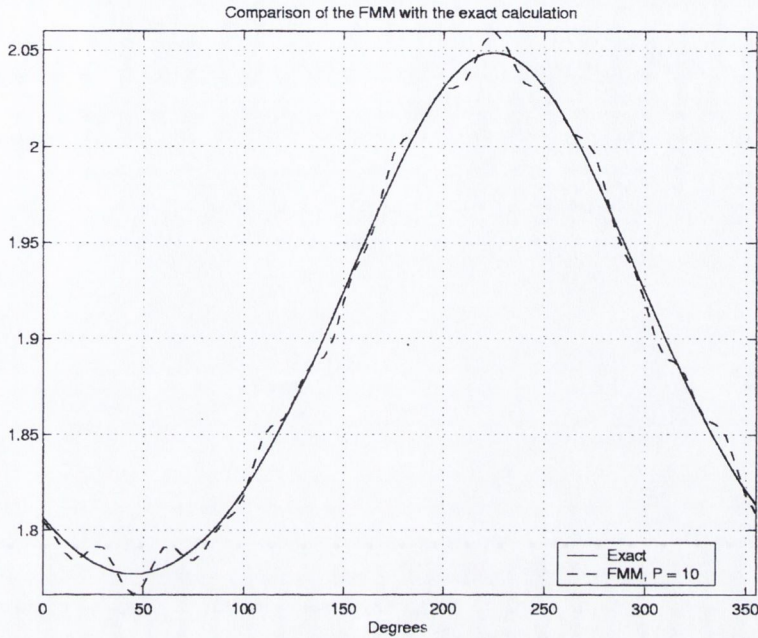


Figure 3.3: Amplitude of the sum (3.15) employing the FMM approximation and equation (3.8) with  $P = 10$  for the geometry illustrated in Fig. 3.2. The dashed line represents the values of the sum (3.15) at  $M = 72$  points located at a radius  $\lambda$  around the centre of the group  $G_{\nu}$ . The result is affected by an evident instability due to the truncation of the series (3.8) at a too small  $P$  with respect to the theoretical limit  $\infty$ .

Fig. 3.5 illustrates the amplitude of the electric current density on the surface of a cylinder of radius  $a = 12\lambda$  illuminated by a  $TM_z$  plane wave. The geometry of the problem is the same as that of Fig. 2.2. The EFIE associated with this scattering problem has been discretised via the moment method and the CG algorithm has been utilised to invert the discretised equation. The FMM has been applied to the CG algorithm and the results are provided in Fig. 3.5. The number of unknowns is  $N = 961$ , the number of groups is  $L = 31$  and  $P = L$  for this numerical experiment. The EFIE solutions, either the exact and the FMM-based one, suffer of inaccuracy, due to the non-uniqueness problem already referred to in section 2.5. Although the CFIE solution is also included in the figure, the purpose of this numerical exercise has been to verify the validity of the FMM approximation and to demonstrate that the numerical solution of the matrix equation, although faster than in the exact case, still leads to unstable results for the unknown current. A solution is to extend the FMM algorithm to the CFIE, operation easily feasible and reported in detail in [48].

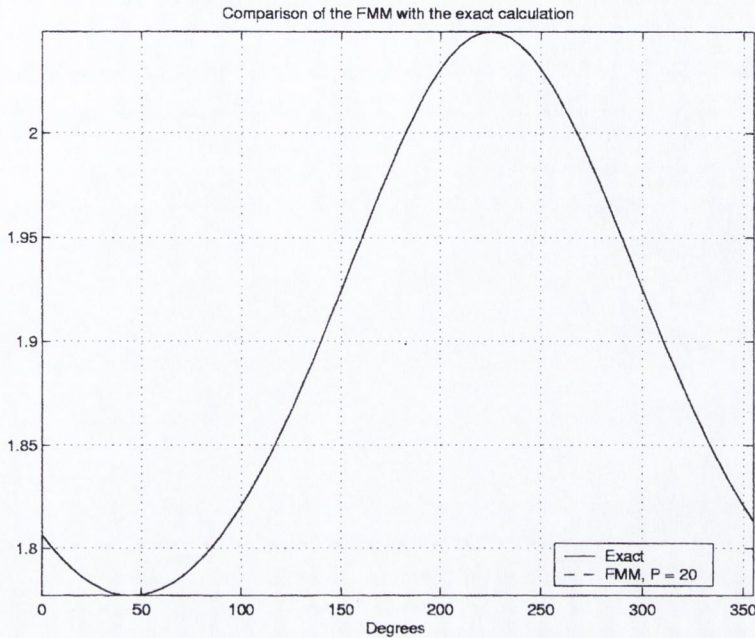


Figure 3.4: Amplitude of the sum (3.15) employing the FMM approximation and equation (3.8) with  $P = 20$  for the geometry illustrated in Fig. 3.2. The dashed line represents matches exactly the solid line. In this case the FMM approximation returns the exact result obtained by evaluating numerically the sum (3.15).

### 3.4 Recent developments of the FMM

#### 3.4.1 Computational issues related to the FMM

In recent years, the FMM has been further improved to tackle the problem of electromagnetic scattering by much larger bodies of arbitrary shape. As for two-dimensional scatterers, it was recognised that the main computational burden of the FMM as given in [48] is the evaluation of the translation functions  $\tilde{\alpha}_{l'l}(\alpha_q)$  as described in (3.8) for each pair of groups  $(l, l')$  at each discretised angle  $\alpha_q$  of the interval  $(0, 2\pi)$ . The cost of a matrix-vector multiplication depends now on the choice of  $P$  and  $Q$  in the evaluation of the sum (3.11). The factor  $\tilde{\alpha}_{l'l}(\alpha_q)$  takes into account the interaction between two groups  $G_{l'}$  and  $G_l$  of the scatterer, which one expects to be strongest along the line joining the transmitting and receiving group centres. The function  $\tilde{\alpha}_{l'l}(\alpha_q)$  is expected to have a maximum at  $\alpha_q = \phi_{l'l}$  and to decrease rapidly away from the neighbourhood of  $\phi_{l'l}$ . Indeed, this is the case, as illustrated in Fig. 3.6, where the translation function resulting from the geometry of Fig. 3.2 is shown. In [49] a new technique is presented for accelerating

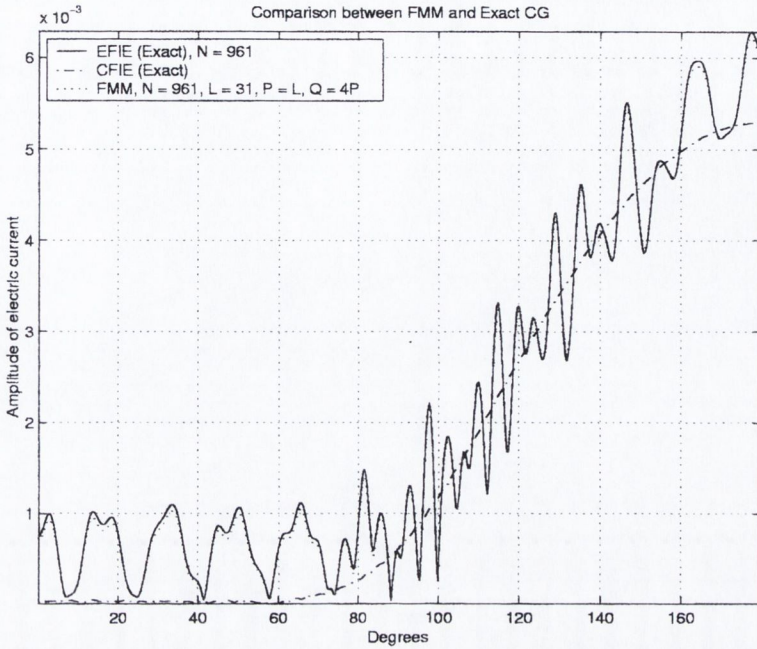


Figure 3.5: FMM results for the scattering by a PEC cylinder: the amplitude of the current density matches perfectly the solution returned by the EFIE inverted using a CG algorithm. Both the solutions are affected by the instability typical of the EFIE.

the FMM. The translation function is computed as a Fourier series with a window function which makes a smooth translation from zero to one. Basically the series becomes

$$\tilde{\alpha}_{\nu l}(\alpha) = \lim_{P \rightarrow \infty} \sum_{p=-P}^P w_p H_p^{(2)}(kr_{\nu l}) e^{-jp(\phi_{\nu l} - \alpha - \pi/2)} \tag{3.17}$$

where  $w_p$  denotes the window function that has a broad flat middle section centred around  $p = 0$  and a cosine taper on both ends.

Another elegant approach to the fast calculation of the translation function  $\tilde{\alpha}_{\nu l}$  has been described in [50]. It is shown that the translation function may be evaluated asymptotically in the high frequency limit, yielding a uniform result which is valid for all group separations. Specifically, this new technique makes use of the definition of the Hankel function:

$$H_p^{(2)}(kr_{\nu l}) = \frac{1}{\pi} \int_{C^{(2)}} e^{-jkr_{\nu l} \cos \beta + jp\beta + jp\pi/2} d\beta \tag{3.18}$$



where the contour  $C^{(2)}$  in the complex  $\beta$  plane is given in [5]. Substituting this into (3.8) and interchanging summation and integration gives

$$\begin{aligned} \tilde{\alpha}_{l'l}(\alpha) &= \lim_{P \rightarrow \infty} \frac{1}{\pi} \int_{C^{(2)}} e^{-jk r_{l'l} \cos \beta} \sum_{p=-P}^P e^{jp(\beta - \alpha + \phi_{l'l})} d\beta = \\ &= \lim_{P \rightarrow \infty} \frac{1}{\pi} \int_{C^{(2)}} \frac{\sin[(2P + 1)(\beta - \alpha + \phi_{l'l})/2]}{\sin[(\beta - \alpha + \phi_{l'l})/2]} d\beta \end{aligned} \quad (3.19)$$

The integral may be evaluated asymptotically using the method of steepest descent [45]. The asymptotic form clearly defines a lit region inside of which the plane wave interaction is strongest. Outside of this region, the translation function consists of two terms associated with the two shadow boundaries of the lit region: in this shadow region the operator gradually decays and is highly oscillatory as illustrated in Fig. 3.6.

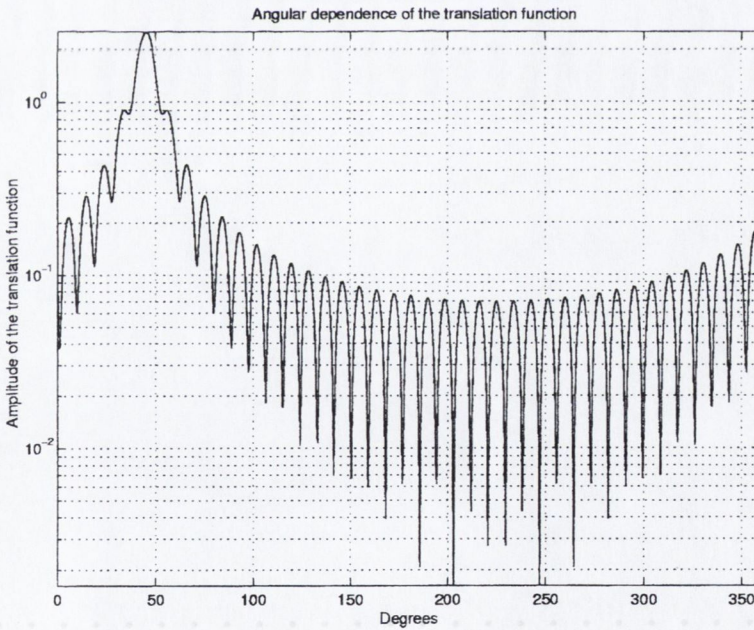


Figure 3.6: Behaviour of the translation function  $\tilde{\alpha}_{l'l}(\alpha)$  associated with the geometry of Fig. 3.2. The function has maximum value at  $\phi_{l'l} = \pi/4$ , i.e. over the direction  $l \rightarrow l'$  and gradually decays outside a narrow interval centred at  $\alpha = \phi_{l'l}$ .

### 3.4.2 FMM in the three-dimensional case

The FMM has also been applied to the solution of the electromagnetic scattering problem in three dimensions. Once again, as described in [52], the main task is

to formulate an expression for the Green's function which allows one to split the interaction between two current elements on the scatterer into three operations: aggregation, translation and disaggregation. As proposed in [52] Gegenbauer's addition theorem may be used to accomplish this task:

$$\frac{e^{-jk|\mathbf{X}+\mathbf{d}|}}{|\mathbf{X}+\mathbf{d}|} = \frac{-jk}{4\pi} \int_{\Omega} d^2\hat{k} e^{-jk\hat{k}\cdot\mathbf{d}} \alpha(k, \hat{k}, \mathbf{X}) \quad (3.20)$$

where  $|\mathbf{d}| < |\mathbf{X}|$ . In (3.20), the surface integral is performed over  $\hat{k}$ -space, with  $\hat{k} = (\sin\theta \cos\phi, \sin\theta \sin\phi, \cos\theta)$ , basically over the spherical domain of unit radius,  $\Omega$ . The function  $\alpha(k, \hat{k}, \mathbf{X})$  is the translation function and may be approximated as

$$\alpha(k, \hat{k}, \mathbf{X}) \approx \sum_{l=0}^L (-j)^l (2l+1) h_l^{(2)}(kX) P_l(\hat{k} \cdot \hat{\mathbf{X}}) \quad (3.21)$$

where  $L \rightarrow \infty$  for equality. To achieve convergence of the series the value of  $L$  is chosen to be

$$L(k|\mathbf{d}|) \geq k|\mathbf{d}| + 10 \log(k|\mathbf{d}| + \pi) \quad (3.22)$$

as prescribed in [52]. The function  $h_l^{(2)}$  is the  $l$ -th order spherical Hankel function of the second kind and  $P_l$  is the  $l$ -th degree Legendre polynomial. Referring to Fig. 3.7, observe that

$$\mathbf{r}_m^+ - \mathbf{r}' = \mathbf{r}_m^+ - \mathbf{r}_l' + \mathbf{r}_l' - \mathbf{r}_l + \mathbf{r}_l - \mathbf{r}' = \mathbf{r}_{ml'} + \mathbf{r}_{l'l} + \mathbf{r}_l - \mathbf{r}' \quad (3.23)$$

then it readily follows that

$$\frac{e^{-jk|\mathbf{r}_m^+ - \mathbf{r}'|}}{|\mathbf{r}_m^+ - \mathbf{r}'|} = \frac{e^{-jk|\mathbf{r}_{ml'} + \mathbf{r}_{l'l} + \mathbf{r}_l - \mathbf{r}'|}}{|\mathbf{r}_{ml'} + \mathbf{r}_{l'l} + \mathbf{r}_l - \mathbf{r}'|} \quad (3.24)$$

Recall now the expressions for the potentials given in (2.81) and (2.82) due to an element of the RWG set. Then the following identities hold

$$\int_{T_n^{+,-}} I_n \mathbf{f}_n(\mathbf{r}') \frac{e^{-jk|\mathbf{r}_m^+ - \mathbf{r}'|}}{|\mathbf{r}_m^+ - \mathbf{r}'|} dS' = \int_{T_n^{+,-}} I_n \mathbf{f}_n(\mathbf{r}') \frac{e^{-jk|\mathbf{r}_{ml'} + \mathbf{r}_{l'l} + \mathbf{r}_l - \mathbf{r}'|}}{|\mathbf{r}_{ml'} + \mathbf{r}_{l'l} + \mathbf{r}_l - \mathbf{r}'|} dS' \quad (3.25)$$

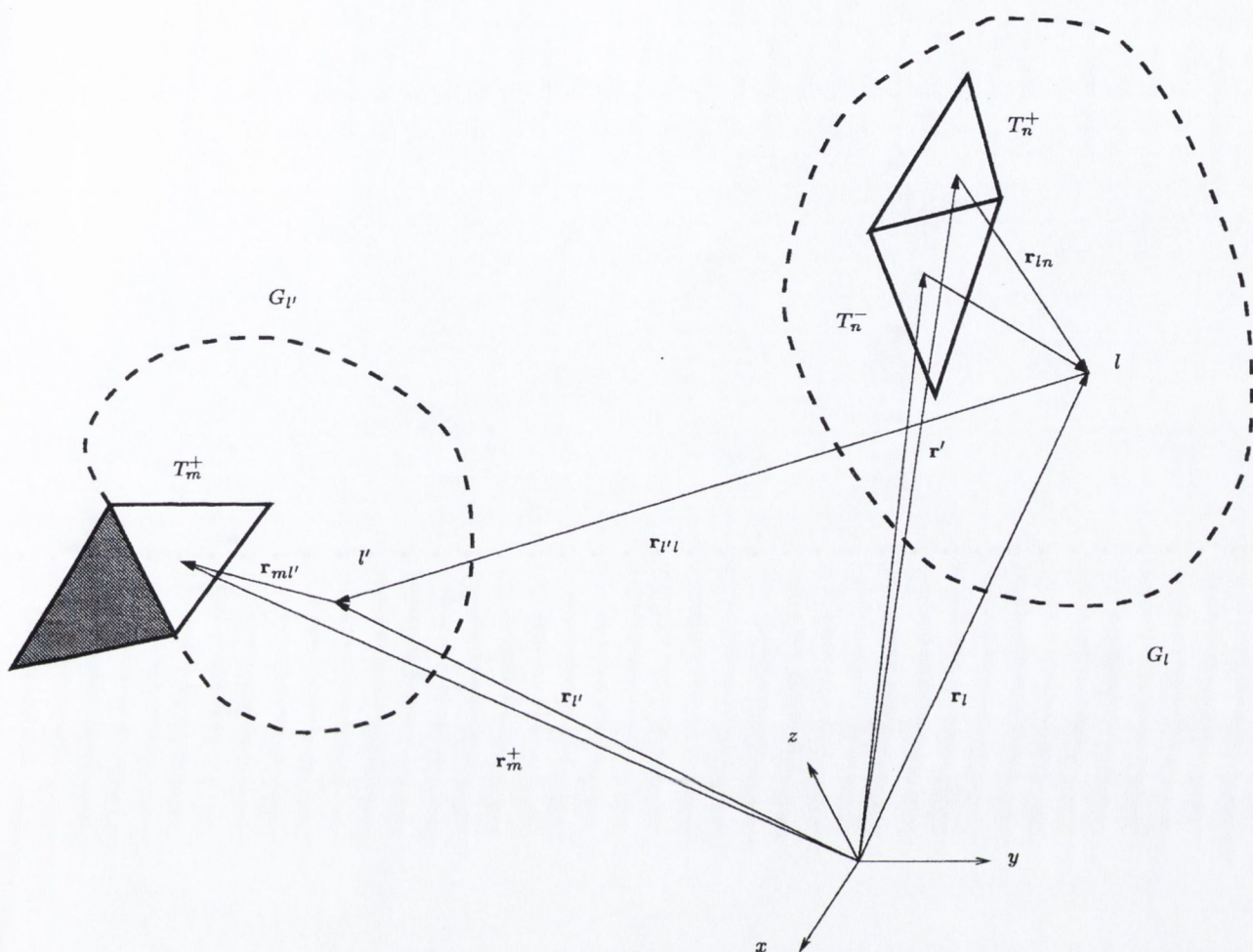


Figure 3.7: Geometry of the FMM in the three-dimensional case: the group  $G_l$  scatters over the group  $G_{l'}$ . The electric current associated with the domains  $T_n^+$  and  $T_n^-$ , i.e.  $I_n$ , radiates the electric field at  $T_m^+$ , which is the triangle included in  $G_{l'}$ . The evaluation of the field scattered by  $G_l$  over  $G_{l'}$  requires the calculation of only a fraction of the impedance term  $Z_{mn}$  (2.79), because domain  $T_m^-$  does not belong to the group  $G_{l'}$ .

$$\int_{T_n^{+,-}} I_n \nabla' S \cdot \mathbf{f}_n(\mathbf{r}') \frac{e^{-jk|\mathbf{r}_m^+ - \mathbf{r}'|}}{|\mathbf{r}_m^+ - \mathbf{r}'|} dS' = \int_{T_n^{+,-}} I_n \nabla' S \cdot \mathbf{f}_n(\mathbf{r}') \frac{e^{-jk|\mathbf{r}_{m'l'} + \mathbf{r}_{l'l} + \mathbf{r}_l - \mathbf{r}'|}}{|\mathbf{r}_{m'l'} + \mathbf{r}_{l'l} + \mathbf{r}_l - \mathbf{r}'|} dS' \quad (3.26)$$

and using Gegenbauer's identity (3.20) it may be written that

$$\int_{T_n^{+,-}} I_n \mathbf{f}_n(\mathbf{r}') \frac{e^{-jk|\mathbf{r}_m^+ - \mathbf{r}'|}}{|\mathbf{r}_m^+ - \mathbf{r}'|} dS' = \frac{-jk}{4\pi} \int_{\Omega} d^2 \hat{k} V_{f_{ml'}}(\hat{k}) \alpha_{l'l}(k, \hat{k}, \mathbf{r}_{l'} - \mathbf{r}_l) \mathbf{V}_{sin}^*(\hat{k}) dS' \quad (3.27)$$

$$\int_{T_n^{+,-}} I_n \nabla' S \cdot \mathbf{f}_n(\mathbf{r}') \frac{e^{-jk|\mathbf{r}_m^+ - \mathbf{r}'|}}{|\mathbf{r}_m^+ - \mathbf{r}'|} dS' =$$

$$\frac{-jk}{4\pi} \int_{\Omega} d^2\hat{k} V_{fml'}(\hat{k}) \alpha_{l'l}(k, \hat{k}, \mathbf{r}_{l'} - \mathbf{r}_l) W_{sln}^*(\hat{k}) dS' \quad (3.28)$$

The terms  $(\mathbf{V}_{sln}^*(\hat{k}), W_{sln}^*(\hat{k}))$  are the basic elements which are used to construct the *outer multipole expansion*<sup>1</sup> for the group  $G_l$ . They depend on the current  $I_n$  and on the location of the domain  $T_n^{+,-}$  with respect to the centre of the group  $G_l$ ,  $\mathbf{r}_l$ ,

$$\mathbf{V}_{sln}^*(\hat{k}) = \int_{T_n^{+,-}} I_n \mathbf{f}_n(\mathbf{r}') e^{-jk\hat{k}\cdot(\mathbf{r}_l - \mathbf{r}')} dS' \quad (3.29)$$

$$W_{sln}^*(\hat{k}) = \int_{T_n^{+,-}} I_n \nabla'_S \cdot \mathbf{f}_n(\mathbf{r}') e^{-jk\hat{k}\cdot(\mathbf{r}_l - \mathbf{r}')} dS' \quad (3.30)$$

Finally, the term  $V_{fml'}(\hat{k})$  represents a contribution to the multipole expansion of the group  $G_{l'}$  and consists of a phase shift operation which disseminates the field due to the current  $I_n$  at the centre of the group  $G_{l'}$ ,  $\mathbf{r}_{l'}$ , to the point  $\mathbf{r}_m^+$ . This term is given by

$$V_{fml'}(\hat{k}) = e^{-jk\hat{k}\cdot(\mathbf{r}_m^+ - \mathbf{r}_{l'})} \quad (3.31)$$

On the basis of this rather cumbersome mathematical background, the FMM can be implemented to deal with electromagnetic scattering by three-dimensional objects of arbitrary shape. The differences between the three-dimensional and the two-dimensional case are evident and reside on the more complex formalism related to the formulation of the problem. Also, while in the two-dimensional case the non-near contributions of different groups is represented as a sum of plane waves having only one angular degree of freedom, for the three-dimensional case, the integral (3.20) over  $\hat{k}$ -space represents a further computational burden which cannot be efficiently tackled using a naive double integration. For each pair of samples

<sup>1</sup>Multipole expansions about the reference point of a current distribution are used to compute the effects of the current elements within a group on distant points. Distant points are those which are outside the sphere of convergence of the expansion. Multipole expansions are remarkably described in [46].

$(\theta_i, \phi_i)$ , the translational operator must be evaluated and this task requires the execution of routines which return the desired value of the Legendre polynomial and spherical Bessel function at that particular value of  $(\theta_i, \phi_i)$ . An efficient numerical integration scheme to deal with spherical domains is described in [51]. With an optimum choice of all parameters, it is reported in [52] that the FMM can be applied to the solution of electromagnetic scattering problems with an order of complexity equal to  $\mathcal{O}(N^{1.5})$ . The FMM has been implemented on a multi-level basis as reported in [53] and using this scheme a complexity of  $\mathcal{O}(N \log N)$  can be reached. A detailed description of the multi-level FMM is not the main purpose of this chapter. In chapter 7 a multi-level technique will be presented and in that context the philosophy of multi-level techniques will become more clear. A very good research paper on this subject is [54] which includes an exhaustive list of references and presents excellent results generated by the FMM on a multi-level basis. Another complex feature to be added to the implementation of the multi-level version of the FMM is the interpolation, necessary to deal with different sized groups of current element which are recursively generated in the algorithm. At the state of the art, to the knowledge of the reader, no contribution in the literature has been submitted to discuss about the complexity of the evaluation of the translation function in the FMM for three-dimensional problems.

### 3.5 Summary

Chapter 3 described the Fast Multipole Method, an alternative iterative scheme which offers the possibility of achieving the complexity of  $\mathcal{O}(N^{1.33})$  operations for the solution of the integral equations in electromagnetic scattering in the two dimensional case. The basic concepts of the FMM were presented in an introductory section of the chapter. The formulation of FMM was then derived in section 3.2. Beginning with the discretised EFIE, it was shown that the interaction between two groups of current elements of the scatterer may be approximated efficiently using an integral expression for the Hankel function. To demonstrate the valid-

ity of this approximation some numerical results have been provided in section 3.3. Further enhancements to the FMM in the two-dimensional and the main mathematical derivation of the necessary quantities to implement the FMM in the three-dimensional case have been presented in section 3.4. The next chapter will present the Fast Far-Field Algorithm and the Tabulated Interaction Method which are strongly related to the FMM.

---

## THE TABULATED INTERACTION METHOD

---

In this chapter, two fast computational methods are described: the Fast Far-Field Approximation (FAFFA), in the form developed and proposed by Lu and Chew [55] and the Tabulated Interaction Method (TIM) developed by Brennan and Cullen [62]. The FAFFA is a less strict version of the FMM described in chapter 3. It accounts for the interaction between current elements in two ways, depending on the electrical distance between them. The TIM is based on the FAFFA and achieves substantial computational savings when applied to electrically massive bodies. The method is based on the rapid evaluation of interactions between subscatterers, as in the FAFFA, but with an additional fast feature which renders the technique superior to the FAFFA.

This chapter is divided in three parts: in section 4.1 the principles of the FAFFA are briefly outlined, in part 4.2 the TIM algorithm is presented mathematically and in section 4.3 numerical results are provided to reveal the behaviour of the algorithms and demonstrate their application to large-size objects. Before beginning the mathematical discussion, it is important to stress that the class of scatterers which is of interest is that of piecewise planar locally smooth large surfaces. This class of bodies allows the modelling of physical objects such as undulating terrain. The characterisation of their interaction with electromagnetic waves is nowadays very important in telecommunications application, mainly in cellular radio-coverage planning and propagation modelling.

### 4.1 The Fast Far-Field Approximation (FAFFA)

In this section, the mathematical essence of the FAFFA is discussed for the two-dimensional case. Consider, as described in chapter 2, Fig. 2.2, a  $TM_z$  plane wave

incident on a two-dimensional PEC scatterer embedded in free space. The surface of the scatterer is defined as  $S$ . The integral equation satisfied by the induced current may be written as

$$\frac{\omega\mu_0}{4} \int_S J_z(\mathbf{r}') H_0^{(2)}(k|\mathbf{r}' - \mathbf{r}|) dS' = E_{inc}(\mathbf{r}) \quad (4.1)$$

where  $dS'$  represents the element of surface of the scatterer. (4.1) may then be discretised as outlined in chapter 2 by applying the usual MoM procedure to give

$$V_m = \sum_{n=1}^N Z_{mn} I_n \quad (4.2)$$

where  $V_m$  is the field  $E_{inc}(\mathbf{r})$  evaluated at the point  $(x_m, y_m) \in S$ ,  $I_n$  is the value of the current  $J_z(\mathbf{r})$  at the point  $(x_n, y_n) \in S$ .  $Z_{mn}$  is the impedance matrix element (2.50), i.e.

$$Z_{mn} = H_0^{(2)}(kr_{mn}) \Delta_n \quad (4.3)$$

where  $\Delta_n$  is the width of the interval in which the pulse basis function (2.45) associated with the coefficient  $I_n$  resides.  $r_{mn} = |\mathbf{r}_m - \mathbf{r}_n|$  is the distance between the point  $(x_m, y_m) \in S$  and the point  $(x_n, y_n) \in S$ . Now, as in the FMM algorithm, the  $N$  unknowns are partitioned into  $L$  groups, each having  $M$  unknowns. Thus, the contribution of the group  $G_l$  to the group  $G_{l'}$  is given by

$$\sum_{n \in G_l} H_0^{(2)}(kr_{mn}) \Delta_n I_n = V_m \quad m \in G_{l'} \quad (4.4)$$

If the groups  $G_l$  and  $G_{l'}$  are relatively far apart then the argument of the Hankel function may be considered sufficiently large to allow the use of an asymptotic expression (see [2], chapter 4) for (4.4) which yields

$$\sum_{n \in G_l} \sqrt{\frac{2}{\pi kr_{mn}}} e^{-j(kr_{mn} - \pi/4)} \Delta_n I_n \approx V_m \quad m \in G_{l'} \quad (4.5)$$



Referring to Fig. 4.1, the vector  $\mathbf{r}_{mn}$  may be decomposed as

$$\mathbf{r}_{mn} = \mathbf{r}_{ml'} + \mathbf{r}_{l'l} + \mathbf{r}_{ln} \tag{4.6}$$

and if  $r_{l'l} \gg r_{ml'}$  and  $r_{l'l} \gg r_{ln}$ , i.e. if the separation between the groups is much larger than the size of the groups, the Fast Far-Field Approximation (FAFFA) may be obtained

$$r_{mn} \approx r_{l'l} + \mathbf{r}_{ml'} \cdot \hat{\mathbf{r}}_{l'l} + \mathbf{r}_{ln} \cdot \hat{\mathbf{r}}_{l'l} \tag{4.7}$$

Hence

$$e^{-jk\mathbf{r}_{ml'} \cdot \hat{\mathbf{r}}_{l'l}} \sum_{n \in G_l} \sqrt{\frac{2}{\pi k r_{mn}}} e^{-j(kr_{mn} - \pi/4)} \Delta_n I_n \approx e^{-jk\mathbf{r}_{ml'} \cdot \hat{\mathbf{r}}_{l'l}} \sqrt{\frac{2}{\pi k r_{l'l}}} e^{-j(kr_{l'l} - \pi/4)} \sum_{n \in G_l} e^{-jk\mathbf{r}_{ln} \cdot \hat{\mathbf{r}}_{l'l}} \Delta_n I_n \tag{4.8}$$

where  $m \in G_{l'}$ . (4.8) contains three factors, in just the same way as the FMM approximation:

- an *aggregation* term, for the evaluation of the sum

$$\sum_{n \in G_l} e^{-jk\mathbf{r}_{ln} \cdot \hat{\mathbf{r}}_{l'l}} \Delta_n I_n = b_{l'l} \tag{4.9}$$

This term is evaluated to group the effects of the single current elements of the group  $G_l$ ,  $I_n$ , with  $n = 1 \dots M$ .

- A *translation* term, corresponding to

$$\sqrt{\frac{2}{\pi k r_{l'l}}} e^{-j(kr_{l'l} - \pi/4)} b_{l'l} = b'_{l'l} \tag{4.10}$$

The term  $b_{l'l}$  is considered as a single current element located at the centre of  $G_l$  and radiating towards the group  $G_{l'}$ .

- Finally a *disaggregation* term, for each point  $m \in G_{l'}$

$$e^{-jkr_{m'l'} \cdot \hat{r}_{l'}} b'_{l'l} \tag{4.11}$$

$b'_{l'l}$  is the value at the centre of  $G_{l'}$  of a plane wave illuminating the group  $G_{l'}$ , incident from the direction  $\hat{r}_{l'l}$ . It is straightforward to evaluate the electric field of the plane wave at the points  $m \in G_{l'}$  by a phase-shift operation.

The FAFFA basic assumption is illustrated in Fig. 4.1. The point  $n$  is the location of the current element associated with  $(x_n, y_n) \in S$ . Similar definition holds for  $m$ . The field radiated by the point  $n$  may be evaluated at the point  $m$  using (4.8) with the geometric quantities illustrated in the figure. The FAFFA procedure is

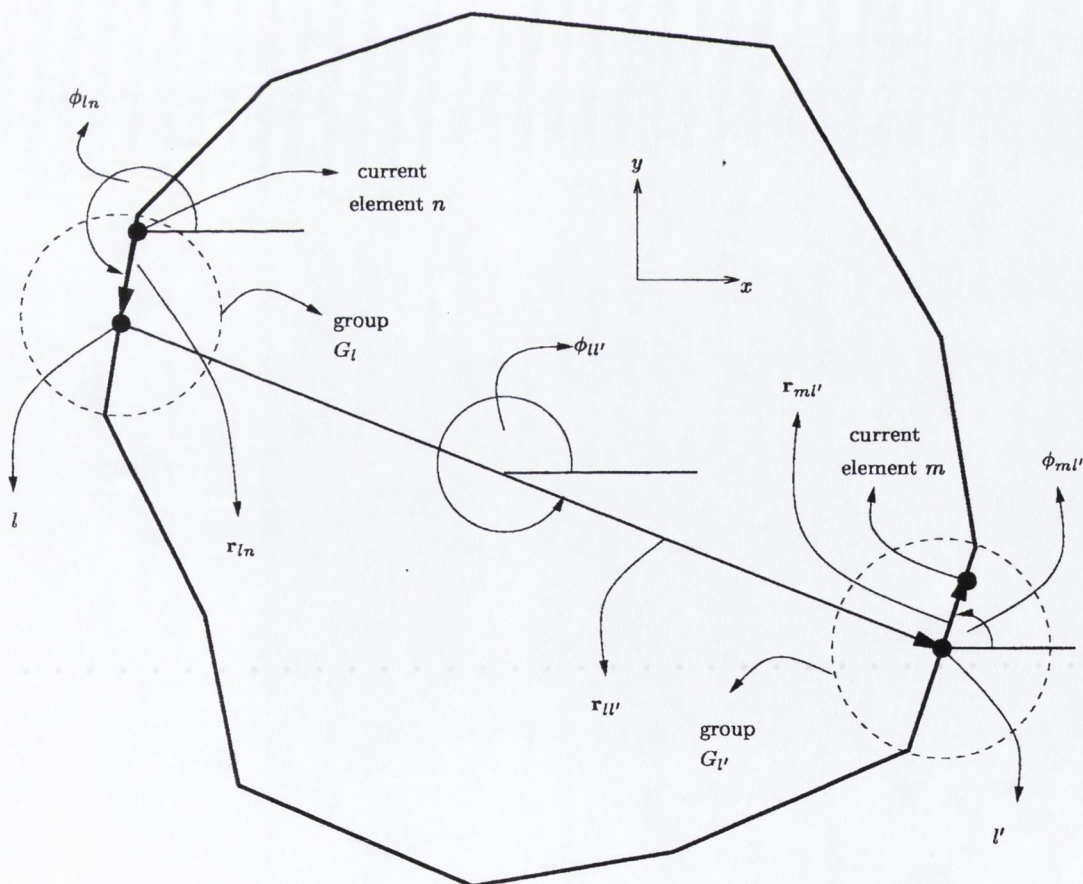


Figure 4.1: Far-field approximation in the two-dimensional case: the electric field due to the group  $G_l$  at  $G_{l'}$  is evaluated using (4.8).

now evident. For each group  $G_l$  two regions of groups  $G_{l'}$ , with  $l' \neq l$  are defined:

a near-field region and a far-field region, depending on the distance between the two groups. The far-field interactions may be evaluated using (4.8), the near-field interactions must be evaluated directly, i.e. using the sum

$$\sum_{n \in G_l} Z_{mn} I_n \quad m \in G_{l'} \quad (4.12)$$

if  $G_{l'}$  is near  $G_l$ . By using FAFFA, the impedance matrix terms  $Z_{mn}$  need not be evaluated if  $m \in G_{l'}$  and  $n \in G_l$  and the groups  $G_{l'}$  and  $G_l$  are far apart. This reduces dramatically the storage requirements and the computation time associated with the algorithm. In the original article by Lu and Chew [55], no mathematical expression is given to define the near-field/far-field boundary. Moreover, the size of the groups is chosen to be  $M = \sqrt{N}$  by formal optimisation. It is reported that this condition leads to a complexity of the CG algorithm of  $\mathcal{O}(N^{1.5})$ . However, the relationship between the size of the groups and the size of their near-field region is not discussed. It seems evident that as a size of a group increases its near-field region increases, too. This results into a computationally heavier direct calculation of the terms (4.12) and a bigger allocation of storage resources for the implementation of FAFFA. In chapter 7 of this thesis the author describes an implementation of a FAFFA algorithm in the three-dimensional case and attempts to characterise mathematically the near-field far-field boundary as well as the computational cost of the numerical method.

## 4.2 The Tabulated Interaction Method (TIM)

In this section, the Tabulated Interaction Method is described mathematically. First of all, beginning with the FAFFA formulation the TIM is presented in terms of a set of basis functions. Specifically, assuming all interactions may be modelled as far-field interactions (except those internal to a group), i.e. the FAFFA also holds for adjacent groups, it follows from (4.8) that for each group  $G_l$

$$\sum_{n \in G_l} Z_{mn} I_n = V_m - \sum_{l' \neq l} W_{ml}(\phi_{l'}) g_{ll'} \sum_{n \in G_{l'}} W_{nl'}^*(\phi_{l'}) I_n \quad m \in G_l \quad (4.13)$$

where  $g_{ll'}$  is the group centre-to-group centre impedance matrix element

$$g_{ll'} = \sqrt{\frac{2}{\pi k r_{ll'}}} e^{-j(k r_{ll'} - \pi/4)} \Delta \quad (4.14)$$

and  $W_{ij}(\alpha)$  is defined for  $\alpha$  as

$$W_{ij}(\alpha) = e^{-j\mathbf{k}\mathbf{r}_{ij}\hat{\mathbf{r}}} \quad (4.15)$$

for each pair of points indexed by  $(i, j)$ , with  $\mathbf{r}_{ij} = \mathbf{r}_i - \mathbf{r}_j$ . The angle  $\alpha$  is such that

$$\hat{\mathbf{r}} = \cos \alpha \hat{\mathbf{x}} + \sin \alpha \hat{\mathbf{y}} \quad (4.16)$$

where  $\hat{\mathbf{x}}$  and  $\hat{\mathbf{y}}$  are the unit vectors associated with the  $(x, y)$  coordinate system. It is also assumed that the width of intervals where the pulse basis functions (2.45) are defined is  $\Delta_n = \Delta$  for each  $n = 1 \cdots N$ . At this stage (4.2) has been rearranged including the FAFFA and (4.13) may be seen as the discretised integral equation for the group  $G_l$ , when the incident field at each point  $m \in G_l$  is

$$V_m - \sum_{l' \neq l} W_{ml}(\phi_{ll'}) g_{ll'} \sum_{n \in G_{l'}} W_{nl'}^*(\phi_{ll'}) I_n \quad (4.17)$$

Assume that the incident field of (4.1) is a plane wave of unit amplitude, with incident wave vector  $\mathbf{k} = k(\cos \theta \hat{\mathbf{x}} + \sin \theta \hat{\mathbf{y}})$ . Thus

$$V_m = e^{-j\mathbf{k}\cdot\mathbf{r}_m} = W_{ml}(\theta) e^{-j\mathbf{k}\cdot\mathbf{r}_l} = W_{ml}(\theta) V_l \quad (4.18)$$

Thus, for each group  $G_l$

$$\sum_{n \in G_l} Z_{mn} I_n = W_{ml}(\theta) V_l - \sum_{l' \neq l} W_{ml}(\phi_{ll'}) g_{ll'} \sum_{n \in G_{l'}} W_{nl'}^*(\phi_{ll'}) I_n \quad (4.19)$$

By introducing the term

$$E_{ll'} = g_{ll'} \sum_{n \in G_{l'}} W_{nl'}^*(\phi_{ll'}) I_n \quad (4.20)$$

(4.19) becomes

$$\sum_{n \in G_l} Z_{mn} I_n = W_{ml}(\theta) V_l - \sum_{l' \neq l} W_{ml}(\phi_{l'}) E_{l'} \quad (4.21)$$

Now, the right-hand side of (4.21) is a superposition of plane waves all evaluated at each point  $m \in G_l$ .

- The term

$$W_{ml}(\theta) V_l = e^{-j\mathbf{k} \cdot \mathbf{r}_m} \quad (4.22)$$

is the field emanated from the source.

- The term

$$\sum_{l' \neq l} W_{ml}(\phi_{l'}) E_{l'} = \sum_{l' \neq l} e^{-j\mathbf{k}_{l'} \cdot \mathbf{r}_m} \quad (4.23)$$

is a sum of plane waves emanated from all groups  $G_{l'}$ ,  $l' \neq l$ , with wave vectors

$$\mathbf{k}_{l'} = k(\cos \phi_{l'} \hat{\mathbf{x}} + \sin \phi_{l'} \hat{\mathbf{y}}) \quad (4.24)$$

By introducing a set of discretised angles  $\alpha_q = q\Delta\alpha$  for  $q = 1 \cdots Q$ , it is possible to approximate the right hand side of (4.21) with the sum of plane waves of amplitude  $I_q^{(l)}$  illuminating the group  $G_l$  at the angles  $\alpha_q$

$$\sum_{q=1}^Q W_{ml}(\alpha_q) I_q^{(l)} \quad (4.25)$$

A single term of the original sum, i.e.

$$W_{ml}(\phi_{l'}) E_{l'} \quad (4.26)$$

may be approximated by the sum of two terms

$$W_{ml}(\phi_{l'}) E_{l'} \approx W_{ml}(\alpha_1) \left(1 - \frac{|\phi_{l'} - \alpha_1|}{\Delta\alpha}\right) E_{l'} + W_{ml}(\alpha_2) \left(1 - \frac{|\phi_{l'} - \alpha_2|}{\Delta\alpha}\right) E_{l'} \quad (4.27)$$

where the angle  $\phi_{l'}$  satisfies the condition

$$\alpha_1 \leq \phi_{l'} \leq \alpha_2 \quad (4.28)$$

Thus, applying the approximation (4.27) to each term of the following sum

$$W_{ml}(\theta)V_l - \sum_{l' \neq l} W_{ml}(\phi_{l'})g_{l'l} \sum_{n \in G_{l'}} W_{nl'}^*(\phi_{l'})I_n \quad (4.29)$$

it follows that the required amplitudes in (4.25) are given by

$$I_q^{(l)} = \psi_q(\theta)V_l - \sum_{l' \neq l} \psi_q(\phi_{l'})g_{l'l} \sum_{n \in G_{l'}} W_{nl'}^*(\phi_{l'})I_n \quad (4.30)$$

where  $\psi(\cdot)$  are interpolating factors, depending on the angle  $\alpha_{q-1} < \gamma < \alpha_q$  and defined as

$$\psi_k(\gamma) = \begin{cases} 1 - \frac{|\gamma - \alpha_k|}{\Delta\alpha} & \text{if } k = q-1, q \\ 0 & \text{otherwise} \end{cases} \quad (4.31)$$

The set of  $QL$  ( $L$  is the number of groups) basis functions  $\phi^{(q)l}$ ,  $q = 1 \cdots Q$ ,  $l = 1 \cdots L$ , can now be introduced. The basis set consists of the solutions to the problem described by the discretised integral equation

$$\sum_{n \in G_l} Z_{mn} \phi_n^{(q)l} = W_{ml}(\alpha_q) \quad (4.32)$$

i.e. plane wave scattering by the group  $G_l$ . Thus, the unknown current at a point  $n \in G_l$  may be expressed as a superposition of  $Q$  basis functions.

$$I_n = \sum_{q=1}^Q I_q^{(l)} \phi_n^{(q)l} \quad (4.33)$$

This is now reasonable since it was assumed that the group  $G_l$  is illuminated by a superposition of plane waves

$$\sum_{q=1}^Q W_{ml}(\alpha_q) I_q^{(l)} \quad (4.34)$$

If all the groups are identical, for example if they are PEC segments of equal length, then it is possible to tabulate the set of basis functions at the points  $n \in G_l$  for one reference group and reuse these functions for all groups. This is the main computational advantage of the TIM over FAFFA as introduced in [62]. The solution of the scattering problem is reduced to the calculation of the unknown basis coefficients  $I_q^{(l)}$  for each group  $G_l$ ,  $q = 1 \cdots Q$  and  $l = 1 \cdots L$ . Inserting (4.33) in (4.30) gives the expression for the coefficients  $I_q^{(l)}$

$$I_q^{(l)} = \psi_q(\theta) V_l - \sum_{l' \neq l} \psi_q(\phi_{l'}) g_{ll'} \sum_{q=1}^Q I_q^{(l')} f_q^{(l')} \quad (4.35)$$

where  $f_q^{(l')}$  is defined to be

$$f_q^{(l')} = \sum_{n \in G_{l'}} W_{nl'}^*(\phi_{l'}) \phi_n^{(q)l'} \quad (4.36)$$

Now, referring to Fig 4.2, the geometry of the evaluation of the far-field scattered by a strip of length  $L$  is illustrated. It follows from [13] that the scattered electric field may be expressed as

$$I = \int_{-L/2}^{L/2} J_z(x) \sqrt{\frac{2}{\pi k \rho}} e^{-jk\rho + j\pi/4} e^{jkx \cos(\theta_s)} dx \quad (4.37)$$

which may be rewritten as

$$I \approx \sqrt{\frac{2}{\pi k \rho}} e^{-jk\rho + j\pi/4} \sum_{n=1}^N J_n \Delta_n e^{jk \mathbf{r}_{nl'} \cdot \hat{\mathbf{r}}} \quad (4.38)$$

where  $\rho$  and  $\theta_s$  are the cylindrical coordinates of the observation point,  $J_n = J_z(x_n)$ ,  $\Delta_n$  is the width of the intervals upon which the pulse basis functions used to represent the current are defined,  $\mathbf{r}_{nl'}$  is the vector connecting the centre  $l'$  of the segment with the point  $n$  and  $\hat{\mathbf{r}}$  is the direction of scattering. Recalling (4.15), it follows that

$$I \approx \sqrt{\frac{2}{\pi k \rho}} e^{-jk\rho + j\pi/4} \sum_{n=1}^N J_n \Delta_n W_{nl'}^*(\theta_s) \quad (4.39)$$

Hence the far-field scattered by the segment is

$$I \approx \sqrt{\frac{2}{\pi k \rho}} e^{-jk\rho + j\pi/4} F(\theta_i, \theta_s) \tag{4.40}$$

where the function

$$F(\theta_i, \theta_s) = \sum_{n=1}^N J_n \Delta_n W_{nl'}^*(\theta_s) \tag{4.41}$$

is the radiation pattern of the strip. In similar way, it follows that the coefficients  $f_q^{(l')}$  of (4.36) represent the far-field patterns of the basis function  $\phi^{(q)l'}$  over the directions  $\phi_{l'}$ . Again, a table of far-field patterns may be calculated a priori,

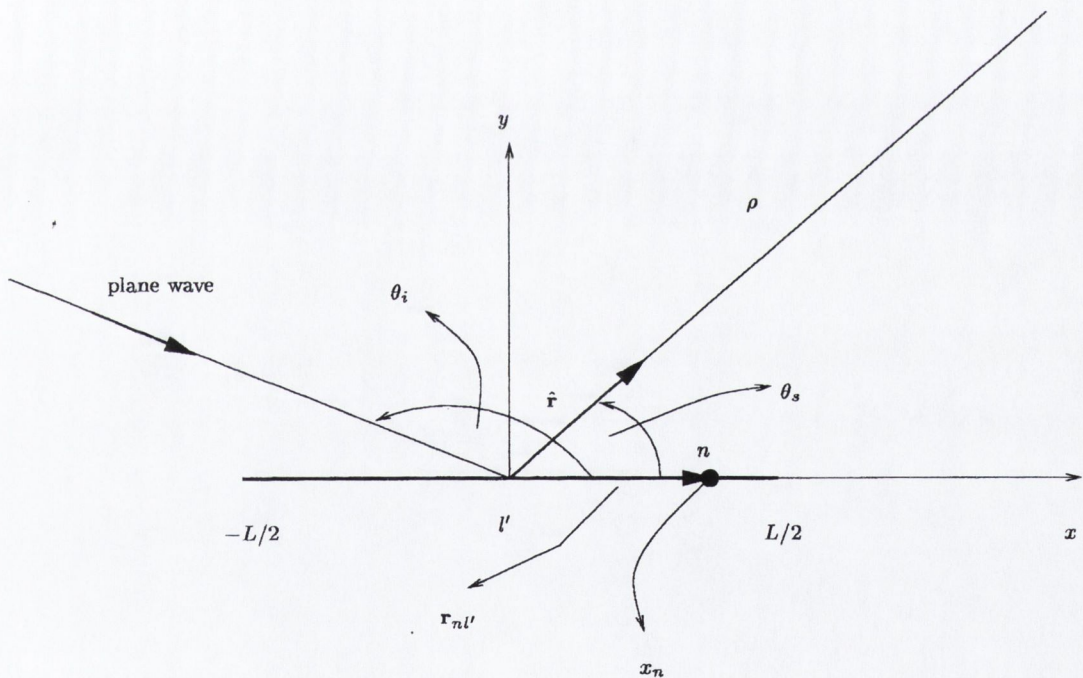


Figure 4.2: Geometry for the evaluation of the far-field scattered by a strip of length  $L$  illuminated by a plane wave.

stored and reused in the implementation of TIM producing huge computational cost savings. In fact, this is the only table required if one is interested in the evaluation of the scattered field.

The TIM presented in this section relies upon two basic assumptions. The first is that the interactions between near-neighbour groups may be evaluated using the FAFFA. This approximation will be adequate only if the near-neighbour groups are



almost collinear. In this case, the error introduced in the phase evaluation of the mutual interactions between current elements is null. To elucidate this, refer to

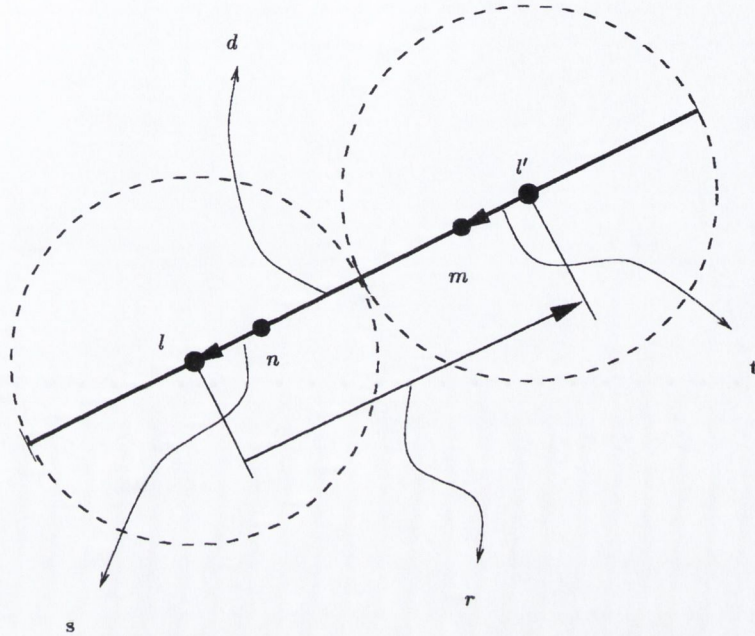


Figure 4.3: Two collinear groups and geometric quantities used in FAFFA.

Fig. 4.3, where two collinear groups ( $l$  and  $l'$ ) are illustrated. It is evident that, using FAFFA

$$Z_{mn} \approx \sqrt{\frac{2}{\pi kd}} e^{-j(kd - \pi/4)} \tag{4.42}$$

where  $Z_{mn}$  is the impedance matrix term obtained by discretising the EFIE using the moment method with pulse basis functions and  $m$  and  $n$  are two discretisation points illustrated in Fig. 4.3. By elementary geometric considerations, it follows that

$$e^{-jkd} = e^{-jk(r-s-t)} \tag{4.43}$$

(4.43) is basically

$$d = r + \mathbf{t} \cdot \hat{\mathbf{r}} + \mathbf{s} \cdot \hat{\mathbf{r}} \tag{4.44}$$

which is the foundation of the FAFFA, as given in (4.7). In the case of non-collinear groups the equality sign of (4.44) must be replaced with the approximation sign. The FAFFA does not introduce any error in the evaluation of the phase of the field scattered by the group  $G_l$  to the group  $G_{l'}$  of Fig. 4.3 if they are collinear.

The second assumption is that the far-field impinging on a group of current elements is a superposition of plane waves at discretised angles of arrival. In general the scattered field by a one-dimensional current distribution, as a PEC strip, may be characterised with a number of angular samples proportional to the spatial samples needed to characterise the current itself. Details of this property may be found in [65]. However, in some cases, as scattering by large locally smooth domains, only a certain portion of the spectrum of incident angles is non-null. Hence a very accurate description of the incident field in terms of plane waves may be achieved retaining a relatively small number of samples.

The TIM algorithm is numerically more efficient than FAFFA. This efficiency is due to the fact that using TIM each group of current elements is a PEC linear segment of fixed length illuminated by a set of plane waves. Hence, the solution to each elementary problem may be read from a look-up table constructed *a priori* and stored, instead of being numerically evaluated for each group. Recently, the TIM has also been applied to the numerical solution of the MFIE, with excellent results [66]. Moreover a multi-level version of TIM has been developed and proposed in [67] again with very satisfactory final results.

### **4.3 Electromagnetic scattering from large terrain profiles: an example of application of FAFFA and TIM**

The main area of application of TIM and FAFFA presented in this chapter has been in the important field of UHF propagation over undulating terrain. This problem was addressed first in [56] and [57]-[58]. Application of FAFFA to terrain-propagation modelling was reported in [61] and [63]-[64], providing massive com-

putational savings with respect to [56] and [60]. The formulation of TIM has found immediate application to the solution of terrain scattering problems, reducing further the computational time associated with the numerical solution, as explained in detail in [64]. An excellent resume of the main TIM foundations and its correlation to other fast numerical methods is given in [68].

The geometry of the problem is illustrated in Fig. 4.4, where a source illuminates an irregular terrain. The source is assumed to be an electric line source radiating

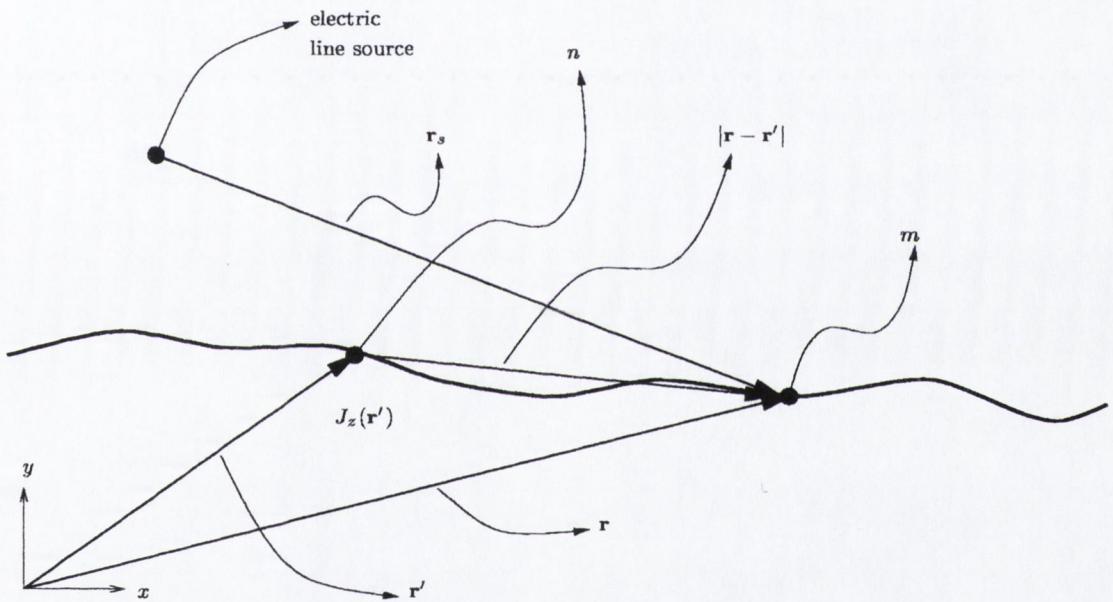


Figure 4.4: Line source illuminates an undulating terrain modelled by a two-dimensional surface.  $m$  and  $n$  are discretisation points where the current  $J_z$  is assumed to take the values  $J_m$  and  $J_n$ .

$TM_z$  polarised waves. The scatterer is a one-dimensional PEC surface ( $y = h(x)$ , where  $h$  is a function) modelling the terrain profile. Each terrain profile<sup>1</sup> employed by the author in carrying out numerical experiments was modelled as a series of linear segments. A segment connects points sampled every  $50m$  in the  $x$  direction. The source was located  $10.4m$  above the leftmost terrain point.

The electric field integral equation was implemented postulating pulse basis functions defined as in (2.45) every quarter wavelength along the terrain surface. The

<sup>1</sup>The author wishes to thank Prof. Bach Andersen of University of Aalborg, Denmark for supplying the terrain profiles.

EFIE

$$\frac{\omega\mu_0}{4} \int_S J_z(\mathbf{r}') H_0^{(2)}(k|\mathbf{r}' - \mathbf{r}|) dS' = E_{inc}(\mathbf{r}) \quad (4.45)$$

was discretised using the MoM, leading to

$$V_m = \sum_{n=1}^N Z_{mn} I_n \quad m = 1 \dots N \quad (4.46)$$

where  $N$  is the number of unknowns, typically  $N = \mathcal{O}(10^5)$ . The quantities  $\mathbf{r}'$ ,  $\mathbf{r}$ ,  $J_z(\mathbf{r}')$  are illustrated in Fig. 4.4. (4.46) may be solved without explicitly storing the matrix  $Z$  [59]. The current is estimated by a forward-backward iterative scheme until a certain error criterion is satisfied. In [56], it is assumed and verified numerically that a pure forward scheme is sufficient to tackle and solve the problem of electromagnetic scattering at grazing incidence.

The fast far-field algorithm (FAFFA) was implemented as described in section 4.1. Each group of current elements was chosen to be a linear segment of the terrain profile. The tabulated interaction method (TIM) was used as described in section 4.2, postulating linear segment groupings of  $50m$  in length and an angular resolution of  $Q = 360$ . In implementing the TIM, the incident field over each linear segment group was approximated as being a plane wave. This approximation is reasonable for groups which are located far away from the source. However, for the groups near the line source the incident field is reflected away from the other groups of the scatterer and the approximation introduced does not affect the final result.

Fig. 4.5 illustrates the numerical results obtained applying both the TIM and the FAFFA to the problem of electromagnetic scattering from terrain. Fig. 4.5 also shows the terrain profile which extends horizontally for thousands of meters. The incident frequency is  $970MHz$ . The field strength at  $2.4m$  over the terrain is represented as a function of the horizontal distance. The author has observed that

$$\frac{T_{FAFFA}}{T_{TIM}} \approx 50 \quad (4.47)$$

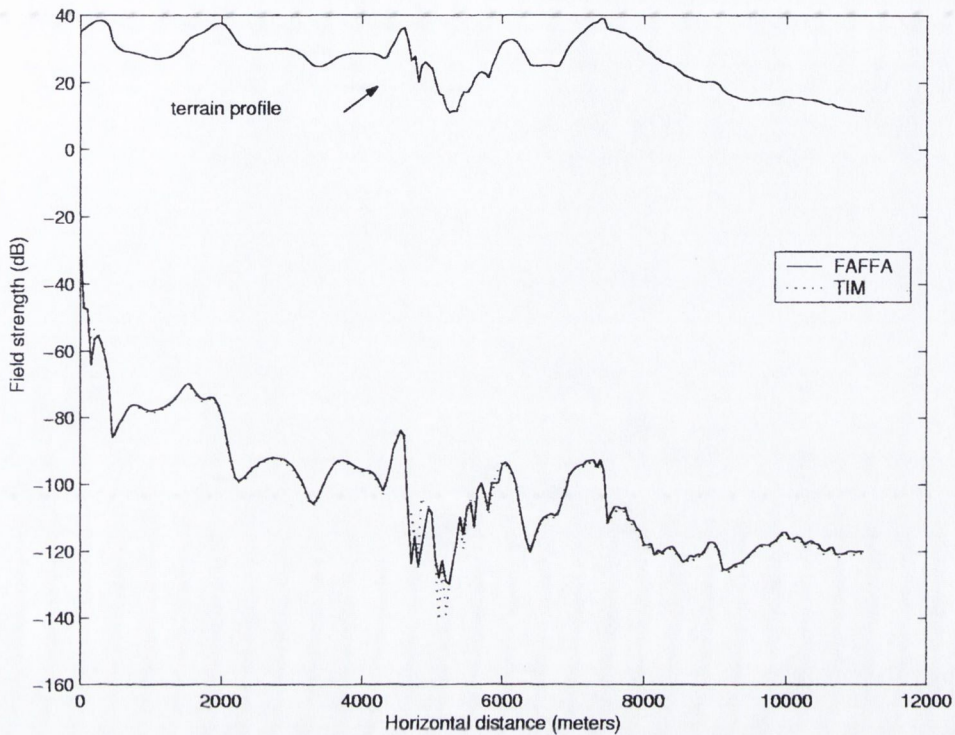


Figure 4.5: Example of application of FAFFA and TIM to the numerical evaluation of the field strength over a terrain profile which extends for several thousands of wavelengths.

for this particular numerical experiment, where  $T_{FAFFA}$  is the computation time for the execution of the FAFFA and similar definition holds for  $T_{TIM}$ . In [64] it is reported that

$$\frac{T_{exact}}{T_{TIM}} \approx 20000 \quad (4.48)$$

where  $T_{exact}$  is the computation time associated with an *exact* solution of the EFIE.

## 4.4 Summary

Chapter 4 presented two fast and efficient numerical methods: the FAFFA and the TIM. The FAFFA formulation was given and it was shown that the method is based on a simple geometric approximation. The FAFFA permits to evaluate the interactions between far apart subscatterers in a fast and accurate way employing the same concepts upon which relies the FMM presented in chapter 3: *aggregation*, *translation* and *disaggregation*. A question about the definition of far-field regions

in the FAFFA was risen. This argument is treated in chapter 7 where the answer is presented mathematically. The TIM was then described. It was shown that the technique may be used to solve the EFIE in the two-dimensional case. The main assumptions of TIM were given:

- The FAFFA may be applied to near-field interactions.
- The groups of current elements are identical: PEC segments of equal length.
- The incident field over each group may be approximated as a sum of plane waves.

The essential speed-up feature of the TIM is due to the possibility of expressing the electric current residing on each subscatterer as the sum of reference currents. Each reference current is the solution of a standard problem, which is plane wave scattering by a PEC segment. It was shown that the far-field scattered by each group depends on a weighted sum of reference far-field patterns. These patterns may be evaluated *una tantum* and reused in many different cases. The assumptions of TIM were discussed and a numerical result was given to demonstrate the behaviour of the FAFFA and TIM in the case of electromagnetic scattering by undulating terrain. The computation time ratio between the two algorithms was reported.

---

## NOVEL ENHANCEMENTS TO TIM

---

Two novel enhancements to TIM are presented in this chapter: the Analytical Interaction Method (ANIM) and the matrix formulation of TIM/ANIM. Both methods can be applied to the solution of two-dimensional EFIE, in the case of piecewise linear smooth scatterers. The ANIM replaces the TIM tables with two analytical results: an approximation of the current density induced on a PEC segment of fixed length by a plane wave incident at grazing angles and the expression of the electric far-field due to this distribution. Section 5.1 presents the motivation of ANIM. This method is formulated in section 5.2, by using Maxwell's equations and a classical result of electromagnetic scattering theory: plane wave scattering by a PEC half-plane. The ANIM is tested and compared with TIM in section 5.3.

In part 5.4, the TIM is formulated in matrix form with the EFIE being discretised using the basis set  $\phi^{(q)l}$  of (4.32). The final result is a compact and rigorous formulation which achieves huge computational savings in storage allocation for the solution of the EFIE by TIM. Application of this compact formulation to the problem of electromagnetic scattering by periodic structures is also proposed.

### 5.1 Motivation of the Analytical Interaction Method (ANIM)

The TIM derives its computational savings from essentially two features, which are now briefly recalled.

- The discretised integral equation (4.21)

$$\sum_{n \in G_l} Z_{mn} I_n = W_{ml}(\theta) V_l - \sum_{l' \neq l} W_{ml}(\phi_{l'}) E_{l'} \quad (5.1)$$

has been derived in chapter 4. It has been shown that the right hand side

$W_{ml}(\theta)V_l + \sum_{l' \neq l} W_{ml}(\phi_{l'})E_{l'}$  is a sum of plane waves, which may be approximated by a sum of plane waves illuminating the group  $G_l$  at discretised angles

$$\sum_{q=1}^Q W_{ml}(\alpha_q)I_q^{(l)} \quad (5.2)$$

where  $\alpha_q = q\Delta\alpha \in (0, 2\pi]$  and  $m \in G_l$ .

- For a certain class of scatterers, whose surface may be modeled with a set of flat PEC strips of equal length, the fact that each group  $G_l$  is illuminated by the sum (5.2) suggests an elegant way to speed up the solution of the discretised equation (5.1). Specifically, the current in each group  $G_l$  may be evaluated by referring to a table which contains the samples  $\phi_n^{(q)l}$ , where  $n \in G_l$  and  $\phi^{(q)l}$  is the solution of (4.32)

$$\sum_{n \in G_l} Z_{mn} \phi_n^{(q)l} = W_{ml}(\alpha_q) \quad (5.3)$$

Additionally, the far-field scattered by any group  $G_l$  is due to the sum of the fields scattered by the functions  $\phi^{(q)l}$  excited on that group. Again, it is possible to refer to a table of far-field radiation patterns, evaluated at discretised angles, read in the necessary values and manipulate them to evaluate the far-field scattered by the group  $G_l$ . In the original formulation [62], the standardised basis currents  $\phi_n^{(q)l}$  and the far-field patterns  $f_q^{(ll')}$  of (4.36) were evaluated numerically.

It is evident that the TIM achieves enormous computational savings by reusing the information contained in the tables instead of solving (4.32) for each group  $G_l$ . However, it is obvious that different tables must be stored for different frequencies and different sizes of the groups  $G_l$ . This drawback has motivated the author to investigate the possibility of expressing the far-field patterns analytically, in order to avoid the numerical construction of the tables in TIM. First results were reported in [69]. Recently, the author has found [70] that it is possible to remove the look-up



tables in the TIM and calculate *on the fly* the necessary far-field patterns using an approximated closed form solution.

## 5.2 Formulation of ANIM

In this section, the incident electric field is assumed to be a  $TM_z$  plane wave with amplitude  $E_0$ . Referring to [14], p. 346, the total electric field due to an incident  $TM_z$  plane wave on a PEC half-plane may be expressed as

$$E_z = E_0 \frac{e^{j\pi/4}}{\sqrt{\pi}} [e^{jks \cos(\theta_s - \theta_i)} F(a_1) - e^{jks \cos(\theta_s + \theta_i)} F(a_2)] \quad (5.4)$$

with

$$a_1 = -\sqrt{2ks} \cos \frac{(\theta_s - \theta_i)}{2} \quad (5.5)$$

and

$$a_2 = -\sqrt{2ks} \cos \frac{(\theta_s + \theta_i)}{2} \quad (5.6)$$

The function  $F(a)$  is defined as

$$\int_a^\infty e^{-j\tau^2} d\tau \quad (5.7)$$

and the geometric parameters  $s$ ,  $\theta_i$  and  $\theta_s$  are illustrated in Fig. 5.1. According to Maxwell's equation

$$\nabla \times \mathbf{E} = -j\omega\mu\mathbf{H} \quad (5.8)$$

in cylindrical coordinates it follows that

$$\nabla \times \mathbf{E} = \frac{\partial E_z}{\partial s} (\hat{\mathbf{s}} \times \hat{\mathbf{z}}) + \frac{1}{s} \frac{\partial E_z}{\partial \theta_s} (\hat{\theta}_s \times \hat{\mathbf{z}}) \quad (5.9)$$

where  $(\hat{\mathbf{s}}, \hat{\theta}_s, \hat{\mathbf{z}})$  is the triplet of unit vectors associated with the cylindrical coordinate system displayed in Fig. 5.1. The scattered field is evaluated at the point  $(s, \theta_s, z)$ . Thus

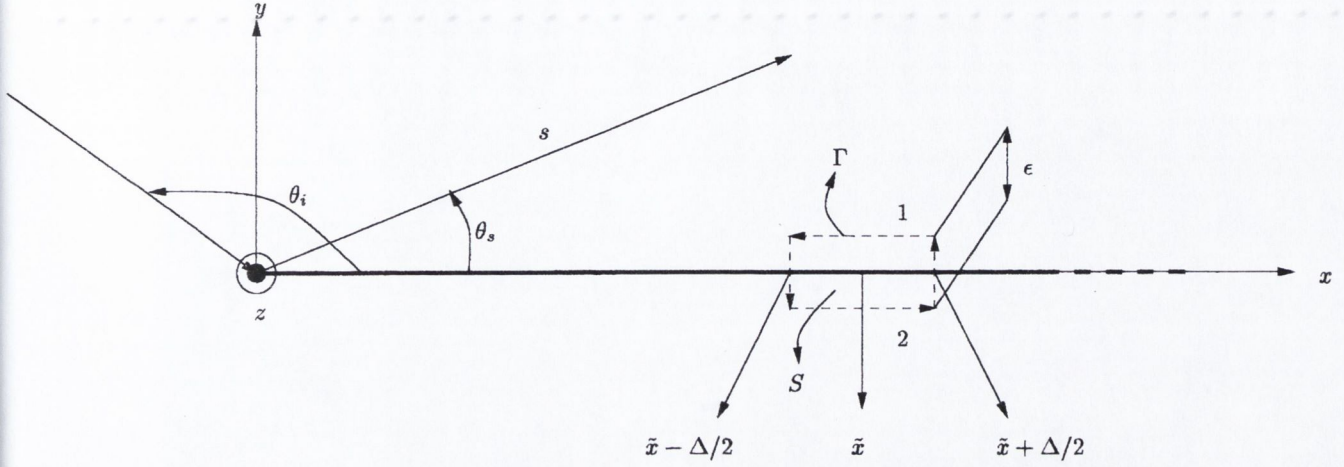


Figure 5.1: A half plane is illuminated by a  $TM_z$  plane wave at a low grazing angle  $\theta_i$ . The electric current residing on the half plane located at ( $s > 0, \theta_s = 0, z = 0$ ) is determined: point  $\tilde{x}$ , closed contour  $\Gamma$  in the neighbourhood of  $\tilde{x}$ , surface  $S$ , rectangular and cylindrical reference coordinate systems.

$$\begin{aligned} \frac{\partial E_z}{\partial s} = E_0 \frac{e^{j\pi/4}}{\sqrt{\pi}} & \left( jk \cos(\theta_s - \theta_i) e^{jks \cos(\theta_s - \theta_i)} F(a_1) \right. \\ & + e^{jks \cos(\theta_s - \theta_i)} e^{-ja_1^2} \sqrt{\frac{k}{2s}} \cos \left[ \frac{(\theta_s - \theta_i)}{2} \right] \\ & - jk \cos(\theta_s + \theta_i) e^{jks \cos(\theta_s + \theta_i)} F(a_2) \\ & \left. - e^{jks \cos(\theta_s + \theta_i)} e^{-ja_2^2} \sqrt{\frac{k}{2s}} \cos \left[ \frac{(\theta_s + \theta_i)}{2} \right] \right) \end{aligned} \quad (5.10)$$

$$\begin{aligned} \frac{\partial E_z}{\partial \theta_s} = E_0 \frac{e^{j\pi/4}}{\sqrt{\pi}} & \left( -jks \sin(\theta_s - \theta_i) e^{jks \cos(\theta_s - \theta_i)} F(a_1) \right. \\ & - e^{jks \cos(\theta_s - \theta_i)} e^{-ja_1^2} \sqrt{\frac{ks}{2}} \sin \left[ \frac{(\theta_s - \theta_i)}{2} \right] \\ & + jks \sin(\theta_s + \theta_i) e^{jks \cos(\theta_s + \theta_i)} F(a_2) \\ & \left. + e^{jks \cos(\theta_s + \theta_i)} e^{-ja_2^2} \sqrt{\frac{ks}{2}} \sin \left[ \frac{(\theta_s + \theta_i)}{2} \right] \right) \end{aligned} \quad (5.11)$$

Referring to the geometry illustrated in Fig. 5.1 and using Maxwell's equation

$$\nabla \times \mathbf{H} = j\omega \mathbf{D} + \mathbf{J} \quad (5.12)$$

by integrating over the surface  $S$  and using of Stokes' theorem (5.12) becomes

$$\int \int_S (\nabla \times \mathbf{H}) \cdot \hat{\mathbf{z}} = \oint_{\Gamma} \mathbf{H} \cdot d\mathbf{l} = \int \int_S (j\omega \mathbf{D} + \mathbf{J}) \cdot \hat{\mathbf{z}} \quad (5.13)$$

If  $\epsilon \ll \Delta$  and provided that  $\Delta$  is relatively small the following limit holds

$$\lim_{\Delta \rightarrow 0} [(\mathbf{H}_2 - \mathbf{H}_1) \cdot \hat{\mathbf{x}}] \Delta = \int \int_S \mathbf{J} \cdot \hat{\mathbf{z}} \quad (5.14)$$

where  $\mathbf{H}_1$  is the magnetic field just above the coordinate  $\tilde{x}$ , i.e.

$$\mathbf{H}_1 = \mathbf{H}(s = \tilde{x}, \theta_s = 0^+, z) \quad (5.15)$$

and similarly  $\mathbf{H}_2$  is given by

$$\mathbf{H}_2 = \mathbf{H}(s = \tilde{x}, \theta_s = 2\pi^-, z) \quad (5.16)$$

with  $z \in (-\infty, \infty)$ . Moreover, the integral in the right-hand of (5.14) side evaluates to  $[\mathbf{J}_S \cdot \hat{\mathbf{z}}] \Delta$ , where  $\mathbf{J}_S$  is the surface current density existing on the boundary. Using the identity  $\hat{\mathbf{x}} = -\hat{\mathbf{z}} \times \hat{\mathbf{y}}$  (5.14) becomes

$$\mathbf{J}_S = \hat{\mathbf{y}} \times (\mathbf{H}_1 - \mathbf{H}_2) \quad (5.17)$$

To obtain a closed form for the current, the term  $\hat{\mathbf{y}} \times (\mathbf{H}_1 - \mathbf{H}_2)$  must be evaluated.

This is done by recalling (5.9)

$$\frac{\partial E_z}{\partial s} (\hat{\mathbf{s}} \times \hat{\mathbf{z}}) + \frac{1}{s} \frac{\partial E_z}{\partial \theta_s} (\hat{\theta}_s \times \hat{\mathbf{z}}) = -j\omega\mu\mathbf{H} \quad (5.18)$$

Thus  $\mathbf{H}_1$  and  $\mathbf{H}_2$  for  $z \in (-\infty, \infty)$  may be expressed as

$$\begin{aligned} -j\omega\mu\mathbf{H}_1 &= -j\omega\mu\mathbf{H}(s = \tilde{x}, \theta_s = 0^+, z) = \\ &\left( \frac{\partial E_z}{\partial s} \right) \Big|_{(s=\tilde{x}, \theta_s=0^+, z)} (\hat{\mathbf{x}} \times \hat{\mathbf{z}}) + \left( \frac{1}{s} \frac{\partial E_z}{\partial \theta_s} \right) \Big|_{(s=\tilde{x}, \theta_s=0^+, z)} (\hat{\mathbf{y}} \times \hat{\mathbf{z}}) \end{aligned} \quad (5.19)$$

and

$$\begin{aligned} -j\omega\mu\mathbf{H}_2 &= -j\omega\mu\mathbf{H}(s = \tilde{x}, \theta_s = 2\pi^-, z) = \\ &\left( \frac{\partial E_z}{\partial s} \right) \Big|_{(s=\tilde{x}, \theta_s=2\pi^-, z)} (\hat{\mathbf{x}} \times \hat{\mathbf{z}}) + \left( \frac{1}{s} \frac{\partial E_z}{\partial \theta_s} \right) \Big|_{(s=\tilde{x}, \theta_s=2\pi^-, z)} (\hat{\mathbf{y}} \times \hat{\mathbf{z}}) \end{aligned} \quad (5.20)$$

Hence, it is possible to write that

$$\mathbf{J}_S = \hat{\mathbf{y}} \times (\mathbf{H}_1 - \mathbf{H}_2) = -\frac{1}{j\omega\mu} \hat{\mathbf{y}} \times (\hat{\mathbf{y}} \times \hat{\mathbf{z}}) \left[ \left( \frac{1}{s} \frac{\partial E_z}{\partial \theta_s} \right) \Big|_{(s=\tilde{x}, \theta_s=0^+, z)} - \left( \frac{1}{s} \frac{\partial E_z}{\partial \theta_s} \right) \Big|_{(s=\tilde{x}, \theta_s=2\pi^-, z)} \right] \quad (5.21)$$

with

$$E_0 \frac{e^{j\pi/4}}{\sqrt{\pi}} \frac{1}{\tilde{x}} \left( 2jk\tilde{x} \sin \theta_i F(\alpha) e^{jk\tilde{x} \cos \theta_i} + 2e^{-j\alpha^2} \sqrt{\frac{k\tilde{x}}{2}} \sin \left( \frac{\theta_i}{2} \right) e^{jk\tilde{x} \cos \theta_i} \right) \left( \frac{1}{s} \frac{\partial E_z}{\partial \theta_s} \right) \Big|_{(s=\tilde{x}, \theta_s=0^+, z)} = \quad (5.22)$$

and

$$E_0 \frac{e^{j\pi/4}}{\sqrt{\pi}} \frac{1}{\tilde{x}} \left( 2jk\tilde{x} \sin \theta_i F(\bar{\alpha}) e^{jk\tilde{x} \cos \theta_i} - 2e^{-j\bar{\alpha}^2} \sqrt{\frac{k\tilde{x}}{2}} \sin \left( \pi - \frac{\theta_i}{2} \right) e^{jk\tilde{x} \cos \theta_i} \right) \left( \frac{1}{s} \frac{\partial E_z}{\partial \theta_s} \right) \Big|_{(s=\tilde{x}, \theta_s=2\pi^-, z)} = \quad (5.23)$$

where

$$\alpha = -\sqrt{2k\tilde{x}} \cos \left( \frac{\theta_i}{2} \right) \quad (5.24)$$

and

$$\bar{\alpha} = -\sqrt{2k\tilde{x}} \cos \left( \pi - \frac{\theta_i}{2} \right). \quad (5.25)$$

Recalling that  $F(\alpha) - F(\bar{\alpha}) = \sqrt{\pi} e^{-j\pi/4}$  and  $-1/(j\omega\mu) \hat{\mathbf{y}} \times (\hat{\mathbf{y}} \times \hat{\mathbf{z}}) = 1/(jk\zeta_0) \hat{\mathbf{z}}$  with  $\zeta_0$  equal to the free space impedance, the following expression for the current may be derived<sup>1</sup>

$$\mathbf{J}_S(\tilde{x}) = \hat{\mathbf{z}} \frac{2E_0}{\zeta_0} e^{jk\tilde{x} \cos \theta_i} \left\{ \sin \theta_i + \sqrt{2} e^{-2jk\tilde{x} \cos^2(\theta_i/2)} e^{-j\pi/4} \frac{1}{\sqrt{\pi k\tilde{x}}} \sin \left( \frac{\theta_i}{2} \right) \right\} \quad (5.26)$$

At grazing incidence, i.e.  $\theta_i \rightarrow \pi$ , at a first approximation, one may assume that the current on a perfectly electric conducting strip located in the interval  $\tilde{x} \in [0, L]$

<sup>1</sup>The result is a well known one which may be found, for example, in [19].

has the expression (5.26) with  $\tilde{x} \in [0, L]$ . The scattered far-field is given by (see [13])

$$\mathbf{E}_s(R_0, \theta_s) = -\hat{\mathbf{z}}\zeta_0 \sqrt{\frac{jk}{8\pi}} \frac{e^{-jkR_0}}{\sqrt{R_0}} \int_0^L J_S^z(\tilde{x}) e^{jk\tilde{x} \cos \theta_s} d\tilde{x} \quad (5.27)$$

where the integral over the strip may now be evaluated analytically. Specifically,

$$\int_0^L \frac{e^{jk\eta\tilde{x}}}{\sqrt{\tilde{x}}} d\tilde{x} = \begin{cases} \sqrt{\frac{2\pi}{k\eta}} \{C(\sqrt{\frac{2k\eta L}{\pi}}) + jS(\sqrt{\frac{2k\eta L}{\pi}})\} & \text{if } \eta > 0 \\ \sqrt{\frac{2\pi}{k|\eta|}} \{C(\sqrt{\frac{2k|\eta|L}{\pi}}) - jS(\sqrt{\frac{2k|\eta|L}{\pi}})\} & \text{if } \eta < 0 \end{cases} \quad (5.28)$$

where the functions  $C(\cdot)$  and  $S(\cdot)$  are the Fresnel integrals defined as follows

$$C(x) = \int_0^x \cos\left(\frac{\pi}{2}q^2\right) dq \quad (5.29)$$

$$S(x) = \int_0^x \sin\left(\frac{\pi}{2}q^2\right) dq \quad (5.30)$$

Hence

$$\int_0^L J_S^z(\tilde{x}) e^{jk\tilde{x} \cos \theta_s} d\tilde{x} = \frac{2E_0}{\zeta_0} \left\{ \sin \theta_i \frac{(e^{jkL[\cos \theta_i + \cos \theta_s]} - 1)}{jk[\cos \theta_i + \cos \theta_s]} + \sin\left(\frac{\theta_i}{2}\right) \frac{1}{k} \sqrt{2}(1-j) \frac{\bar{F}\left(\sqrt{\frac{2k|\eta|L}{\pi}}\right)}{\sqrt{|\eta|}} \right\} \quad (5.31)$$

where the function  $\bar{F}(\cdot)$  has been introduced:

$$\bar{F}\left(\sqrt{\frac{2k|\eta|L}{\pi}}\right) = \begin{cases} C\left(\sqrt{\frac{2k\eta L}{\pi}}\right) + jS\left(\sqrt{\frac{2k\eta L}{\pi}}\right) & \text{if } \eta > 0 \\ C\left(\sqrt{\frac{2k|\eta|L}{\pi}}\right) - jS\left(\sqrt{\frac{2k|\eta|L}{\pi}}\right) & \text{if } \eta < 0 \end{cases} \quad (5.32)$$

Moreover, in the analytical evaluation of the integral over the strip, the coefficient  $\eta = \cos \theta_i + \cos \theta_s - \cos^2\left(\frac{\theta_i}{2}\right)$  has been defined.

The electric far-field scattered by the current  $\mathbf{J}_S$  is given by

$$\mathbf{E}_s(R_0, \theta_s) = -\hat{\mathbf{z}} \sqrt{\frac{j}{8\pi}} \frac{e^{-jkR_0}}{\sqrt{kR_0}} 2E_0 \left\{ \sin \theta_i \frac{(e^{jkL[\cos \theta_i + \cos \theta_s]} - 1)}{j[\cos \theta_i + \cos \theta_s]} + \sin\left(\frac{\theta_i}{2}\right) \sqrt{2}(1-j) \frac{\bar{F}}{\sqrt{|\eta|}} \right\} \quad (5.33)$$

where the limit of (5.32) for  $kL \gg 1$  has been calculated as

$$\bar{F} = \begin{cases} \frac{1}{2}(1 + j) & \text{if } \eta > 0 \\ \frac{1}{2}(1 - j) & \text{if } \eta < 0 \end{cases} \quad (5.34)$$

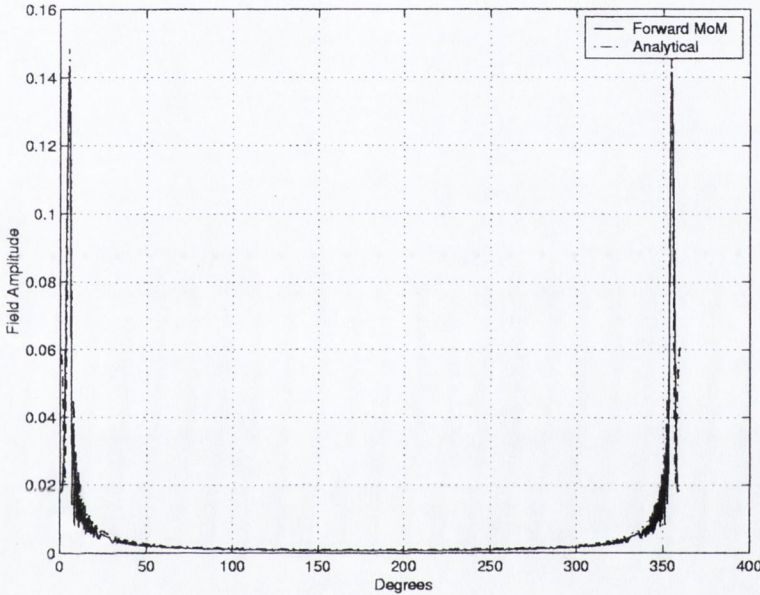


Figure 5.2: Amplitude of the scattered far-field due to a PEC strip of length  $L = 256\lambda$ . The strip is impinged by a plane wave at an angle  $\theta_i = 175/180\pi$  and the field is evaluated at a far distance  $R_0 = 100L$ . The results displayed are obtained applying the analytical expression given in (5.33) and the numerical results returned by a classical forward moment method (MoM).

The analytical expression of the scattered far-field has been compared with the numerical solution obtained through the typical method of moments (MoM) for a strip of length  $256\lambda$  illuminated by a  $TM_z$  plane wave with  $\theta_i = (175/180)\pi$ , in accordance with the assumptions made in obtaining the closed form approximation, i.e.  $L \gg \lambda$  and  $\theta_i \rightarrow \pi$  (grazing incidence). Fig. 5.2 illustrates the absolute value of the scattered far-field evaluated by numerical integration of the current obtained solving a classical MoM and the analytical expression reported here, when  $\theta_s \in (0, 2\pi)$  and  $R_0 = 100L$ . The two results are slightly different for the interval of angles  $\theta_s$  close to 0, where the electromagnetic power scattered by the strip evaluated analytically results to be greater than the power evaluated numerically. The reason for this appears that, when  $[\cos \theta_i + \cos \theta_s] \rightarrow 0$ , as is the case at grazing

incidence, and for  $\theta_s \rightarrow 0$ , the scattered field can be approximated by

$$\mathbf{E}_s(R_0, \theta_s) = -\hat{\mathbf{z}} \sqrt{\frac{j}{8\pi}} \frac{e^{-jkR_0}}{\sqrt{kR_0}} 2E_0 \left\{ \sqrt{2}(1-j) \frac{\bar{F}}{\sqrt{|\eta|}} \right\} \quad (5.35)$$

which physically represents the effect of the edge of the half-plane. It is known that the current parallel to the edge is singular and the MoM solution obtained by approximating the current distribution with nonsingular pulses may be not very accurate in the subdomains near the edge itself (see [31]). An under-evaluation of such current may result then into a lower evaluation of the scattered fields at those angles  $\theta_s$  for which the edge current is the dominant term. Moreover, the current assumed as the truncation of the half-plane current results to be affected by a slight backward scattering contribution which is not included in the MoM solution, evaluated in a pure forward scheme. Though, the latter difference is negligible, as the difference between the full MoM solution and the forward scattering MoM solution is negligible when  $\theta_i \rightarrow \pi$ .

Given the satisfactory result illustrated in Fig. 5.2, it is of interest to apply (5.33) to the solution of two-dimensional EFIE to demonstrate the possibility of implementing the TIM without tables. Section 5.3 presents numerical results which justify the substitution of TIM tables by the closed form expressions (5.26) and (5.33). The main advantages of an analytical extension of TIM, which may be renamed as Analytical Interaction Method (ANIM), are

- The numerical construction of the look-up tables is avoided: this results in a computational time and storage saving.
- The groups of current elements are not necessarily equal in length, as they must be in TIM. This is due to the higher flexibility of the analytical expression (5.33), which has the length of the PEC strip as an input parameter, when implemented as a routine.
- It is not necessary to store different look-up tables at different frequencies as it is in TIM.

The discretised integral equation (5.1) may hence be solved for each PEC segment  $G_l$ . Recalling (4.33), the unknown current at a point  $n \in G_l$  may be expressed as

$$I_n = \sum_{q=1}^Q I_q^{(l)} \phi_n^{(q)l} \quad (5.36)$$

where the generic basis function  $\phi^{(q)l}$  has the analytical expression given by (5.26). The coefficients  $I_q^{(l)}$  are determined as derived in (4.35), i.e.

$$I_q^{(l)} = \psi_q(\theta) V_l - \sum_{l' \neq l} \psi_q(\phi_{ll'}) g_{ll'} \sum_{q=1}^Q I_q^{(l')} f_q^{(ll')} \quad (5.37)$$

where the far-fields  $g_{ll'} \sum_{q=1}^Q I_q^{(l')} f_q^{(ll')}$ , for each  $l' \neq l$ , are now calculated analytically as in (5.33).

### 5.3 Numerical results

In this section ANIM is compared with TIM, a reference numerical scheme and measurements. The numerical experiments carried out are the calculation of the field strength in dB at 2.4m over irregular terrains<sup>2</sup> that have been modeled as a one dimensional PEC scatterers, as pointed out in section 4.3. Specifically, each profile was modelled as a series of linear segments. A segment connects points sampled every 50m in the  $x$  direction (see Fig. 4.4). Each of these PEC segment was assumed to be a group of current elements in both TIM and ANIM. For all simulation examples, the author recorded an execution time of ANIM of the same order as TIM. This result demonstrates that ANIM preserves TIM speed-up features, as expected.

#### 5.3.1 Numerical results for Jerslev profile

The first set of results is illustrated in Fig. 5.3. In part (a) of the figure, the geometry of the problem is described: a line source is placed 10.4m above the

<sup>2</sup>The author wishes to thank Prof. Bach Andersen of University of Aalborg, Denmark for supplying the terrain profiles and measured data.



leftmost terrain point and radiates at  $1900\text{MHz}$ . The field strength over the terrain profile Jerslev was evaluated using three different fast numerical methods.

- The FAFFA described in section 4.1 was implemented using groups of current elements of  $50\text{m}$  in length.
- The numerical version of TIM was implemented as described in section 4.2, with an angular resolution of  $Q = 360$ .
- The ANIM was implemented as described in section 5.2. Each subscatterer (PEC segment) was assumed to be illuminated by the set of plane waves (5.2) with a resolution of  $Q = 720$ .

In comparing ANIM with FAFFA from a computational point of view, the ratio between execution times was evaluated. It was observed that

$$\frac{T_{FAFFA}}{T_{ANIM}} \approx 100 \quad (5.38)$$

where  $T_{(\cdot)}$  is the execution time related to the numerical method employed. Fig. 5.3(b) shows an overall excellent agreement between TIM and ANIM. FAFFA results are also reported for comparison. Another numerical experiment was carried out at the frequency of  $970\text{MHz}$  for the same terrain profile. The software implementing ANIM was not modified whereas the TIM code was provided with a different set of tables with respect to that one related to  $1900\text{MHz}$ . The results are illustrated in Fig. 5.4. For this case, the ratio

$$\frac{T_{FAFFA}}{T_{ANIM}} \approx 50 \quad (5.39)$$

was observed. An excellent overall level of agreement between the three methods was again obtained.

### 5.3.2 Numerical results for Hjørringvei profile

Fig. 5.5(a) illustrates the geometry of the second problem tackled. The terrain profile considered is Hjørringvei and the incident frequency was chosen to be  $1900\text{MHz}$ .

Fig. 5.5(b) illustrates the field strength numerically evaluated using three different numerical schemes.

- ANIM described in section 5.2 with each subscatterer assumed to be illuminated by the set of plane waves (5.2) with  $Q = 720$ .
- TIM presented in section 4.2 with an angular resolution of  $Q = 360$ .
- NBS (Natural Basis Set), a method reported in [57].

For this case, the author recorded a ratio of execution times of

$$\frac{T_{NBS}}{T_{ANIM}} \approx 10. \quad (5.40)$$

For the same terrain profile at the same frequency, the comparison of ANIM with FAFFA yielded

$$\frac{T_{FAFFA}}{T_{ANIM}} \approx 40: \quad (5.41)$$

Despite the substantial computational time savings achieved, ANIM results offer an excellent overall agreement with NBS and TIM results.

### 5.3.3 Comparison with measured data and reference results

ANIM was compared also with a reference solution which requires a computation time of the order of a day, approximately 20000 times the computation time of ANIM. This reference solution was produced using the forward-backward scheme [59] referenced also in section 4.3. The results are shown in Fig. 5.6 for the terrain Hjorringvei at the frequency of  $970MHz$ . Note the excellent agreement between the reference and the ANIM solution and measured data except for the discrepancy over the last kilometre due to the presence of an urban area not included in the terrain model. Similar results were obtained for the profile Jerslev at the frequency of  $970MHz$ . They are illustrated in Fig. 5.7. An outstanding agreement between ANIM and reference solution was again obtained and a very good overall level of agreement with measurements was achieved.

### 5.4 Matrix formulation of TIM/ANIM

In this section the matrix formulation of the TIM/ANIM is presented. Recall that the TIM employs the solution to the standard problem of the plane wave scattering by a flat strip indexed by  $l$  at which resides the group of current elements labelled as  $G_l$ . The discretised integral equation (4.32) for the standard problem is

$$\sum_{n \in G_l} Z_{mn} \phi_n^{(q)l} = W_{ml}(\alpha_q) \quad (5.42)$$

The set of plane waves incident on a group  $G_l$  is due to the source and the scattered field from subscatterers  $l'$ ,  $l' \neq l$ . Using the notation of section 4.2 and assuming that the incident electric field is a plane wave of complex amplitude  $E_0$ , for each point  $t \in G_l$  it may be written that

$$\begin{aligned} & - \sum_{q=1}^Q I_q^{(l)} \phi^{(q)l}(t) = \\ & - E_0 V_l \left( \psi_{m_{inc}}^{(l)} \phi^{(m_{inc})l}(t) + \psi_{m_{inc}+1}^{(l)} \phi^{(m_{inc}+1)l}(t) \right) + \\ & \sum_{l' \neq l} \left( \sum_{q=1}^Q I_q^{(l')} F_q^{ll'} \left( \psi_{m_{ll'}}^{(l)} \phi^{(m_{ll'})l}(t) + \psi_{m_{ll'}+1}^{(l)} \phi^{(m_{ll'}+1)l}(t) \right) \right) \end{aligned} \quad (5.43)$$

where  $F_q^{ll'}$  represents the scattered far-field of the set of current elements represented by  $\phi^{(q)l'}$  in group  $G_{l'}$  in the region of group  $G_l$ . Following Balanis in [13], p. 699, the scattered far-field may be expressed as

$$F_q^{ll'} = \chi \frac{\int_0^L \phi^{(q)l'}(x) e^{jkx \cos \phi_{ll'}} e^{-jk r_{ll'}} dx}{\sqrt{r_{ll'}}} \quad (5.44)$$

where  $\chi = \zeta_0 \sqrt{jk/8\pi} e^{-jk(L/2) \cos \phi_{ll'}}$ ,  $r_{ll'}$  is the distance between the centre of the group  $G_l$  and the centre of  $G_{l'}$ ,  $\phi_{ll'}$  is the angle subtended by the vector  $\mathbf{r}_{ll'}$  and the  $x$  axis and  $L$  is the length of the segment  $G_{l'}$ . The evaluation of  $F_q^{ll'}$  may be performed numerically or by using the ANIM approximations suggested in section

5.2. Equation (5.43) may be expressed in more compact form making use of matrix notation:

$$\begin{aligned}
 & -(\phi^{(1)l}(t), \phi^{(2)l}(t), \dots, \phi^{(Q)l}(t)) \begin{pmatrix} I_1^{(l)} \\ I_2^{(l)} \\ \cdot \\ \cdot \\ I_Q^{(l)} \end{pmatrix} = \\
 & -E_0 V_l (\phi^{(1)l}(t), \phi^{(2)l}(t), \dots, \phi^{(Q)l}(t)) \begin{pmatrix} 0 \\ \cdot \\ 0 \\ \psi_{m_{inc}}^{(l)} \\ \psi_{m_{inc}+1}^{(l)} \\ 0 \\ \cdot \\ 0 \end{pmatrix} + \\
 & (\phi^{(1)l}(t), \phi^{(2)l}(t), \dots, \phi^{(Q)l}(t)) \sum_{l' \neq l} \begin{pmatrix} 0 & 0 & \dots & 0 \\ & & \dots & \\ 0 & 0 & \dots & 0 \\ * & * & \dots & * \\ * & * & \dots & * \\ 0 & 0 & \dots & 0 \\ & & \dots & \\ 0 & 0 & \dots & 0 \end{pmatrix} \begin{pmatrix} I_1^{(l')} \\ I_2^{(l')} \\ \cdot \\ \cdot \\ I_Q^{(l')} \end{pmatrix} \quad (5.45)
 \end{aligned}$$

$$\begin{pmatrix} I_1^{(l)} \\ I_2^{(l)} \\ \cdot \\ \cdot \\ I_Q^{(l)} \end{pmatrix} + \sum_{l' \neq l} \begin{pmatrix} 0 & 0 & \cdots & 0 \\ & & \cdots & \\ 0 & 0 & \cdots & 0 \\ * & * & \cdots & * \\ * & * & \cdots & * \\ 0 & 0 & \cdots & 0 \\ & & \cdots & \\ 0 & 0 & \cdots & 0 \end{pmatrix} \begin{pmatrix} I_1^{(l')} \\ I_2^{(l')} \\ \cdot \\ \cdot \\ I_Q^{(l')} \end{pmatrix} = E_0 V_l \begin{pmatrix} 0 \\ \cdot \\ 0 \\ \psi_{m_{inc}}^{(l)} \\ \psi_{m_{inc}+1}^{(l)} \\ 0 \\ \cdot \\ 0 \end{pmatrix} \tag{5.46}$$

Thus

$$\mathbf{I}^{(l)} + \sum_{l' \neq l} \mathbf{F}^{ll'} \mathbf{I}^{(l')} = \mathbf{V}_{inc}^{(l)} \quad l, l' = 1 \cdots L \tag{5.47}$$

where

$$\mathbf{I}^{(l)} = \begin{pmatrix} I_1^{(l)} \\ I_2^{(l)} \\ \cdot \\ \cdot \\ I_Q^{(l)} \end{pmatrix} \quad l = 1 \cdots L \tag{5.48}$$

is the vector of unknown basis coefficients for the group  $G_l$ . The ultimate task is to determine these coefficients for all groups, i.e. for  $l = 1 \cdots L$ . (5.47) is a matrix equation with  $Q \times L$  equations. Specifically, (5.47) leads to the matrix equation

$$\mathbf{J} + \mathbf{FJ} = \mathbf{V}_{inc} \tag{5.49}$$

where

$$\mathbf{J} = \begin{pmatrix} \mathbf{I}^{(1)} \\ \mathbf{I}^{(2)} \\ \cdot \\ \cdot \\ \cdot \\ \mathbf{I}^{(L)} \end{pmatrix}, \quad (5.50)$$

$$\mathbf{V}_{inc} = \begin{pmatrix} \mathbf{V}_{inc}^{(1)} \\ \mathbf{V}_{inc}^{(2)} \\ \cdot \\ \cdot \\ \cdot \\ \mathbf{V}_{inc}^{(L)} \end{pmatrix} \quad (5.51)$$

and  $\mathbf{F}$  is the matrix made of blocks  $\mathbf{F}^{ll'}$ , where  $\mathbf{F}^{ll} = 0, \forall l$  and the block associated with the mutual interaction  $(l, l')$  is given by the  $Q \times Q$  matrix

$$\mathbf{F}^{ll'} = \begin{pmatrix} 0 & 0 & \cdots & 0 \\ & & \cdots & \\ 0 & 0 & \cdots & 0 \\ * & * & \cdots & * \\ * & * & \cdots & * \\ 0 & 0 & \cdots & 0 \\ & & \cdots & \\ 0 & 0 & \cdots & 0 \end{pmatrix} \quad (5.52)$$

The symbols \* represent elements of the rows of  $\mathbf{F}^{ll'}$  which are non-zero. The group  $G_{l'}$  radiates a plane wave over the group  $G_l$ . With the aid of interpolating factors (4.31), this plane wave may be approximated with the sum of two plane waves, which, in turn, excite two basis functions on the group  $G_l$ :  $\phi^{(m_{ll'})^l}$  and  $\phi^{(m_{ll'}+1)^l}$ . This is the reason why *only two out of  $Q$  rows of the matrix  $\mathbf{F}^{ll'}$  are non-null*. Each

element of these rows ( $m_{l'}$  and  $m_{l'} + 1$ ) represents mathematically the contribution of each basis function excited on  $G_{l'}$  to the evaluation of the far-field scattered by  $G_{l'}$  over  $G_l$ . Thus, the  $n$ -th element ( $m_{l'}, n$ ) of the row  $m_{l'}$  is given by

$$\mathbf{F}_{(m_{l'}, n)}^{l'} = \chi \frac{\int_0^L \phi^{(n)l'}(x) e^{jkx \cos \phi_{l'}} dx e^{-jkr_{l'}}}{\sqrt{r_{l'}}} \psi_{m_{l'}}^{(l)} \tag{5.53}$$

if the basis function  $\phi^{(n)}$  is excited on  $G_{l'}$ , otherwise  $\mathbf{F}_{(m_{l'}, n)}^{l'} = 0$ . Hence even the rows may be non-dense in principle. The known vector is due to the incident field and is given by

$$\mathbf{V}_{inc}^{(l)} = E_0 V_l \begin{pmatrix} 0 \\ \cdot \\ 0 \\ \psi_{m_{inc}}^{(l)} \\ \psi_{m_{inc}+1}^{(l)} \\ 0 \\ \cdot \\ 0 \end{pmatrix} \tag{5.54}$$

Now, observe that the vector of unknown basis coefficients must be determined using the MoM-CG scheme. The number of these coefficients is  $Q$  for each group  $G_l$ ,  $l = 1 \dots L$ . It might appear that the problem has numerical complexity  $\mathcal{O}((Q \times L)^2)$ . However, upon inspection of (5.52), it has been observed that each block (of size  $Q \times Q$ ) of the matrix is highly sparse. Each block is sparse due to the fact that only two basis functions are excited on each group  $G_l$  by the set of basis functions excited in  $G_{l'}$ . In the implementation of the matrix form of TIM, it makes computational sense, therefore, to carry out a preprocessing step, identifying the basis currents that will be needed on each group and then one may work solely in terms of this reduced set. Many redundant calculations involving non-excited basis currents can thus be eliminated. The entire procedure is geometry-driven and delivers a compression of the operation which reduces complexity. To illustrate the complexity reduction

achieved by the matrix formulation of TIM/ANIM, refer to Fig. 5.8, where a scatterer made of four PEC segments of equal length  $L = 100\lambda$  is illuminated by a plane wave. By geometric inspection, it is evident that for each group, say  $G_l$ ,  $l = 1 \dots 4$ , only a few basis functions are excited out of the postulated  $Q$  functions. It is hence possible to set up the matrix equation (5.49) deleting a priori all the redundant equations (of the kind  $0 = 0$ ). For the example of Fig. 5.8, applying the typical MoM procedure to discretise the EFIE a dense matrix of  $N^2 \approx (3000)^2$  complex numbers is produced. Its solution by CG technique requires  $\mathcal{O}(N^2)$  operations. By applying a matrix formulation of TIM/ANIM, the initial matrix of (5.49) is  $\mathcal{O}((Q \times L)^2 = (360 \times 4)^2)$ , but after the preprocessing step one would obtain a sparse matrix of  $\mathcal{O}((30)^2)$ , as illustrated in Fig. 5.9. The storage complexity reduces by a factor of 10000.

## 5.5 Application of TIM/ANIM matrix formulation to electromagnetic scattering from periodic surfaces

The matrix formulation derived in the previous section may be extended to the problem of electromagnetic scattering from periodic surfaces [71]. Periodic scatterers find application as electromagnetic filters and polarisers. The problem tackled in this section is  $TM_z$  scattering from a PEC half-space having a periodic surface. The geometry is illustrated in Fig. 5.10. The typical approach to this class of problems is to restrict the computational domain to one period of the structure. As given in [21], chapter 7, the electric current density  $J_z(x, y)$  located on the periodic surface satisfies the so called Floquet's condition:

$$J_z(x + a, y) = J_z(x, y)e^{-jk_x a} \tag{5.55}$$

where  $a$  is the period of the structure and

$$k_x = k \cos \theta \tag{5.56}$$



where  $\theta$  is the angle of incidence of the  $TM_z$  plane wave illustrated in Fig. 5.10. As a consequence of (5.55), it is possible to reduce the domain of the EFIE to a single period. The procedure is described in detail in [21], chapter 7. Here it suffices to say that to reduce the domain of the integral equation to a single period, the periodic Green's function must be introduced. Given two current elements,  $m$  and  $n_0$ , the periodic Green's function takes into account the interaction of element  $n_0$  and its periodically shifted versions, say  $n_p$  ( $p = -\infty \cdots -1, 1 \cdots \infty$ ), and the element  $m$ . Referring to Fig. 5.11, the meaning of the periodic Green's functions becomes clear. This function accounts for all interactions between  $n_p$  and  $m$ , with  $p = -\infty \cdots \infty$ . Specifically, the periodic Green's function has the expression

$$\tilde{G}(\mathbf{r}, \mathbf{r}') = \sum_{p=-\infty}^{\infty} H_0^{(2)}(k|\mathbf{r} - \mathbf{r}'|) e^{-jk_x p a} \quad (5.57)$$

where  $a$  is the period of the structure. Each group of the unit cell is illuminated by the plane waves radiated by all the other groups of the unit cell itself and the other cells. Referring to Fig. 5.12 for example, the group  $G_l$  is illuminated by the fields emanating from the centres of groups  $G_{l_p}$ , with  $p = -2, -1, 1, 2$  and from all other periodically shifted versions of  $G_{l_0}$ , which are not illustrated for the sake of simplicity. These plane waves, in turn, excite basis functions over  $G_l$ , such as those described in the previous section, i.e.  $\phi^{(q)l}$ , satisfying the discretised EFIE (4.32). The matrix equation for the unknown coefficients of the basis functions excited on each segment of the unit cell may be set up, following the approach described in the previous section.

To clarify the method here proposed, the periodic structure having the unit cell illustrated in Fig. 5.13 is now considered. The periodic surface has a period  $a = 200\lambda$ , and  $h = 1\lambda$ . A  $TM_z$  plane wave illuminates the scatterer with an angle of incidence  $\theta = 358$  degrees. The unit cell, for this example, is made of two groups of current elements. Each of these groups is illuminated by the other group of the unit cell and all the periodic shifted versions of the unit cell itself. For this example, the number of shifted periods considered is  $P = 32$  in the directions  $x < 0$  and

$x > a$ . The TIM matrix was set up for this problem and successively inverted by the CG algorithm. The current distribution on each cell was hence derived using (5.55). The far-field pattern at sampled angles lying on a circle located on the half-space  $y > 0$  centred at the point  $(x, y) = (a/2, 0)$  was evaluated and compared with a reference solution obtained using a moment method scheme with pulse basis functions with an interval width of  $\lambda/8$ . Both results are illustrated in Fig. 5.14. A satisfactory agreement between the field amplitudes may be noted at the peaks of the patterns, specifically along the *specular* and *backward* scattering directions. It is evident, however, that the TIM results present a non-smooth behaviour in contrast to the exact solution. The reason of the presence of the error in the TIM results of Fig. 5.14 is found in the fact that the near-field calculations, using TIM, are evaluated in an approximated fashion, using FAFFA. This issue was discussed in section 4.2. Indeed, by evaluating the near-field interaction exactly, better results may be achieved. Fig. 5.15 shows the result obtained using a TIM procedure in which the near-field interactions are evaluated exactly, using a MoM scheme with pulse basis functions with interval width of  $\lambda/8$ . The TIM solution is highly satisfactory and exhibits slightly non-smooth behaviour, due to the fact that only the near-neighbour interactions were evaluated exactly, i.e. a residual error is still introduced by FAFFA. The application of FAFFA to the near-field is however necessary to retain the basis function approach presented in section 5.4. It must be recalled that, using this approach, the current on each group is expressed as a superposition of reference currents excited by plane waves. If one evaluates the near-field related to a group exactly, one inevitably assumes that the field illuminating the group is not a set of plane waves, because the near-field is not a plane wave. A heuristic way of retaining the plane wave interaction model for near neighbours may be proposed referring to Fig. 5.16, where two near groups of current elements are illustrated. To evaluate the field due to  $G_n$  on  $G_m$  a buffer zone is introduced and the two groups  $G_{n-}$  and  $G_{m+}$  are considered. Specifically,  $G_{n-}$  is the group  $G_n$  minus the final part NF.  $G_{m+}$  is the group  $G_m$  plus the buffer zone that *substitutes* the final part of  $G_n$  (NF) for the field calculation. The electric

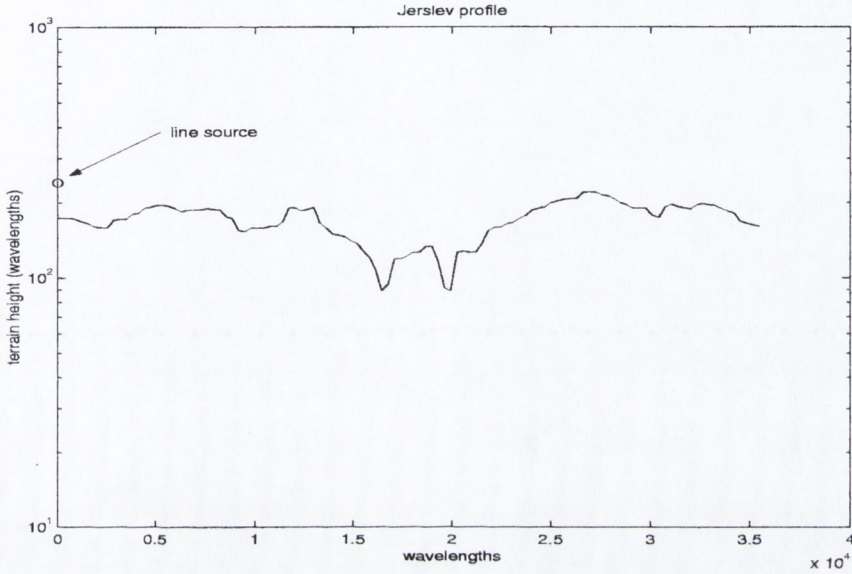
current due to the field illuminating  $G_m$  and radiated by  $G_n$  is then evaluated using FAFFA. The current residing on  $G_m$  is the current due to the plane wave radiated from  $G_{n-}$  to the enlarged group  $G_{m+}$ . The result of the introduction of the buffer zone in the TIM matrix method is shown in Fig. 5.17, where the far-field patterns discussed in Fig. 5.14 are illustrated. The TIM solution offers now a smoother behaviour when compared with the TIM solution of Fig. 5.14 and the agreement with the reference solution is now of the same order of the agreement obtained in the case of exact near-field calculations, illustrated in Fig. 5.15. The heuristic technique here proposed is only a first attempt to express near-field interactions in terms of plane waves. The author hopes that future research will be addressed to improve the technique introduced.

## 5.6 Summary

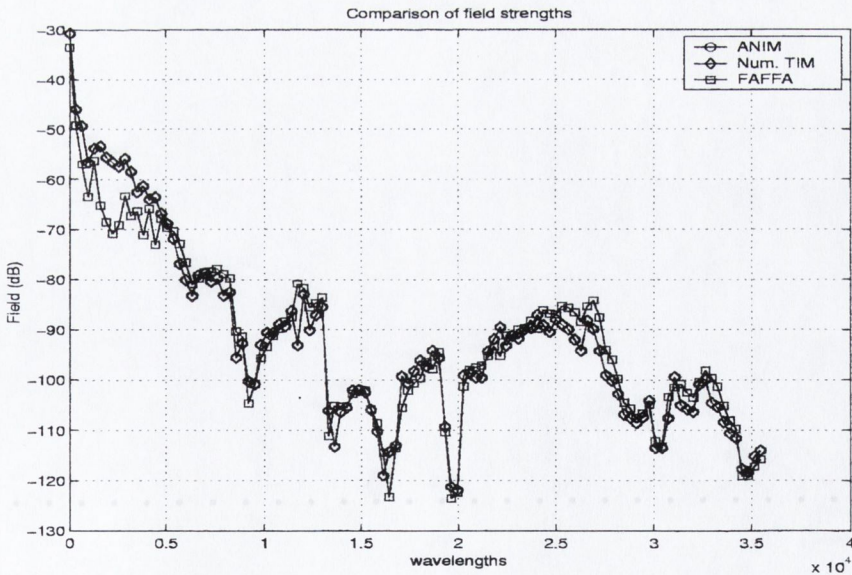
This chapter presented three enhancements to TIM. The first was the Analytical Interaction Method (ANIM), which derives from TIM. In chapter 4 it was shown that TIM achieves substantial computational savings allowing the interactions between portions of the scatterer to be written in terms of tabulated calculations. These tables, however, depend on the frequency of the incident radiation and on the size of the portions of the scatterer, i.e. length of PEC segments. The ANIM was presented to overcome the necessity of storing TIM tables in order to render the original method more flexible with respect to frequency. Specifically, it was seen that the recurring problem of electromagnetic scattering by a PEC segment may be solved analytically introducing a reasonable approximation. It was verified that if a segment is many wavelengths long and the incidence is at grazing angles, the electric current density located on the segment may be approximated with the current induced on an half-plane illuminated by a plane wave. The approximated electric current was analytically integrated using Fresnel integrals. The result is the electric far-field scattered by a PEC segment illuminated at grazing angles by a plane-wave. This expression was then used to replace the TIM tables. The

advantages of this substitution were listed. Numerical results were presented to demonstrate the successful application of ANIM to the problem of UHF propagation over irregular terrain. Specifically, the ANIM was compared with the FAFFA and the TIM both described in chapter 4 and it was shown that the final results are highly satisfactory. Moreover, a comparison between ANIM and exact (reference) results was illustrated to emphasise the massive computational savings achieved by the new method. Also, it was shown that ANIM results agree with measurements for two specific examples. In chapter D of Appendix a mathematical extension of ANIM in three dimensions is proposed using the Physical Optics approximation.

The matrix formulation of TIM/ANIM was also presented. It was shown, by geometric arguments, that the TIM matrix is very sparse and may be rearranged in order to reduce the storage of redundant (zero) elements. An example of storage allocation savings for a simple problem was given. Application of the TIM/ANIM matrix formulation to the problem of electromagnetic scattering by finite periodic structures was discussed. Numerical results were provided and commented for this case.



(a)



(b)

Figure 5.3: Field strength over Jerslev profile. The terrain extension over the  $x$  direction is of the order of tens of thousands the incident wavelength: terrain profile, line source location and simulation results (field strength at 2.4m above the terrain).

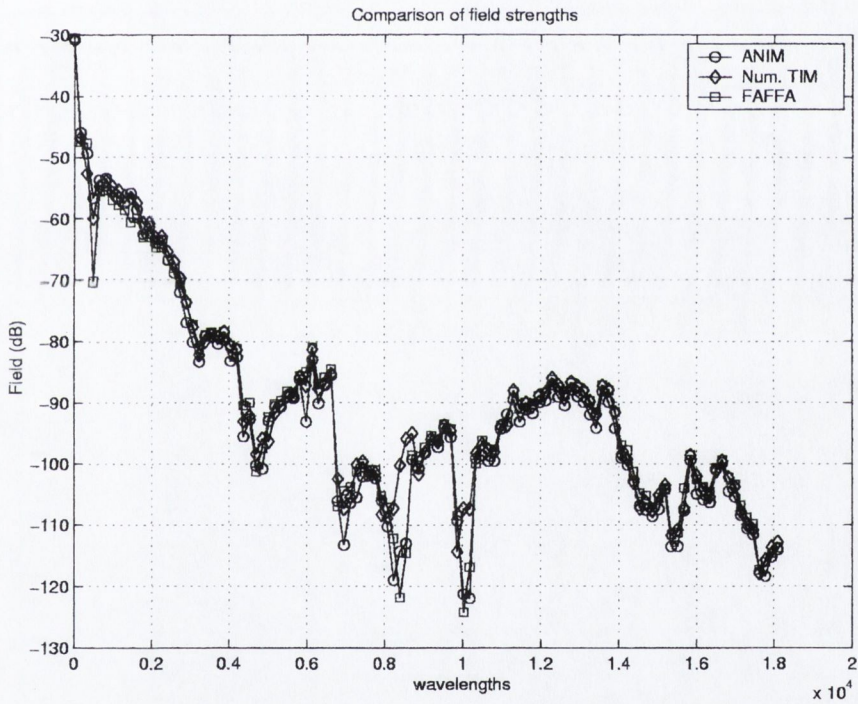


Figure 5.4: Field strength over Jerslev profile. The terrain extension over the  $x$  direction is of the order of tens of thousands the incident wavelength: simulation results (field strength at 2.4m above the terrain).

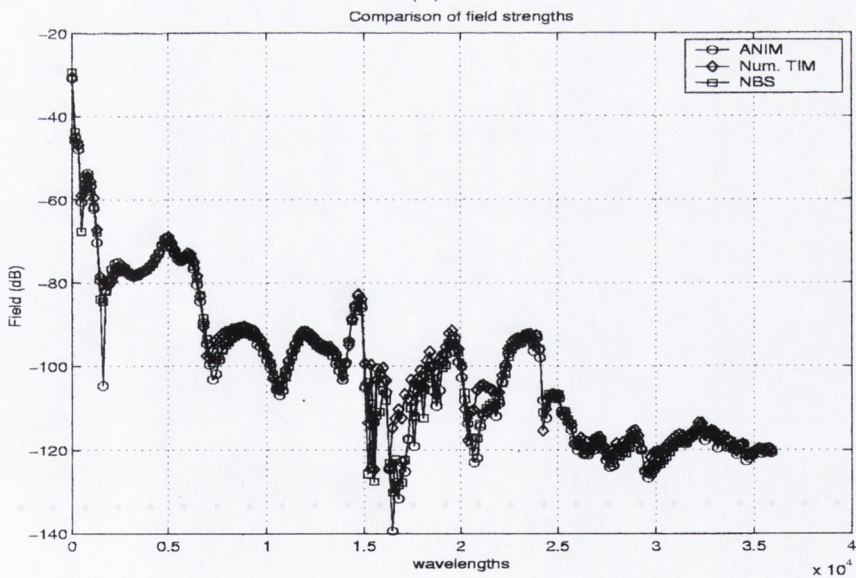
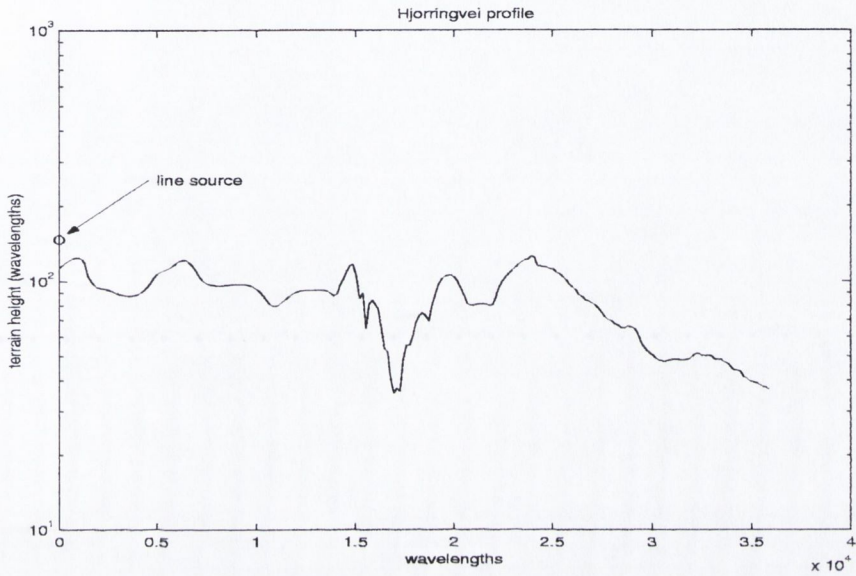


Figure 5.5: Field strength over Hjorringvei profile. The terrain extension over the  $x$  direction is of the order of tens of thousands the incident wavelength: terrain profile, line source location and simulation results (field strength at  $2.4m$  above the terrain).

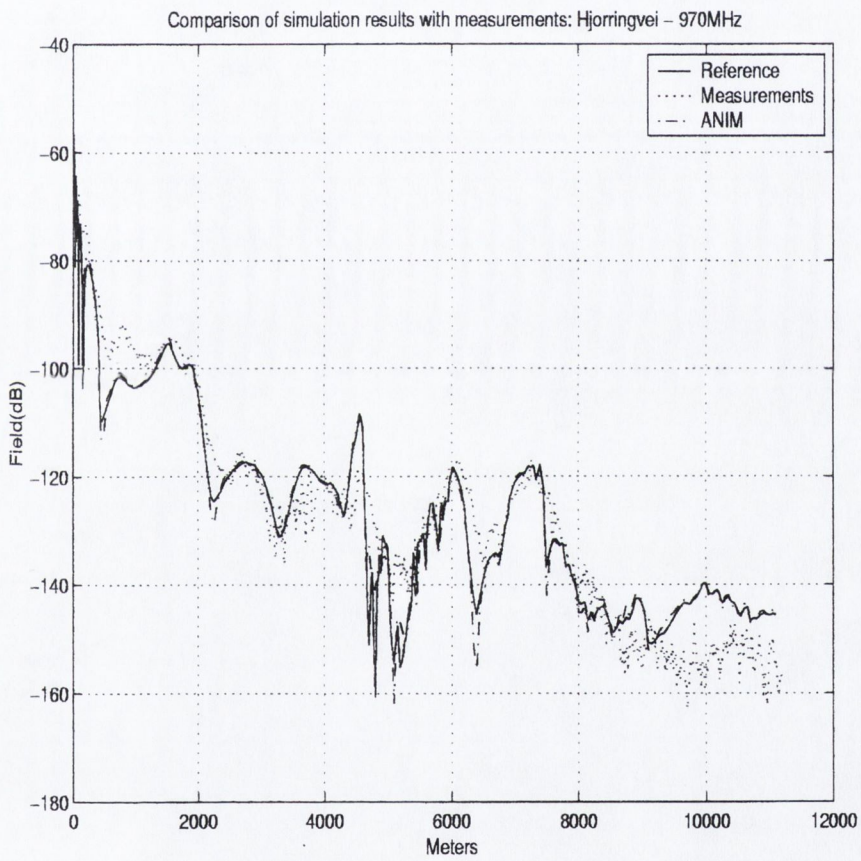


Figure 5.6: Field strength over Hjorringvei terrain profile.



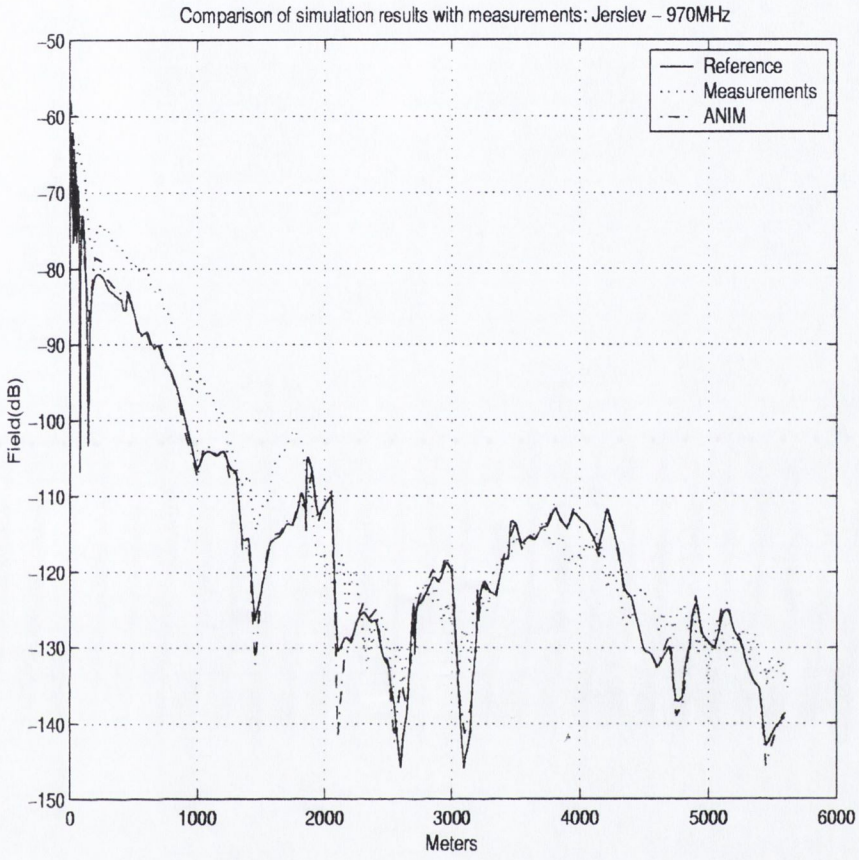


Figure 5.7: Field strength over Jerslev terrain profile.

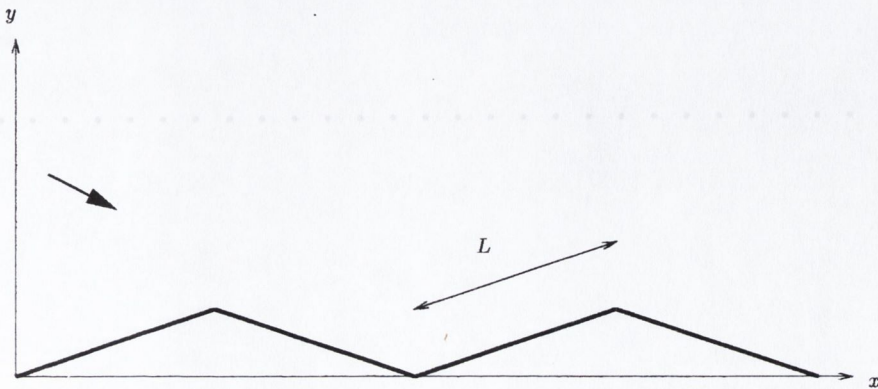


Figure 5.8: Simple scatterer geometry for the application of matrix formulation of TIM/ANIM.

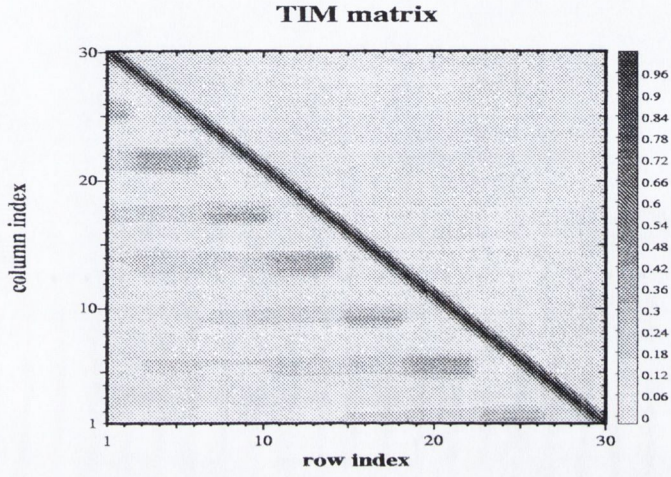


Figure 5.9: Sparse matrix obtained using TIM for the example of Fig. 5.8.

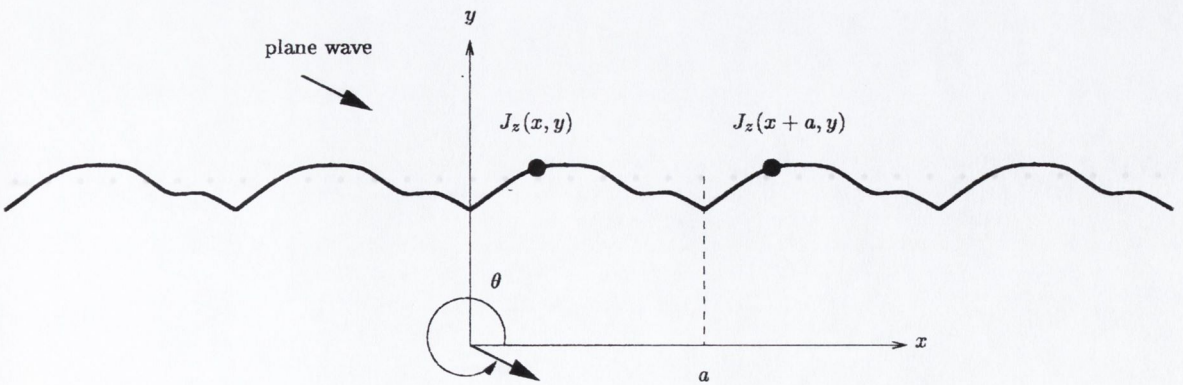


Figure 5.10:  $TM_z$  plane wave incident on a periodic surface with period  $a$ .

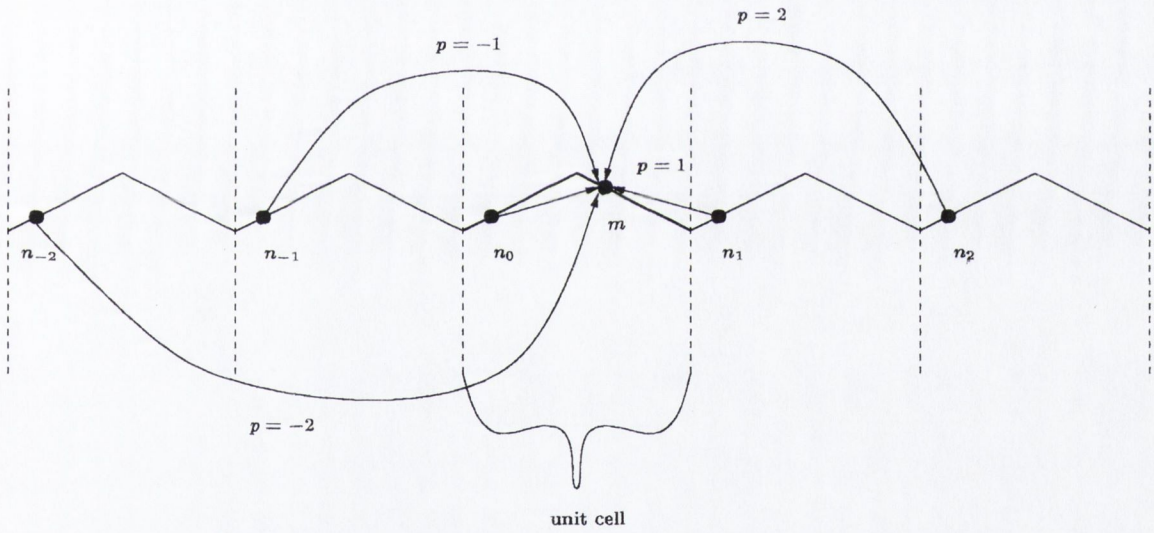
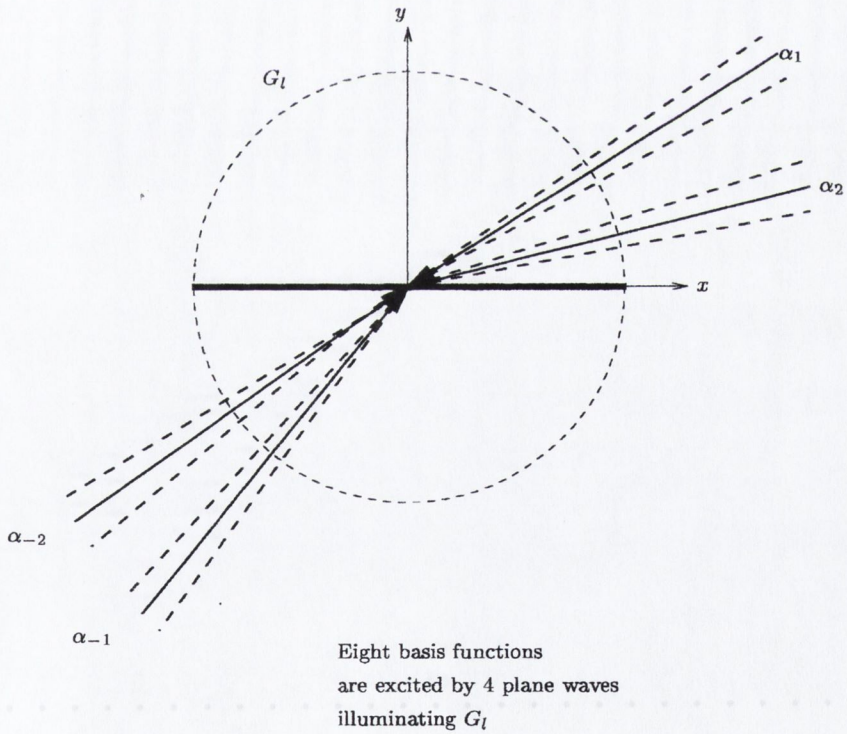
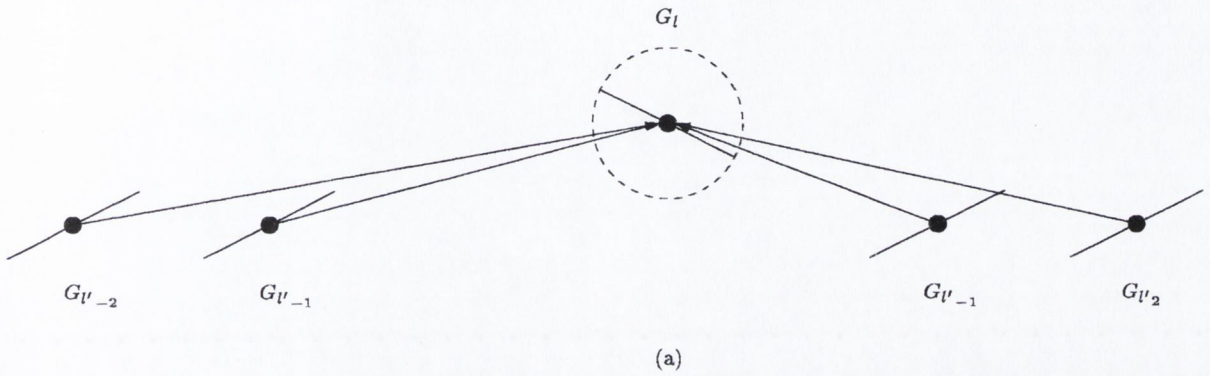


Figure 5.11: Physical meaning of the periodic Green's function: the function describes the interaction between the observation point  $m$  and all the periodic shifted versions of  $n_0$ , which are defined as  $n_p$ , with  $p = -\infty \cdots -1, 1, \infty$ .



(b)

Figure 5.12: Plane waves due to periodic shifted versions of  $G_{l'}$  illuminating the group  $G_l$ . In the example here illustrated, four different angles of incidence are counted which, in turn, excite eight different basis functions. These are the fields radiated by groups  $G_{l'p}$ , with  $p = -2, -1, 1, 2$ .

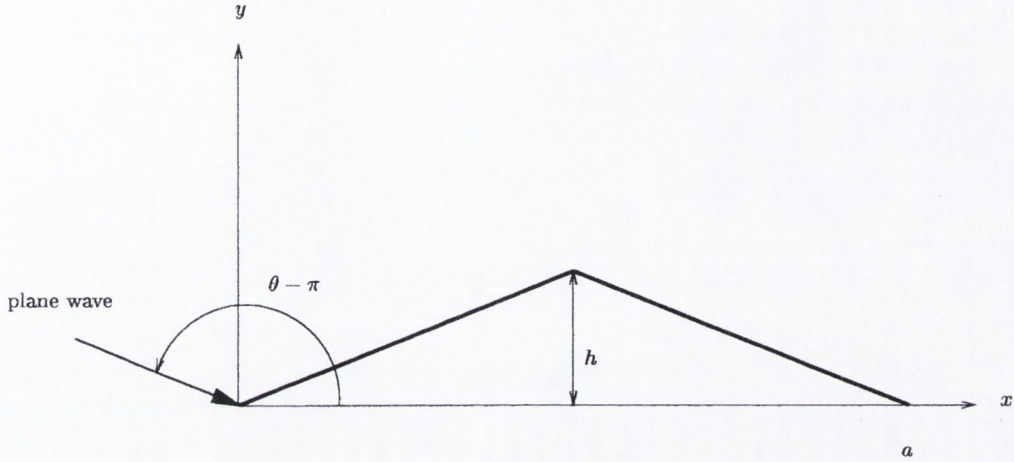


Figure 5.13: Unit cell of a periodic scatterer illuminated by a plane wave.

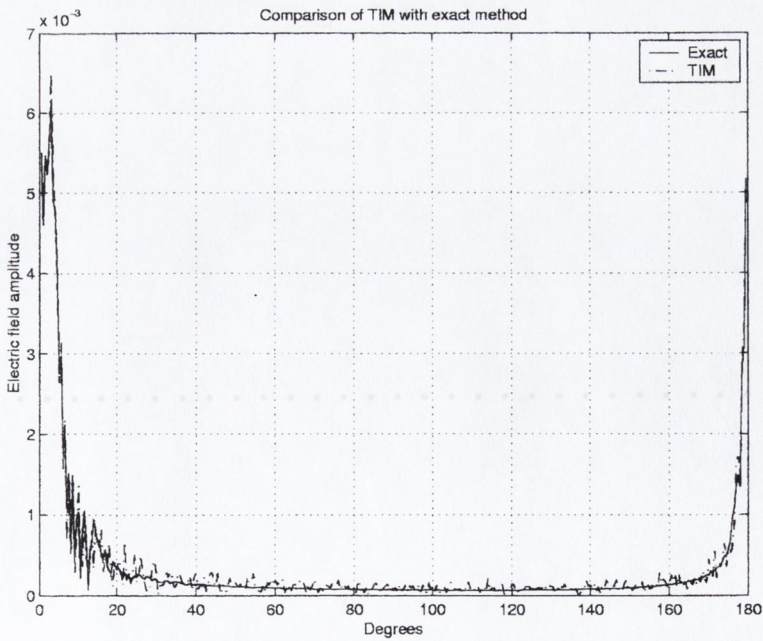


Figure 5.14: Comparison of the far-field patterns for the problem illustrated in Fig. 5.13: the TIM differs from the exact solution for its non-smoothness.

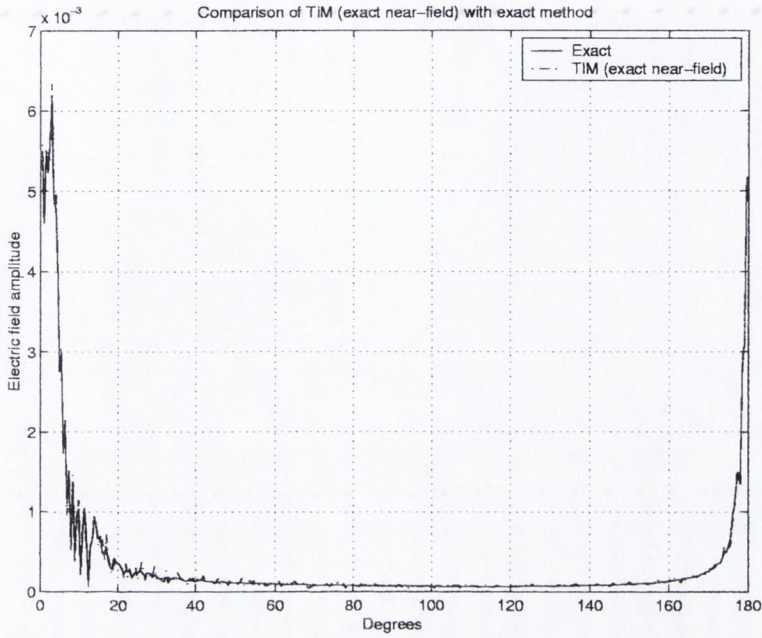


Figure 5.15: Comparison of the far-field patterns for the problem illustrated in Fig. 5.13: exact calculation of the near-field interaction renders the TIM solution smoother with respect to the result shown in Fig. 5.14.

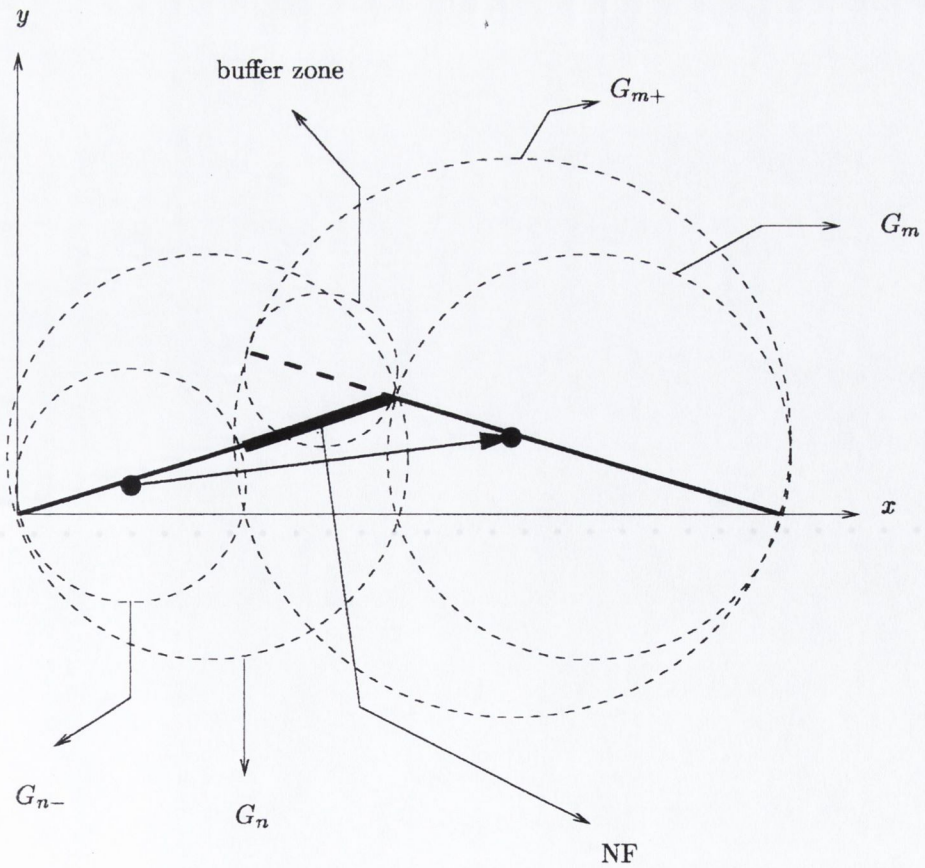


Figure 5.16: Introduction of the buffer zone to allow the use of FAFFA between two near neighbours.

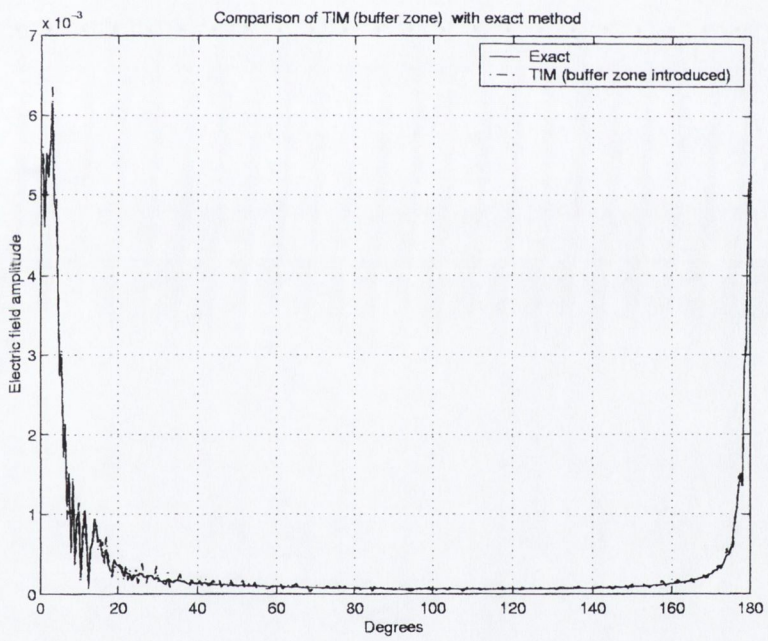


Figure 5.17: Far-field patterns obtained using a buffer-zone approach.

---

## VALUATION OF EFIE MATRIX TERMS IN THE RWG APPROACH

---

This chapter is related to the discretisation of the EFIE as described in section 2.6, specifically the numerical evaluation of the self-terms of the impedance matrix. This operation is critical and must always be performed. Section 6.1 presents the typical approach to the evaluation of impedance matrix terms of the discretised EFIE in the three-dimensional case, using the RWG basis functions defined in section 2.6.1. It is shown that the numerical evaluation of these terms involves surface integrals defined on the triangular domains of the RWG functions. The numerical evaluation of the integrals where the observation point belongs to the same domain as the basis functions is carried out in two steps, as described in section 6.1.2. In section 6.2 the author presents a novel numerical technique which permits the evaluation of the integrals referred to in section 6.1.2 in a fast and accurate fashion. The novel method represents an efficient alternative to the common approaches described in the literature. Numerical results are provided in section 6.3 to demonstrate the validity of the new method.

### 6.1 Calculation of the impedance matrix elements: the typical approach

In the RWG approach, the EFIE is discretised as discussed in 2.6.1. The resulting matrix equation (2.78) has been derived in section 2.6. A typical element of the impedance matrix  $Z_{mn}$  (2.79) represents the field radiated by the basis function  $\mathbf{f}_n$  over the domain where the basis function  $\mathbf{f}_m$  is defined. Specifically, the field radiated by the basis function  $\mathbf{f}_n$  is an integral over the domain  $T_n^+ \cup T_n^-$ . Testing this field (see section 2.6.2) involves performing a surface integral of the field over the domain  $T_m^+ \cup T_m^-$ . Basically, the evaluation of the matrix term involves four



terms due to the possible combinations of the pairs:  $(T_n^+, T_n^-)$  and  $(T_m^+, T_m^-)$ . It is evident that a correct evaluation of those elements is critical for the accurate solution of the integral equation. Consider a pair of triangles, say  $T_n^+$  and  $T_m^+$ . To

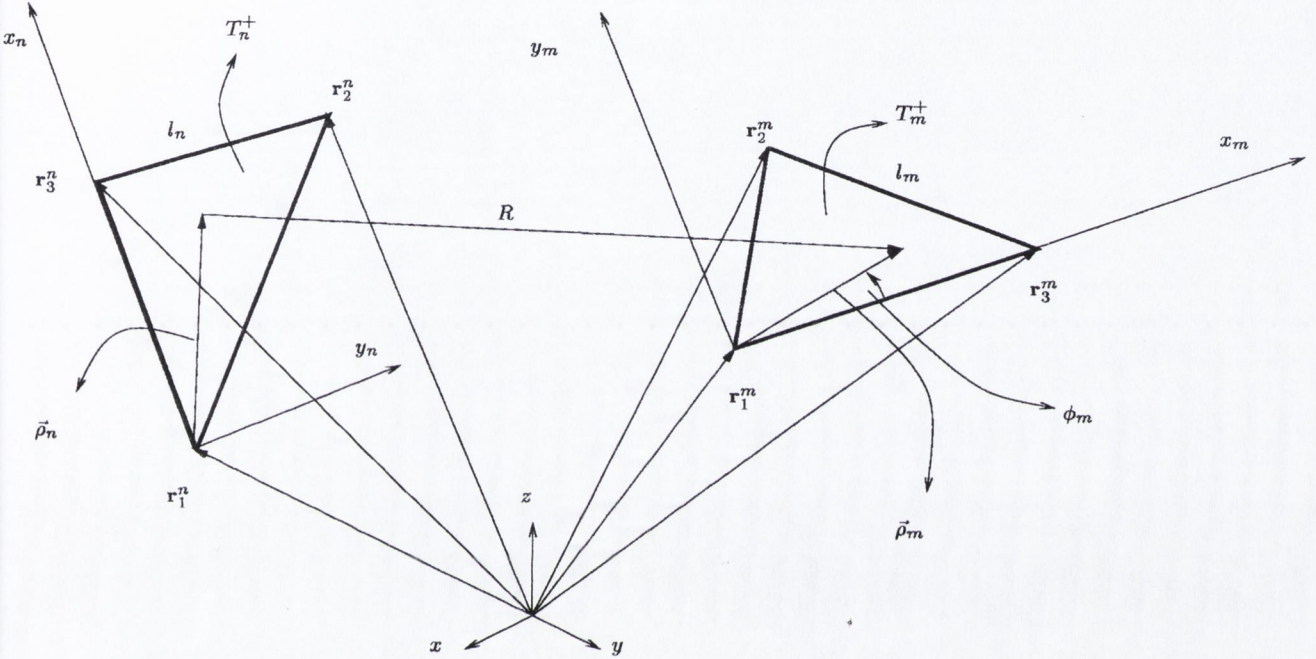


Figure 6.1: Geometry of the impedance term calculation when  $m \neq n$ : the current associated with the edge  $l_n$  radiates over the domain  $T_m^+$ . In the figure, only the interaction between the domains  $T_n^+$  and  $T_m^+$  is displayed. Each triangle is characterised by a local planar coordinate system, such as  $(x_n, y_n)$  and  $(x_m, y_m)$ .

evaluate the field due to the  $n$ -th current source at the triangle  $T_m^+$ , in order to compute the matrix element  $Z_{mn}$ , the following integral must be calculated

$$\begin{aligned} & \frac{-j\omega\mu_0}{4\pi} \int_{T_m^+} \frac{l_m}{2A_m^+} \vec{\rho}_m \cdot \left( \int_{T_n^+} \frac{l_n}{2A_n^+} \vec{\rho}_n \frac{e^{-jkR}}{R} dS' \right) dS + \\ & \frac{-1}{j4\omega\pi\epsilon_0} \int_{T_m^+} \nabla_S \cdot \left( \frac{l_m}{2A_m^+} \vec{\rho}_m \right) \left( \int_{T_n^+} \nabla'_S \cdot \left( \frac{l_n}{2A_n^+} \vec{\rho}_n \right) \frac{e^{-jkR}}{R} dS' \right) dS \end{aligned} \quad (6.1)$$

### 6.1.1 Numerical evaluation of integrals involving different triangles

Referring to Fig. 6.1, suppose now that  $m \neq n$ , i.e. the two triangles are different. Then it is possible to write (see [33])

$$\int_{T_n^+} \frac{l_n}{2A_n^+} \vec{\rho}_n \frac{e^{-jkR}}{R} dS' = l_n \left( \mathbf{r}_1^n \mathcal{I}_\xi^n + \mathbf{r}_2^n \mathcal{I}_\eta^n + \mathbf{r}_3^n \mathcal{I}_\zeta^n - \mathbf{r}_1^n \mathcal{I}^n \right) \quad (6.2)$$

where

$$\mathcal{I}_\xi^n = \int_0^1 \int_0^{1-\eta} \xi \frac{e^{-jkR}}{R} d\xi d\eta \quad (6.3)$$

$$\mathcal{I}_\eta^n = \int_0^1 \int_0^{1-\eta} \eta \frac{e^{-jkR}}{R} d\xi d\eta \quad (6.4)$$

$$\mathcal{I}^n = \int_0^1 \int_0^{1-\eta} \frac{e^{-jkR}}{R} d\xi d\eta \quad (6.5)$$

with

$$\mathcal{I}^n = \mathcal{I}_\xi^n + \mathcal{I}_\eta^n + \mathcal{I}_\zeta^n \quad (6.6)$$

and

$$\int_{T_m^+} \frac{l_n e^{-jkR}}{A_n^+ R} dS' = l_n \mathcal{I}^n \quad (6.7)$$

Using (2.67), (6.1) can be expressed as

$$\begin{aligned} \frac{-j\omega\mu_0}{4\pi} \int_{T_m^+} \frac{l_m}{2A_m^+} \vec{\rho}_m \cdot l_n \left( \mathbf{r}_1^n \mathcal{I}_\xi^n + \mathbf{r}_2^n \mathcal{I}_\eta^n + \mathbf{r}_3^n \mathcal{I}_\zeta^n - \mathbf{r}_1^n \mathcal{I}^n \right) dS + \\ \frac{-1}{j4\omega\pi\epsilon_0} \int_{T_m^+} \nabla_S \cdot \left( \frac{l_m}{2A_m^+} \vec{\rho}_m \right) l_n \mathcal{I}^n dS \end{aligned} \quad (6.8)$$

Now, the integrals in (6.3) - (6.6) can be evaluated numerically through an optimised quadrature rule given in [72] and hence (6.8) can be evaluated. For example, let

$$\mathbf{v}_n = l_n \left( \mathbf{r}_1^n \mathcal{I}_\xi^n + \mathbf{r}_2^n \mathcal{I}_\eta^n + \mathbf{r}_3^n \mathcal{I}_\zeta^n - \mathbf{r}_1^n \mathcal{I}^n \right) \quad (6.9)$$

then the first integral in (6.8) becomes

$$\frac{-j\omega\mu_0}{4\pi} \int_{T_m^+} \frac{l_m}{2A_m^+} \vec{\rho}_m \cdot \mathbf{v}_n dS \quad (6.10)$$

which can be performed by of a change of coordinate system on the plane of the triangle  $T_m^+$ . Referring to the polar system  $(\rho_m, \phi_m)$  illustrated in Fig. 6.1, if

$(\hat{\mathbf{x}}_m, \hat{\mathbf{y}}_m)$  are the unit vectors associated with the rectangular coordinate system defined in the same plane as  $T_m^+$ , then the vector  $\vec{\rho}_m$  can be written as

$$\vec{\rho}_m = \rho_m \cos \phi_m \hat{\mathbf{x}}_m + \rho_m \sin \phi_m \hat{\mathbf{y}}_m \tag{6.11}$$

where  $\rho_m$  and  $\phi_m$  are the polar coordinates related to  $(\hat{\mathbf{x}}_m, \hat{\mathbf{y}}_m)$ . In this way, the integral evaluates to

$$\frac{-j\omega\mu_0}{4\pi} \frac{l_m}{2A_m^+} \int_{\phi_m^3}^{\phi_m^2} d\phi_m \int_0^{l_m(\phi_m)} \left( (\mathbf{v}_n \cdot \hat{\mathbf{x}}_m) \rho_m \cos \phi_m + (\mathbf{v}_n \cdot \hat{\mathbf{y}}_m) \rho_m \sin \phi_m \right) \rho_m d\rho_m \tag{6.12}$$

where  $\phi_m^3$  and  $\phi_m^2$  are the polar angles of the vertices  $\mathbf{r}_3^m$  and  $\mathbf{r}_2^m$ ,  $l_m(\phi_m)$  is the equation of the segment  $l_m$  with respect to the angle  $\phi$ . Such integral is now amenable to a double quadrature rule, as described in [11]. The same procedure can obviously be applied to the second integral of (6.8). Usually, however, the integration over the domain  $T_m^+$  is carried out using a single-point quadrature rule (with the average value of the function to be integrated assumed to be the value of the function at the centroid of  $T_m^+$ ).

### 6.1.2 Numerical evaluation of integrals involving the same triangle

In the case of identical triangular domains, i.e.  $T_m^+ = T_m^- = T$ , the numerical evaluation of the integrals (6.3) - (6.6) is a delicate task to accomplish because of the singular behaviour of the Green's function on  $T$ . The integrals are, however, finite. The issue here encountered is the same as the one arising in the evaluation of the elementary one-dimensional integral

$$\int_0^1 \frac{1}{\sqrt{x}} dx \tag{6.13}$$

which is finite (its value being 2) although  $(1/\sqrt{x}) \rightarrow \infty$  as  $x \rightarrow 0$ . A numerical evaluation of (6.13) can be highly unreliable. The usual approach to overcome the difficulty inherent the calculation of integrals (6.3) - (6.6) is to split the integrand

into the sum of two functions: one singular part, which can be integrated analytically, and the remaining part, non singular, which can be treated numerically without convergence problems. Thus, (6.3), for example, becomes

$$\mathcal{I}_\xi^n = \int_0^1 \int_0^{1-\eta} \xi \frac{e^{-jkR} - 1}{R} d\xi d\eta + \int_0^1 \int_0^{1-\eta} \xi \frac{1}{R} d\xi d\eta = \widehat{\mathcal{I}}_\xi^n + \widetilde{\mathcal{I}}_\xi^n \quad (6.14)$$

where  $\widehat{\mathcal{I}}_\xi^n$  is the integral evaluated numerically and  $\widetilde{\mathcal{I}}_\xi^n$  is the integral evaluated analytically. This approach has been thoroughly described in [73] and by Graglia in [74], where kernels with singularity of order  $\nabla(R^{-1})$  are also dealt with. Analytical formulae for the singular field contributions of linear source distributions on triangular domains were presented in [75], too. Alternatively, a simpler expression of the integrals evaluated analytically may be obtained and is now presented.

Referring to (6.1), given a triangular patch  $T$ , the following integrals must be evaluated

$$\int_T \vec{\rho} \frac{e^{-jkR}}{R} dS' \quad (6.15)$$

$$\int_T \frac{e^{-jkR}}{R} dS' \quad (6.16)$$

where the subscript related to the identity of the triangular patch has been omitted, without loss of generality. Hence, using a more compact expression, it is of interest to evaluate the integral

$$\mathcal{I} = \int_T \begin{pmatrix} 1 \\ x' \\ y' \end{pmatrix} \frac{e^{-jkR}}{R} dS' \quad (6.17)$$

where  $R$  is the distance between the integration point  $(x', y')$  and the observation point  $(x_0, y_0) \in T$ . For completeness, observe that the following series of inequalities holds

$$\left| \int_T \begin{pmatrix} 1 \\ x' \\ y' \end{pmatrix} \frac{e^{-jkR}}{R} dS' \right| < \int_T \left| \begin{pmatrix} 1 \\ x' \\ y' \end{pmatrix} \frac{1}{R} \right| dS' < \int_{c_{max}} \begin{pmatrix} 1 \\ \rho \\ \rho \end{pmatrix} d\rho d\phi < \infty \quad (6.18)$$

where  $C_{max}$  is the circular domain centred at  $(x_0, y_0)$  and having radius equal to the maximum distance between any of the three vertices of  $T$  and the observation point itself ( $T \subset C_{max}$ ). Hence,  $\mathcal{I}$  exists and is finite, however care must be taken with its numerical evaluation, due to the presence of the singularity in the integrand. The triangular domain  $T$  may be decomposed as the sum of three triangular domains:  $T_1, T_2$  and  $T_3$  as illustrated in Fig. 6.2. Thus the integral to be evaluated analytically becomes

$$\mathcal{I}_{anal} = \int_{T_1+T_2+T_3} \begin{pmatrix} 1 \\ x' \\ y' \end{pmatrix} \frac{1}{R} dx' dy' \tag{6.19}$$

Referring to the polar coordinate system centred at the observation point  $(x_0, y_0)$  with the polar axis  $x_a$  parallel to the  $x$  axis<sup>1</sup> as illustrated in Fig. 6.2, the integral over a single sub-domain  $T_i, i = 1, 2, 3$ , is given by

$$\int_{T_i} \begin{pmatrix} 1 \\ x' \\ y' \end{pmatrix} \frac{1}{R} dx' dy' = \int_{\phi_1}^{\phi_2} d\phi \int_0^{r(\phi)} \begin{pmatrix} 1 \\ \rho \cos \phi + x_0 \\ \rho \sin \phi + y_0 \end{pmatrix} \frac{1}{\rho} \rho d\rho \tag{6.20}$$

which evaluates to

$$\int_{\phi_1}^{\phi_2} \begin{pmatrix} r(\phi) \\ \frac{r^2(\phi)}{2} \cos \phi + x_0 r(\phi) \\ \frac{r^2(\phi)}{2} \sin \phi + y_0 r(\phi) \end{pmatrix} d\phi \tag{6.21}$$

The function  $r(\phi)$  has been introduced. For each sub-triangle  $T_i, i = 1, 2, 3$ , it represents the equation in polar coordinates satisfied by the side that the sub-triangle has in common with the triangle  $T$ . Generally the function  $r(\phi)$  has the expression

$$r(\phi) = \frac{q}{\sin \phi - m \cos \phi} \tag{6.22}$$

---

<sup>1</sup>The relationships between the rectangular coordinates  $(x', y')$  of a point with reference to the observation point  $(x_0, y_0)$  and the polar coordinates  $(\rho, \phi)$  are  $x' - x_0 = \rho \cos \phi$  and  $y' - y_0 = \rho \sin \phi$ .

where  $q$  and  $m$  are real numbers. Hence the evaluation of (6.21) requires the quadrature of three different kinds of integrals:

$$\int_{\phi_1}^{\phi_2} \frac{r^2(\phi)}{2} \cos \phi d\phi \tag{6.23}$$

$$\int_{\phi_1}^{\phi_2} \frac{r^2(\phi)}{2} \sin \phi d\phi \tag{6.24}$$

and

$$\int_{\phi_1}^{\phi_2} r(\phi) d\phi \tag{6.25}$$

which may be carried out analytically. Specifically one must evaluate the following items.

- Integral of the form

$$\int_{\phi_1}^{\phi_2} \frac{r^2(\phi)}{2} \cos \phi d\phi = \int_{\phi_1}^{\phi_2} \frac{q^2}{2(\sin \phi - m \cos \phi)^2} \cos \phi d\phi \tag{6.26}$$

may be reduced ([9], formula 2.558) to

$$\begin{aligned} & \frac{q^2}{2} \left( \frac{1}{(-m^2 - 1)(\sin \phi - m \cos \phi)} \right)_{\phi_1}^{\phi_2} + \\ & \frac{q^2}{2} \frac{1}{(-m^2 - 1)} \int_{\phi_1}^{\phi_2} \frac{m}{(\sin \phi - m \cos \phi)} d\phi \end{aligned} \tag{6.27}$$

- Integral of the form

$$\int_{\phi_1}^{\phi_2} \frac{r^2(\phi)}{2} \sin \phi d\phi = \int_{\phi_1}^{\phi_2} \frac{q^2}{2(\sin \phi - m \cos \phi)^2} \sin \phi d\phi \tag{6.28}$$

may be reduced ([9], formula 2.558) to

$$\begin{aligned} & \frac{q^2}{2} \left( \frac{m}{(-m^2 - 1)(\sin \phi - m \cos \phi)} \right)_{\phi_1}^{\phi_2} + \\ & \frac{q^2}{2} \frac{1}{(-m^2 - 1)} \int_{\phi_1}^{\phi_2} \frac{-1}{(\sin \phi - m \cos \phi)} d\phi \end{aligned} \tag{6.29}$$

- Integral of the form

$$\int_{\phi_1}^{\phi_2} \frac{1}{a \cos \phi + b \sin \phi} d\phi \tag{6.30}$$

which appears also in (6.27) and (6.29) may be evaluated in an elegant way.

It is

$$a \cos \phi + b \sin \phi = \sqrt{a^2 + b^2} \left( \cos \phi \frac{a}{\sqrt{a^2 + b^2}} + \sin \phi \frac{b}{\sqrt{a^2 + b^2}} \right) \tag{6.31}$$

which may be written as

$$a \cos \phi + b \sin \phi = \sqrt{a^2 + b^2} \left( \cos \phi \sin(\tan^{-1}(a/b)) + \sin \phi \cos(\tan^{-1}(a/b)) \right) \tag{6.32}$$

By recalling the trigonometric identity

$$\sin(\alpha + \beta) = \sin \alpha \cos \beta + \cos \alpha \sin \beta \tag{6.33}$$

(6.32) becomes

$$a \cos \phi + b \sin \phi = \sqrt{a^2 + b^2} \sin(\phi + \tan^{-1}(a/b)) \tag{6.34}$$

thus the integral (6.30) may be expressed as

$$\int_{\phi_1}^{\phi_2} \frac{1}{2\sqrt{a^2 + b^2} \sin(\phi + \tan^{-1}(a/b))} d\phi \tag{6.35}$$

By applying again (6.33) and by recalling the definition of the function  $\tan(\cdot)$ , it follows that (6.30) is given by

$$\int_{\phi_1}^{\phi_2} \frac{1}{2\sqrt{a^2 + b^2} \tan\left(\frac{1}{2}(\phi + \tan^{-1}(a/b))\right) \cos^2\left(\frac{1}{2}(\phi + \tan^{-1}(a/b))\right)} d\phi \tag{6.36}$$

Observe that the function

$$\frac{1}{\cos^2\left(\frac{1}{2}(\phi + \tan^{-1}(a/b))\right)} \tag{6.37}$$

is the first derivative of the function

$$\tan \left( \frac{1}{2}(\phi + \tan^{-1}(a/b)) \right) \tag{6.38}$$

thus the integral (6.30) becomes

$$\int_{\phi_1}^{\phi_2} \frac{1}{\sqrt{a^2 + b^2}} \frac{1}{z} dz \tag{6.39}$$

where  $z$  is the function

$$z(\phi) = \tan \left( \frac{1}{2}(\phi + \tan^{-1}(a/b)) \right). \tag{6.40}$$

By recalling that

$$\int \frac{1}{z} dz = \log |z| \tag{6.41}$$

a closed form expression for (6.30) is obtained

$$\int_{\phi_1}^{\phi_2} \frac{1}{a \cos \phi + b \sin \phi} d\phi = \frac{\log \left| \tan \left( \frac{1}{2}(\phi + \tan^{-1}(a/b)) \right) \right|}{\sqrt{a^2 + b^2}} \tag{6.42}$$

The typical approach [74] to the calculation of  $\mathcal{I}$  is to evaluate separately the integrals  $\mathcal{I}_{anl}$  and  $\mathcal{I}_{num}$

$$\mathcal{I}_{anl} = \int_T \begin{pmatrix} 1 \\ x' \\ y' \end{pmatrix} \frac{1}{R} dS' \tag{6.43}$$

$$\mathcal{I}_{num} = \int_T \begin{pmatrix} 1 \\ x' \\ y' \end{pmatrix} \frac{e^{-jkR} - 1}{R} dS' \tag{6.44}$$

where  $\mathcal{I} = \mathcal{I}_{anl} + \mathcal{I}_{num}$ . The task may be hence accomplished using the following procedure.



Referring to the coordinate system  $(x_a, y_a)$  centred at  $(x_0, y_0)$  illustrated in Fig. 6.2 for each side of  $T$  the characteristic coefficients  $m^i$ ,  $q^i$  and  $c^i$  of the line  $l_i$  containing the side itself are defined, so that either the equation

$$y - y_0 = m^i(x - x_0) + q^i \tag{6.45}$$

or the equation (in the case of a *vertical* line  $l_i$ )

$$x - x_0 = c^i \tag{6.46}$$

is satisfied by the coordinate pairs of the endpoints of  $\delta T_i$ , which defines the  $i$ -th side of  $T$ . Furthermore, referring to Fig. 6.2, let  $\phi_a^i$  and  $\phi_b^i$  be the angles associated with the endpoints of  $\delta T_i$ . The reference axis for measuring the angles is chosen to be  $x_a$  with angles increasing in counterclockwise direction. As can be seen in Fig. 6.2,

$$\phi_a^i \in \{\phi_1, \phi_2, \phi_3\}, \quad \phi_b^i \in \{\phi_1, \phi_2, \phi_3\} \tag{6.47}$$

The subscripts  $a$  and  $b$  are related to the  $a$  and the  $b$  endpoint of  $\delta T_i$  defined as follows  $\delta T_m$  connects the points  $|m|_3 + 1$  (subscript  $a$ ) and  $|m + 1|_3 + 1$  (subscript  $b$ ),  $m = 1, 2, 3$  where  $|n|_m$  denotes the remainder of  $n/m$ , where  $n, m$  are integers. By recalling the results (6.27), (6.29) and (6.42), it can be then obtained that

$$\mathcal{I}_{ant} = \sum_{i=1}^3 \begin{pmatrix} b^i(\phi_b^i) - b^i(\phi_a^i) \\ b_x^i(\phi_b^i) - b_x^i(\phi_a^i) \\ b_y^i(\phi_b^i) - b_y^i(\phi_a^i) \end{pmatrix} \tag{6.48}$$

where the following triplet of functions of the angle  $\phi$  has been introduced:

$$b^i(\phi) = q^i C^i(\phi) \tag{6.49}$$

$$b_x^i(\phi) = (q^i)^2 A^i(\phi) + ((q^i)^2 B^i + q^i x_0) C^i(\phi) \tag{6.50}$$

$$b_y^i(\phi) = (m^i)(q^i)^2 A^i(\phi) + \left(-\frac{1}{m^i}(q^i)^2 B^i + q^i y_0\right) C^i(\phi) \tag{6.51}$$

with

$$A^i(\phi) = \frac{1}{2[(m^i)^2 + 1][m^i \cos \phi - \sin \phi]} \quad (6.52)$$

$$B^i = -\frac{m^i}{2[(m^i)^2 + 1]} \quad (6.53)$$

$$C^i(\phi) = \frac{\log |\tan \{\frac{1}{2}[\phi - \tan^{-1}(m^i)]\}|}{\sqrt{1 + (m^i)^2}} \quad (6.54)$$

when (6.45) is satisfied, or

$$b^i(\phi) = c^i C^i(\phi) \quad (6.55)$$

$$b_x^i(\phi) = \left( \frac{(c^i)^2}{2} + c^i x_0 \right) C^i(\phi) \quad (6.56)$$

$$b_y^i(\phi) = \frac{(c^i)^2}{2} A^i(\phi) + c^i y_0 C^i(\phi) \quad (6.57)$$

with

$$A^i(\phi) = \frac{1}{\cos \phi} \quad (6.58)$$

$$C^i(\phi) = \log \left| \tan \left( \frac{1}{2}(\phi + \pi/2) \right) \right| \quad (6.59)$$

when (6.46) is satisfied. Notice that when  $(x_0, y_0) \in \delta T_i$  the  $i$ -th term of the sum given in (6.48) is zero, by definition. The results achieved using (6.48) are identical to those obtained using the formulae given in [74].

The integral (6.44), that is  $\mathcal{I}_{num}$ , can be evaluated numerically without difficulties, the integrand being bounded over the integration domain  $T$ . As described in [74], the numerical multiple integration of a bounded function over a triangular domain  $T$  can always be deduced from an integral of the following type

$$\mathcal{F} = \int_0^1 \int_0^{1-\eta} F(\xi, \eta) d\xi d\eta \quad (6.60)$$

where  $(\xi, \eta)$  are the triangle area coordinates, which are related to the coordinates  $(x, y)$  by a linear operator. The numerical integration of (6.60) can be performed

by several methods. For example, a generalised product rule (combination of two Gaussian rules, for instance) can be applied

$$\mathcal{F} = \sum_{k=1}^N w_k \sum_{j=1}^M v_{jk} F(\xi_k, \eta_{jk}) \tag{6.61}$$

or alternatively an  $L$ -point quadrature formula, as reported in [72], can be considered

$$\mathcal{F} = \sum_{l=1}^L w_l F(\xi_l, \eta_l) \tag{6.62}$$

where  $w_k$ ,  $v_{jk}$  and  $w_l$  are the weights. Thus, the final result is given by

$$\mathcal{I} = \mathcal{I}_{ani} + \mathcal{I}_{num}(\mathcal{F}) \tag{6.63}$$

In summary then, to evaluate the integral  $\mathcal{I}$  it is first split into two parts. The first part  $\mathcal{I}_{ani}$  is performed analytically using (6.48) and the second  $\mathcal{I}_{num}$  is evaluated numerically.

## 6.2 Alternative approach to the numerical evaluation of integrals involving the same triangle

The typical procedure for the evaluation of  $\mathcal{I}$  was outlined in the previous section along with a modified formulation of the analytical part of that method which the author finds useful. In this section, an alternative approach for the evaluation of the  $\mathcal{I}$  is developed. The new technique is both conceptually simpler and also easier to apply. The formulation begins by splitting the integral into two parts, but in this case the analytical part is zero. Observe that

$$\mathcal{I} = \mathcal{I}_1 + \mathcal{I}_2 \tag{6.64}$$

with

$$\mathcal{I}_1 = \lim_{\epsilon \rightarrow 0} \int_{T-D_\epsilon} \begin{pmatrix} 1 \\ x' \\ y' \end{pmatrix} \frac{e^{-jkR}}{R} dS' \tag{6.65}$$

and

$$\mathcal{I}_2 = \lim_{\epsilon \rightarrow 0} \int_{D_\epsilon} \begin{pmatrix} 1 \\ x' \\ y' \end{pmatrix} \frac{e^{-jkR}}{R} dS' \tag{6.66}$$

$D_\epsilon$  is the intersection between a disk of radius  $\epsilon$  centred at the observation point  $(x_0, y_0)$  and  $T$ . It is straightforward to obtain that

$$\mathcal{I}_2 = \begin{pmatrix} 1 \\ x_0 \\ y_0 \end{pmatrix} C(x_0, y_0) \lim_{\epsilon \rightarrow 0} \int_0^\epsilon e^{-jkR} dR = 0 \tag{6.67}$$

where the function  $C(x_0, y_0)$  is defined as ( $\delta T$  is the contour of  $T$ )

$$C(x_0, y_0) = \begin{cases} 2\pi & \text{if } (x_0, y_0) \in T - \delta T \\ \gamma & \text{if } (x_0, y_0) \in \delta T \end{cases} \tag{6.68}$$

and  $\gamma = \pi$  if  $(x_0, y_0)$  is not located at a vertex, otherwise  $\gamma$  is the angle between the two sides of  $T$  meeting at the vertex where  $(x_0, y_0)$  falls.

(6.65) may be expressed as

$$\mathcal{I}_1 = \lim_{\epsilon \rightarrow 0} \sum_{i=1}^3 \int_{T_i-D_{\epsilon_i}} \begin{pmatrix} 1 \\ x' \\ y' \end{pmatrix} \frac{e^{-jkR}}{R} dS' \tag{6.69}$$

where the sum over  $i$  extends to the three triangles  $T_i$  formed by the observation point and the endpoints of  $\delta T_i$ :  $T_1 + T_2 + T_3 = T$  (see Fig. 6.2).  $D_{\epsilon_i}$  is the domain

given by the intersection between  $T_i$  and  $D_\epsilon$ . Now, it follows that

$$\mathcal{I}_1 = \sum_{i=1}^3 \int_{\phi_a^i}^{\phi_b^i} \begin{pmatrix} f^i(\phi) \\ f_x^i(\phi) \\ f_y^i(\phi) \end{pmatrix} d\phi \tag{6.70}$$

where

$$\begin{pmatrix} f^i(\phi) \\ f_x^i(\phi) \\ f_y^i(\phi) \end{pmatrix} = \lim_{\epsilon \rightarrow 0} \int_{\epsilon}^{r_i(\phi)} \begin{pmatrix} 1 \\ \rho \cos \phi + x_0 \\ \rho \sin \phi + y_0 \end{pmatrix} e^{-jk\rho} d\rho \tag{6.71}$$

and  $\rho$  is the distance between the integration point and the observation point which is considered as the origin of a polar coordinate system ( $x_a$  is the reference axis, as already stated above).  $r_i(\phi)$  is the distance of any point of  $\delta T_i$  from the observation point and is a function of the characteristic coefficients  $q^i$  and  $m^i$  in (6.45)

$$r_i(\phi) = \frac{q^i}{\sin \phi - m^i \cos \phi}, \quad \phi_a^i < \phi < \phi_b^i \tag{6.72}$$

or the coefficient  $c^i$  in (6.46)

$$r_i(\phi) = \frac{c^i}{\cos \phi}, \quad \phi_a^i < \phi < \phi_b^i \tag{6.73}$$

with  $\phi_a^i$  and  $\phi_b^i$  defined as in (6.47). Once again, observe that if  $(x_0, y_0) \in \delta T_i$  then the terms associated with  $i$  in (6.71) are zero. The integrals in (6.71) are easily evaluated. The results are

$$f^i(\phi) = \frac{1}{jk} [1 - e^{-jkr_i(\phi)}] \tag{6.74}$$

$$f_x^i(\phi) = \frac{1}{(jk)^2} [\alpha_x(\phi) - e^{-jkr_i(\phi)} \beta_x(\phi)] \tag{6.75}$$

$$f_y^i(\phi) = \frac{1}{(jk)^2} [\alpha_y(\phi) - e^{-jkr_i(\phi)} \beta_y(\phi)] \tag{6.76}$$

where

$$\alpha_x(\phi) = [\cos \phi + jkx_0] \quad (6.77)$$

$$\beta_x(\phi) = \{[jkr_i(\phi) + 1] \cos \phi + jkx_0\} \quad (6.78)$$

$$\alpha_y(\phi) = [\sin \phi + jky_0] \quad (6.79)$$

$$\beta_y(\phi) = \{[jkr_i(\phi) + 1] \sin \phi + jky_0\} \quad (6.80)$$

The final step in the solution of the original problem is the evaluation of the three integrals involving the functions  $f^i(\phi)$ ,  $f_x^i(\phi)$  and  $f_y^i(\phi)$  over the domains  $\Phi^i = \{\phi_a^i < \phi < \phi_b^i\}$ . This can be achieved numerically employing, for example, a Gaussian quadrature formula

$$\mathcal{I} = \mathcal{I}_1 = \sum_{i=1}^3 \begin{pmatrix} \sum_l w_l f^i(\phi_l) \\ \sum_l w_l f_x^i(\phi_l) \\ \sum_l w_l f_y^i(\phi_l) \end{pmatrix} \quad (6.81)$$

where  $\{w_l\}_{l=1 \dots L}$  and  $\{\phi_l\}_{l=1 \dots L}$  are, respectively, the sets of weights and abscissas considered for each  $\Phi^i$ .

The first remark about the alternative approach presented here relates to the integrand functions  $f^i(\phi)$ ,  $f_x^i(\phi)$  and  $f_y^i(\phi)$ . We observe that the longer side of a triangular patch, where a basis current function shall be defined, is smaller than  $\lambda/x$ , with  $x > 4$  for an accurate implementation of the moment method. Thus

$$0 < kr_i(\phi) < \left(\frac{2\pi}{x}\right), \quad \phi_a^i < \phi < \phi_b^i \quad (6.82)$$

which shows that the domains  $\Phi^i = \{\phi_a^i < \phi < \phi_b^i\}$  correspond to a relatively small portion of the period  $\Omega = 2\pi$  of the  $e^{-jkr_i(\phi)}$  function. This guarantees a sufficiently smooth behaviour of the functions to be integrated numerically, which in turns provides a closer approximation. Essentially, the alternative method presented in this section is fully numerical, since the analytical part  $\mathcal{I}_2$  evaluates to

$(u_0, v_0)$	(0.1, 0.1)	(0.2, 0.2)	(0.3, 0.3)	$(\frac{1}{3}, \frac{1}{3})$	(0.4, 0.4)
$\mathcal{I}^{G8}$	1.89818 - j0.309025 0.434035 - j0.102436 0.434035 - j0.102436	2.24628 - j0.311111 0.601287 - j0.103454 0.601287 - j0.103454	2.381 - j0.311817 0.745461 - j0.103823 0.745461 - j0.103823	2.37762 - j0.31185 0.780064 - j0.103871 0.780064 - j0.103871	2.28374 - j0.311502 0.813426 - j0.10381 0.813426 - j0.10381
$\mathcal{I}^{G10}$	1.89853 - j0.309515 0.43439 - j0.102763 0.43439 - j0.102763	2.24629 - j0.311141 0.601306 - j0.103483 0.601306 - j0.103483	2.381 - j0.311826 0.745462 - j0.103828 0.745462 - j0.103828	2.37763 - j0.31187 0.780066 - j0.103881 0.780066 - j0.103881	2.28386 - j0.311661 0.813479 - j0.103884 0.813479 - j0.103884
$\mathcal{I}_{ani} + \mathcal{I}_{num}^G$	1.89841 - j0.309643 0.433746 - j0.102774 0.435156 - j0.102972	2.24615 - j0.311144 0.60055 - j0.103387 0.602054 - j0.103586	2.38177 - j0.311826 0.745028 - j0.103729 0.746422 - j0.103927	2.37916 - j0.311872 0.779873 - j0.103782 0.781247 - j0.10398	2.284 - j0.311688 0.812779 - j0.103797 0.814163 - j0.103995
$\mathcal{I}_{ani} + \mathcal{I}_{num}^{G8}$	1.89861 - j0.309643 0.434471 - j0.102873 0.434471 - j0.102873	2.2463 - j0.311144 0.601312 - j0.10348 0.601312 - j0.10348	2.38097 - j0.311826 0.74545 - j0.103828 0.74545 - j0.103828	2.37759 - j0.311872 0.780056 - j0.103881 0.780056 - j0.103881	2.28391 - j0.311688 0.813502 - j0.10389 0.813502 - j0.10389
$\mathcal{M}$	1.89857 - j0.309643 0.434468 - j0.102873 0.434468 - j0.102873	2.24628 - j0.311144 0.601305 - j0.103487 0.601305 - j0.103487	2.38099 - j0.311826 0.745456 - j0.103828 0.745456 - j0.103828	2.37762 - j0.311872 0.780063 - j0.103881 0.780063 - j0.103881	2.28386 - j0.311688 0.813481 - j0.103896 0.813481 - j0.103896

Table 6.1: Numerical and reference results for five different observation points.

zero. The problem of calculating  $\mathcal{I}$  is now reduced to the problem of evaluating three triplets of integrals (one triplet for each side of  $T$ ) of functions of one variable  $\phi$ . In the conventional approach outlined in the previous section,  $\mathcal{I}$  is evaluated as the sum of three triplets of integrals calculated analytically ( $\mathcal{I}_{ani}$ ) and one triplet of multiple integrals carried out numerically ( $\mathcal{I}_{num}$ ). Thus, the alternative technique is certainly simpler than the usual one (the difficulty in handling numerical integrations decreases in passing from two dimensions to one dimension). Another factor to be taken into account is the accuracy of the two methods. In the conventional approach, the evaluation of  $\mathcal{I}_{num}$  can be done by employing a product rule ( $MN$  points considered) or a simpler quadrature formula ( $L$  points sampled), with  $L < MN$ , which is obviously faster as well as less accurate than the product rule. However, with the alternative method,  $\mathcal{I}$  is calculated readily by an  $L$ -point Gaussian scheme, with satisfactory results. Finally, it is straightforward to generalise the method here exposed in the case of planar polygonal domains. In fact, a planar polygon  $P$  having  $S$  sides can always be represented as the union of  $S$  disjointed plane triangles.

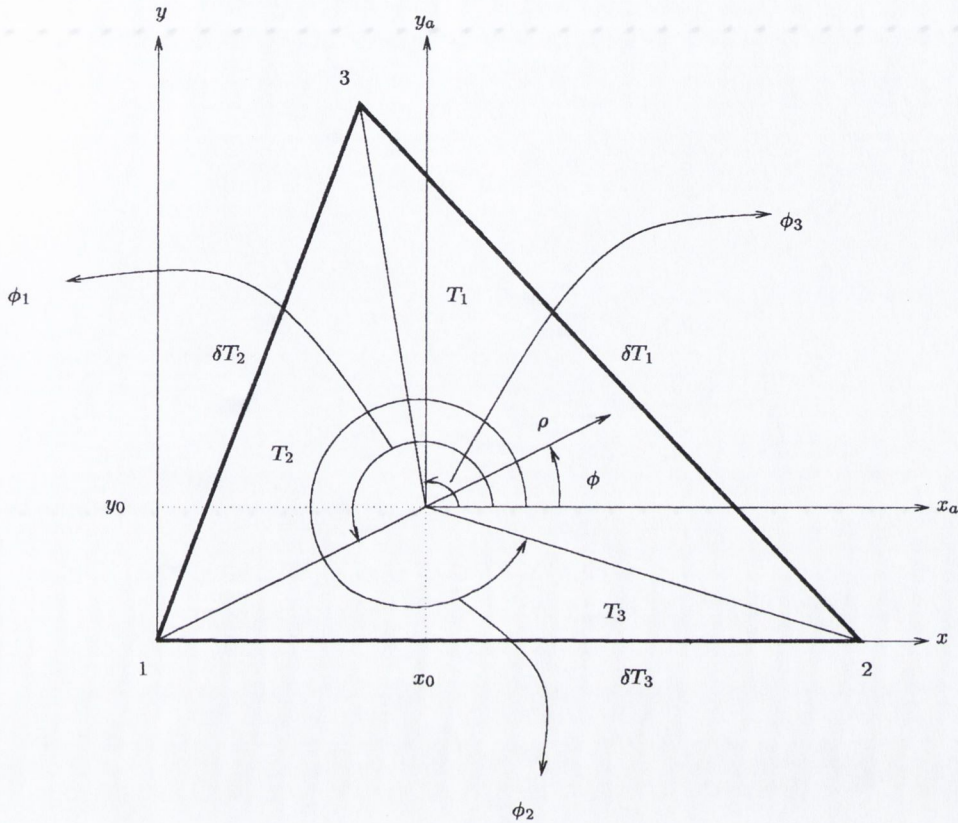


Figure 6.2: Geometry of the self term calculation for the triangle  $T$ . The local coordinate systems  $(x, y)$  and  $(\rho, \phi)$  are displayed. Given the observation point  $(x_0, y_0)$ , three triangles are considered:  $T_1$ ,  $T_2$  and  $T_3$  obtained by a connection of the observation point with the three vertices of  $T$ . The integral given in (6.17) may be considered as the sum of three integrals, each one computed over the triangular domain  $T_i$ ,  $i = 1, 2, 3$ . More precisely, the integral over the whole domain  $T$  is split into the sum of two integrals: one over a disk of radius  $\epsilon \rightarrow 0$  centred at  $(x_0, y_0)$ , which evaluates to zero, and the other over the three triangles  $T_i$ ,  $i = 1, 2, 3$ . Each integral over  $T_i$  may now be carried out referring to the polar coordinate system  $(\rho, \phi)$ , obtaining the final result (6.81).

### 6.3 Numerical results

The novel numerical technique has been implemented and compared with the usual approach for a triangle  $T$  as the one displayed in Fig. 6.2 with the points 2 and 3 having coordinates  $(x_2, y_2) = (0.1\lambda, 0)$  and  $(x_3, y_3) = (0, 0.1\lambda)$ , with  $k = 2\pi/\lambda$ . Table 6.1 displays five different sets of results obtained for five different observation points  $(x_0, y_0)$  belonging to the line  $x = y$ . The first two rows refer to two different numerical evaluation of the integral (6.81), by a one-dimensional Gaussian quadrature rule with 8 and 10 abscissas and weights, indicated by  $\mathcal{I}^{G8}$  and  $\mathcal{I}^{G10}$  respectively. In the successive couple of rows, results returned implementing the



usual method proposed by Graglia in [74] are reported. The term  $\mathcal{I}_{anl}$  is the integral evaluated analytically, i.e.

$$\int_T \begin{pmatrix} 1 \\ x' \\ y' \end{pmatrix} \frac{1}{R} dS' \quad (6.83)$$

Such term may be evaluated by direct integration as described in [74] or [76]. The remaining term, i.e.

$$\int_T \begin{pmatrix} 1 \\ x' \\ y' \end{pmatrix} \frac{e^{-jkR} - 1}{R} dS' \quad (6.84)$$

may be evaluated using a seven-point numerical quadrature rule described in [72], whose result has been indicated in the table by  $\mathcal{I}_{num}^n$  or by a two-dimensional  $8 \times 8$  Gaussian rule, indicated by  $\mathcal{I}_{num}^{G8}$ . Finally, the last row, labelled by  $\mathcal{M}$  shows the reference results returned by a specialised mathematical software package, Mathematica 3.0. The results returned by Mathematica 3.0 have been generated by an accurate procedure which guarantees their reliability, although it requires an execution time of order of hours to achieve the desired final stable result. Among the two numerical techniques, the classical one based on [74] and the novel one [76], the author has registered a faster execution time for the latter. Both have been implemented using C++.

Fig. 6.3 illustrates the smooth behaviour of the functions (6.75) and (6.76) in the case of (6.72) given by

$$r(\phi) = \frac{1}{\sin \phi - (-1) \cos \phi}, \quad 0 < \phi < 1.5 \quad (6.85)$$

where  $\phi$  is given in radians and  $x_0 = y_0 = 0$  (see (6.75) and (6.76)). The function  $r(\phi)$  is also illustrated.

## 6.4 Summary

This chapter presented the problem of the numerical evaluation of surface integrals arising in the discretisation of the EFIE in the three-dimensional case using the RWG basis functions. The typical approach to the numerical evaluation of singular functions was described. This approach derives from splitting the integrand into two parts: one part is analytically integrable and the other, non-singular, is numerically integrable.

Instead of splitting the kernel, it was suggested to split the domain of integration into two subdomains: a disk of radius  $\epsilon$  (or a portion of disk, if the observation point  $(x_0, y_0)$  falls onto the contour of  $T$ ) and the remaining part of  $T$ . The advantage of this approach is that the integral over the disk evaluates to zero. By means of a limit operation it is shown that the evaluation of (6.17) can be carried out fully numerically. The advantages of the fully numerical procedure proposed here and published in [76] are essentially:

- The integrals are one-dimensional, while in the usual approach the non-singular functions to be integrated numerically depend on the pair of real variables  $(\xi, \eta)$ .
- The functions  $f^i(\phi)$ ,  $f_x^i(\phi)$  and  $f_y^i(\phi)$  in (6.81) are smooth over the domains of integration, so that a simple quadrature rule, such as a Gaussian formula with a limited number of abscissas, can be implemented to achieve the desired accuracy.
- The integral (6.17) is evaluated through one single step, being the limit of the integral over the disk zero.

In summary, the technique is reliable, fast and simpler to implement than the usual method. Numerical results were provided to show the accuracy obtained by using the alternative approach.

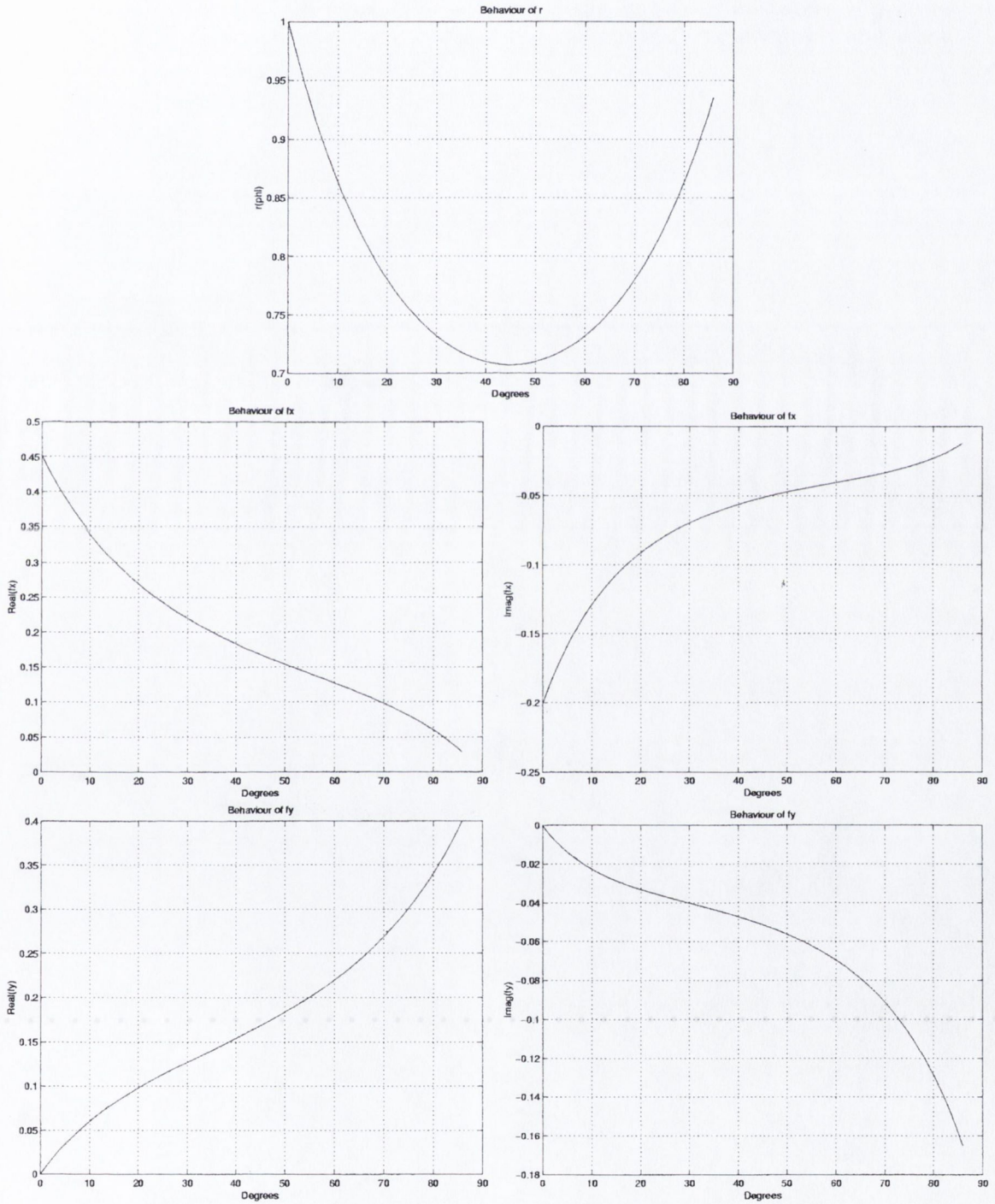


Figure 6.3: Behaviour of the function  $r(\phi)$  as given in (6.72) and the resulting functions (6.75) and (6.76) employed in the evaluation of the integral using the alternative approach.

---

## THE MULTI-LEVEL FAST FAR-FIELD ALGORITHM

---

Chapters 3-5 were dedicated to the description of both existing and novel acceleration techniques to tackle the problem of electromagnetic scattering in two dimensions. The general EFIE formulation for the three-dimensional case has been derived and sample numerical results were presented in chapter 2. The FMM has been described for the three-dimensional case at the end of chapter 3. In the two-dimensional case, both the FAFFA and the FMM are extensively described in literature. Although the FAFFA may be considered as a derivation of the FMM, its computational simplicity represents a significant advantage with respect to the FMM. This is due to its less complicated *translation* step in the group-to-group interactions. However, the FAFFA formulation for the three-dimensional case had not been reported in the literature and no attempts to implement a multi-level version of this algorithm had never been made. The author has investigated the possibility of a multi-level version of the FAFFA method in the three-dimensional case and has experienced that again in this context the FAFFA algorithm possesses advantages against the more popular FMM due to its implementation simplicity. The result is the work reported in [80]-[81]. A description of the multi-level FAFFA algorithm is given in this chapter, with final results which confirm the applicability of this fast method to three-dimensional scattering problems. A similar technique, without the multi-level feature has been applied recently to the modeling of reflector antennas [79].

## 7.1 Formulation of the Multi-Level Fast Far-Field Algorithm (MLFAFFA)

In this section, the implementation of a three-dimensional *multi-level* fast far-field algorithm which accelerates the matrix-vector multiply of iterative techniques such as the CG method in three dimensional scattering problems is described. The approach is a multi-level three dimensional extension of the FAFFA described in section 4.1.

### 7.1.1 The far-field approximation applied to the RWG basis set

As pointed out in section 2.6 the terms  $Z_{mn}$  represent the effect of the field on the domain  $T_m^+ \cup T_m^-$  produced by the current  $I_n \mathbf{f}_n(\mathbf{r})$ , defined by (2.66). The field generated by  $I_n \mathbf{f}_n(\mathbf{r})$  at a point  $P$  is

$$\begin{aligned} \mathbf{E}_n(P) = & \frac{-j\omega\mu_0}{4\pi} I_n \left( \int_{T_n^+} \frac{l_n}{2A_n^+} \bar{\rho}_n^+ \frac{e^{-jkR_n^+}}{R_n^+} dS' + \int_{T_n^-} \frac{l_n}{2A_n^-} \bar{\rho}_n^- \frac{e^{-jkR_n^-}}{R_n^-} dS' \right) \\ & + \frac{1}{j\omega 4\pi\epsilon_0} I_n \left( \int_{T_n^+} \frac{l_n}{A_n^+} \nabla_P \frac{e^{-jkR_n^+}}{R_n^+} dS' + \int_{T_n^-} \frac{-l_n}{A_n^-} \nabla_P \frac{e^{-jkR_n^-}}{R_n^-} dS' \right) \end{aligned} \quad (7.1)$$

where  $R_n^\sigma$ ,  $\sigma \in \{+, -\}$ , is the distance between the point  $P$  and the point  $\mathbf{r}' \in T_n^\sigma$  and  $\nabla_P$  is the gradient operating on a function of the coordinates of  $P$ . For example, in a rectangular coordinate system,  $\nabla_P = \partial/\partial x_P \hat{\mathbf{x}} + \partial/\partial y_P \hat{\mathbf{y}} + \partial/\partial z_P \hat{\mathbf{z}}$ , if  $\mathbf{r}_P = x_P \hat{\mathbf{x}} + y_P \hat{\mathbf{y}} + z_P \hat{\mathbf{z}}$ . Consider a set  $G$  of currents  $\{I_n\}_{n \in G}$  and assume that the distribution  $\{I_n \mathbf{f}_n(\mathbf{r})\}_{n \in G}$  is located over a surface  $S$  which may either enclose a volume  $V$  or be open. The electric field produced by this set  $G$  at point  $P$  is the sum of the fields  $\{\mathbf{E}_n(P)\}_{n \in G}$ , associated with  $\{I_n\}_{n \in G}$ . Now, for some point  $O$  ( $O \in V$  or  $O \in S$  depending on the geometry of the distribution) and the triangle  $T_n^\sigma$  with  $n \in G$ , referring to Fig. 7.1, it follows that

$$\mathbf{R}_n^\sigma = \mathbf{r}_P - \mathbf{r}_O + \mathbf{r}_O - \mathbf{r}' = \mathbf{R}_O + \mathbf{s}_n^\sigma \quad (7.2)$$

where

$$\mathbf{R}_O = \mathbf{r}_P - \mathbf{r}_O \quad (7.3)$$



$$W_n(\widehat{\mathbf{R}}_O) = W_n^+(\widehat{\mathbf{R}}_O) + W_n^-(\widehat{\mathbf{R}}_O) \quad (7.9)$$

with

$$\mathbf{M}_n^\sigma(\widehat{\mathbf{R}}_O) = \int_{T_n^\sigma} \frac{l_n}{2A_n^\sigma} \rho_n^\sigma e^{-jk\widehat{\mathbf{R}}_O \cdot \mathbf{s}_n^\sigma} dS' \quad (7.10)$$

$$W_n^\sigma(\widehat{\mathbf{R}}_O) = \int_{T_n^\sigma} \frac{\sigma l_n}{A_n^\sigma} e^{-jk\widehat{\mathbf{R}}_O \cdot \mathbf{s}_n^\sigma} dS' \quad (7.11)$$

where  $\sigma \in \{+, -\}$ . Referring again to Fig. 7.1, consider the point  $Q$  and define the vector  $\mathbf{s} = \mathbf{r}_Q - \mathbf{r}_P$ . If  $s \ll R_O$ , then the amplitude of the vector  $\mathbf{r}_Q - \mathbf{r}_O$  - on which  $\mathbf{E}_G(Q)$  depends - can be approximated by

$$|\mathbf{r}_Q - \mathbf{r}_O| \approx R_O + \widehat{\mathbf{R}}_O \cdot \mathbf{s} \quad (7.12)$$

Defining  $\sum_{n \in G} I_n \mathbf{M}_n(\widehat{\mathbf{R}}_O) = \mathbf{M}_G(\widehat{\mathbf{R}}_O)$  and  $\sum_{n \in G} I_n W_n(\widehat{\mathbf{R}}_O) = W_G(\widehat{\mathbf{R}}_O)$  the scattered electric field, caused by the currents in  $G$  at point  $Q$ , may be approximated as

$$\mathbf{E}_G(Q) \approx \frac{-j\omega\mu_0}{4\pi} \frac{e^{-jkR_O}}{R_O} \mathbf{M}_G(\widehat{\mathbf{R}}_O) e^{-jk\widehat{\mathbf{R}}_O \cdot \mathbf{s}} + \frac{1}{j\omega 4\pi\epsilon_0} \frac{e^{-jkR_O}}{R_O} W_G(\widehat{\mathbf{R}}_O) \nabla_Q e^{-jk\widehat{\mathbf{R}}_O \cdot \mathbf{s}} \quad (7.13)$$

with

$$\nabla_Q e^{-jk\widehat{\mathbf{R}}_O \cdot \mathbf{s}} = -jk\widehat{\mathbf{R}}_O e^{-jk\widehat{\mathbf{R}}_O \cdot \mathbf{s}} \quad (7.14)$$

At this point it has been shown that the field due to the current  $\sum_{n \in G} I_n \mathbf{f}_n(\mathbf{r}')$  at a far point  $P$  can be approximated as a function of the vector  $\mathbf{R}_O = \mathbf{r}_P - \mathbf{r}_O$

$$\mathbf{E}_G(P) \approx -j\omega \mathbf{A}_G(\mathbf{R}_O) - \nabla_P \Phi_G(\mathbf{R}_O) \quad (7.15)$$

with

$$\mathbf{A}_G(\mathbf{R}_O) = \frac{\mu_0}{4\pi} \frac{e^{-jkR_O}}{R_O} \mathbf{M}_G(\widehat{\mathbf{R}}_O) = \frac{\mu_0}{4\pi} \frac{e^{-jkR_O}}{R_O} \sum_{n \in G} I_n \mathbf{M}_n(\widehat{\mathbf{R}}_O) \quad (7.16)$$

and

$$\Phi_G(\mathbf{R}_O) = -\frac{1}{j\omega 4\pi\epsilon_0} \frac{e^{-jkR_O}}{R_O} W_G(\widehat{\mathbf{R}}_O) = -\frac{1}{j\omega 4\pi\epsilon_0} \frac{e^{-jkR_O}}{R_O} \sum_{n \in G} I_n W_n(\widehat{\mathbf{R}}_O) \quad (7.17)$$

which are respectively the magnetic vector and the electric scalar potentials corresponding to the distribution  $G$ . Now, the evaluation of the field at a neighbouring point  $Q$ , one relatively close to  $P$ , only requires a simple phase-shift extension of the potentials  $\mathbf{A}_G(\mathbf{R}_O)$  and  $\Phi_G(\mathbf{R}_O)$ , specifically

$$\mathbf{E}_G(Q) \approx -j\omega \mathbf{A}_G(\mathbf{R}_O) e^{-jk\widehat{\mathbf{R}}_O \cdot \mathbf{s}} - \nabla_Q \Phi_G(\mathbf{R}_O) e^{-jk\widehat{\mathbf{R}}_O \cdot \mathbf{s}} \quad (7.18)$$

Let the group  $G$  contains  $N_G$  current elements and consider a set of  $N_P = N_G$  points  $\{Q_q\}$ , with  $q = 1 \cdots N_G$ , located in the neighbourhood of  $P$ . These should be all *far* from  $O$  the reference point for group  $G$ . Using the *far-field* approximation then, the computational cost of calculating the  $N_P = N_G$  electric field values at the points  $\{Q_q\}$  is made up of

- $\mathcal{O}(N_G)$  operations to calculate  $\mathbf{M}_G(\widehat{\mathbf{R}}_O)$  and  $W_G(\widehat{\mathbf{R}}_O)$
- 3 operations to evaluate  $\mathbf{E}_G(P)$ ;
- $\mathcal{O}(N_G)$  operations to calculate the final results.

The overall cost is  $\mathcal{O}(N_G)$  compared to a direct evaluation cost of  $\mathcal{O}(N_G^2)$ , which is due to the calculation of the  $N_G$  fields of each  $I_n \mathbf{f}_n(\mathbf{r}')$ , with  $n \in G$ , at each point  $\{Q_q\}$ . The far-field algorithm approach allows one to evaluate the far interactions between pairs of parts of the surface through  $\mathcal{O}(N_G)$  operations, where  $N_G$  is the number of unknowns located in each portion of the surface.

### 7.1.2 Choosing the far-field/near-field regions

The distance which defines the limit of the far-field zone (also called the *Fraunhofer region*) satisfies [20]

$$R_O > \frac{2d^2}{\lambda} \quad (7.19)$$



where  $d$  is the maximum transverse dimension of the source group with respect to  $\mathbf{R}_O$ . As an illustration of the level of accuracy achievable using the far-field approximation, consider a set of square planar patches or plates of side  $L = l\lambda$ , with  $l = 0.5, 1.0, 2.0, 4.0$ . The current on the plate is represented using a 2D triangular grid  $N$  basis functions (refer to Fig. 7.7) and the result obtained using the far-field approximation to evaluate the electric field produced by a sample set of currents  $\{I_n = e^{j\frac{\pi}{4}}\}_{n=1\dots N}$  is then examined. Fig. 7.2 illustrates the amplitude of the electric field calculated using both the approximate method and a numerically exact method at a distance  $(2d^2/\lambda)m_L$ ,  $m_L$  is a scaling factor which depends on  $L$  and takes the values 3, 2, 1, 1 for  $L = 0.5\lambda, 1.0\lambda, 2.0\lambda, 4.0\lambda$ . The field points are in the same plane as the patch at angles  $\phi = 0 \dots 2\pi$ . The agreement is within

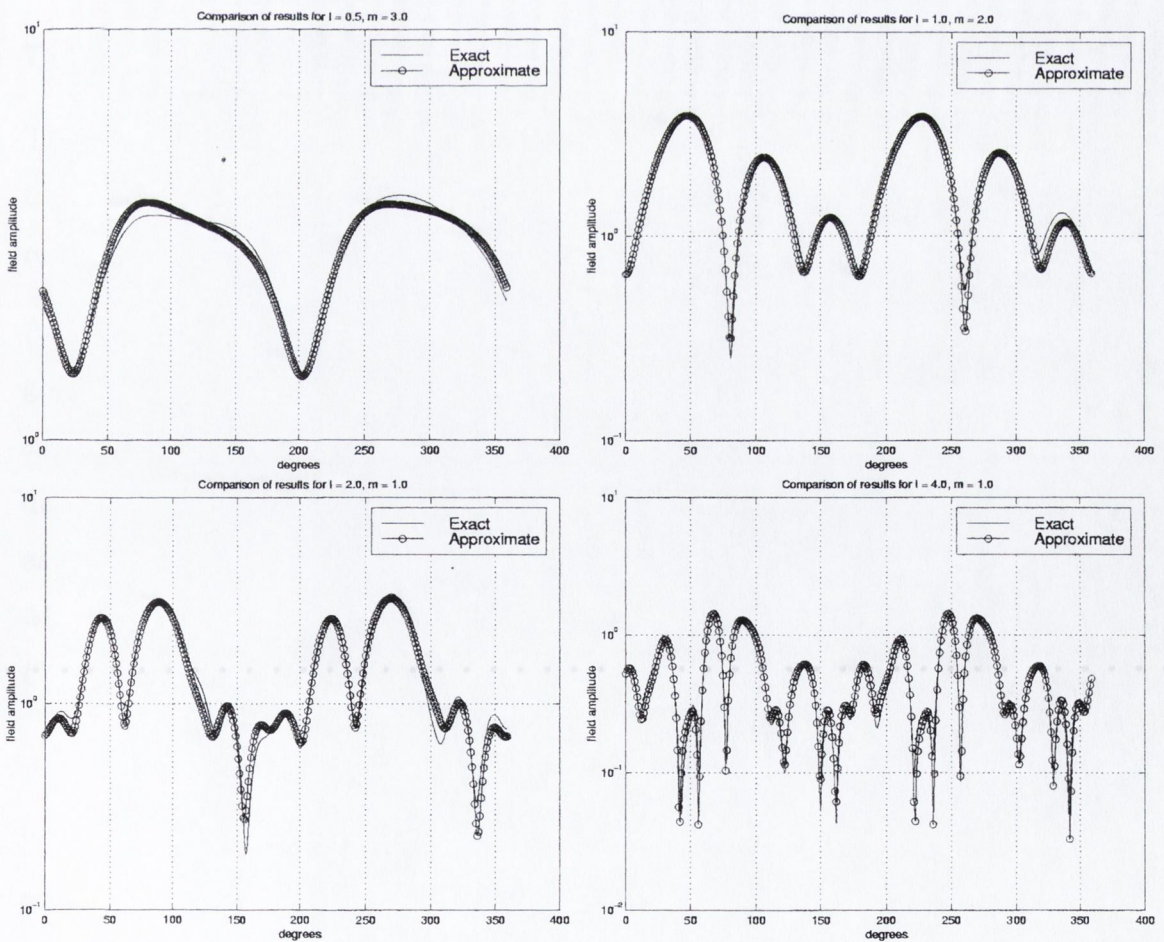


Figure 7.2: Approximated and exact far-field patterns due to a given current distribution over a square flat plate of sides  $l\lambda$ ,  $l = 0.5, 1.0, 2.0$  and  $4.0$ .

less than 0.5 dB in the worst case. Note that the distance expressed by (7.19) has been modified by the introduction of the factor  $m_L \geq 1$ . In fact, when applying the far-field approximation (see Fig. 7.1), for the purpose of computing the amplitude (*not the phase*), the distance between a triangular domain  $T_n^\sigma$  and any field point  $P$  is approximated by  $R_O$ , the distance between  $P$  and the reference point  $O$ . This approximation holds well when the point  $P$  is relatively far from the scatterer, i.e. from  $O$ , a condition that is not guaranteed by  $|\mathbf{r}_P - \mathbf{r}_O| > (2d^2/\lambda)$  when the size of the patch is comparable with the wavelength. It must be emphasised, then, that the far-field approximation as employed in (7.6) is more accurate for the phase than the amplitude. It is for these reasons that the inequality (7.19) is modified, by the introduction of the factor  $m_L \geq 1$ , such that  $R_O > (2d^2/\lambda)m_L$

### 7.1.3 Multi-level scheme

The fast far-field (FAFFA) technique achieves its computational savings by grouping together current elements to evaluate (allowing certain calculations to be repeatedly reused) their mutual interaction with lesser complexity than the direct method.

As one moves further away from a given region containing current elements the group sizes can be made larger. One way of doing this is to *regroup* sets of adjacent smaller groups. This kind of multi-level strategy for the FMM method has been described by Greengard and Rokhlin in [78], and has been adopted also in [53] as well as in [77]. Consider a set of current elements  $\mathcal{G}$  (the parent) containing  $M$  (non-overlapping) adjacent sets  $G_m$ ,  $m = 1 \dots M$  (the children), for a point  $\mathcal{O}_G \in \mathcal{G}$ , it may be seen, for direction  $\hat{\mathbf{R}}_O$ , that

$$\mathbf{M}_{\mathcal{G}}(\hat{\mathbf{R}}_O) = \sum_{m=1}^M \mathbf{M}_{G_m}(\hat{\mathbf{R}}_O) e^{-jk\hat{\mathbf{R}}_O \cdot \mathbf{s}_m} \quad (7.20)$$

where  $\mathbf{s}_m = \mathbf{r}_{\mathcal{O}_G} - \mathbf{r}_{\mathcal{O}_m}$ , is the vector representing the distance between the centre of the parent group  $\mathcal{G}$  and the centre of the child group  $G_m$ . The same relationship holds for the scalar  $W_G(\hat{\mathbf{R}}_O)$  and can be used to regroup groups of the scatterer for evaluating their far-field at a given direction.

## 7.2 Implementation of the MLFAFFA

In this section the implementation of the MLFAFFA is discussed. For simplicity a planar scatterer is considered to illustrate the features of the MLFAFFA. This formulation and the method can be applied to more complicated scatterers.

### 7.2.1 Memory requirements

Recall that the MLFAFFA aims to accelerate the matrix-vector multiplication  $\sum_{n=1}^N Z_{mn} I_n = V_m$ ,  $m = 1 \cdots N$ . For a given  $m$ , the sum  $\sum_{n=1}^N Z_{mn} I_n$  is split into two terms: the first, say  $\sum_{n \in \mathcal{NF}_m} Z_{mn} I_n$ , is the contribution of the currents belonging to the near field area  $\mathcal{NF}_m$  and it is evaluated *exactly* using the direct method; the second term is the scattered field at the element  $m$  arising from the set of surface currents which have element  $m$  in their far-field. This set of currents can be split up into groups (see Fig. 7.6). Group fields scattered towards the surface element  $m$  may be calculated using (7.7). It is important to note that the field thus obtained is for a point. However, it can be disseminated to calculate the field values at neighbouring points. As the distance between the groups and the observation point increases, it is somewhere convenient to aggregate the adjacent groups into a super groups, and so on. The storage and computation time for the evaluation of the matrix elements  $Z_{mn}$  is reduced significantly, because not all elements need to be explicitly computed or stored. Only a small proportion of the impedance matrix elements is evaluated.

Fig. 7.3 illustrates the observed relation between the storage requirement and the number of unknowns for both an iterative CG method and the MLFAFFA, applied to a planar homogeneous scatterer. The storage requirements of the MLFAFFA become superior once the number of unknowns is greater than a threshold value. The reason for this will emerge in the next section.

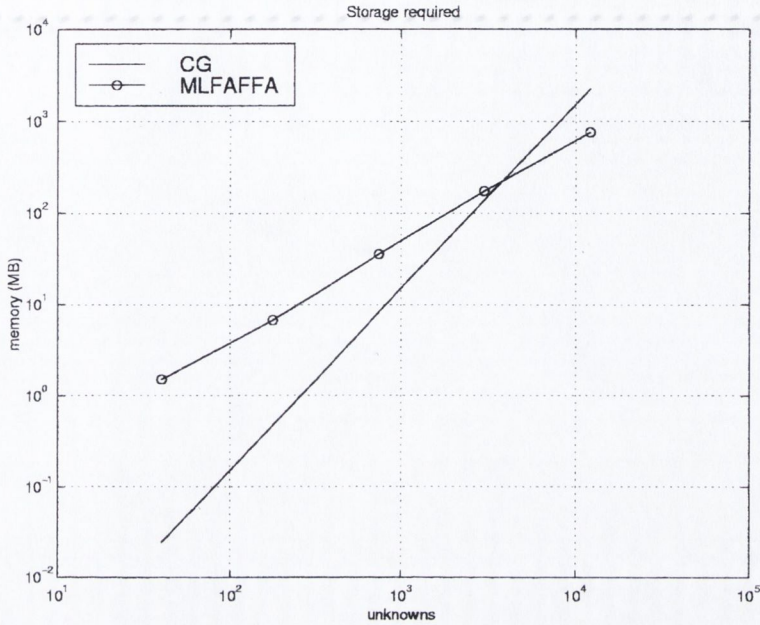


Figure 7.3: Storage requirements (in MB) for the implementation of the MLFAFFA and the classical CG methods.

### 7.2.2 The algorithm

Having explored the building blocks, in this section, the main features of the MLFAFFA are encountered: building the tree-structured grid, storage of necessary entities, evaluation of the matrix-vector product.

#### Building the tree-structured grid

Here the algorithm is presented by way of example. A rectangular planar scatterer is considered and is enclosed by a square boundary (level 0) upon which a recursive subdivision by 4 is performed up to the finest level (level  $N_\ell$ ), at which point the side of a single square has length of order of  $\lambda/2$ . Fig. 7.4 illustrates a planar scatterer, a square enclosing it and the recursive subdivision up to the finest level (3 in the figure). In this way a tree-structured collection of squares is built, which is organised in levels ranging from 0 to  $N_\ell$ . A square, at level  $N_\ell > \ell \geq 0$ , is said to be *parent* of four *children*. Note that some of the basis functions will end up split over two such adjacent squares, this is because the pair of triangles on which they are defined reside in adjacent squares at the finest level, i.e. the edge shared by

the pair lies either on or across the border of two adjacent squares (see for example edges  $m$  and  $n$  in Fig. 7.6). After this grouping operation, a square  $G^l$  (at any level  $l$ ) contains a group of current elements of the RWG basis set.

### Evaluation and storage of coefficients $\mathbf{M}_n$ and $W_n$

For each square at the finest level, say  $G_i^{N_l}$ ,  $i = 0 \dots 4^{N_l} - 1$ , the following coefficients (which will be used to generate the potentials (7.16) and (7.17)) are evaluated and stored

$$\mathbf{M}_n(\widehat{\mathbf{R}}_O) = \delta_n^+ \mathbf{M}_n^+(\widehat{\mathbf{R}}_O) + \delta_n^- \mathbf{M}_n^-(\widehat{\mathbf{R}}_O) \quad (7.21)$$

$$W_n(\widehat{\mathbf{R}}_O) = \delta_n^+ W_n^+(\widehat{\mathbf{R}}_O) + \delta_n^- W_n^-(\widehat{\mathbf{R}}_O) \quad (7.22)$$

where  $\delta_n^\sigma$ ,  $\sigma \in \{+, -\}$ , is equal to 1 if the triangle  $T_n^\sigma$  belongs to  $G_i^{N_l}$  and 0 otherwise, with  $n = 0 \dots N_{T_i}$ , and  $N_{T_i}$  is the number of edges falling in  $G_i^{N_l}$ . These coefficients are evaluated for the  $K$  discrete directions:  $\phi_k = 2\pi k/K$ ,  $k = 0 \dots K - 1$ , i.e. for the following  $\widehat{\mathbf{R}}_{O_k}$

$$\widehat{\mathbf{R}}_{O_k} = \cos \phi_k \widehat{\mathbf{i}} + \sin \phi_k \widehat{\mathbf{j}} \quad (7.23)$$

with  $\{\widehat{\mathbf{i}}, \widehat{\mathbf{j}}\}$  being the set of orthogonal unit vectors coplanar to the scatterer.

For each square  $G_i^{N_l}$  the characteristic coefficients  $\mathbf{M}_n(\widehat{\mathbf{R}}_{O_k})$  and  $W_n(\widehat{\mathbf{R}}_{O_k})$  of the basis currents in  $G_i^{N_l}$ , at  $K$  regularly discretised directions need be stored. Later, it will be necessary to interpolate these values to evaluate the vector and the scalar potentials  $\mathbf{A}_{G_i^{N_l}}$  and  $\Phi_{G_i^{N_l}}$  using (7.16) and (7.17). This step corresponds to the construction of the *outer multipole expansions* (3.29) and (3.30) of the MLFMA method, when the RWG basis set is employed. To complete the set-up for the matrix-vector multiplication, the impedance matrix elements which correspond to the *near-field* interactions must be evaluated and stored. To evaluate the impedance matrix self-terms  $Z_{mm}$ , the numerical procedure described in [76] may be applied.

### Implementation of the matrix-vector multiplication

The matrix-vector multiplication is carried out by first evaluating the near-field sums  $\sum_{n \in \mathcal{NF}_m} Z_{mn} I_n$ ,  $m = 1 \cdots N$ , where  $\mathcal{NF}_m$  is the set of edges near  $m$  and thereafter evaluating the far-field interactions. For each square at the finest level  $N_l$ , for example  $G_j^{N_l}$  in Fig. 7.6, the near-field squares are detected. In Fig. 7.6, for example,  $G_l^{N_l}$  is near  $G_j^{N_l}$ . For each edge belonging to the square currently observed, say  $m \in G_j^{N_l}$ , the contribution to  $\sum_{n \in \mathcal{NF}_m} Z_{mn} I_n$  due to all other edges contained in the near squares, such as  $n \in G_l^{N_l}$  in Fig. 7.6, is evaluated. Some contributions may involve only subdomains of the domains where the  $m$ -th and the  $n$ -th current are defined.

The far-field evaluation is performed in two sweeps: the first sweep traverses from the finest level up to a coarsest level  $\ell_{min}$ ; then the second sweep traverses back down to the finest level. In the first sweep, starting at the finest level  $N_l$ , for each square  $G_i^{N_l}$ ,  $i = 0 \cdots 4^{N_l} - 1$ , the coefficients  $\sum_{n \in G_i^{N_l}} I_n \mathbf{M}_n(\hat{\mathbf{R}}_O) = \mathbf{M}_{G_i^{N_l}}(\hat{\mathbf{R}}_O)$  and  $\sum_{n \in G_i^{N_l}} I_n W_n(\hat{\mathbf{R}}_O) = W_{G_i^{N_l}}(\hat{\mathbf{R}}_O)$  are evaluated using the new estimate  $\{I_n\}$  for the current in the new iteration of the CG algorithm. This evaluation requires the quantities given in (7.21) and (7.22), which have been previously stored. Then the coefficients  $\mathbf{M}_{G_i^\ell}(\hat{\mathbf{R}}_O)$  and  $W_{G_i^\ell}(\hat{\mathbf{R}}_O)$  for each square  $G_i^\ell$ ,  $i = 0 \cdots 4^\ell - 1$ , at each level  $\ell < N_l$  are evaluated. A square  $G_i^\ell$ ,  $i = 0 \cdots 4^\ell - 1$ , is now parent of four children and is sufficient to phase-shift the coefficients already calculated at the previous level, as described in (7.20).

A far-field interaction at a given level  $\ell$  involves squares which are suitably far apart, certainly not adjacent. Hence, it is evident that no far interaction exists at level 1 (the four squares are adjacent each other) and it is not necessary to evaluate the coefficients  $\mathbf{M}_{G_i^1}$  and  $W_{G_i^1}$  for  $i = 0 \cdots 4$ . Therefore, the upward sweep can be halted at the minimum level  $\ell_{min}$  at which is still possible to have far-field interactions between squares. Referring to Fig. 7.5, for example,  $\ell_{min} = 2$ . At this level  $\ell_{min}$ , the side of a square is  $L/2^{\ell_{min}}$  where the edge of the square enclosing the scatterer has length  $L = l\lambda$ . To allow the possibility of far-field interactions, the

far-field distance (7.19) (suitably multiplied by the factor  $m_{\ell_{min}}$ ) must not exceed the maximum transverse dimension of the scatterer, i.e.

$$2 \frac{\left(\frac{L}{2^{\ell_{min}}} \sqrt{2}\right)^2}{\lambda} m_{\ell_{min}} < \sqrt{2}L \quad (7.24)$$

which yields

$$4^{\ell_{min}-1} > \frac{m_{\ell_{min}} l}{\sqrt{2}} \quad (7.25)$$

Once this step is completed all the characteristic coefficients associated with  $4^\ell$  squares at each level  $\ell$  have been evaluated. These quantities are required to calculate the far-fields of each group of currents at each level  $N_\ell \leq \ell \leq \ell_{min}$  in all discretised directions  $\widehat{\mathbf{R}}_{O_k}$  and will be used in the downward sweep.

In the second (downward) sweep, at a level  $\ell$ , for each square  $G_j^\ell$ , all far-field groups  $G_i^\ell$ ,  $i \neq j$ , are detected and their scattered fields in the direction of interaction  $i \rightarrow j$ , identified by the angle  $\tilde{\phi}$  are evaluated. In doing this the following interpolation rule for the coefficients  $\mathbf{M}_{G_i^\ell}$  and  $W_{G_i^\ell}$  is used

$$\begin{aligned} \begin{pmatrix} \mathbf{M}_{G_i^\ell} \\ W_{G_i^\ell} \end{pmatrix} (\tilde{\mathbf{R}}_O) = & \begin{pmatrix} \mathbf{M}_{G_i^\ell}(\widehat{\mathbf{R}}_{O_{\bar{k}+1}}) - \mathbf{M}_{G_i^\ell}(\widehat{\mathbf{R}}_{O_{\bar{k}}}) \\ W_{G_i^\ell}(\widehat{\mathbf{R}}_{O_{\bar{k}+1}}) - W_{G_i^\ell}(\widehat{\mathbf{R}}_{O_{\bar{k}}}) \end{pmatrix} \frac{\tilde{\phi}}{(\phi_{\bar{k}+1} - \phi_{\bar{k}})} \\ & + \begin{pmatrix} \phi_{\bar{k}+1} \mathbf{M}_{G_i^\ell}(\widehat{\mathbf{R}}_{O_{\bar{k}}}) - \phi_{\bar{k}} \mathbf{M}_{G_i^\ell}(\widehat{\mathbf{R}}_{O_{\bar{k}+1}}) \\ \phi_{\bar{k}+1} W_{G_i^\ell}(\widehat{\mathbf{R}}_{O_{\bar{k}}}) - \phi_{\bar{k}} W_{G_i^\ell}(\widehat{\mathbf{R}}_{O_{\bar{k}+1}}) \end{pmatrix} \frac{1}{(\phi_{\bar{k}+1} - \phi_{\bar{k}})} \end{aligned} \quad (7.26)$$

with  $\tilde{\mathbf{R}}_O = \cos \tilde{\phi} \widehat{\mathbf{i}} + \sin \tilde{\phi} \widehat{\mathbf{j}} = \mathbf{r}_{G_j^\ell} - \mathbf{r}_{G_i^\ell} / |\mathbf{r}_{G_j^\ell} - \mathbf{r}_{G_i^\ell}|$  and  $\phi_{\bar{k}} \leq \tilde{\phi} < \phi_{\bar{k}+1}$ . The coefficients are then multiplied by terms involving the Green's function of the distance between the far groups, as given in (7.16) and (7.17). Note that this step is conceptually equivalent to the *translation* operation of the MLFMA. However, there is the following difference: using (7.15), if  $P$  is the centre of the receiving group  $G_j^\ell$ , the electric field due to  $G_i^\ell$  over  $P$  is

$$\mathbf{E}_{G_i^\ell}(P) \approx -j\omega \mathbf{A}_{G_i^\ell}(\mathbf{R}_O) - \nabla_P \Phi_{G_i^\ell}(\mathbf{R}_O) \quad (7.27)$$

where

$$\mathbf{A}_{G_i^\ell}(\mathbf{R}_O) = \frac{\mu_0}{4\pi} \frac{e^{-jkR_O}}{R_O} \mathbf{M}_{G_i^\ell}(\tilde{\mathbf{R}}_O) \quad (7.28)$$

and

$$\Phi_{G_i^\ell}(\mathbf{R}_O) = -\frac{1}{j\omega 4\pi \epsilon_0} \frac{e^{-jkR_O}}{R_O} W_{G_i^\ell}(\tilde{\mathbf{R}}_O); \quad (7.29)$$

whereas, in the fast multipole approach, the field due to  $G_i^\ell$  would require the evaluation of the numerically more cumbersome term (3.21).

At this point one can distribute the far-field to the children of the square currently observed, i.e.  $G_j^\ell$ , through a phase-shifting operation, assuming the incoming far-field to be a plane wave impinging on  $G_j^\ell$ . The angle of arrival  $\phi_{inc}$  is such that  $|\phi_{inc} - \phi_i|_{i \in \{\bar{k}, \bar{k}+1\}}$  is minimum. At the next level, the far interactions between the children of the square observed ( $G_j^\ell$ ) and the children of the far groups  $G_i^\ell$ ,  $i \neq j$ , will not be computed, because they have already been accounted for at the parent level. Referring to Fig. 7.5, for example, the group  $G_0^2$  at level 2 is illuminated by the plane waves emanated by the far groups as illustrated. These plane waves, hence, may be shifted to the centres of the four children of  $G_0^2$ . For the group  $G_0^3$ , at level 3, the near-field area is detected. Part of the far-fields contributions to the field incoming on  $G_0^3$ , however, will not be evaluated, because it has been accounted for at the previous level (the gray region in the figure). At the finest level, the far-field incident on each square  $G_j^{N_l}$  from all of the registered directions is distributed to the triangular patches where the current basis functions reside. To help elucidate the last step of the downward sweep procedure, refer to Fig. 7.6 and consider the portion of the scatterer where  $G_j^{N_l}$  is located. The field, over that domain where the  $m$ -th current is (partially) defined  $T_m^\sigma$ , is due to the contributions from the nearby current elements, such as  $I_n \mathbf{f}_n(\mathbf{r})$ , and to the far-field contributions arriving from far groups, such as  $G_i^{N_l}$  and  $G_i^{N_l-1}$ . The far-field due to  $G_i^{N_l}$  is evaluated, with the aid of interpolation, using the quantities calculated and stored during the upward sweep and  $\phi_{\bar{k}} \leq \phi_{ij}^{N_l} < \phi_{\bar{k}+1}$ . The field is then distributed to  $T_m^\sigma$ . The far-field due to  $G_i^{N_l-1}$  has been evaluated simply using the plane wave which models



the field scattered by  $G_i^{N_i-1}$ , which was calculated at the previous level and then disseminated towards the four children of  $G_j^{N_i}$ .

The MLFAFFA, in common with all multi-level techniques, is most efficient when the scatterer is very large. In fact, in the upward pass a high number of entities is evaluated and stored. In regard to either the storage complexity or the computational complexity of the method, the savings will be made when a significant percentage of the stored quantities can be reused<sup>1</sup>. This occurs when the total number of far-field interactions (which decreases as the level decreases) is relatively high. When the number of unknowns is relatively large, say  $N > 10^4$ , the technique can be efficiently implemented with a storage that is  $\mathcal{O}(\alpha(N)N)$ , with  $\alpha(N) \ll N$ , as illustrated in Fig. 7.3 and a decreased computational complexity, because all the far interactions at each level  $\ell$  between groups of size  $N_G(\ell)$  are evaluated by  $\mathcal{O}(N_G(\ell))$  operations, as shown in the previous section.

### 7.2.3 Computational cost

In this section,  $N$  is the number of unknowns, i.e. the number of edges of the triangular mesh modelling the scatterer and  $N_\ell$  is the number of levels. An estimate of the computational cost of the MLFAFFA is sought. The upward pass requires, at each level, the evaluation of the characteristic coefficients. At the finest level, this requires

$$c_1 = \mathcal{O}(NK) \tag{7.30}$$

operations. In fact, the  $K$  characteristic coefficients must be evaluated for each triangle of the mesh and the number of triangles is of the same order as the number of edges. For the upper levels, the children's characteristic coefficients must be shifted and added for each parent square. Because at level  $\ell$ , there are  $4^\ell$  squares with each one having a maximum of four children (depending on the shape of the

<sup>1</sup>This is the reason for the threshold mentioned in section 7.2.1

scatterer) the number of operations to complete the upward pass may be written as

$$c_2 \leq \mathcal{O}\left(4K \sum_{\ell=N_\ell-1}^{\ell_{min}} 4^\ell\right) \quad (7.31)$$

with  $\ell_{min}$  being the minimum level at which far-field interactions can still be computed. For the downward pass, at each level  $\ell$ , for each square, the far-field incoming from the far groups in all the discretised directions must be calculated and this operation requires

$$c_3 = \mathcal{O}\left(\sum_{\ell=\ell_{min}}^{N_\ell} 4^\ell \widehat{F}(\ell)\right) \quad (7.32)$$

operations, where  $4^\ell \widehat{F}(\ell)$  may be thought of as the average number of far interactions at level  $\ell$ . To distribute the results at the finest level, following the same reasoning as for  $c_1$ ,

$$c_4 \leq \mathcal{O}(N\widehat{K}) \quad (7.33)$$

operations are performed where in this case  $\widehat{K}$  is the average number of plane wave far-fields impinging on each triangle of the mesh.

Thus, the total computational cost is given by

$$C = \sum_{n=1}^4 c_n + \mathcal{O}(N\alpha_{\mathcal{NF}}) \quad (7.34)$$

where  $\alpha_{\mathcal{NF}}$  is a constant related to the computation of the near-field interactions. Now, if  $N$  is relatively very large, i.e. if  $N \gg K$  and  $N \gg \alpha_{\mathcal{NF}}$ , the computational cost of the entire matrix-vector multiply is  $\mathcal{O}(\beta(N)N)$ , being  $\beta(N) \ll N$ .

### 7.3 Numerical results

Some numerical results are presented here for a flat square plate under plane wave incidence. The side of the square is  $L = 1.0m = 8.0\lambda$ , its vertices are located at

points  $(0, 0, 0)$ ,  $(L, 0, 0)$ ,  $(0, L, 0)$ ,  $(L, L, 0)$ . The electric field incident on the scatterer is a plane wave of unit amplitude

$$\mathbf{E}^i(\mathbf{r}) = e^{-j\mathbf{k}\cdot\mathbf{r}}\hat{\mathbf{x}} \quad (7.35)$$

where

$$\mathbf{k} = -\sin\theta_i\hat{\mathbf{y}} + \cos\theta_i\hat{\mathbf{z}}. \quad (7.36)$$

Referring to Fig. 7.7,  $\theta_i$  is the angle between the direction normal to the flat plate and the direction of incidence of the plane wave. The flat plate is modelled by a grid of triangular patches (see Fig. 7.7). In this case, the number of unknowns is  $N = 3008$ . This is the coarsest discretisation which is likely to provide us with a sufficiently accurate solution of the EFIE. For a better approximation  $N$  must be increased, say up to about 10000 for this particular example. One can appreciate now the huge storage complexity involved in numerically solving the EFIE using the ordinary CG method, for  $N^2$  complex values of the impedance matrix must be stored.

The electric current  $\mathbf{J}$  induced on the plate radiates the electric scattered field, i.e.  $\mathbf{E}^s(\mathbf{r})$ . Fig. 7.8 shows the amplitudes of the vector  $\mathbf{E}^s(\mathbf{r})$  evaluated for the two current distributions obtained by the usual CG method and the MLFAFFA when  $\theta_i = \pi/4$ . The observation point is chosen to be in the plane of the scatterer at angles  $\phi_k = 0.5k$  degrees,  $k = 0 \dots 719$ , at a distance  $1000\lambda$  from the centre of the plate.

Although the field results are satisfactory, they are related to far-field quantities, obtained by integrating the electric current and thereby possibly smoothing the effects of significant errors. Therefore to be fully convincing about the accuracy MLFAFFA results, another test result is presented out to reveal the quality of the MLFAFFA for the electric current. Fig. 7.9 shows the amplitude of the normalised component  $J_x$  of the current along the cut at  $x = L/2$  on the square flat plate, when  $\theta_i = \pi/2$ , obtained applying the MLFAFFA, the usual CG method and the

CG-FFT method as given in [40]. A very good agreement between the MLFAFFA solution and the CG-FFT and CG distributions is registered, especially around the edge  $y = L$ . Also, Fig. 7.10 compares the amplitudes of the vector  $\mathbf{E}^s(\mathbf{r})$  evaluated for the two current distributions obtained by the usual CG method and the MLFAFFA when  $\theta_i = \pi/2$ .

## 7.4 Summary

This chapter presented the Multi-Level Fast Far-Field Algorithm (MLFAFFA) for electromagnetic scattering in the three-dimensional case. The RWG basis function set was used to approximate the electric current density. The fast far-field approximation was derived in the three-dimensional case. It was shown that the electric field radiated at a far point by a distribution of electric current may be approximated in an elegant fashion upon which builds the MLFAFFA. The definition of far-field region was recalled and the issue of the selection of the near-field area was investigated mathematically.

The implementation of MLFAFFA was then presented. First of all, the necessary memory requirements were illustrated, reporting the observed behaviour of the storage required as a function of the number of unknowns related to the problem. It was shown that when the number of unknowns exceeds a given threshold, the MLFAFFA memory requirements are less cumbersome than in the typical MoM-CG case. The algorithm was presented, emphasising the multi-level feature of the FAFFA, introducing and illustrating the concept of levels. It was demonstrated that the translation step of the MLFAFFA is less complex than that of MLFMA. The computational cost of the MLFAFFA was then analysed and was shown that the computational complexity of the algorithm is less than the typical one of the MoM-CG algorithm. The MLFAFFA offers substantial memory and computational time savings when the number of unknowns is large. Numerical results were provided in the final part of the chapter to demonstrate the excellent agreement between the MoM-CG and the MLFAFFA algorithms for the numerical computation of scattered

fields and surface current distributions using the EFIE.

---

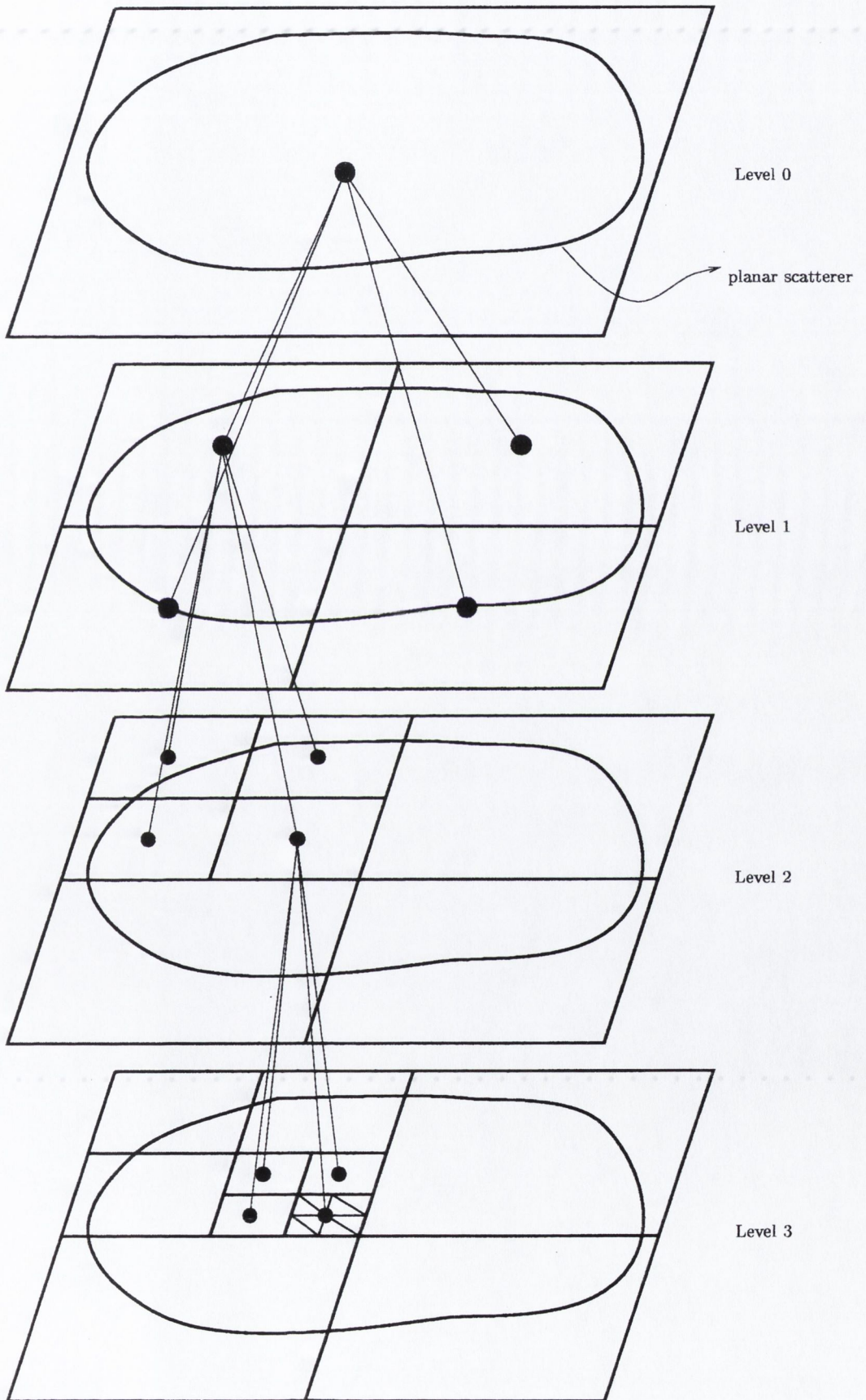


Figure 7.4: Tree-structured grid of groups at all levels in the MLFAFFA. At each level, a square contains triangular patches where current elements are defined.

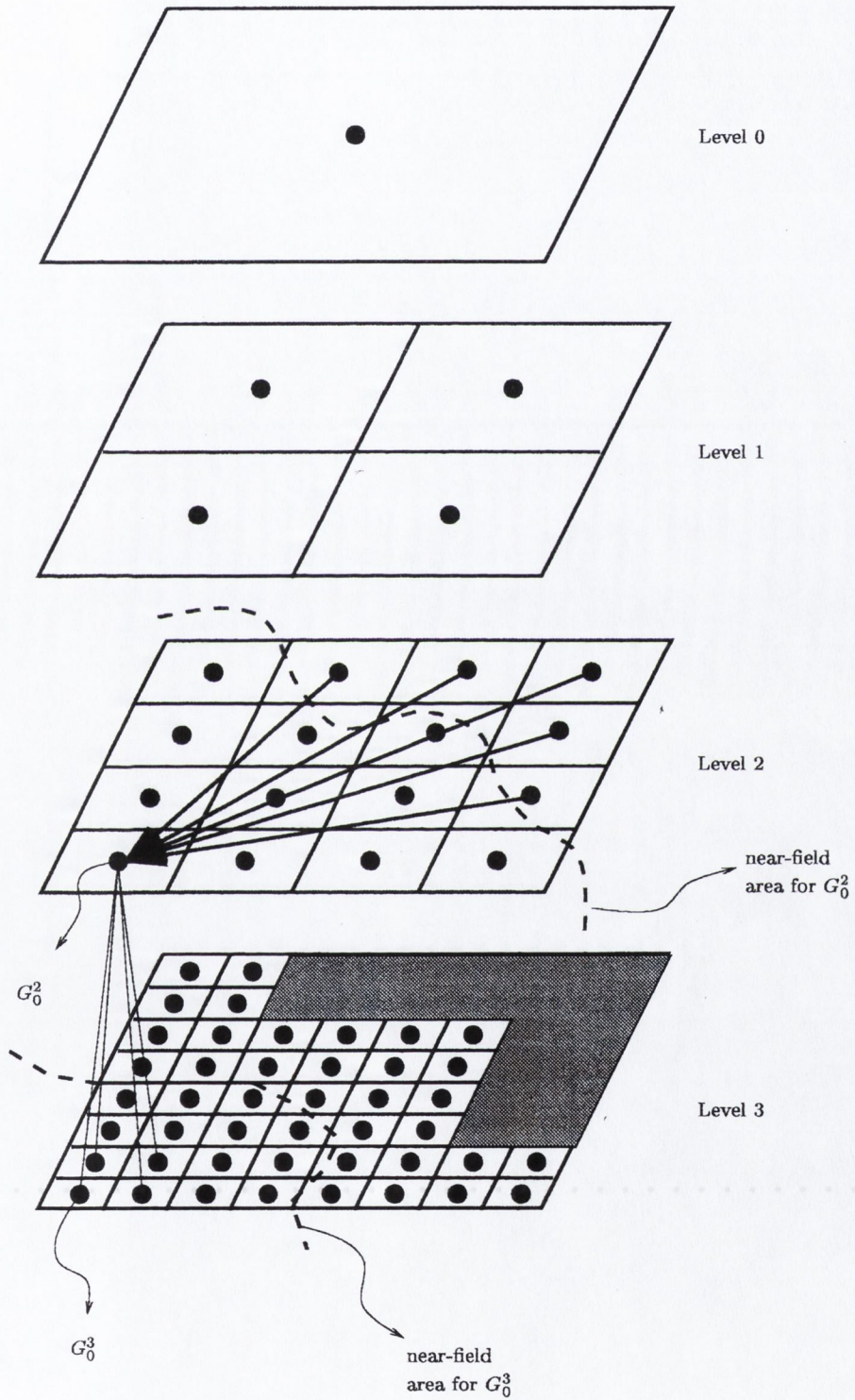


Figure 7.5: Far-field interactions at different levels in the MLFAFFA.

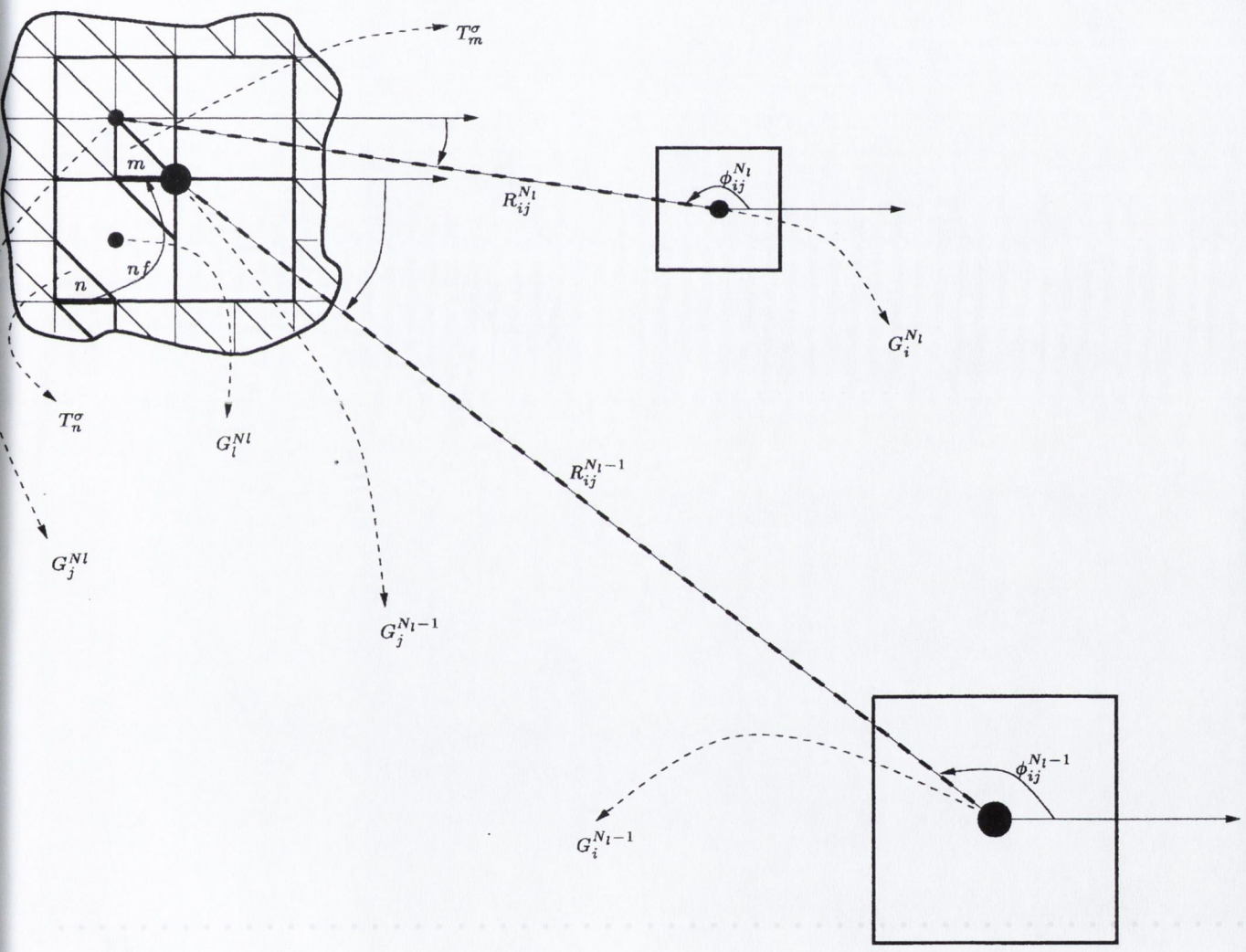


Figure 7.6: MLFAFFA downward sweep at the final level  $N_l$ : the near field interaction between  $n$  and  $m$  is labelled as  $nf$ .



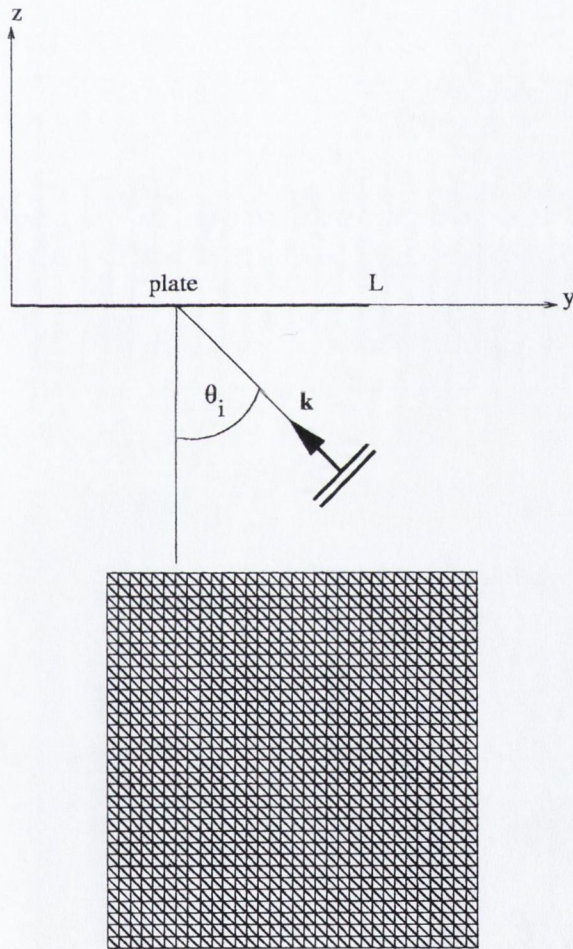


Figure 7.7: Geometry of the scattering problem and triangular mesh associated with the scatterer.

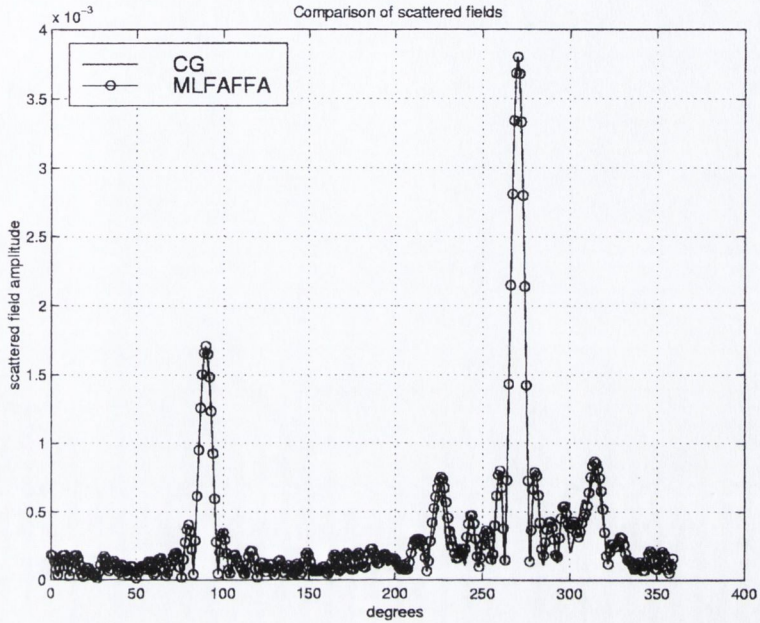


Figure 7.8: Amplitude of the scattered far-field due to the MLFAFFA and the CG currents induced on the plate when  $\theta_i = \pi/4$ .

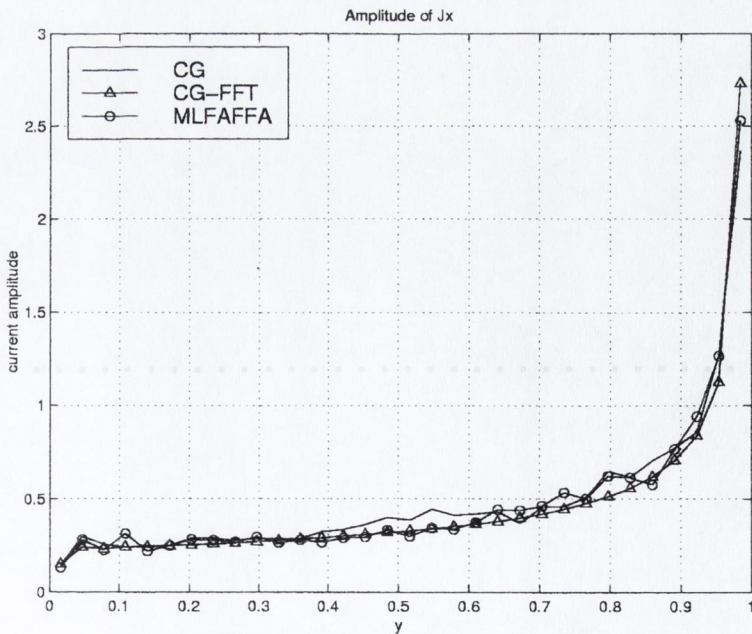


Figure 7.9: Amplitude of the MLFAFFA, the CG-FFT and the CG  $J_x/|\mathbf{H}^i|$  solutions along the cut at  $x = L/2$ .

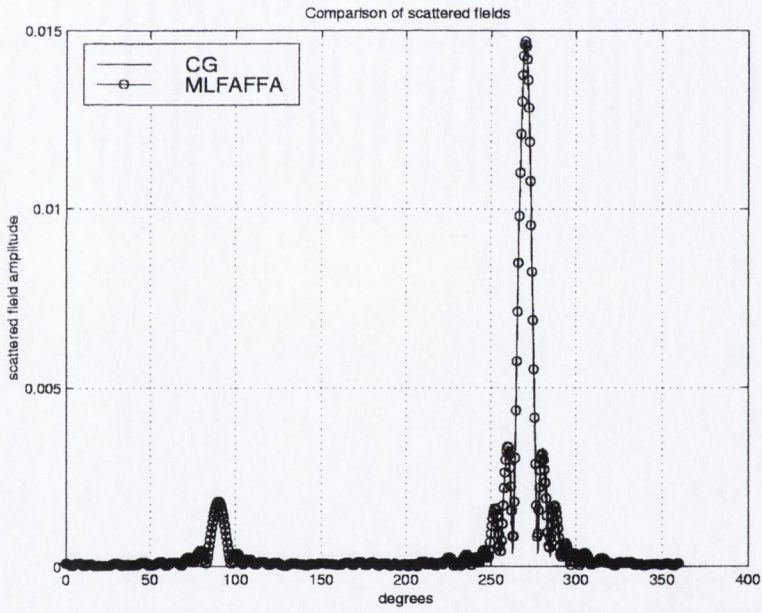


Figure 7.10: Amplitude of the scattered far-field due to the MLFAFFA and the CG currents induced on the plate when  $\theta_i = \pi/2$ .

---

## CONCLUSIONS

---

The contributions of this thesis are two novel extensions, to existing efficient computational methods for the analysis of high-frequency electromagnetic scattering from perfect electric conductors. The first, referred to by the acronym ANIM, is applicable to one-dimensional surfaces and extends the TIM method and the second, MLFAFFA, is applicable to two-dimensional surfaces and extends the FAFFA method. Also, a matrix formulation of TIM/ANIM and a novel numerical technique to evaluate the impedance matrix terms for the discretised EFIE using RWG basis functions are included in this work.

The ANIM (Analytical Interaction Method) renders the TIM (Tabulated Interaction Method) [62] more flexible. Both methods enable the rapid solution of grazing incidence high frequency propagation over large scale piecewise linear smooth conductors such as those used to render the abstraction of rolling terrain. Problems which require computational times of many hours using standard methods may be solved without substantial loss of accuracy in a few seconds using TIM or ANIM. Both methods achieve their savings in the spirit of FAFFA by grouping and reuse. Specifically, interactions between pairs of large subdomains are transmitted by plane waves travelling along the line connecting the subdomain centre-points. In contrast to FAFFA, the surface current density on linear subdomains of the surface is represented by a superposition of reference currents (FAFFA uses pulse functions). The reference currents are simply the currents excited by a discrete set of incident plane waves on a 2D planar strip of length equal to that of the subdomain. In the case of the TIM these reference currents are numerically evaluated and tabulated along with their far-field radiation patterns. The ANIM does away with the need for tabulation by proposing using carefully derived analytical results. The TIM tables

---

depend on the frequency and on the size of the portions of scatterer. When these both vary ANIM offers considerable storage savings over TIM. ANIM approximates the reference currents using a truncated version of the current induced on a PEC half-plane, truncated at the length of linear subdomain. It was shown that after expressing the reference currents in this simple way, the far-field radiated by those currents may be evaluated analytically using Fresnel's integrals. Numerical results were provided to demonstrate the accuracy of the scheme proposed.

The Multi-Level Fast Far-Field Algorithm was developed to speed up computation in large three-dimensional scattering problems. In contrast to TIM and ANIM which achieve their savings for a restricted, but important, class of scatterers, this method is general and may be applied to the numerical computation of electromagnetic wave scattering by objects of arbitrary shape and size. The integral equation was discretised using the Rao-Wilton-Glisson approach. It was demonstrated that electromagnetic interactions between surface subdomains of a homogeneous three-dimensional scatterer may be efficiently evaluated using a simple geometric approximation for the distance between pairs of interacting current elements on the two subdomains upon which depends the three-dimensional Green's function. This approximation is the essence of the three-dimensional extension of the FAFFA. The three-dimensional version of FAFFA adds no new fundamental ideas to that were not already implicit in the two-dimensional case. However, the implementation requires considerably more care and it was considered useful to investigate this extension using the Rao-Wilton-Glisson basis functions. The importance of pinpointing the near-field/far-field geometric threshold was also discussed and a novel recommendation was suggested. The Multi-Level Fast Far-Field Algorithm was then developed, implemented and tested. It was demonstrated that this technique can give substantial computational savings over MoM-CG when applied to the problem of electromagnetic scattering by electrically large bodies. The storage requirements of the method were also evaluated. In summary, the implementation of the Multi-Level Fast Far-Field Algorithm possesses the following features.

- The method is applicable to scattering by bodies of arbitrary shape embedded in an homogeneous three-dimensional medium containing sources.
- The algorithm has a computational complexity of  $\mathcal{O}(\beta(N)N)$  with  $\beta(N) \ll N$  when  $N \gg N_0$ , where  $N$  is the number of unknowns to be determined and  $N_0$  a threshold experimentally given by  $10^3 < N < 10^4$ . The complexity of the Moment Method-Conjugate Gradient scheme is  $\mathcal{O}(N^2)$ .
- The storage requirements of the method follow the same behaviour as the computational complexity. In contrast, the Moment Method-Conjugate Gradient scheme has a memory requirement of  $\mathcal{O}(N^2)$ .
- The algorithm is simple and may be implemented with lesser complexity than the Multi-Level Fast Multipole Algorithm (MLFMA). Specifically, there is no need to perform any operation involving Gegenbauer's addition theorem, whose implementation is somewhat complex.

Numerical results were provided to demonstrate the accuracy of the scheme proposed compared with reference solutions.

In addition to the aforementioned algorithms, two useful new results have been presented in this thesis. These are the matrix formulation of TIM/ANIM and a numerical method for evaluating the impedance matrix terms arising when the 3D EFIE is discretised using the Rao-Wilton-Glisson basis set. In order to obtain a full wave solution of the Electric Field Integral Equation, the Tabulated Interaction Method was developed in matrix form. It was demonstrated that the matrix produced is sparse. As a result, a significant reduction in storage requirements may be achieved. The Tabulated Interaction Method was also applied to the problem of electromagnetic scattering by periodic structures. Numerical results were provided to demonstrate the possibility of tackling this class of problems with substantial storage and CPU time savings. In solving the discretised EFIE using the new matrix formulation of TIM/ANIM a problem regarding the computations of

near-field interactions using FAFFA arose. A first attempt to overcome this feature was outlined.

A novel numerical technique to evaluate the impedance matrix terms for the electric field integral equation discretised using the Rao-Wilton-Glisson approach was also presented. The problem of interest is the numerical integration of the linear-shape functions times the three-dimensional Green's function on a plane triangle. This issue is of critical importance for the moment method discretisation of electrical field integral equations in the three-dimensional case. The typical approach to the solution of this problem was presented. This approach is based on the possibility of expressing the integrand as a sum of two functions: one singular function, which may be integrated analytically and a non-singular part which may be evaluated numerically. For the analytical evaluation of the singular part, a simple integration procedure was proposed. This involved dividing the domain of integration into two subdomains. One of these domains was chosen to be of infinitesimal size. As a result of a rigorous limit procedure, the integral over the infinitesimal domain evaluates to zero. The integral over the remaining domain was then evaluated using a simple numerical integration rule, after a change of coordinate system. It was shown that the final result converges in a faster way than that of the typical approach. Numerical results were provided to illustrate the accuracy of the fully numerical method proposed.

The extension of ANIM to three dimensions is an interesting prospect. Some issues that arise in this extension are outlined in the last chapter of the Appendix. Specifically, some mathematical tools for an extension of the Analytical Interaction Method to three dimensions are provided using the Physical Optics approximation. While more work is required to accomplish this task, directions for further research are provided.

---

## REVIEW OF BASIC ELECTROMAGNETICS

---

### A.1 Maxwell's equations

Electromagnetic phenomena are governed by a set of equations, known as Maxwell's equations. In differential form, Maxwell's equations are

$$\nabla \times \mathbf{e}(\mathbf{r}, t) = -\frac{\partial \mathbf{b}(\mathbf{r}, t)}{\partial t} \quad (\text{A.1})$$

$$\nabla \times \mathbf{h}(\mathbf{r}, t) = \frac{\partial \mathbf{d}(\mathbf{r}, t)}{\partial t} + \mathbf{j}(\mathbf{r}, t) \quad (\text{A.2})$$

$$\nabla \cdot \mathbf{d}(\mathbf{r}, t) = \rho(\mathbf{r}, t) \quad (\text{A.3})$$

$$\nabla \cdot \mathbf{b}(\mathbf{r}, t) = 0 \quad (\text{A.4})$$

where  $\mathbf{e}$  is the electric field intensity (volts/metre),  $\mathbf{b}$  the magnetic flux density (webers/square metre),  $\mathbf{h}$  the magnetic field intensity (amperes/metre),  $\mathbf{d}$  the electric flux density (coulombs/square metre),  $\mathbf{j}$  is the electric current density (amperes/square metre), which can include the conduction current density (due to charged particles moving over a certain direction) and the impressed electric current density (by a source),  $\rho$  represents the electric charge density (coulombs/cubic metre).

The fields  $\mathbf{b}$  and  $\mathbf{d}$  are not independent of the fields  $\mathbf{h}$  and  $\mathbf{e}$ :  $\mathbf{b} = \mathcal{F}_h(\mathbf{h})$  and  $\mathbf{d} = \mathcal{F}_e(\mathbf{e})$  where  $\mathcal{F}$  represents some operator. These relations are called *constitutive relations*. The operators  $\mathcal{F}_h$  and  $\mathcal{F}_e$  depend on the material properties of the medium. The simplest case is:  $\mathbf{b} = \mu\mathbf{h}$ ,  $\mathbf{d} = \epsilon\mathbf{e}$ . This is the case for a *linear, isotropic, causal, non dispersive, homogeneous, lossless* medium.  $\epsilon$  is the dielectric



permittivity ( $\epsilon = 8.854 \times 10^{-12}$  for free space) and  $\mu$  is the magnetic permeability of the medium ( $\mu = 4\pi \times 10^{-7}$  for free space).

By applying the divergence theorem and Stokes' theorem, the set of differential equations can be transformed into a set of integro-differential equations where the derivative is performed with respect to  $t$ . Further details may be found in [13], pp. 5-6.

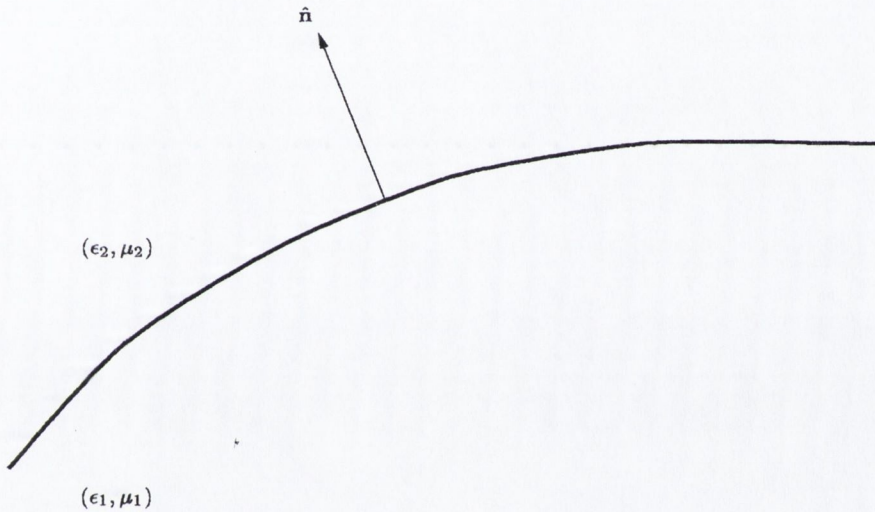


Figure A.1: Geometry for boundary conditions of electric and magnetic field: the interface between two different media (solid line) and its normal unit vector  $\hat{\mathbf{n}}$ . Medium 1 has properties  $\epsilon_1, \mu_1$ , medium 2 has properties  $\epsilon_2, \mu_2$ .

Maxwell's equations in integral form can be applied at an interface between two different media. The relations between the fields on either side of the interface are referred to as *boundary conditions*. Their derivation is straightforward and can be found in [13], pp. 13-19 and they are presented here for convenience. If  $\hat{\mathbf{n}}$  is the unit vector normal to the interface directed from medium 1 to medium 2, as illustrated in Fig. A.1, then the following conditions apply.

- $$\hat{\mathbf{n}} \times (\mathbf{e}_2 - \mathbf{e}_1) = 0 \tag{A.5}$$

*The tangential components of the electric field across an interface between two media are continuous.*

- $$\hat{\mathbf{n}} \cdot (\mathbf{d}_2 - \mathbf{d}_1) = \rho_s \tag{A.6}$$

The difference between the normal components of the electric flux density across an interface between two media is equal to the surface electric charge density  $\rho_S$ .

$$\bullet \quad \hat{\mathbf{n}} \times (\mathbf{h}_2 - \mathbf{h}_1) = \mathbf{j}_S \quad (\text{A.7})$$

The difference between the tangential components of the magnetic field across an interface between two media is equal to the linear electric current density  $\mathbf{j}_S$  residing on the surface.

$$\bullet \quad \hat{\mathbf{n}} \cdot (\mathbf{b}_2 - \mathbf{b}_1) = 0 \quad (\text{A.8})$$

The normal components of the magnetic flux density across an interface between two media are continuous.

The linear electric current density  $\mathbf{j}_S$  and the surface electric charge density  $\rho_S$  may exist along the interface or may be induced if either of the two media is a perfect electric conductor. Similar entities may be introduced if either of the two media is a perfect magnetic conductor. Although magnetic charges and magnetic currents are not physically realizable, equivalent magnetic charges and currents may be used to represent physical problems.

For time-harmonic fields  $\mathbf{v}(\mathbf{r}; t)$  such that

$$\mathbf{v}(\mathbf{r}; t) = \text{Re}\{\mathbf{V}(\mathbf{r})e^{j\omega t}\} \quad (\text{A.9})$$

the set of Maxwell's equations may be simplified

$$\nabla \times \mathbf{E}(\mathbf{r}) = -j\omega\mathbf{B}(\mathbf{r}) \quad (\text{A.10})$$

$$\nabla \times \mathbf{H}(\mathbf{r}) = j\omega\mathbf{D}(\mathbf{r}) + \mathbf{J}(\mathbf{r}) \quad (\text{A.11})$$

$$\nabla \cdot \mathbf{D}(\mathbf{r}) = \rho(\mathbf{r}) \quad (\text{A.12})$$

$$\nabla \cdot \mathbf{B}(\mathbf{r}) = 0 \quad (\text{A.13})$$

where  $\mathbf{E}, \mathbf{B}, \mathbf{J}, \mathbf{D}, \rho, \mathbf{H}$  are the time-harmonic forms of  $\mathbf{e}, \mathbf{b}, \mathbf{j}, \mathbf{d}, \rho, \mathbf{h}$ .

## A.2 Equivalence theorem and Induction theorem

The equivalence theorem and the induction theorem are outlined in this section. They arise frequently and will be stated with precision since they play a crucial role in electromagnetics. Other fundamental principles and theorems are clearly explained in [3], chapter 3.

- **Equivalence theorem**

The electric and magnetic fields due to sources bounded by a closed surface  $S$  may be expressed at the exterior of  $S$  in terms of equivalent sources located on  $S$ .

- **Induction theorem**

The electric and magnetic scattered fields outside a closed obstacle  $S$  illuminated by sources located at the exterior of  $S$  may be evaluated by placing, along the boundary of the obstacle, equivalent sources that radiate in the presence of the obstacle.

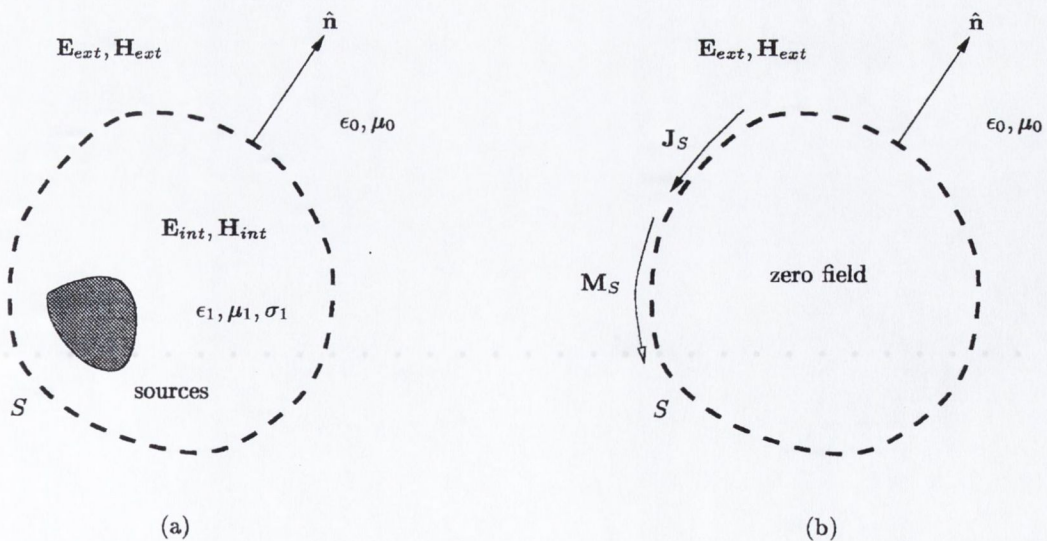


Figure A.2: Equivalence theorem geometry and transformation: (a) is the original problem, where  $S$  is a surface which encloses the sources, its exterior is free space; (b) is the equivalent geometry to determine the fields  $(\mathbf{E}_{ext}, \mathbf{H}_{ext})$  outside  $S$  due to the equivalent sources  $\mathbf{J}_S$  and  $\mathbf{M}_S$ .

## A.2.1 Equivalence theorem

Referring to Fig. A.2(a) let the sources internal to  $S$  produce the electromagnetic fields  $(\mathbf{E}_{int}, \mathbf{H}_{int})$  inside  $S$  and  $(\mathbf{E}_{ext}, \mathbf{H}_{ext})$  outside  $S$ . Suppose that the space external to  $S$  is free space. Now, the field 0 in the interior of  $S$  and  $(\mathbf{E}_{ext}, \mathbf{H}_{ext})$  outside  $S$  is postulated. To support this field, which is discontinuous over  $S$ , there must exist surface currents  $\mathbf{J}_S$  and  $\mathbf{M}_S$  such that (see boundary conditions introduced in section A.1)

$$\mathbf{J}_S = \hat{\mathbf{n}} \times \mathbf{H}_S \quad \mathbf{M}_S = -\hat{\mathbf{n}} \times \mathbf{E}_S \quad (\text{A.14})$$

where the fields  $\mathbf{E}_S$  and  $\mathbf{H}_S$  are the values of  $\mathbf{E}$  of the fields due to the sources evaluated at  $S$  and  $\hat{\mathbf{n}}$  is the unit normal vector pointing outward the surface  $S$ . Using theory of potentials, as described in [13], it can be shown that formal expressions may be employed to derive the electromagnetic fields due to the equivalent sources given in (A.14), which radiate in an unbounded medium having the same properties as the exterior of  $S$ , i.e. free space in this case. Specifically, the fields radiated by a set of sources  $\mathbf{J}$ ,  $\mathbf{M}$  in free space may be expressed in terms of the magnetic and vector potentials,  $\mathbf{A}$  and  $\mathbf{F}$ , using

$$\mathbf{E} = \frac{\nabla \nabla \cdot \mathbf{A} + k^2 \mathbf{A}}{j\omega\epsilon_0} - \nabla \times \mathbf{F} \quad (\text{A.15})$$

$$\mathbf{H} = \frac{\nabla \nabla \cdot \mathbf{F} + k^2 \mathbf{F}}{j\omega\mu_0} + \nabla \times \mathbf{A} \quad (\text{A.16})$$

where

$$\mathbf{A}(\mathbf{r}) = \int_S \mathbf{J}(\mathbf{r}') \frac{e^{-jk|\mathbf{r}-\mathbf{r}'|}}{4\pi|\mathbf{r}-\mathbf{r}'|} dS' \quad (\text{A.17})$$

and

$$\mathbf{F}(\mathbf{r}) = \int_S \mathbf{M}(\mathbf{r}') \frac{e^{-jk|\mathbf{r}-\mathbf{r}'|}}{4\pi|\mathbf{r}-\mathbf{r}'|} dS' \quad (\text{A.18})$$

where  $S$  is the surface that contains the sources,  $\mathbf{r}$  is the field point and  $\mathbf{r}'$  is the source point (or integration point) and  $k^2 = \omega^2 \epsilon_0 \mu_0$ . The field evaluated using the formal expressions (A.15) and (A.16) is the field postulated a priori, i.e. 0 at the interior of  $S$  and  $(\mathbf{E}_{ext}, \mathbf{H}_{ext})$  outside  $S$ . Thus, *it is possible to express the field external to a surface  $S$  which contains sources as a function of the tangential components of the electromagnetic fields over  $S$ .*

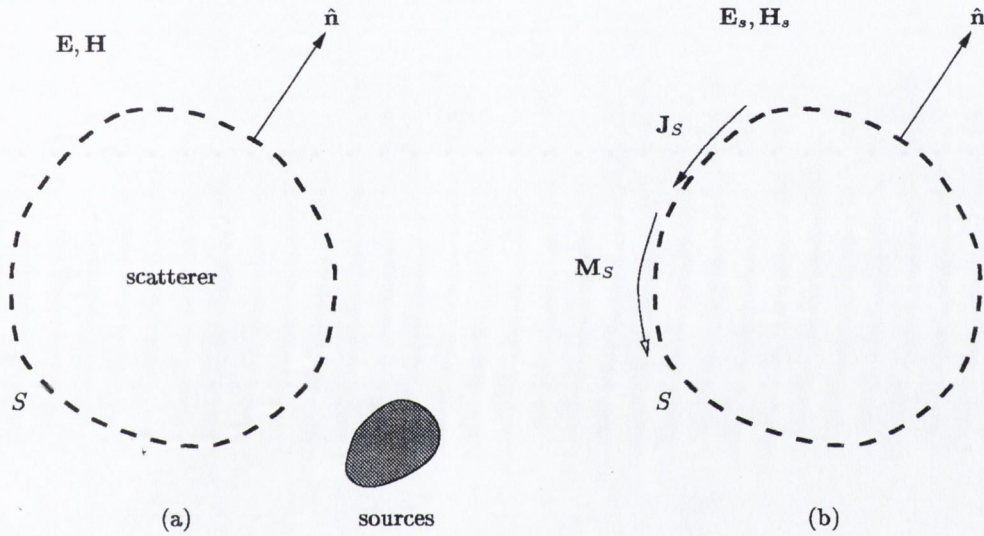


Figure A.3: Induction theorem geometry and transformation: (a) is the original problem; (b) is the resulting problem to be solved to determine the scattered fields  $(\mathbf{E}_s, \mathbf{H}_s)$  outside the scatterer.

### A.2.2 Induction theorem

The geometry displayed in Fig. A.3 is now considered: the sources are external to a surface  $S$  which bounds the *scatterer*. Define the incident field as the field due to the sources when the scatterer is absent, say  $(\mathbf{E}_i, \mathbf{H}_i)$ . Define the *scattered* field as the field external to the obstacle due to the currents (polarization and conduction) on the surface  $S$ . Now define the following electromagnetic fields  $(\mathbf{E}, \mathbf{H})$  internal to the obstacle and  $(\mathbf{E}_s, \mathbf{H}_s)$  external to the scatterer. Again to support these fields, which are discontinuous across  $S$  one must postulate the surface currents

$$\mathbf{J}_S = \hat{\mathbf{n}} \times (\mathbf{H}_s - \mathbf{H}) \quad \mathbf{M}_S = -\hat{\mathbf{n}} \times (\mathbf{E}_s - \mathbf{E}) \quad (\text{A.19})$$

and using the fact that  $\mathbf{E} = \mathbf{E}_s + \mathbf{E}_i$  and  $\mathbf{H} = \mathbf{H}_s + \mathbf{H}_i$ , it follows that

$$\mathbf{J}_S = \mathbf{H}_i \times \hat{\mathbf{n}} \quad \mathbf{M}_S = \hat{\mathbf{n}} \times \mathbf{E}_i \quad (\text{A.20})$$

These currents produce the postulated fields when they radiate in the presence of the obstacle. It is useful to point out that the currents given by (A.20) do not radiate in an unbounded medium, as the equivalent currents given in the equivalence theorem. We cannot use, thus, the formal expressions derived using a classical potential theory approach as it is instead possible in the equivalence theorem.

The geometry represented in Fig. A.3 represents the *scattering problem*: the problem is to determine the scattered fields due to the presence of the body illuminated by the external sources. Computational electromagnetics is that area of scientific research which develops, explores and implements numerical techniques to solve the scattering problem.

### A.3 Surface integral equations

Consider the geometry illustrated in Fig. A.4, where two regions of space, defined as  $\Gamma_1$  and  $\Gamma_2$ , are separated by a surface  $S$ .  $\Gamma_2$  contains a set of sources and one or more perfectly electrically conducting objects. Furthermore, the material properties ( $\epsilon$  and  $\mu$ ) of the two spaces are different:  $\Gamma_2$  is inhomogeneous, while  $\Gamma_1$  is assumed to be perfectly homogeneous. It is assumed also that region  $\Gamma_1$  contains sources which, without loss of generality, will be taken to be electrical current sources.  $S_\infty$  is any closed surface at infinity. Applying Maxwell's equations (see [21], pp. 11-12) the following equation is obtained

$$\int \int_S [\mathbf{E}_1 \cdot (-\hat{\mathbf{n}} \times \mathbf{H}_2 - \mathbf{H}_1 \cdot (-\mathbf{E}_2 \times \hat{\mathbf{n}})] dS' = \int \int \int_{\Gamma_1} \mathbf{E}_2 \cdot \mathbf{J}_1 dV' \quad (\text{A.21})$$

In (A.21),  $\mathbf{E}_1$  and  $\mathbf{H}_1$  are the electric and magnetic fields due to the electric current source  $\mathbf{J}_1$  radiating in  $\Gamma_1$ ,  $\mathbf{E}_2$  and  $\mathbf{H}_2$  are the fields in  $\Gamma_1$  produced by the sources in the inhomogeneous space  $\Gamma_2$ . It is assumed that the electric current source is such

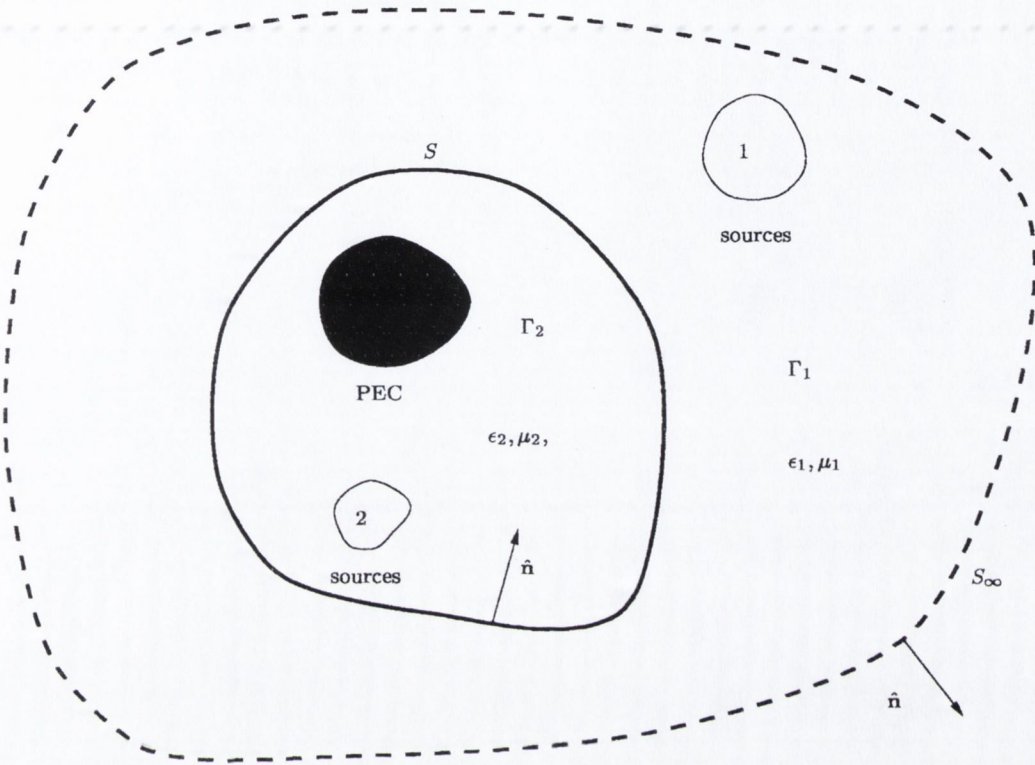


Figure A.4: Illustration to explain the surface equivalence principle: two media of different properties are separated by  $S$ ,  $\Gamma_1$  and  $\Gamma_2$  are the volumes enclosed by  $S$  and  $S_\infty - S$ .  $S_\infty$  extends to infinity. The presence of a perfect electric conductor in  $\Gamma_2$  is also assumed.

that  $\mathbf{J}_1 = \hat{\mathbf{u}}\delta(\mathbf{r} - \mathbf{r}')$  where  $\mathbf{r}$  is the source point and  $\mathbf{r}'$  is the integration point in the integral of (A.21) and  $\delta(\mathbf{r} - \mathbf{r}')$  is the Dirac delta function <sup>1</sup> of the difference  $\mathbf{r} - \mathbf{r}'$ . Then (A.21) can be written as

$$\hat{\mathbf{u}} \cdot \mathbf{E}_2|_{\mathbf{r} \in \Gamma_1} = \int \int_S [\mathbf{E}_1 \cdot (-\hat{\mathbf{n}} \times \mathbf{H}_2 - \mathbf{H}_1 \cdot (-\mathbf{E}_2 \times \hat{\mathbf{n}})] dS' \tag{A.24}$$

<sup>1</sup>The Dirac delta function is a distribution function which may be defined as

$$\int \delta(\mathbf{r} - \mathbf{r}') dV' = 1 \tag{A.22}$$

$$\int \delta(\mathbf{r} - \mathbf{r}') f(\mathbf{r}') dV' = f(\mathbf{r}) \tag{A.23}$$

where the integral is evaluated over a volume which contains both the points  $\mathbf{r}$  and  $\mathbf{r}'$ .

The fields due to  $\mathbf{J}_1$  may be evaluated using potential theory, as pointed out in section A.2, specifically, it may be written

$$\mathbf{E}_1 = \frac{\nabla' \nabla' \cdot + k^2}{j\omega\epsilon_1} (\hat{\mathbf{u}} G(|\mathbf{r} - \mathbf{r}'|)) \quad (\text{A.25})$$

$$\mathbf{H}_1 = \nabla' \times (\hat{\mathbf{u}} G(|\mathbf{r} - \mathbf{r}'|)) \quad (\text{A.26})$$

where use of dyadic notation is made (see chapter 2) and  $G(|\mathbf{r} - \mathbf{r}'|)$  is the Green's function. The properties of Green's function are given in [5] and it is

$$G(|\mathbf{r} - \mathbf{r}'|) = \frac{e^{-jk|\mathbf{r} - \mathbf{r}'|}}{4\pi|\mathbf{r} - \mathbf{r}'|} \quad (\text{A.27})$$

where  $k$  is the wavenumber associated with the homogeneous medium. For the space  $\Gamma_1$ ,  $k = \omega\sqrt{\mu_1\epsilon_1}$ , and  $\epsilon_1$  and  $\mu_1$  are, respectively, the permittivity and permeability of the medium. Exploiting the symmetry of the Green's function, one may write.

$$\begin{aligned} \hat{\mathbf{u}} \cdot \mathbf{E}_2|_{\mathbf{r}} = \hat{\mathbf{u}} \cdot \frac{\nabla \nabla \cdot + k^2}{j\omega\epsilon_1} \int \int_S (-\hat{\mathbf{n}} \times \mathbf{H}_2) G(|\mathbf{r} - \mathbf{r}'|) dS' \\ - \hat{\mathbf{u}} \cdot \nabla \times \int \int_S (-\mathbf{E}_2 \times \hat{\mathbf{n}}) G(|\mathbf{r} - \mathbf{r}'|) dS' \end{aligned} \quad (\text{A.28})$$

Equation (A.28) is a consequence of the equivalence theorem which is outlined in section A.2. *The field due to the sources of the inhomogeneous medium  $\Gamma_2$  at a location  $\mathbf{r} \in \Gamma_1$  can be expressed as a function of the tangential fields on the surface  $S$ , using the equivalent surface currents  $\mathbf{J}_S = -\hat{\mathbf{n}} \times \mathbf{H}_2$  and  $\mathbf{M}_S = -\mathbf{E}_2 \times \hat{\mathbf{n}}$ .* Assume now that the normal vector points out the region  $\Gamma_2$  (Fig. A.4). Recalling the equivalence theorem, the combination of the original sources and the equivalent surface currents defined in (A.28) give null fields into  $\Gamma_2$ . Thus, the inhomogeneities in region  $\Gamma_2$  may be removed without perturbing the fields located in  $\Gamma_1$  and the original problem is replaced by the *equivalent exterior (to  $S$ ) problem* in which the original sources are joined by a set of equivalent surface currents given by  $\hat{\mathbf{n}} \times \mathbf{H}_2 = \hat{\mathbf{n}} \times \mathbf{H}_1$  and  $\mathbf{E}_2 \times \hat{\mathbf{n}} = \mathbf{E}_1 \times \hat{\mathbf{n}}$ . The advantage of this transformation is that although the original problem is not solved yet, since the equivalent surface



currents are not determined, all the sources (known and unknown) now radiate in a homogeneous space and the task of finding the electromagnetic fields in this environment is more straightforward than that one associated with the inhomogeneous space of the original problem.

Suppose now that region  $\Gamma_2$  is a PEC. In this case, because of the boundary conditions, the equivalent magnetic surface current is zero. In region  $\Gamma_1$  the electromagnetic field ( $\mathbf{E}$ ,  $\mathbf{H}$ ) is the sum of the field due to the sources labelled as 1 in Fig. A.4, which radiates in the unbounded medium having the same material properties of  $\Gamma_1$ , and the field due to the equivalent (in this case physically residing on  $S$ ) electric surface current located on  $S$ ,

$$\mathbf{J}_S = \hat{\mathbf{n}} \times \mathbf{H}. \quad (\text{A.29})$$

Since this current is unknown, it is necessary to set up an equation for it. Having defined the field due to the sources labelled with 1 in Fig. A.4 as ( $\mathbf{E}_i$ ,  $\mathbf{H}_i$ ), it follows from (A.28) that

$$\mathbf{E}_i = \mathbf{E} - \frac{\nabla \nabla \cdot + k^2}{j\omega\epsilon_1} \mathbf{A} \quad (\text{A.30})$$

$$\mathbf{H}_i = \mathbf{H} - \nabla \times \mathbf{A} \quad (\text{A.31})$$

with

$$\mathbf{A} = \int \int_S \mathbf{J}_S G(|\mathbf{r} - \mathbf{r}'|) dS' \quad (\text{A.32})$$

Imposing the boundary conditions on the surface  $S$ , one obtains a pair of integro-differential equations, valid at any point on  $S$ <sup>2</sup>

$$\hat{\mathbf{n}} \times \mathbf{E}_i = -\hat{\mathbf{n}} \times \left( \frac{\nabla \nabla \cdot + k^2}{j\omega\epsilon_1} \mathbf{A} \right)_S \quad (\text{A.33})$$

<sup>2</sup>The notation  $(f(\mathbf{r}))_S$  means that the scalar field  $f$  is evaluated at  $\mathbf{r} \in S$ . Similar notation holds for vector fields.

$$\hat{\mathbf{n}} \times \mathbf{H}_i = \mathbf{J}_S - \hat{\mathbf{n}} \times (\nabla \times \mathbf{A})_{S^+} \quad (\text{A.34})$$

where  $\hat{\mathbf{n}}$  is the unit vector normal to the surface  $S$ , pointing outwards. Equation (A.33) is usually referred to as electric field integral equation (EFIE), while equation (A.34) is called magnetic field integral equation (MFIE). (A.34) is valid at an infinitesimal distance outside the surface of the scatterer (which is indicated by  $S^+$  in (A.34)).

---

## HIGH FREQUENCY TECHNIQUES

---

In a scattering problem, the term *high frequency* refers to the size of the scatterer compared with the incident wavelength. When the scatterer is more than ten wavelengths in size then the interaction can be considered in the *high-frequency range*. In this range, prediction techniques can be developed essentially assuming that each part of the body interacts with the incident field independently of all other parts. This approximation, however, is not valid when the scatterer is for example a reentrant structure in which case internal reflections must be taken into account. Furthermore, high-frequency techniques can be applied only to shapes that can be described mathematically. When the geometry of the body is complex, the scatterer must be approximated as a set of adjacent simple geometries, such as elementary surfaces and simple curves. What follows is a brief and by no means exhaustive historical description of high-frequency methods is outlined.

### B.1 Geometric Optics

The oldest and simplest high-frequency technique is the Geometric Optics (GO) method developed in the earliest stages of astronomy to build optical systems. The method assumes that the incident wavelength is infinitesimal and in this limit it is derived that the energy propagates along tubes, using the relation

$$U(x, y, z) = P(x, y, z)e^{jkS(x, y, z)} \quad (\text{B.1})$$

where  $U$  is the energy and  $P$  and  $S$  are functions of the spatial coordinates  $(x, y, z)$ . The GO method is essentially a *ray tracing* technique as it predicts the direction of ray-tubes in which the energy emanates from the scatterer when this is illuminated by an external source.

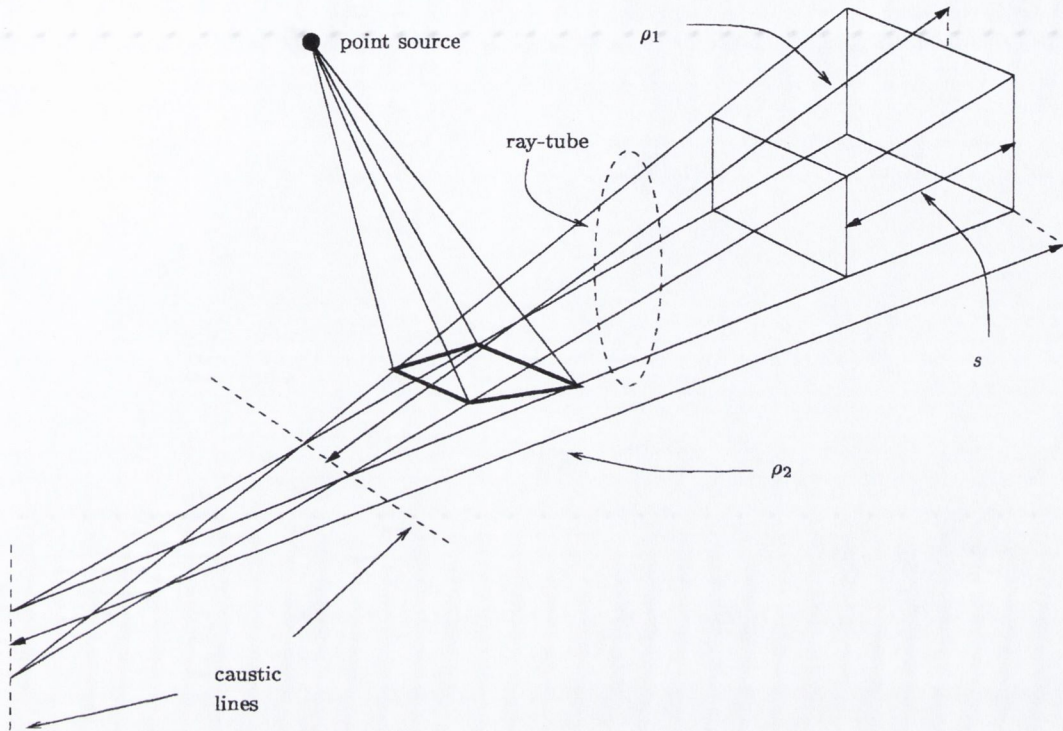


Figure B.1: Geometrical optics reflection from a doubly curved surface.

To illustrate the essence of GO method, refer to Fig. B.1: a point source illuminates a doubly curved surface patch. As a result of the principle of conservation of energy along a ray tube, it is found that:

$$\frac{A_s^2}{A_0^2} = \frac{\rho_1 \rho_2}{(s + \rho_1)(s + \rho_2)} \quad (\text{B.2})$$

where  $s$  is the distance between the two ends of the tube and  $\rho_1$  and  $\rho_2$  are the principal radii of curvature of the wavefront at the output of the tube.  $\rho_1$  and  $\rho_2$  are functions of the radii of curvature of the incident wavefront and of the scatterer at the point of reflection, as given in [27]. The ratio  $A_s/A_0$  is between the field intensities at the input and the output of the tube. Because of the differences in the surface curvature, the sides of the ray-tube do not intersect at a point, but at two different segments that lie on the *caustic lines*. It is this the reason why the specular reflection of a point by a curved mirror is blurred and the effect is called *astigmatism*. Eq.(B.2) describes the decay of electromagnetic energy as we

move further away from the surface of the scatterer. However, it fails to have any mathematical meaning when both  $\rho_1$  and  $\rho_2$  tend to  $\infty$ , which is the case of planar scatterers.

## B.2 Physical Optics

The mathematical catastrophe returned by the application of GO to planar scatterers can be avoided by means of the Physical Optics (PO) technique. The starting point is the well known Stratton-Chu formula, which is derived in detail in [14]. It gives the scattered field in terms of a closed surface integral. The scattered far field by a closed body can be expressed as follows

$$\mathbf{E}_s = jkG_0 \int_S \hat{\mathbf{s}} \times [\hat{\mathbf{n}} \times \mathbf{E} - \zeta_0 \hat{\mathbf{s}} \times (\hat{\mathbf{n}} \times \mathbf{H})] e^{jk\mathbf{r} \cdot (\hat{\mathbf{i}} - \hat{\mathbf{s}})} dS \quad (\text{B.3})$$

where  $k$  is the wavenumber,  $G_0$  is the Green's function (A.27) evaluated from a fixed point  $O$ , included in the volume enclosed by  $S$ ,  $\hat{\mathbf{s}}$  is the unit vector along the scattering direction,  $\hat{\mathbf{n}}$  is the unit vector normal to  $S$  pointing outwards,  $\mathbf{E}$  is the electric field on  $S$ ,  $\zeta_0$  is the free space impedance,  $\mathbf{H}$  is the magnetic field on  $S$ ,  $\mathbf{r}$  is the position vector from the fixed point  $O$  and  $\hat{\mathbf{i}}$  is the unit vector along the direction of incidence. Observe that although the Stratton-Chu formula is valid for closed surfaces, a generalisation of it to open surfaces by adding a line integral term is given in Stratton's book [1], pp. 464-470.

The PO approximation consists of taking the tangential components of the fields in the integral in (B.3) as those that would be present if the body had been perfectly smooth and flat at the surface element of integration  $dS$ . Moreover, the tangential components are assumed to be zero in the shadowed region, i.e. the region of the scatterer which is not directly illuminated by the source. The PO method provides satisfactory results if the surface is not too small in size and if the scattering direction does not differ too much from the specular direction. Although PO overcomes GO's failures, it does not yield accurate results away from the specular direction, because the contributions from the edges of the finite structure are ignored.

### B.3 Geometrical Theory of Diffraction

In one of his works, published in 1957 [23], Keller proposed a new general expression for the field scattered by an edge. Although Sommerfeld had already tackled the problem of scattering from an infinite half-plane in his book about Optics [6], Keller adjusted this solution to the three-dimensional case, introducing hence the Geometrical Theory of Diffraction (GTD). Keller also introduced the concept of *cone of diffracted rays* from an edge. Suppose to have an infinite edge and an electromagnetic wave illuminates it. The component of the electric field parallel to the edge will be reflected in one direction, because of the infinite dimension of the edge over that direction. Instead, the transverse component will propagate in all directions perpendicular to the edge, because the transverse dimension of the edge is null. The effect is that from a point on the infinite edge a cone of rays emanates. Keller gave an expression for the field propagating in this cone-tube. The result is that the diffracted electric field by an edge is

$$\mathbf{E}_d = -\Gamma \frac{e^{jks}}{\sin^3(\beta)} [(\hat{\mathbf{t}} \cdot \mathbf{E}_i)(X - Y)\hat{\mathbf{s}} \times (\hat{\mathbf{s}} \times \hat{\mathbf{t}}) + \zeta_0(\hat{\mathbf{t}} \cdot \mathbf{H}_i)(X + Y)(\hat{\mathbf{s}} \times \hat{\mathbf{t}})] \quad (\text{B.4})$$

where  $\Gamma$  is a factor that depends on the type of excitation,  $\beta$  is the angle that the incident wave makes with the edge,  $\hat{\mathbf{t}}$  is the unit vector directed along the edge,  $\hat{\mathbf{s}}$  is the unit vector directed along the distance between the edge and the far field point  $\mathbf{r}$ ,  $X$  and  $Y$  are two coefficients, *Keller's coefficients*, which depend on the angle of incidence and diffraction,  $\psi_i$  and  $\psi_s$

$$X = \frac{(1/n) \sin(\pi/n)}{\cos(\pi/n) - \cos[(\psi_s - \psi_i)/n]} \quad (\text{B.5})$$

$$Y = \frac{(1/n) \sin(\pi/n)}{\cos(\pi/n) - \cos[(\psi_s + \psi_i)/n]} \quad (\text{B.6})$$

Referring to Fig. B.2, there are two directions along which either  $X$  or  $Y$  become infinite. Specifically, when  $\psi_s = \pi - \psi_i$  then  $Y \rightarrow \infty$ . This direction is usually defined as *Reflection Boundary (RB) direction*. When  $\psi_s = \pi + \psi_i$  then  $X \rightarrow \infty$ . This direction is referred to as *Shadow Boundary (SB) direction*.

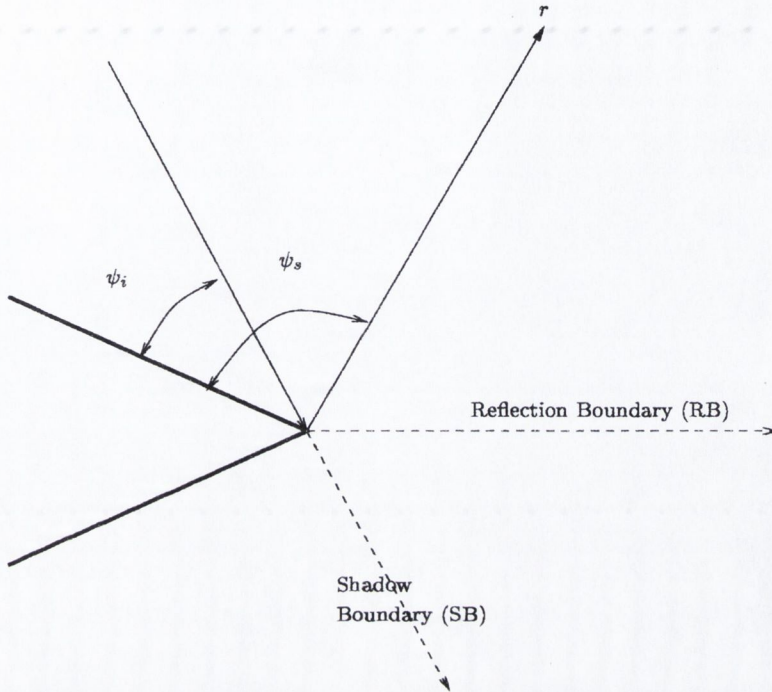


Figure B.2: Edge diffraction geometry.

The drawbacks of Keller's theory, which represented a breakthrough in the field of high-frequency techniques, are essentially three. The scattered field becomes infinite when the observation point lies on one of the two boundaries, the reflection or the shadow. The expression for the scattered field is valid only for the points contained in Keller's cone. Finally, the number of points which contribute to the scattered fields arising from a curved edge is infinite and an infinite result is then obtained.

## B.4 Uniform Theory of Diffraction

Because of the failure of Keller's theory at curved edges and because of the importance of achieving a sound theory to describe scattering from obstacles such as rings or tubes, a further breakthrough had to occur in the development of high-frequency methods. In 1974 an article [27] was published in which a Uniform Theory of Diffraction (UTD) was introduced to the electromagnetic research community.

Essentially, a new expression for both Keller's coefficients  $X$  and  $Y$  was given. The new equations were such that the problem of infinite values of  $X$  and  $Y$  at RB and SB was overcome. However, UTD does not release Keller's GTD from presenting mathematical catastrophes for cases of bodies of revolution. Thus, a new approach was to be developed.

## B.5 Method of Equivalent Currents

The method of equivalent currents was introduced by Millar [22]. Essentially, it employs equivalent fictitious currents to determine the scattered fields. Knott and Senior [25] proposed the following equivalent currents existing at all points on a ring illuminated by an incident field  $(\mathbf{E}_i, \mathbf{H}_i)$

$$\mathbf{I}_e = \frac{-2\hat{\mathbf{t}}(\mathbf{E}_i \cdot \hat{\mathbf{t}})(X - Y)}{jk\zeta_0 \sin^2(\beta)} \quad (\text{B.7})$$

$$\mathbf{I}_m = \frac{-2\hat{\mathbf{t}}(\mathbf{H}_i \cdot \hat{\mathbf{t}})(X + Y)\zeta_0}{jk \sin^2(\beta)} \quad (\text{B.8})$$

In fact, these currents are postulated and their values depend on Keller's coefficients. The expressions of these currents was then further refined by Michaeli [28]. Here a rigorous derivation of the equivalent currents for a wedge is illustrated. The expressions are rather cumbersome, however they pose no problems for numerical calculation. Finally, although the scattering direction is not longer confined to a generator of Keller's cone, the currents become singular in the transition regions SB and RB.

## B.6 Physical Theory of Diffraction

Along with Keller, Ufimtsev developed a theoretical model which could overcome the limits of PO by a different approach [24]. His theory is referred to Physical Theory of Diffraction (PTD). Ufimtsev started from the expression of the diffracted field by a half-plane. The solution of this problem is well known and is given in



terms of an integral performed on the complex plane along the Sommerfeld contour, given in [5]. Being interested to evaluate the contribution of the edge, Ufimtsev further subtracted the incident field and the PO approximation of the scattered field. In this process, he mathematically justified the truncation of the surface integral yielding the PO contribution. Finally, he expressed the edge diffracted field as function of diffraction coefficients which do not possess the singular behaviour as Keller's  $X$  and  $Y$ .

GTD coefficients diverge to  $\infty$  over the direction RB and SB. The first phenomenon can be physically explained by the fact that Keller derived the coefficients referring to the infinite wedge solution. Thus in the specular direction there is an infinity of rays. Also, consider the shadow boundary. Just inside it, the incident field vanishes, just outside it, it is the full incident field. The diffraction coefficient must cancel completely the incident field over the entire half-space screened from the incident wave by the edge structure. Hence the coefficient raises to  $\infty$ .

The PO contribution from an infinite surface must also rise to  $\infty$  because of the size of the surface. Indeed, in Ufimtsev's theory the PO contribution is subtracted from Keller's coefficients and that is why what remains in the diffraction from the edge alone is finite. In order to deal with finite structure the approach hence can be: calculate the edge-diffracted fields by means of PTD and surface contribution (finite) by PO. However, as in Keller's UTD, also in Ufimtsev's PTD the results provided are valid only if the observation point belongs to the cone of diffracted rays.

## B.7 The Incremental Length Diffraction Theory

As Michaeli proposed a set of equivalent current to compute the scattered field by a wedge at any angle of observation, hence extending Keller's GTD, Mitzner introduced the concept of Incremental Length Diffraction Coefficient (ILDC) to extend PTD to any angle of observation. In his work [26], Mitzner expresses the far field diffracted by an element of the illuminated wedge  $dt$  in terms of a dyadic

diffraction coefficient  $\bar{D}$

$$\mathbf{E}_d = E_i \frac{e^{j(kR - \pi/4)}}{\sqrt{2\pi R}} \bar{D} \hat{\mathbf{e}} dt \quad (\text{B.9})$$

where  $\hat{\mathbf{e}}$  is a unit vector aligned along the incident electric field polarisation. The expression of the dyadic coefficient is a function of the angles of incidence and scattering, as well as the interior half-wedge half angle. In this brief section, it is important to emphasise that Mitzner's results extended Ufimtsev's PTD to arbitrary directions, the same way Michaeli's equivalent currents extend Keller's theory.

Unfortunately, none of the four theories provides accurate results for the solution of scattering problems where long structures are illuminated at grazing incidence. The main point is that although high-frequency methods can describe accurately electromagnetic scattering by simple structures for which it is possible to recall classical results, they fail to be a satisfactory candidate to model a large set of geometries that often arise in reality, such as long smooth objects.

---

## DIFFERENTIAL EQUATIONS SOLVERS

---

Differential equation methods numerically solve Maxwell's equations or partial differential equations associated with the electromagnetic problem. These techniques can be subdivided into Finite Element Method (FEM) and Finite Difference Time Domain method (FDTD). They are simple as far their formulation is concerned, they are useful to model scattering from complex penetrable bodies and they are associated with sparse matrices, while integral equation methods lead to fully dense matrices. However, the differential equation solvers do not incorporate the Sommerfeld boundary condition that is essential to the solution of Maxwell's equations. Sommerfeld's boundary condition states that the electromagnetic fields due to a set of sources all contained into a finite volume  $V$  and radiating in free space comply with the following relation at infinity

$$\lim_{r \rightarrow \infty} r(\mathbf{E} + \zeta_0 \hat{\mathbf{r}} \times \mathbf{H}) = 0 \quad (\text{C.1})$$

Thus, to model the usual scattering problem, with a set of sources and a finite body radiating in an unbounded medium, Sommerfeld's condition, also known as *radiation condition* must be necessarily taken into account.

### C.1 Finite Difference Time Domain

The Finite Difference Time Domain (FDTD) method is a numerical technique which is applicable to a wide range of problems. One of the main advantages of using such technique is that FDTD method treats transients in time domain. The starting point is the set of the two Maxwell's curl equations in the time domain. The problem is displayed in Fig. C.1, where the scatterer having material properties different

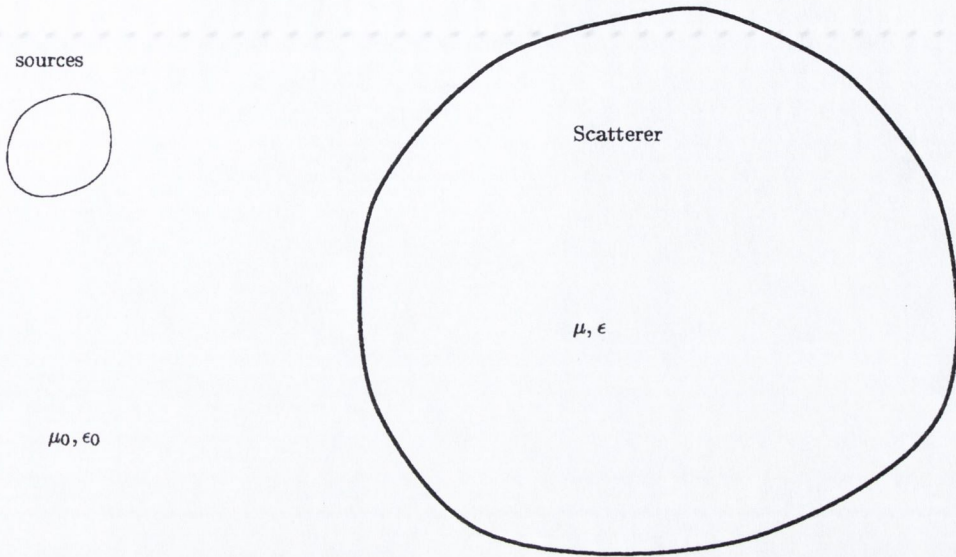


Figure C.1: FDTD method

from free space is illuminated by the sources located outside it. By splitting the total field into the two components *incident* and *scattered* fields, it can be shown (see [16], pp. 12-16) that the scattered field satisfies the following equations, either inside and outside  $V$

$$\nabla \times \mathbf{e}_s = -\mu \frac{\partial \mathbf{h}_s}{\partial t} - (\mu - \mu_0) \frac{\partial \mathbf{h}_i}{\partial t} \quad (\text{C.2})$$

$$\nabla \times \mathbf{h}_s = \epsilon \frac{\partial \mathbf{e}_s}{\partial t} + \sigma \mathbf{e}_s + (\epsilon - \epsilon_0) \frac{\partial \mathbf{e}_i}{\partial t} + \sigma \mathbf{e}_i \quad (\text{C.3})$$

If the scatterer is a perfect electric conductor (PEC) then the equations for the electric scattered field are

$$\frac{\partial \mathbf{e}_s}{\partial t} = \frac{1}{\epsilon_0} \nabla \times \mathbf{h}_s \quad (\text{C.4})$$

outside the scatterer and

$$\mathbf{e}_s = -\mathbf{e}_i \quad (\text{C.5})$$

inside the scatterer.

Replacing derivatives with finite differences, we obtain a set of equations, valid for the  $x$  component of the electric scattered field

$$\frac{e_{x,s}^n - e_{x,s}^{n-1}}{\Delta t} = \frac{1}{\epsilon_0} \left( \frac{\Delta h_{z,s}^{n-\frac{1}{2}}}{\Delta y} - \frac{\Delta h_{y,s}^{n-\frac{1}{2}}}{\Delta z} \right) \quad (\text{C.6})$$

Equation (C.6) is in essence the FDTD code: the  $x$  component of the electric scattered field is updated from its prior value at  $(n - 1)$  and the curl of  $\mathbf{h}$  at the time  $(n - 1/2)$ . The temporal interleaving between  $\mathbf{e}$  and  $\mathbf{h}$  is called *leap-frog in time* approach. After each update of  $\mathbf{e}$  and  $\mathbf{h}$  the process is repeated.

Constructing a FDTD code requires preliminary considerations, such as choosing the size of the cell of the grid where the discretisation of the differential equations is performed. It is obviously very difficult to provide a universal rule, being the accuracy of the numerical simulation varying with the type of problem analysed. In cases of very accurate radar cross section determination, the size of the side of a cell can be  $\lambda/20$  and in other cases reasonable results have been achieved for  $\lambda/4$ . Intimately related to the size of the cell is the time step  $\Delta t$ . Once the cell has been fixed in size,  $\Delta t$  must obey the Courant condition, given in [16] p. 32. Finally, when the problem one attempts to solve is located in free space, as the case of a scatterer radiating towards infinity, the FDTD approach must be suitably modified by applying an outer radiation boundary condition which estimates the missing field components just outside the problem space. A typical technique is to assume that a locally plane wave is propagating out of the space and estimating the fields for the outward travelling plane wave on the boundary by looking at the fields just within the boundary.

## C.2 Finite Element Method

In this section, we formulate the essence of the Finite Element Method (FEM) in one of its more popular hybridisation with the boundary integral methods, as given in [29].

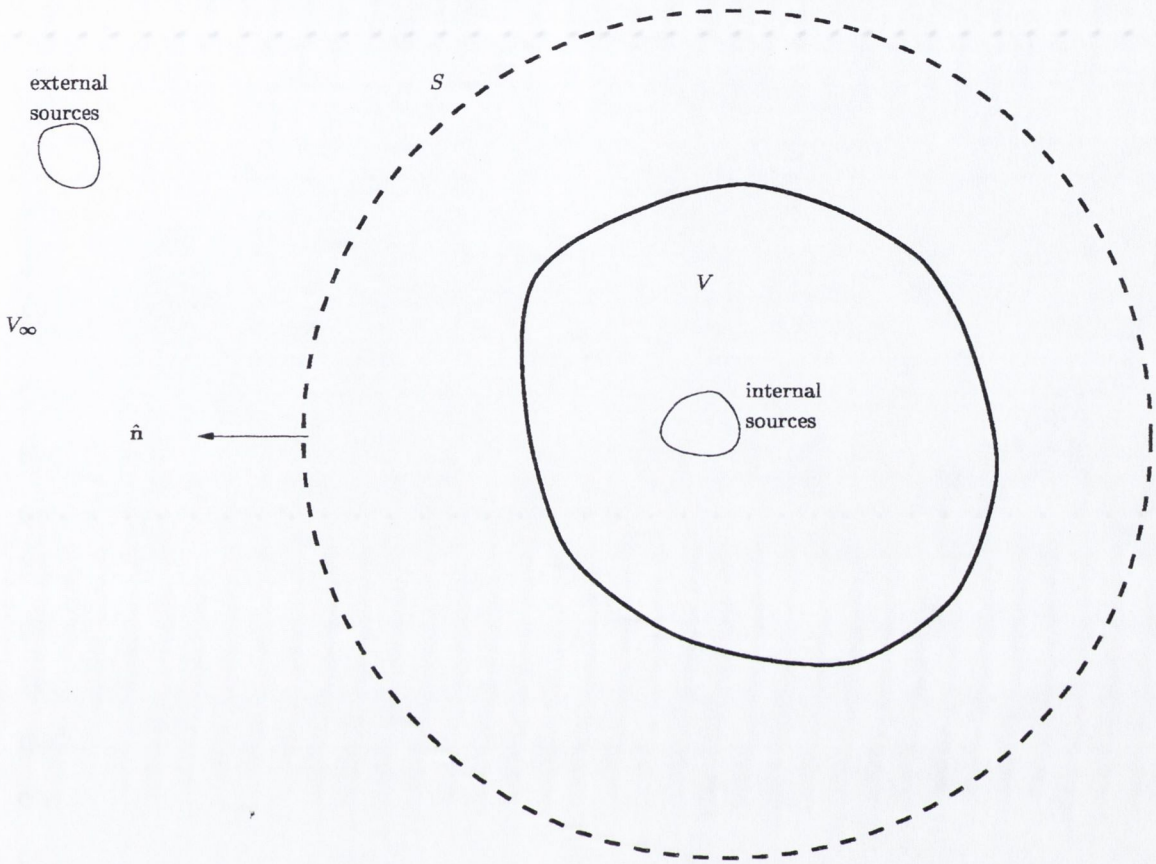


Figure C.2: FEM problem

Referring to Fig. C.2, it is of interest to compute the fields due to the sources (external or internal) in the presence of three-dimensional structure immersed in an infinite homogeneous medium. The three-dimensional body is enclosed in a fictitious surface  $S$ . In the volume  $V$ , the following vector equation holds

$$\nabla \times \left( \frac{1}{\mu_r} \nabla \times \mathbf{E} \right) - k^2 \epsilon_r \mathbf{E} = -jk\zeta_0 \mathbf{J}_{int} + \nabla \times \left( \frac{1}{\mu_r} \mathbf{M}_{int} \right) \quad (\text{C.7})$$

In solving (C.7), a usual approach is considering a functional of the field  $\mathbf{E}$ ,  $F(\mathbf{E})$ , which is stationary with respect to the solution of (C.7). Following this reasoning, the vector  $\mathbf{E}$  can be found by enforcing

$$\delta F(\mathbf{E}) = 0 \quad (\text{C.8})$$

where the symbol  $\delta$  denotes the first-order variation of  $F$  about  $\mathbf{E}$ . The fields outside  $S$  can be instead represented, using the equivalence theorem as the sum of the incident field, due to the sources external to  $S$ , and the field radiated outside  $S$  in an unbounded medium by the set of equivalent sources located on the fictitious surface  $S$  and function of the unknown fields on  $S$ . Basically, these formal expressions are to be matched with the solution of the equation (C.7) at the boundary  $S$ .

The FEM discretisation is the subdivision of the volume  $V$  into a finite number of small volume elements, such as rectangular bricks. Then, either the electric field and the magnetic field are expressed as a superposition of suitably weighted vector basis functions which are defined in  $V$ . The coefficients of the expansions are to be determined. The expressions of the fields are then substituted in (C.8) and applying the Rayleigh-Ritz procedure, a matrix equation is obtained. This procedure is described for example in [15]. To solve the matrix equation, a boundary condition on  $S$  is required and this is provided by the equation which is satisfied by the fields outside  $S$  in terms of the tangential components of the fields over  $S$  itself. Once a complete system of equations for the coefficients of the basis expansions of the fields is obtained, it can be solved by means of various techniques as pointed out in [29]. The resultant matrix is sparse and can be efficiently solved and stored.

---

## MATHEMATICAL FORMULAE FOR ANIM IN THREE DIMENSIONS

---

Chapter 5 presented the ANIM, a numerical technique that achieves massive computational savings when compared to other numerical schemes, such as MoM-CG, FMM and FAFFA described, respectively, in chapters 2, 3 and 4. ANIM was developed for the case of electromagnetic scattering from two-dimensional piecewise linear smooth electrically large surfaces. This chapter presents some mathematical tools that might be found useful in developing an extension of ANIM to three dimensions, for the case of scattering from piecewise *planar* smooth surfaces. In three dimensions, a surface may be modeled as an aggregation of triangular patches. If the surface is *large*, the application of FMM or FAFFA becomes prohibitive, due to enormous storage requirements.

ANIM is based upon two main results: (i) the incident field on portions of scatterer may be expressed as a sum of plane waves arriving from a finite number of directions, (ii) the far-field scattered by portions of scatterer may be expressed analytically. Section D.1 and section D.2 present a possible extension of ANIM main results to three dimensions. Section D.3 is devoted to the plane wave expansion of the near-field due to the PO current induced on a triangular patch illuminated by a plane wave.

### D.1 Extension of ANIM to the three-dimensional case

The subscatterers are PEC planar triangular patches. They correspond to the PEC segments for the two-dimensional case introduced along TIM in chapter 4. A plane wave incident on a planar triangular patch is illustrated in Fig. D.1. The incident



electric field  $\mathbf{E}_{inc}$ , hence, may be expressed as

$$\mathbf{E}_{inc} = \mathbf{E}_0 e^{-j\mathbf{k}\cdot\mathbf{r}} \quad (\text{D.1})$$

where

$$\mathbf{k} = -k(\sin \theta \cos \phi \hat{\mathbf{x}} + \sin \theta \sin \phi \hat{\mathbf{y}} + \cos \phi \hat{\mathbf{z}}) \quad (\text{D.2})$$

is the wave vector and  $\theta$  and  $\phi$  are related to the direction of incidence, as illustrated in Fig. D.1 and  $\hat{\mathbf{x}}$  is the unit vector related to the  $x$  axis and similar definition holds for  $\hat{\mathbf{y}}$  and  $\hat{\mathbf{z}}$ . A discretisation of the angles of incidence may be now introduced, so that if (see Fig. D.1)

$$\theta_a < \theta < \theta_b \quad (\text{D.3})$$

and

$$\phi_a < \phi < \phi_b \quad (\text{D.4})$$

then the following approximation holds

$$\mathbf{E}_{inc} = \mathbf{E}_0 e^{-j\mathbf{k}\cdot\mathbf{r}} \approx \sum_{i=1}^4 \mathbf{E}_0^i e^{-j\mathbf{k}_i\cdot\mathbf{r}} \quad (\text{D.5})$$

which is the extension of (4.27) to the three-dimensional case. In (D.5), the index  $i$  assumes the values  $1 \cdots 4$  and

$$\mathbf{k}_1 = -k(\sin \theta_a \cos \phi_a \hat{\mathbf{x}} + \sin \theta_a \sin \phi_a \hat{\mathbf{y}} + \cos \phi_a \hat{\mathbf{z}}) \quad (\text{D.6})$$

$$\mathbf{k}_2 = -k(\sin \theta_a \cos \phi_b \hat{\mathbf{x}} + \sin \theta_a \sin \phi_b \hat{\mathbf{y}} + \cos \phi_b \hat{\mathbf{z}}) \quad (\text{D.7})$$

$$\mathbf{k}_3 = -k(\sin \theta_b \cos \phi_a \hat{\mathbf{x}} + \sin \theta_b \sin \phi_a \hat{\mathbf{y}} + \cos \phi_a \hat{\mathbf{z}}) \quad (\text{D.8})$$

$$\mathbf{k}_4 = -k(\sin \theta_b \cos \phi_b \hat{\mathbf{x}} + \sin \theta_b \sin \phi_b \hat{\mathbf{y}} + \cos \phi_b \hat{\mathbf{z}}) \quad (\text{D.9})$$

$$\mathbf{E}_0^1 = \mathbf{E}_0 \psi_{aa} \quad (\text{D.10})$$

$$\mathbf{E}_0^2 = \mathbf{E}_0 \psi_{ab} \quad (\text{D.11})$$

$$\mathbf{E}_0^3 = \mathbf{E}_0 \psi_{ba} \quad (\text{D.12})$$

$$\mathbf{E}_0^4 = \mathbf{E}_0 \psi_{bb} \quad (\text{D.13})$$

where the interpolating factors  $\psi$  are defined in a similar fashion as in (4.31). For example

$$\psi_{aa} = \left(1 - \frac{|\theta - \theta_a|}{\Delta_\theta}\right) \left(1 - \frac{|\phi - \phi_a|}{\Delta_\phi}\right) \quad (\text{D.14})$$

where

$$\Delta_\theta = \theta_b - \theta_a \quad (\text{D.15})$$

and

$$\Delta_\phi = \phi_b - \phi_a \quad (\text{D.16})$$

with  $\theta_a, \theta_b, \phi_a$  and  $\phi_b$  illustrated in Fig. D.1. The electric current induced on  $T$  by the plane wave illustrated in Fig. D.1 is approximated using the PO approximation, introduced in section B.2. Hence, the current  $\mathbf{J}(x, y)$  residing on  $T$  lying on the plane  $x - y$  is approximated as

$$\mathbf{J}(x, y) \approx 2\hat{\mathbf{n}} \times \mathbf{H}_{inc}(x, y) \quad (\text{D.17})$$

where  $\mathbf{H}_{inc}(x, y)$  is the incident magnetic field and  $\hat{\mathbf{n}}$  is the unit vector normal to  $T$  illustrated in Fig. D.2. Next section presents the evaluation of the far-field scattered by the PO current.

## D.2 Far-field scattered by a triangular patch illuminated by a plane wave using the PO approximation

The far-field scattered by a triangular patch  $T$  illuminated by a plane wave is evaluated in this section. The geometry is illustrated in Fig. D.3(a). The physical

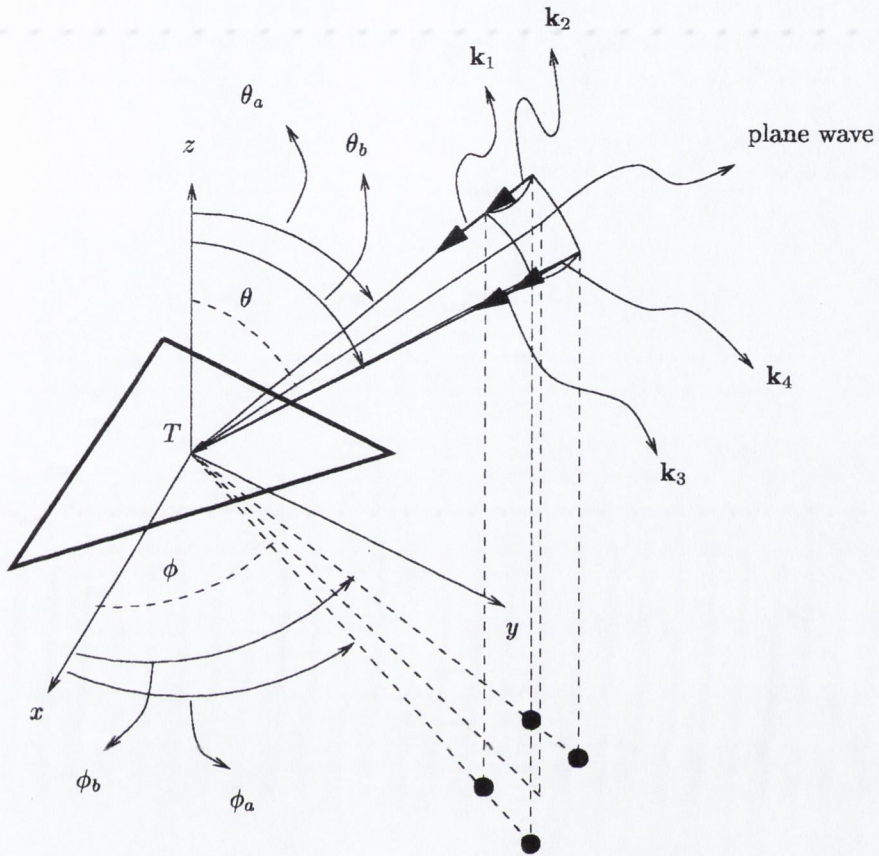


Figure D.1: Geometry of the discretisation (D.5) for the three-dimensional case.

optics (PO) current is postulated (see (D.17)). The incident electric field is a plane wave, i.e.

$$\mathbf{E}_{inc} = \mathbf{E}_0 e^{-j\mathbf{k}\cdot\mathbf{r}} \tag{D.18}$$

where the propagation vector  $\mathbf{k}$  is given by

$$\mathbf{k} = -k(\sin \theta_i \cos \phi_i \hat{\mathbf{x}}_c + \sin \theta_i \sin \phi_i \hat{\mathbf{y}}_c + \cos \theta_i \hat{\mathbf{z}}_c) \tag{D.19}$$

with the angles  $\theta_i$  and  $\phi_i$  illustrated in Fig. D.3(a). The unit vectors associated with the rectangular coordinate system (for convenience centred at the centroid of the triangle) are  $\hat{\mathbf{x}}_c$ ,  $\hat{\mathbf{y}}_c$  and  $\hat{\mathbf{z}}_c$ . In (D.18)  $\mathbf{E}_0$  is a vector of rectangular components

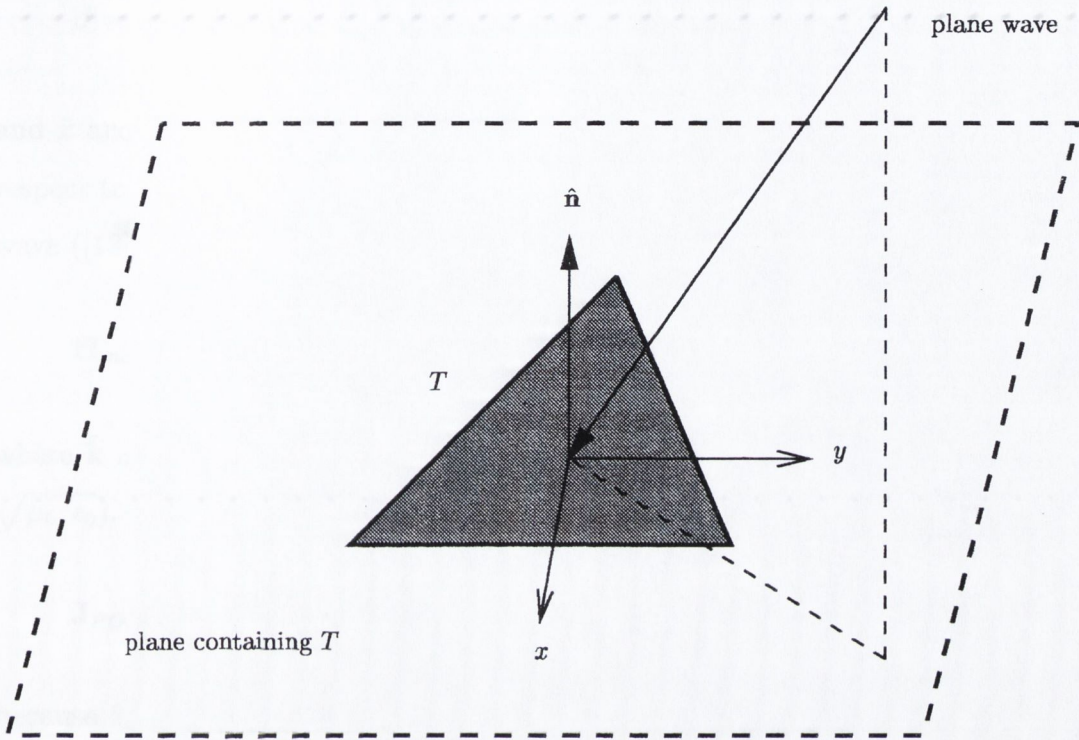


Figure D.2: Physical Optics approximation for the current on  $T$ . The vector  $\hat{\mathbf{n}}$  points outwards the plane containing  $T$ .

$E_{0_x}$ ,  $E_{0_y}$  and  $E_{0_z}$  and  $\mathbf{r}$  is the vector

$$\mathbf{r} = \tilde{x}\hat{\mathbf{x}}_c + \tilde{y}\hat{\mathbf{y}}_c + \tilde{z}\hat{\mathbf{z}}_c \tag{D.20}$$

It follows readily that

$$\mathbf{E}_0 = \mathbf{E}_{inc}(\tilde{x} = 0, \tilde{y} = 0, \tilde{z} = 0) \tag{D.21}$$

i.e. the vector  $\mathbf{E}_0$  is the value of the incident electric field at the centroid of the triangular patch.  $T$  is assumed to be on the plane  $z_c = 0$ . Then the incident electric field on  $T$  is

$$\mathbf{E}_{inc}|_{(z_c=0)} = \mathbf{E}_0 e^{-jk(\alpha\tilde{x} + \beta\tilde{y})} \quad (\tilde{x}, \tilde{y}) \in T \tag{D.22}$$

where

$$\alpha = -\sin \theta_i \cos \phi_i \tag{D.23}$$

$$\beta = -\sin \theta_i \sin \phi_i \quad (D.24)$$

and  $\tilde{x}$  and  $\tilde{y}$  are the coordinates of any point  $\mathbf{r}'$  in the plane of the triangle with respect to its centroid  $C$ , as illustrated in Fig. D.3(b). From the definition of plane wave ([13], chapter 4), the magnetic field is given by

$$\mathbf{H}_{inc} = \frac{1}{\zeta_0} \hat{\mathbf{k}} \times \mathbf{E}_{inc} \quad (D.25)$$

where  $\hat{\mathbf{k}}$  is the unit vector parallel to  $\mathbf{k}$  and  $\zeta_0$  is the free space impedance ( $\zeta_0 = \sqrt{\mu_0/\epsilon_0}$ ). It follows that the PO current (D.17) over the triangle is

$$\mathbf{J}_{PO} = 2\hat{\mathbf{z}}_c \times \mathbf{H}_{inc} \quad (D.26)$$

because  $\hat{\mathbf{z}}_c$  is the unit vector normal to the triangle. Developing the cross product

$$\hat{\mathbf{k}} \times \mathbf{E}_{inc} = \alpha E_{0_x} (-\hat{\mathbf{y}}_c) + \beta E_{0_z} \hat{\mathbf{x}}_c + \gamma E_{0_x} \hat{\mathbf{y}}_c + \gamma E_{0_y} (-\hat{\mathbf{x}}_c) \quad (D.27)$$

where  $\alpha$  is given in (D.23),  $\beta$  in (D.24) and

$$\gamma = -\cos \theta_i, \quad (D.28)$$

a compact expression for the PO current may be derived

$$\mathbf{J}_{PO} = \frac{2}{\zeta_0} e^{-jk(\alpha\tilde{x} + \beta\tilde{y})} \mathbf{v} \quad (D.29)$$

where the vector  $\mathbf{v}$  has been defined as

$$\mathbf{v} = (\beta E_{0_z} - \gamma E_{0_y}) \hat{\mathbf{y}}_c - (\gamma E_{0_x} - \alpha E_{0_z}) \hat{\mathbf{x}}_c. \quad (D.30)$$

To evaluate the field scattered by the PO current, it is necessary to calculate the vector potential  $\mathbf{A}$ , that depends on the term ([13], chapter 6)

$$\frac{\mu}{4\pi} \int_T \mathbf{J}_{PO} \frac{e^{-jkR}}{R} dS_c \quad (D.31)$$

where  $R$  is the distance between the observation point (its spherical coordinates are  $(r, \phi_s, \theta_s)$  illustrated in Fig. D.3(a)) and the integration point of rectangular coordinates  $(\tilde{x}, \tilde{y}, 0)$  illustrated in Fig. D.3(b). If the observation point is *far* then the vector potential may be approximated to ([13], chapter 6)

$$\mathbf{A} \approx \frac{\mu}{4\pi} \frac{e^{-jkR}}{R} \int_T \mathbf{J}_{PO} e^{jk\mathbf{r}' \cdot \hat{\mathbf{r}}} dS_c \quad (\text{D.32})$$

where  $\hat{\mathbf{r}}$  is the unit vector parallel to  $\mathbf{r}$ , that is the vector connecting the observation point and the centroid of  $T$  and  $\mathbf{r}' = \tilde{x}\hat{\mathbf{x}}_c + \tilde{y}\hat{\mathbf{y}}_c$  is the source or integration point ( $dS_c = d\tilde{x}d\tilde{y}$ ). Recalling (D.29) and given that

$$\mathbf{r}' \cdot \hat{\mathbf{r}} = \tilde{x} \sin \theta_s \cos \theta_s + \tilde{y} \sin \theta_s \sin \theta_s \quad (\text{D.33})$$

the vector potential may be written as

$$\mathbf{A} \approx \frac{\mu}{4\pi} \frac{e^{-jkR}}{R} \int_T \frac{2}{\zeta_0} e^{-jk(\alpha\tilde{x} + \beta\tilde{y})} (v_{x_c}\hat{\mathbf{x}}_c + v_{y_c}\hat{\mathbf{y}}_c) e^{jk(\sigma\tilde{x} + \tau\tilde{y})} d\tilde{x}d\tilde{y} \quad (\text{D.34})$$

where, using (D.30) and (D.33), the following coefficients have been introduced

$$v_{x_c} = \gamma E_{0_x} - \alpha E_{0_z} \quad (\text{D.35})$$

$$v_{y_c} = \beta E_{0_z} - \gamma E_{0_y} \quad (\text{D.36})$$

$$\sigma = \sin \theta_s \cos \theta_s \quad (\text{D.37})$$

$$\tau = \sin \theta_s \sin \theta_s \quad (\text{D.38})$$

with the coefficients  $\alpha$ ,  $\beta$  and  $\gamma$  given in (D.23), (D.24) and (D.28).

Hence, it is necessary to evaluate the integral

$$I_T = \int_T e^{-jk(\alpha\tilde{x} + \beta\tilde{y})} e^{jk(\sigma\tilde{x} + \tau\tilde{y})} d\tilde{x}d\tilde{y} \quad (\text{D.39})$$

to have the vector potential

$$\mathbf{A} \approx \frac{\mu}{4\pi} \frac{e^{-jk r}}{r} \frac{2}{\zeta_0} (v_{x_c} \hat{\mathbf{x}}_c + v_{y_c} \hat{\mathbf{y}}_c) I_T. \quad (\text{D.40})$$

Referring to the coordinate system  $(x', y')$  illustrated in Fig. D.3(b), it is

$$I_T = \mathcal{S} \int_T e^{-jk(\alpha x' + \beta y')} e^{jk(\sigma x' + \tau y')} dx' dy' \quad (\text{D.41})$$

where the shifting factor  $\mathcal{S}$  is

$$e^{jk(\alpha - \sigma)x_c} e^{jk(\beta - \tau)y_c} \quad (\text{D.42})$$

It follows, hence, that  $I_T = I_1 + I_2$  where

$$I_1 = \mathcal{S} \int_{T_a} e^{-jk(\alpha x' + \beta y')} e^{jk(\sigma x' + \tau y')} dx' dy' = \mathcal{S} \int_0^{x_3} \int_0^{(y_3 x')/x_3} e^{-jk(\alpha x' + \beta y')} e^{jk(\sigma x' + \tau y')} dx' dy' \quad (\text{D.43})$$

and

$$I_2 = \mathcal{S} \int_{T_b} e^{-jk(\alpha x' + \beta y')} e^{jk(\sigma x' + \tau y')} dx' dy' = \mathcal{S} \int_{x_3}^{x_2} \int_0^{-(y_3 x')/(x_2 - x_3) + (y_3 x_2)/(x_2 - x_3)} e^{-jk(\alpha x' + \beta y')} e^{jk(\sigma x' + \tau y')} dx' dy' \quad (\text{D.44})$$

where  $(x_i, y_i)$ , with  $i = 1 \dots 3$ , are the coordinates of the points 1, 2 and 3 illustrated in Fig. D.3(b) and  $T_a$  and  $T_b$  are the two subtriangles into which is subdivided  $T$ . It is clear from the definition of  $I_1$  and  $I_2$  that the integral  $I_T$  may be evaluated in a closed form, the integrand functions being exponential functions. The closed form for the expression of the scattered far-field radiated by a flat conducting polygon illuminated by a plane wave, is a direct consequence (see also [84]) of the Maggi-Rubinowicz representation, presented in [8], [82]-[83] and [85].

As reported in [13], p. 281, the electric far-field scattered by a current distribution may be approximated by

$$\mathbf{E} \approx -j\omega \mathbf{A} \quad (\text{D.45})$$

where  $\omega$  is the angular frequency of the incident plane wave ( $\omega = k\sqrt{\epsilon_0\mu_0}$ ). Hence, using (D.40), the electric field radiated by  $T$  is

$$\mathbf{E} \approx -j\omega \frac{\mu}{4\pi} \frac{e^{-jkr}}{r} \frac{2}{\zeta_0} (v_{x_c} \hat{\mathbf{x}}_c + v_{y_c} \hat{\mathbf{y}}_c) I_T \quad (\text{D.46})$$

and it follows from [13], pp. 287-288, that

$$E_r \approx 0 \quad (\text{D.47})$$

$$E_\theta \approx -\frac{jke^{-jkr}}{4\pi r} \zeta_0 N_\theta \quad (\text{D.48})$$

$$E_\phi \approx -\frac{jke^{-jkr}}{4\pi r} \zeta_0 N_\phi \quad (\text{D.49})$$

where

$$N_\theta = \frac{2}{\zeta_0} (v_{x_c} \cos \theta_s \cos \phi_s + v_{y_c} \cos \theta_s \sin \phi_s) I_T \quad (\text{D.50})$$

$$N_\phi = \frac{2}{\zeta_0} (-v_{x_c} \sin \theta_s + v_{y_c} \cos \theta_s) I_T \quad (\text{D.51})$$

and  $E_\theta$  and  $E_\phi$  are the  $\theta$  and  $\phi$  component of the electric field at the observation point of spherical coordinates  $(r, \theta_s, \phi_s)$  illustrated in Fig. D.3(a). Hence, the far-field radiated by the triangular patch at a point  $(r, \theta_s, \phi_s)$  may be approximated as a plane wave propagating along the  $r$  direction.

In summary, this section has presented the essential mathematical tool to express the far-field scattered by a PEC triangular patch illuminated by a *plane wave*, using the PO approximation. The result expressed in (D.48) and (D.49) may be seen as the extension of (5.33) to three dimensions.

### D.3 Plane wave expansion of the near-field

In this section, a plane wave expansion of the near-field radiated by a triangular patch illuminated by a plane wave is obtained. This task is accomplished using the



definition of multipole expansions given in [53] and Gegenbauer's addition theorem introduced in section 3.4.2.

To evaluate the electric field scattered by a triangular patch, the integral

$$\frac{\mu}{4\pi} \int_T \mathbf{J}_{PO} \frac{e^{-jkR}}{R} dS_c \tag{D.52}$$

must be performed (see [13], chapter 6). In (D.52),  $R$  is the distance between the source point  $(\tilde{x}, \tilde{y}, 0)$  and the observation point of spherical coordinates  $(r, \theta_s, \phi_s)$  (see Fig. D.3),  $\mathbf{J}_{PO}$  is the electric current density residing on  $T$ .

Referring to Fig. D.4, it is

$$\mathbf{R} = \mathbf{R}_c + \mathbf{d}_c. \tag{D.53}$$

Hence, recalling (3.20) it follows that

$$\frac{e^{-jkR}}{R} = \frac{e^{-jk|\mathbf{R}_c + \mathbf{d}_c|}}{|\mathbf{R}_c + \mathbf{d}_c|} = \frac{-jk}{4\pi} \int_{\Omega} d^2\hat{\mathbf{k}} e^{-jk\hat{\mathbf{k}} \cdot \mathbf{d}_c} \alpha(k, \hat{\mathbf{k}}, \mathbf{R}_c) \tag{D.54}$$

where the unit vector  $\hat{\mathbf{k}}$  has the spherical coordinates  $(\sin \theta \cos \phi, \sin \theta \sin \phi, \cos \theta)$ , as illustrated in Fig. D.4 and  $\alpha(k, \hat{\mathbf{k}}, \mathbf{R}_c)$  is the function

$$\alpha(k, \hat{\mathbf{k}}, \mathbf{R}_c) = \lim_{L \rightarrow \infty} \sum_{l=0}^L (-j)^l (2l+1) h_l^{(2)}(kR_c) P_l(\hat{\mathbf{k}} \cdot \hat{\mathbf{R}}_c). \tag{D.55}$$

Thus, (D.52) becomes

$$\frac{\mu}{4\pi} \int_T \mathbf{J}_{PO} \left( \frac{-jk}{4\pi} \right) \int_{\Omega} d^2\hat{\mathbf{k}} e^{-jk\hat{\mathbf{k}} \cdot \mathbf{d}_c} \alpha(k, \hat{\mathbf{k}}, \mathbf{R}_c) dS_c \tag{D.56}$$

In (D.52), the function  $\mathbf{J}_{PO}$  is expressed as in (D.29). Hence, one obtains the following plane wave expansion

$$\frac{\mu}{4\pi} \int_T \mathbf{J}_{PO} \frac{e^{-jkR}}{R} dS_c = -\frac{j\mu k}{(4\pi)^2} \int_{\Omega} d^2\hat{\mathbf{k}} \alpha(k, \hat{\mathbf{k}}, \mathbf{R}_c) \mathbf{M}_J(\hat{\mathbf{k}}) \tag{D.57}$$

where the multipole expansion  $\mathbf{M}_J(\hat{\mathbf{k}})$  has been introduced

$$\mathbf{M}_J(\hat{\mathbf{k}}) = \int_T \mathbf{J}_{PO} e^{-j\mathbf{k}\hat{\mathbf{k}}\cdot\mathbf{d}_c} dS_c. \quad (\text{D.58})$$

Recalling (D.29), the multipole expansion becomes

$$\mathbf{M}_J(\hat{\mathbf{k}}) = \frac{2}{\zeta_0} \mathbf{v} \int_T e^{-jk(\alpha\tilde{x}+\beta\tilde{y})} e^{-j\mathbf{k}\hat{\mathbf{k}}\cdot\mathbf{d}_c} d\tilde{x}d\tilde{y} \quad (\text{D.59})$$

The last step is to express the scalar product  $\hat{\mathbf{k}} \cdot \mathbf{d}_c$  as a function of the coordinates  $\tilde{x}$  and  $\tilde{y}$ . It is

$$\hat{\mathbf{k}} \cdot \mathbf{d}_c = -\sin\theta \cos\phi\tilde{x} - \sin\theta \sin\phi\tilde{y} \quad (\text{D.60})$$

and  $\mathbf{M}_J(\hat{\mathbf{k}})$  becomes

$$\frac{2}{\zeta_0} \mathbf{v} \int_T e^{-jk(\alpha\tilde{x}+\beta\tilde{y})} e^{-jk(-\sin\theta \cos\phi\tilde{x} - \sin\theta \sin\phi\tilde{y})} d\tilde{x}d\tilde{y} \quad (\text{D.61})$$

and may be evaluated analytically. In implementing (D.55), for the case of  $\mathbf{R}_c \approx \mathbf{d}_c$ , the number of terms needed for the series to converge may be very high. This could represent a slowing factor in the calculation of the plane wave expansion of the near-field due to the PO current. Nevertheless, the equality (D.54) is satisfied when  $\mathbf{R}_c > \mathbf{d}_c$ .

## D.4 Conclusion

A set of known results was presented in this chapter. Specifically, it was shown that the far-field scattered by the Physical Optics (PO) current induced on a triangular patch illuminated by a plane wave may be evaluated analytically in a simple way. Furthermore, a plane wave expansion of the near-field due to the PO current was derived using Gegenbauer's theorem (3.20).

The two expressions derived may represent a set of key formulae to begin an investigation on the possibility of an extension of ANIM, the method developed in

chapter 5, to three dimensions. The set of basis functions, for this case, may be chosen to be the PO currents excited on triangular patches by plane waves. It could appear that a PO approximation introduces considerable errors. It is true, however, that PO is a good approximation for modeling the current induced on a large surface whose radius of curvature is large compared with the wavelength, as discussed in [14], p. 356. Indeed, a very recent result [66] demonstrates that the PO current may be employed efficiently in modeling electromagnetic scattering by piecewise, large, smooth surfaces in two dimensions.

The incorporation of PO approximation into surface integral equations tackled using TIM/ANIM would allow massive computational savings, because the MoM impedance matrix need not be stored in memory. The current induced on planar triangular patches could be evaluated directly applying (D.29) and the scattered fields due to the PO currents would be readily evaluated applying (D.46).

A simple problem is currently tackled by Trinity College group using the formulation suggested. Specifically, the problem of scattering by a square flat plate of side of length  $500\lambda$  illuminated by an electric dipole located vertically over its centre is being investigated. It is important to stress that such a problem would require a complexity of  $\mathcal{O}(10^{15})$  using the MoM-CG scheme and a complexity of  $\mathcal{O}(10^8)$  using a multi-level FMM or FAFFA. Neither of these methods could be implemented even on the best available workstation. A successful implementation of TIM/ANIM, on the contrary, would render this problem solvable in the order of a few hours. The results, obviously for the case of a planar surface, are expected to be highly satisfactory.

A second stage of research investigation would consist of applying the same method to a slowly corrugated version of the square flat plate, by modeling the near interactions using a single plane wave, as is done in TIM/ANIM. Results could be then compared with reference data. Should be found any disagreement, the plane wave expansion of the near-field developed in section D.3 would need be incorporated, in order to model the near-field interactions in a more accurate way, as is suggested

in [68].

In conclusion, it is proposed that a PO approximation of the electric current would be sufficiently adequate to embark an extension of TIM/ANIM to three dimensions. It is expected, however, that care must be taken in evaluating the near-field interactions, which may be modeled using the plane wave expansion discussed in section D.3. It is argued that an extension to three dimensions of the method proposed in [68] using the PO approximation may be developed in the future.

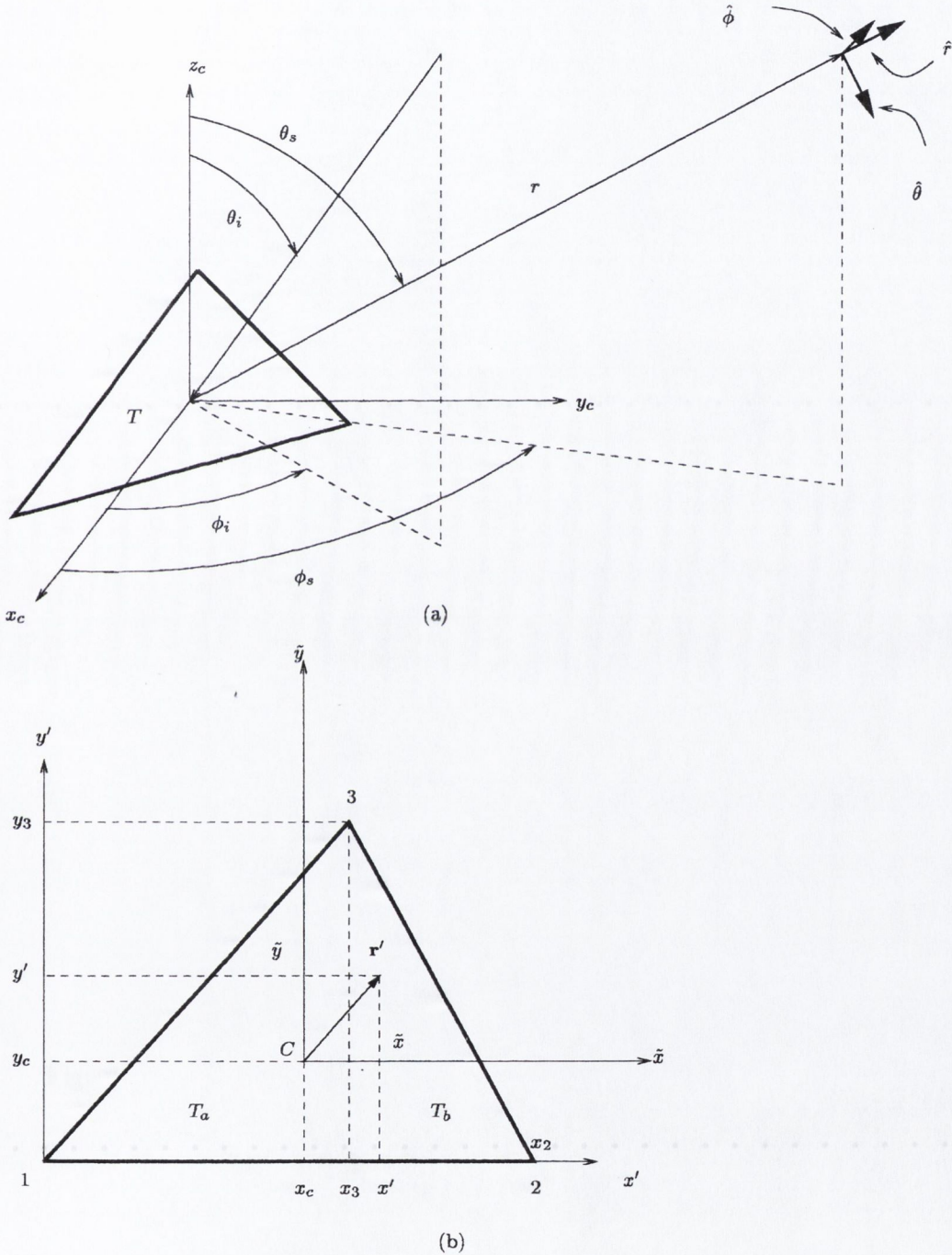


Figure D.3: Geometry of the far-field evaluation for a planar triangular patch illuminated by a plane wave incident at angles  $\theta_i$  and  $\phi_i$ . In (a) the triangle  $T$  and the observation point  $(r, \theta, \phi)$  are illustrated, with the spherical coordinate system centred at the centroid of  $T$  and the rectangular coordinate system  $(x_c, y_c, z_c)$ . In (b) the plane of the triangle is illustrated with the two different coordinate system  $(x_c, y_c)$  and  $(x', y')$ . For each point  $\mathbf{r}'$ , its coordinate  $\tilde{x}$  with respect to the centroid  $C$  of  $T$  is such that  $x_c + \tilde{x} = x'$ . Similar relation holds for  $y_c$ . The closed form integral  $I_T$  given in (D.40) is evaluated referring to the coordinate system  $(x', y')$ .

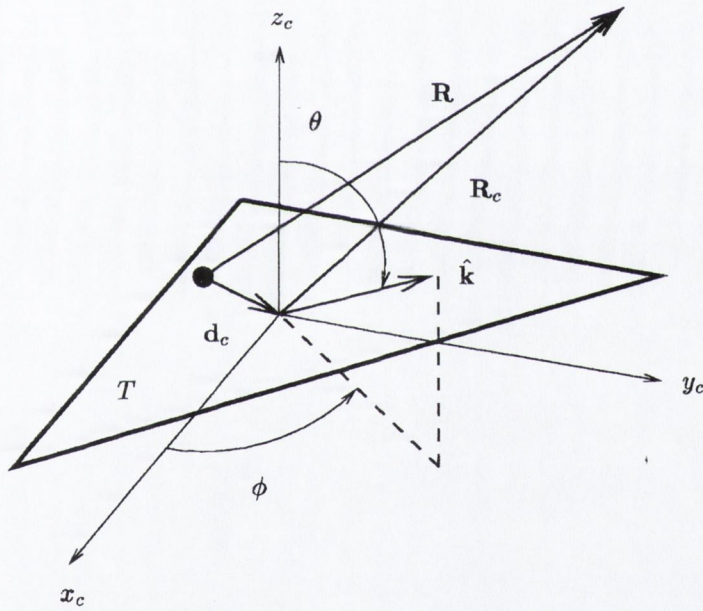


Figure D.4: Geometry for the calculation of the near-field scattered by  $T$ .

---

**BIBLIOGRAPHY**

---

- [1] J. A. Stratton, *Electromagnetic Theory*, McGraw-Hill, 1941.
- [2] A. Erdelyi, *Asymptotic Expansions*, Dover, 1956.
- [3] R. F. Harrington, *Time-Harmonic Electromagnetic Fields*, McGraw-Hill, 1961.
- [4] P. Beckmann and A. Spizzichino, *The Scattering of Electromagnetic Waves from Rough Surfaces*, Pergamon Press, 1963.
- [5] A. Sommerfeld, *Partial Differential Equations in Physics*, Academic Press, 1964.
- [6] A. Sommerfeld, *Optics*, Academic Press, 1964.
- [7] R. F. Harrington, *Field Computation by Moment Methods*, Macmillan, 1968.
- [8] M. Born and E. Wolf, *Principles of Optics*, Sixth Ed., Pergamon Press, 1980.
- [9] I. S. Gradshteyn and I. M. Ryzhik, *Tables of Integrals, Series and Products*. Academic Press, 1980.
- [10] J. Stoer, "Solution of large linear systems of equations by conjugate gradient type methods," in *Mathematical Programming: The State of the Art*, eds. A. Bachem, M. Grottschel, and B. Korte, Springer Verlag, 1983.
- [11] P. J. Davis and P. Rabinowitz *Methods of numerical integration*, Academic Press, 1984.
- [12] G. Strang, *Linear Algebra and Its Applications*, Harcourt Brace Javanovich, 1988.

- 
- [13] C. A. Balanis, *Advanced Engineering Electromagnetics*, John Wiley & Sons, 1989.
- [14] A. Ishimaru, *Electromagnetic Wave Propagation Radiation and Scattering*, Prentice-Hall, 1991.
- [15] J. Jin, *The Finite Element Method in Electromagnetics*, John Wiley and Sons, 1993.
- [16] K. S. Kunz and R. Luebbers, *The Finite Difference Time Domain Method for Electromagnetics*, CRC Press, 1993.
- [17] D. S. Jones, *Methods in Electromagnetic Propagation*, second ed., Oxford Press, 1994.
- [18] D. G. Dudley, *Mathematical Foundations for Electromagnetic Theory*, IEEE Press, 1994.
- [19] T. B. A. Senior and J. L. Volakis, *Approximate Boundary Conditions in Electromagnetics*, IEE Press, 1995.
- [20] G. Franceschetti, *Electromagnetics: Theory, Techniques and Engineering Paradigms*, Plenum Press, New York, 1997.
- [21] A. F. Peterson, S. L. Ray, and R. Mittra, *Computational Methods for Electromagnetics*, IEEE Press, 1998.
- [22] R. F. Millar, "An Approximate Theory of the Diffraction of an Electromagnetic Wave by an Aperture in a Plane Screen," *Proc. IEEE*, Vol. 103, Part C, March 1956, pp. 177-185.
- [23] J. B. Keller, "Diffraction by an Aperture," *J. App. Phys.*, Vol. 28, No. 4, April 1957, pp. 426-444.
- [24] P. Ia. Ufimtsev, "Approximate Computation of the Diffraction of Plane Electromagnetic Waves at Certain Metal Bodies: Pt. I. Diffraction Patterns at



- a Wedge and a Ribbon," *Zh. Tekhn. Fiz.* (USSR), Vol. 27, No. 8, 1957, pp. 1708-1718.
- [25] E. F. Knott, and T. B. A. Senior, "Equivalent Currents for a Ring Discontinuity," *IEEE Trans. Antennas and Propagation*, Vol. AP-21, September 1973, pp. 693-695.
- [26] K. M. Mitzner, "Incremental Length Diffraction Coefficients," Technical Report No. AFAL-TR-73-296, Northrop Corporation, Aircraft Division, April 1974.
- [27] R. G. Kouyoumjian, and P. H. Pathak, "A Uniform Theory of Diffraction for an Edge in a Perfectly Conducting Surface," *Proc. IEEE*, Vol. 62, No. 11, November 1974, pp. 1448-1461.
- [28] A. Michaeli, "Equivalent Edge Currents for Arbitrary Aspects of Observation," *IEEE Trans. Antennas and Propagation*, Vol. AP-32, No. 3, March 1984, pp. 252-258.
- [29] J. M. Jin, J. L. Volakis, and J. D. Collins, "A Finite-Element - Boundary-Integral Method for Scattering and Radiation by Two- and Three-Dimensional Structures," *IEEE Antennas and Propagation Magazine*, Vol. 33, No. 3, June 1991, pp. 22-32.
- [30] J. Meixner, "The Behavior of Electromagnetic Fields at Edges," *IEEE Trans. Antennas and Propagation*, Vol. AP-20, No. 4, July 1972, pp. 442-446.
- [31] D. R. Wilton, and S. Govind, "Incorporation of Edge Conditions in Moment Method Solutions," *IEEE Trans. Antennas and Propagation*, Vol. AP-25, No. 6, November 1977, pp. 845-850.
- [32] N. Morita, "Resonant Solutions Involved in the Integral Equation Approach to Scattering from Conducting and Dielectric Cylinders," *IEEE Trans. Antennas and Propagation*, Vol. AP-27, No. 6, November 1979, pp. 869-871.

- 
- [33] S. M. Rao, D. R. Wilton, and A. W. Glisson, "Electromagnetic Scattering by Surfaces of Arbitrary Shape," *IEEE Trans. Antennas and Propagation*, Vol. AP-30, No. 3, May 1982, pp. 409-418.
- [34] M. R. Hestenes and E. Stiefel, "Methods of Conjugate Gradients for Solving Linear Systems," *Jnl. of Res. Nat. Bur. Standards*, Vol. 49, No. 6, December 1952, pp. 409-436.
- [35] T. K. Sarkar, K. R. Siarkiewicz, and R. F. Stratton, "Survey of Numerical Methods for Solution of Large Systems of Linear Equations for Electromagnetic Field problems," *IEEE Trans. Antennas and Propagation*, Vol. AP-29, No. 6, November 1981, pp. 847-856.
- [36] A. F. Peterson, and R. Mittra, "Convergence of the Conjugate Gradient Method when Applied to Matrix Equations Representing Electromagnetic Scattering Problems," *IEEE Trans. Antennas and Propagation*, Vol. AP-34, No. 12, December 1986, pp. 1447-1454.
- [37] A. F. Peterson, C. F. Smith, and R. Mittra, "Eigenvalues of the Moment-Method Matrix and Their Effect on the Convergence of the Conjugate Gradient Algorithm," *IEEE Trans. Antennas and Propagation*, Vol. AP-36, No. 8, August 1988, pp. 1177-1179.
- [38] J. W. Cooley, and J. W. Tukey, "An Algorithm for the Machine Calculation of Complex Fourier Series," *Math. of Computat.*, Vol. 19, No. 90, 1965, pp. 297-301.
- [39] L. W. Pearson, "A Technique for Organizing Large Moment Calculations for Use with Iterative Solutions Methods," *IEEE Trans. Antennas and Propagation*, Vol. AP-33, No. 9, September 1985, pp. 1031-1033.
- [40] T. K. Sarkar, E. Arvas, and S. M. Rao, "Application of FFT and Conjugate Gradient Method for the Solution of Electromagnetic Radiation from Elec-

- 
- trically Large and Small Conducting Bodies," *IEEE Trans. Antennas and Propagation*, Vol. AP-34, No. 5, May 1986, pp. 635-640.
- [41] T. J. Peters, and J. L. Volakis, "Application of a Conjugate Gradient FFT Method to Scattering from Thin Planar Material Plates," *IEEE Trans. Antennas and Propagation*, Vol. AP-36, No. 4, April 1988, pp. 318-326.
- [42] M. F. Catedra, J. G. Cuevas, and L. Nuno, "A Scheme to Analyze Conducting Plates of Resonant Size Using the Conjugate-Gradient Method and the Fast Fourier Transform," *IEEE Trans. Antennas and Propagation*, Vol. AP-36, No. 12, December 1988, pp. 1744-1752.
- [43] E. J. Rothwell, and M. J. Cloud, "A Hallen-Type Integral Equation for Symmetric Scattering from Lossy Circular Disks," *IEEE Trans. Antennas and Propagation*, Vol. AP-40, No. 8, August 1992, pp. 920-925.
- [44] U. Jakobus, and F. Landstorfer, "Improved PO-MM Hybrid Formulation for Scattering from Three-Dimensional Perfectly Conducting Bodies of Arbitrary Shape," *IEEE Trans. Antennas and Propagation*, Vol. AP-43, No. 2, February 1995, pp. 162-169.
- [45] P. C. Clemmow, "Some extensions to the method of integration by steepest descents," *Q. J. Mech. Appl. Math.*, 3, 1950, pp. 241-256.
- [46] C. J. Bouwkamp, and H. B. G. Casimir, "On Multipole Expansions in the Theory of Electromagnetic Radiation," *Physica*, XX, 1954, pp. 539-554.
- [47] V. Rokhlin, "Rapid solution of integral equations of classical potential theory," *J. Comput. Phys.*, Vol. 60, No. 2, September 1985, pp. 187-207.
- [48] C. C. Lu and W. C. Chew, "Fast Algorithm for Solving Hybrid Integral Equations," *IEE Proceedings-H*, Vol. 140, pp. 455-460, December 1993.
- [49] R. L. Wagner, and W. C. Chew, "A Ray-Propagation Fast Multipole Algorithm," *Micro. Opt. Tech. Lett.*, Vol. 7, No. 10, pp. 435-438, July 1994.

- 
- [50] R. J. Burkholder, and D. H. Kwon, "High-frequency asymptotic acceleration of the fast multipole method," *Radio Science*, Vol. 31, No. 5, pp. 1199-1206, September-October 1996.
- [51] A. D. McLaren, "Optimal numerical integration over a sphere," *Mathematics of Computation*, Vol. 17, pp. 361-383, 1963.
- [52] R. Coifman, V. Rokhlin, and S. Wandzura, "The Fast Multipole Method for the Wave Equation: A Pedestrian Description," *IEEE Antennas and Propagation Magazine*, Vol. 35, No. 3, pp. 7-12, June 1993.
- [53] J. M. Song, and W. C. Chew, "Multilevel fast-multipole algorithm for solving combined field integral equations for electromagnetic scattering," *Micro. Opt. Technol. Lett.*, Vol. 10, No. 1, pp. 14-19, Sept. 1995.
- [54] J. M. Song, C. C. Lu, and W. C. Chew, "Multilevel Fast Multipole Algorithm for Electromagnetic Scattering by Large Complex Objects," *IEEE Transactions on Antennas and Propagation*, Vol. 45, No. 10, pp. 1488-1493, October 1997.
- [55] C. C. Lu, and W. C. Chew, "Fast Far-Field Approximation for Calculating the RCS of Large Objects," *Micro. Opt. Techn. Lett.*, Vol. 8, No. 5, pp. 238-240, April 1995.
- [56] J. T. Hviid, J. Bach Andersen, J. Toftgård, and J. Bøjer, "Terrain Based Propagation Model for Rural Areas-An Integral Equation Approach," *IEEE Transactions on Antennas and Propagation*, Vol. 43, No. 1, pp. 41-46, January 1995.
- [57] D. Moroney, and P. J. Cullen, "A fast integral equation approach to UHF coverage estimation," in *Mobile Personal Communications: Proc. 2nd Joint COST 227/231 Workshop on Mobile Personal Commun.*, Florence, Italy, pp. 20-21, April 1995.

- 
- [58] D. Moroney, "Computational methods for the calculation of electromagnetic scattering from large-scale perfect electric conductors," Ph.D. dissertation, University of Dublin, Trinity College, Ireland, 1995.
- [59] D. Holliday, L. L. DeRaad, and G. J. St-Cyr, "Forward Backward: a New Method for Computing Low Grazing Angle Scattering," *IEEE Transactions on Antennas and Propagation*, Vol. 44, No. 5, pp. 722-729, May 1996.
- [60] J. T. Johnson, R. T. Shin, J. C. Eidson, L. Tsang, and L. A. Kong, "A Method of Moments Model for VHF Propagation," *IEEE Transactions on Antennas and Propagation*, Vol. 45, No. 1, pp. 115-125, January 1997.
- [61] C. Brennan, P. J. Cullen, and L. Rossi, "A high speed adaptive methodology for calculating UHF propagation loss over terrain," in *8th IEEE Int. Symp. personal, Indoor, Mobile Radio Comm.*, Helsinki, Finland, pp. 629-634, September 1997.
- [62] C. Brennan and P. J. Cullen, "Tabulated Interaction Method for UHF Terrain Propagation Problems," *IEEE Trans. Antennas and Propagation*, Vol. 46, pp. 738-739, May 1998.
- [63] C. Brennan, and P. J. Cullen, "Application of the Fast Far-Field Approximation to the Computation of UHF Pathloss over Irregular Terrain," *IEEE Transactions on Antennas and Propagation*, Vol. 46, No. 6, pp. 881-890, June 1998.
- [64] C. Brennan, "Numerical methods for the efficient computation of electromagnetic scattering from a class of large scale perfect electric conductors," Ph.D. dissertation, University of Dublin, Trinity College, Ireland, 1998.
- [65] O. M. Bucci, and G. Franceschetti, "On the Degrees of Freedom of Scattered Fields," *IEEE Trans. Antennas and Propagation*, Vol. 37, No. 7, pp. 918-926, July 1989.

- 
- [66] C. Brennan, P. J. Cullen, and L. Rossi, "An MFIE-based Tabulated Interaction Method for UHF Terrain Propagation problems," submitted to *IEEE Trans. Antennas and Propagation*, 1999.
- [67] C. Brennan and P. J. Cullen, "Multilevel Tabulated Interaction Method Applied to UHF Propagation over Irregular Terrain," to appear in *IEEE Trans. Antennas and Propagation*.
- [68] C. Brennan, and P. J. Cullen, "A Method for Producing a Sparse Discretised Integral Operator Allowing A Priori Determination of the Interaction Terms," ICEAA99 Conference, Turin, September 1999.
- [69] L. Rossi, P. J. Cullen, and C. Brennan, "An Analytical Approximation of the TIM Look-up Table," COST259 TD(99) Meeting, Thessaloniki, January 1999.
- [70] L. Rossi, P. J. Cullen, and C. Brennan, "A Method to Produce a Sparse Discretised First Kind Scalar Integral Equation Operator Allowing A Priori Determination of the Interaction Terms," submitted to *Journal of Acoustical Society of America*, 1999.
- [71] C. Brennan, L. Rossi, and P. J. Cullen, "Efficient Integral Equation Based Analysis of Plane-Wave Scattering from Infinite Periodic Perfectly Conducting Structures," ICEAA99 Conference, Turin, September 1999.
- [72] C. T. Reddy, D. J. Shippy, "Alternative Integration Formulae for Triangular Finite Elements," *International Journal for Numerical Methods in Engineering*, Vol. 17, pp. 133-139, 1981.
- [73] D. R. Wilton, S. M. Rao, A. W. Glisson, D. H. Schaubert, O. M. Al-Bundak, and C. M. Butler, "Potential Integrals for Uniform and Linear Source Distributions on Polygonal and Polyhedral Domains," *IEEE Trans. Antennas and Propagation*, Vol. AP-32, No. 3, March 1984, pp. 276-281.

- 
- [74] R. D. Graglia, "On the Numerical Integration of the Linear Shape Functions Times the 3-D Green's Function or its Gradient on a Plane Triangle," *IEEE Trans. Antennas and Propagation*, Vol. 41, No. 10, October 1993, pp. 1448-1455.
- [75] T. F. Eibert, and V. Hansen, "On the Calculation of Potential Integrals for Linear Source Distributions on Triangular Domains," *IEEE Trans. Antennas and Propagation*, Vol. 43, No. 12, December 1995, pp. 1499-1502.
- [76] L. Rossi, and P. J. Cullen, "On the Fully Numerical Evaluation of the Linear-Shape Function Times the 3-D Green's Function on a Plane Triangle," *IEEE Trans. Microwave Theory and Techniques*, Vol. MTT-47, No. 4, April 1999, pp.398-402.
- [77] J. Barnes, and P. Hut, "A Hierarchical  $O(N \log N)$  Force-calculated Algorithm," *Nature*, Vol. 324, pp. 446-449, December 4, 1986.
- [78] L. Greengard, and V. Rokhlin, "A Fast Algorithm for Particle Simulations," *Journal of Computational Physics*, Vol. 73, pp. 325-348, December 1987.
- [79] A. McCowen, "Efficient 3D moment-method analysis for reflector antennas using a far-field approximation technique," *IEE Proceedings-H*, Vol. 146, pp. 7-13, February 1999.
- [80] L. Rossi, and P. J. Cullen, "An Implementation of a Multilevel Fast Far-Field Algorithm for Solving Electric Field Integral Equations - Abstract", PIERS99 Conference, Taipei, March 1999.
- [81] L. Rossi, P. J. Cullen, and C. Brennan, "An Implementation of a Multilevel Fast Far-Field Algorithm for Solving Electric Field Integral Equations", *IEE Proceedings-H*, to appear.
- [82] K. Miyamoto, and E. Wolf, "Generalization of the Maggi-Rubinowicz Theory of the Boundary Diffraction Wave-part I," *Journal of the Optical Society of America*, Vol. 52, No. 6, pp. 615-625, June 1962.

- [83] K. Miyamoto, and E. Wolf, "Generalization of the Maggi-Rubinowicz Theory of the Boundary Diffraction Wave-part II," *Journal of the Optical Society of America*, Vol. 52, No. 6, pp. 626-637, June 1962.
- [84] W. B. Gordon, "Far-Field Approximations to the Kirchhoff-Helmholtz Representations of Scattered Fields," *IEEE Transactions on Antennas and Propagation*, pp. 590-592, July 1975.
- [85] R. Meneghini, P. Shu, and J. Bay, "Several Maggi-Rubinowicz Representation of the Electric Field," *IEEE Transactions on Antennas and Propagation*, Vol. AP-30, No. 3, pp. 516-520, May 1982.